Internal Report
DESY F35D-97-08
August 1997

G

Radiation Tolerance of Silicon Particle Detectors for High-Energy Physics Experiments

by

H. Feick

Radiation Tolerance of Silicon Particle Detectors for High-Energy Physics Experiments

Dissertation
zur Erlangung des Doktorgrades
des Fachbereichs Physik
der Universität Hamburg

vorgelegt von
Henning Feick
aus Stade

Hamburg
1997

Radiation Tolerance of Silicon Particle Detectors for High-Energy Physics Experiments

Dissertation
zur Erlangung des Doktorgrades
des Fachbereichs Physik
der Universität Hamburg

vorgelegt von
Henning Feick
aus Stade

Hamburg
1997

Gutachter der Dissertation	:	Prof. Dr. Dr. hc. G. Lindström Prof. Dr. R. Klanner Prof. Dr. E. Weber
Gutachter der Disputation	:	Prof. Dr. Dr. hc. G. Lindström Prof. Dr. A. Wagner
Datum der Disputation	:	15.08.1997
Dekan des Fachbereichs Physik und Vorsitzender des Promotionsausschusses	:	Prof. Dr. B. Kramer

Abstract

This work provides a study on the radiation tolerance of silicon particle detectors in the light of their application in present-day and future high-energy physics (HEP) experiments. These devices are typically placed close to the interaction points where they have to face high radiation levels inducing both displacement (bulk) and ionization (surface) damage. While the problems connected with the reverse currents can be circumvented by operation at reduced temperatures ($\approx$ 0°C), the bulk damage induced change in the doping concentration causes a serious increase in the operational voltage, even enhanced by long term annealing. Further aspects are elucidated in this field, however, the focus of the thesis is on the new approach to examine the displacement damage defects on the microscopic scale and to explore their relation to the macroscopic properties.

Firstly, the test structures fabricated from high resistivity float zone silicon are characterized by standard capacitance/current voltage (CV/IV) curves, and peculiarities related to the shape of the electric field zone are discussed in conjunction with results from proton micro-beam studies. Further, laser-induced current pulse shapes are used to determine the field distribution in the detectors, allowing for the verification of the doping concentrations as inferred from CV data.

The elevated temperature annealing behavior of the leakage current and the doping concentration in weakly and heavily damaged devices has been investigated, giving rise to a critical revision of the model descriptions of the damage-induced changes in the operational parameters. The constants characterizing these models are studied as function of the type of the damaging particle (n, p, π, ^{60}Co-γ) and of the properties of the starting material. While the former allows for an intercalibration of the different sources, the latter is considered as both an experimental search for a material of improved radiation hardness and an effort to correlate the macroscopic damage effects with the microscopic composition of the doping. In particular, lower resistivity n-type silicon is found to be more radiation hard.

A full account is given of the measurement of Thermally Stimulated Currents (TSC) which has proven to be the most successful method of recognizing the microscopic features of the displacement damage. However, an unambiguous interpretation of the spectra is not straight-forward, and considerable efforts have been made to unveil the influence of the experimental conditions, chiefly aiming at an accurate extraction of the defect concentrations. Concerning the effect of the filling temperature, the carbon-oxygen complex is found to play a major role. Moreover, deep level ionization energies and cross sections have been evaluated. In this respect more plentiful data have been obtained by means of current Deep Level Transient Spectroscopy (I-DLTS), which in contrast to TSC even allows for the examination of close-to-midgap and very shallow defect levels. Finally, current pulse shape measurements were employed to characterize close-to-midgap traps in neutron and ^{60}Co-gamma damaged samples.

It is shown that none of the usually encountered damage-induced defects (VO_i, C_iO_i, VV, and C_iC_s) can account for the observed deterioration of the silicon detectors. Thus less abundant and otherwise overlooked traps have been considered. The observations made on ^{60}Co-gamma damaged samples allow for conclusions regarding their presently unknown chemical nature. TSC has been used to monitor the defect evolution during isochronous annealing, allowing a correlation with the simultaneous macroscopic changes. For the first time evidence is provided for the connection of a sole defect level, exhibiting a metastable behavior, with negative space charge. The defect might also play a role in the long term annealing of the doping concentration.

Ionization damage has been investigated using 20 keV electrons from an electron microscope and ^{60}Co-gammas. Both the positive oxide charge and the interface recombination velocity are found to be growing as function of the ionization dose and to approach a saturation level.

Finally, the deterioration of the silicon devices to be expected in the inner detector of the approved ATLAS experiment at the LHC is predicted. These calculations, which have been a key design consideration in the ATLAS Technical Proposal, are based on a compilation of all experimental bulk damage data available at that time. The derivation of the world average damage constants and the implementation of the numerical models is presented, and the simulation results are discussed in the framework of the current understanding of the radiation damage processes.

Kurzfassung

In dieser Arbeit wird die Strahlenhärte von Silizium-Teilchendetektoren im Hinblick auf ihren Einsatz in heutigen und zukünftigen Experimenten der Hochenergiephysik untersucht. Die Detektoren werden zum Nachweis der Teilchenspuren im Innendetektor eingesetzt, wo sie einem hohen Strahlungsniveau ausgesetzt sind. Dies führt sowohl zu Versetzungs- (*bulk*) als auch Ionisationsschäden (Oberflächen). Der durch *bulk*-Schäden bewirkte Anstieg des Sperrstroms kann durch den Betrieb bei moderat tiefen Temperaturen ($\approx$ 0°C) umgangen werden, wohingegen die Änderung der Dotierung einen bedeutenden Anstieg der Betriebsspannung verursacht, der durch Langzeiteffekte noch verstärkt wird. Obgleich hinsichtlich dieser Effekte weitere Aspekte untersucht werden, liegt der Schwerpunkt der Arbeit auf der mikroskopischen Analyse der Versetzungsdefekte und der Darlegung ihrer Beziehung zu den makroskopischen Eigenschaften.

Zuerst werden die aus hochohmigem Silizium gefertigten Teststrukturen mit Kapazitäts/Strom-Spannungs Kennlinien (CV/IV) charakterisiert, wobei Besonderheiten, verknüpft mit der Ausdehnung der elektrischen Feldzone, im Zusammenhang mit Protonen-Mikrostrahlmessungen diskutiert werden. Zusätzlich wird die Feldverteilung mit laserinduzierten Stromimpulsen bestimmt, wodurch die Überprüfung der aus CV Daten gewonnenen Dotierungskonzentrationen ermöglicht wird.

Das Ausheilverhalten des Sperrstroms und der Dotierung bei erhöhten Temperaturen wurde an schwach und stark bestrahlten Proben untersucht, woraus eine kritische Revision der Modellbeschreibungen der schädigungsinduzierten Änderungen der Betriebsparameter resultiert. Die Konstanten in diesen Modellen werden systematisch als Funktion des Typs des schädigenden Teilchens (n, p, π, ^{60}Co-γ) und der Eigenschaften des Ausgangmaterials bestimmt. Ersteres liefert Kalibrierungsfaktoren für die einzelnen Quellen, während letzteres sowohl als eine experimentelle Suche nach strahlenhärterem Material, als auch als ein Versuch, die makroskopischen Größen mit der mikroskopischen Zusammensetzung der Dotierung zu korrelieren, aufgefaßt werden kann. Insbesondere wird niederohmigerem n-Silizium eine größere Strahlenhärte bescheinigt.

Das TSC Verfahren (Thermally Stimulated Current) erweist sich als das Erfolgreichste beim Nachweis der mikroskopischen Eigenschaften der Versetzungsschäden und wird im Detail behandelt. Beträchtliche Anstrengungen wurden unternommen, um den Einfluß der experimentellen Bedingungen zu analysieren und somit eine eindeutige Interpretation der Spektren zu erlangen. Weiterhin werden Ionisierungsenergien und Wirkungsquerschnitte von Störstellen bestimmt. Reichhaltigere Ergebnisse wurden hier mit dem Strom-DLTS (Deep Level Transient Spectroscopy) Verfahren erzielt, welches im Gegensatz zu TSC auch die Untersuchung von Niveaus nahe der Bandlückenmitte und den Bandkanten erlaubt. Schließlich werden Stromimpulsmessungen zur spektroskopischen Charakterisierung besonders tiefer Haftstellen in Neutronen- und ^{60}Co-γ bestrahlten Proben benutzt.

Es wird gezeigt, daß die vorwiegend auftretenden strahleninduzierten Defekte (VO_i, C_iO_i, VV und C_iC_s) nicht für die Schädigungseffekte in den Detektoreigenschaften verantwortlich sein können, so daß anderweitig übersehene Störstellen in diesem Zusammenhang diskutiert werden müssen. Schlußfolgerungen bezüglich ihrer bislang unbekannten chemischen Zusammensetzung können aus den Beobachtungen nach ^{60}Co-γ Bestrahlung gezogen werden. Das TSC Verfahren wurde benutzt, um Defektumwandlungen bei isochronaler Ausheilung zu messen, was eine Korrelation mit den gleichzeitig ablaufenden makroskopischen Prozessen erlaubt. Erstmals konnte ein einzelnes metastabiles Defektniveau mit negativer Raumladung in Verbindung gebracht werden. Dieser Defekt könnte auch für die Langzeitausheilung der Dotierung von Bedeutung sein.

Ionisationsschädigung wurde untersucht mit 20 keV Elektronen aus einem Elektronenmikroskop und ^{60}Co-γ Strahlung. Sowohl die positive Oxidladung als auch die Grenzflächenrekombinationsgeschwindigkeit steigen als Funktion der Dosis an und nähern sich einem Sättigungswert.

Schließlich wird die Schädigung der Siliziumkomponenten im genehmigten ATLAS Experiment beim LHC vorausgesagt. Diese Rechnungen, welche ein wesentliches Designkriterium im Technical Proposal waren, stützen sich auf eine Sammlung aller experimentellen *bulk*-Schädigungsdaten, die zu dem Zeitpunkt verfügbar waren. Die Ableitung der Weltmittelwerte der Schädigungskonstanten und die Implementierung der numerischen Modelle werden vorgestellt. Die Resultate der Simulationen werden im Rahmen des jetzigen Verständnisses der Strahlenschädigungsprozesse diskutiert.

Contents

1 Introduction

It was emphasized by A.M. Litke and A.S. Schwarz that the progress in high-energy physics is based on the superior spatial resolution and short recognition time achievable with silicon detectors employed for the tracking of ionizing particle traces close to the interaction point of collider experiments [LIT95]. One example that has gained much public interest in this respect is the confirmation of the existence of the top quark in March 1995 from the Fermi National Accelerator Laboratory (FNAL), Batavia, Illinois at the Tevatron 900 GeV proton-antiproton collider, which would have been very difficult without the use of silicon microstrip detectors. Besides the ability to accurately measure the momenta of energetic charged particles from the slight bending of their trajectories in a magnetic field, a key feature of modern tracking systems is the capability to distinguish secondary from primary vertices. The secondary vertex arises from the decay of a short-lived particle, which is the subject of the investigation, and which is created in the primary interaction of the colliding beam particles. For instance charmed particles, containing a charm quark, and tau leptons, which have been studied using such detection systems, live for around one picosecond and 0.3 picoseconds, respectively. At a speed close to the speed of light they can then travel only some millimeters before they decay. The traces of the longer-lived particles emerging at that point are reconstructed from the corresponding observations made in the outer gaseous wire chambers, Transition Radiation Trackers (TRTs), and the hits noticed in few layers of silicon detectors, frequently arranged cylindrical around the beam pipe, compare Fig. 1.1. It turns out that the spatial resolution in these layers needs to be of the order of a few tens of microns in order to unambiguously isolate secondary or even the tertiary vertices.

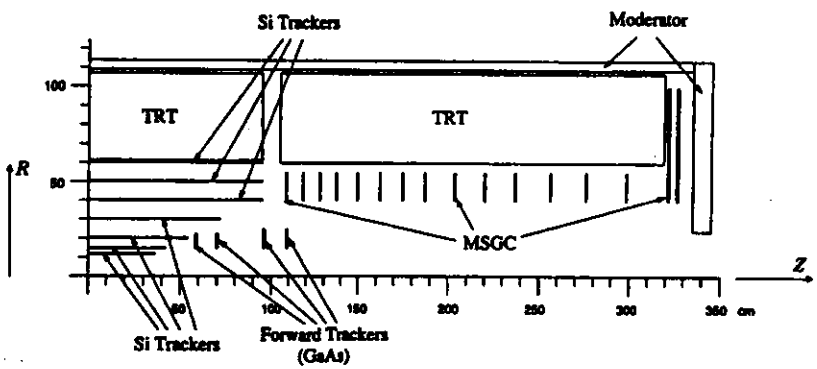

Fig. 1.1 An inner detector design for the ATLAS detector at the LHC with a single TRT (Transition Radiation Tracker) in the barrel region, silicon and GaAs modules comprising the SCT (SemiConductor Tracker), and MSGCs (MicroStrip Gas Counters) throughout the end-cap TRT, from reference [GOR94].

Bottom particles containing a bottom quark have a lifetime of 1.5 ps and therefore are also the objective of such tracking systems. For instance, particles containing the top quark decay nearly all the time into bottom particles. Future experiments will examine the differences in bottom and antibottom particles, giving important insights into the field of CP violation. Moreover, the elusive Higgs boson, hypothesized to endow matter with mass, decays into bottom and antibottom particles, given it is not too massive. Thus, silicon microstrip detectors are also central for the newest and future investigations. One example is the currently constructed HERA-B experiment, employing a wire target in the 820 GeV proton beam halo of HERA (Hadron Elektron Ring-Anlage) at DESY (Deutsches Elektronen SYnchrotron) in Hamburg, Germany. Further, there are the approved ATLAS (A Toroidal Lhc ApparatuS) and CMS (Central Muon Solenoid) experiments located at two of the four interaction points of the planned Large

Hadron Collider (LHC), that will provide proton-proton interactions at 14 TeV in the 27 km long LEP (Large Electron-Positron collider) tunnel at the French-Swiss border near Geneva.

The required spatial tracking resolution is achieved by fine segmentation. Regarding a strip detector for the ATLAS SemiConductor Tracker (SCT), 1536 6 cm long narrow junctions are implanted on a typical 300 µm thick silicon layer at a distance of 37.5 µm (readout pitch 112.5 µm) [ATL94]. Two of such elements are bonded together, giving an overall active area of around 12 cm times 6 cm. Since the long strips do not provide a sufficient position information, the same number of diodes is placed on the backplane of these elements at a small stereo angle of 40 mrad, either by correspondingly processing the wafer or by simply gluing two elements back-to-back. The resulting module is attached to a fixture and the electronic readout chips are placed in the direct vicinity. Several thousands of such modules will be arranged on the four barrel strip-layers around the beam axis, compare Fig. 1.1. Evidently, simultaneous particle hits on the same strip can cause ambiguities. Therefore further segmentation is necessary in the innermost layers, where an extreme density of particles is anticipated. The whole silicon layer is then subdivided into small pixels of the area of e.g. 50×300 µm^2. Local electronic readout is realized by bump-bonding a device with equally spaced readout chips to the pixel layer.

Promising new physical results are unfortunately related to some very rarely produced particles. To the experimental end this requires a very high event rate, almost 10^9 per second at LHC. Therefore, the detectors and the electronics will be harshly irradiated in these experiments, and almost certainly will the radiation damage effects lead to the ultimate failure of some devices after a certain period of operation, depending on the position within the experimental environment. The radiation level can be expressed in terms of the equivalent 1 MeV neutron particle fluence absorbed per year, shown in Fig. 1.2 for the ATLAS Inner Detector according to the simulations carried out by G. Gorfine [GOR95]. A distinction is made between charged particles (top), which are mainly pions, and neutrons (bottom). While the charged particles stem from the proton-proton interaction and the corresponding secondaries, the neutrons arise from the showers in the outer calorimeters and comprise a flat albedo background in the center of the detector. However, enhanced neutron damage is expected close to the end caps of the inner detector, where the charged particles hit the forward calorimeter. A close to $1/r^2$ distribution is observed for the charged particle damage, rendering the operation of silicon detectors close to the beam pipe particularly difficult. Operating at full luminosity, silicon tracking detectors at LHC will have to withstand annual equivalent 1 MeV neutron fluences approximately ranging from 5×10^{12} cm^{-2} to 5×10^{13} cm^{-2}.

Predictions of the radiation damage effects on the silicon detectors have already largely influenced the design of the modules and the choice of the operational parameters. For example, cooling-pipes are found to be inevitable to prevent excessive self-heating of the detectors that is originating from the radiation damage-induced leakage current increase. Moreover, radiation damage transforms the initial n- into p-type silicon with progressively growing concentrations of negative space charges, which due to the corresponding increase in the minimum bias voltage needed to fully activate the devices is now considered to decide on the lifetime of the silicon detectors. Low temperatures are also necessary to control the complex annealing behavior of the radiation damage-induced changes in the doping concentration. Further, since partially depleted operation is awaited for many detectors, it appears to be advantageous to use n$^+$ strips on initial n-type material, so that an electric field zone exists below the strips after type inversion, even if the state of full depletion can not be achieved anymore. All p$^+$ strips would be expected to be short circuited by the p-type bulk material in this situation and thus would lose their spatial sensitivity. Although the radiation damage-induced deterioration has become a major issue, reduction of the costs, arising for example from the large area covered with detector grade silicon (several 10 m^2), often requires down-scaling of the entire system, i.e., the barrel radius is diminished, which of course results in pronounced damage effects.

In the following section an introduction into the basic features of silicon detectors will be given, emphasizing the electrical characterization methods that have been used in this work to study radiation damage effects. Section 3 considers bulk damage effects and is essentially organized into three parts. The first one contains a survey of the currently accepted model descriptions of the damage-induced changes in the doping concentration, leakage current, and charge collection (macroscopic properties) and offers new results on the elevated temperature annealing behavior, the influence of the particle type (neutron, proton, pion, ^{60}Co-gamma) and energy, and the dependence on the resistivity of the material used for the manufacture of the detectors. The second part begins with an overview of the microscopic origins of the damage effects and presents detailed investigations into the damage-induced defects using the

spectroscopic methods TSC, I-DLTS, and TCT. Finally, an attempt is made to explain the macroscopically observed deterioration by the knowledge gained about the microscopic causes. In Section 4 a cursory check of the radiation sensitivity of the oxide passivation is presented, and finally, in Section 5, a prediction of the damage effects in the Inner Detector environment of the ATLAS detector at LHC is performed. Due to the complexity of the subject matter, each of these sections closes with a summary, as do the sections dealing with the individual spectroscopic methods.

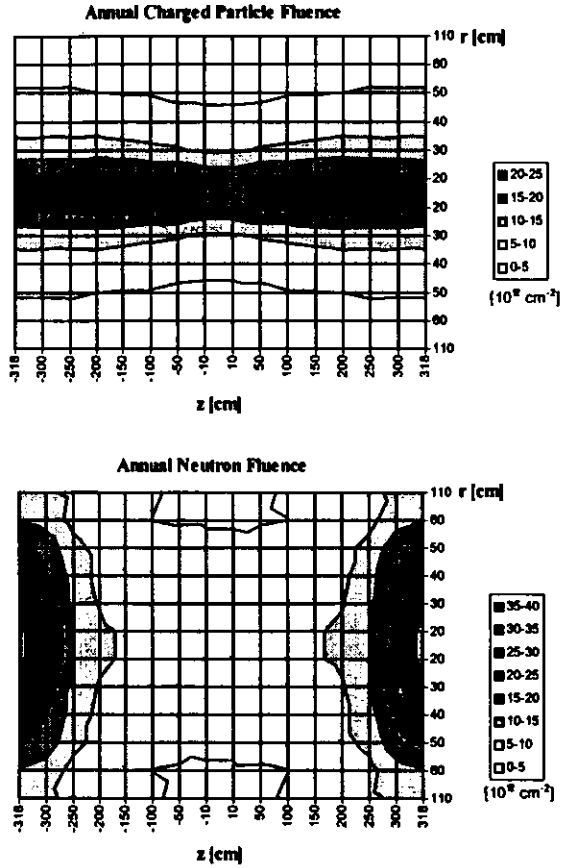

Fig. 1.2 Annual equivalent 1-MeV neutron fluences predicted by a Monte Carlo simulation for the ATLAS inner detector region, compare Fig. 1.1. Note that the subdivisions of the scales are not equidistant and that the symmetry of the data with respect to the interaction point at (0,0) is not perfectly reproduced by this graphical representation (single TRT design configuration B with integrated forward calorimeter, assumed p-p cross-section σ = 71 mb, luminosity L = 10^{34} $cm^{-2}s^{-1}$, 10^7 s beam on per year, [GOR95]).

2 Basic Features of Silicon Detectors

2.1 Principles of Operation

Fundamental to the operation of a semiconductor detector is the fact that the drift of the charges created in an electric field zone by a traversing ionizing particle induces a current pulse on the attached electrodes. Concerning a parallel plate geometry, the total instant current signal $I_{n,p}$ arising from a small cloud of $N_{n,p}$ negative or positive elementary charges q_0 drifting with the velocity $v_{dr,n,p}$ is given by (Ramo's theorem)

eq. 2.1 $$I_{n,p} = N_{n,p} q_0 \frac{v_{dr,n,p}}{W},$$

where W is the distance between the plates. The extent of the electric field region essentially defines the sensitive volume, since only there $v_{dr,n,p}$ is distinct from zero. The above expression had been speculated to not hold in the presence of fixed space charges, however, the first principles derivation given by G. Cavalleri et al. proves its general validity and also provides an extension to arbitrary electrode configurations [CAV71].

In a semiconductor, both electrons and holes contribute to the current signal. They are always created in pairs by the ionization process, i.e. $N_e(t = 0) = N_p(t = 0) = N$, and subsequently drift apart with different velocities. Regarding the efficiency of the material employed for the manufacture of the detectors, the following items have to be taken into consideration: The average energy E_{ion} required for the creation of one electron-hole pair, the magnitude of the drift velocities $v_{dr,n,p}$, and the size of the region in which a significant electric field can be established. Silicon is a good candidate with respect to the first two points (E_{ion} = 3.6 eV [DES67], v_{dr} up to the order of 10^7 cm/s). Other materials, for example Ge or GaAs, do however provide improvements in one or the other respect. As will be shown below, the latter point requires material of highest purity. Only for silicon is this nowadays readily available in large amounts and at relatively small costs, as it is the most widespread used semiconductor in the electronics industry*.

Fig. 2.1 illustrates the principle of a silicon detector for the detection of ionizing particles. The basic structure is a rectifying junction operated under a large reverse bias voltage V such that a zone of width W devoid of free carriers evolves under the electrode area. Given an ionizing particle passes through the sensitive volume, the resulting current pulse signal (a few 10 ns long) is sunk into the high frequency branch of the electrical circuit constituted of the coupling capacitor and the charge integrating amplifier. The output signal is proportional to the overall collected charge. Thus, if the impinging particle is stopped within the field zone, the signal provides a measure of the particle energy. In order to ensure the absolute calibration it is then important to make the junction contact and the electrode material on the entrance window as thin as possible, because otherwise charges are lost in these dead-layers. On the other hand, high energetic particles will easily traverse through all of the detector (of the order of few 100 µm) and liberate a narrow column of electron-hole pairs, most probably around 85 per µm for minimum ionizing particles (mips). The silicon detector can then only register, whether a particle was observed, or not, at the particular position where the device is positioned. This mode of operation is suitable for tracking purposes as for instance in a high-energy physics experiment. It will be noted that for mips the number of collected charges depends on the sensitive width W, i.e., it is desirable to extend the field zone all over the device thickness d. A serious reduction of the signal amplitude must be envisaged if the applied reverse bias is not sufficient to fully deplete the detector.

It is when the usable signal becomes too small compared with the electronic noise level that a reliable operation is not possible anymore. Thus, for a silicon detector application the lowest tolerable limit for the signal to noise ratio S/N is a key design specification. The major noise sources are related to the detector capacitance and leakage current, and the minimum electronic noise level for a particular

* It will be assumed in the following that the concentration of defects is sufficiently small, such that the free carriers drifting in the field zone have a high chance to reach the electrodes rather than being trapped.

detector can only be achieved by specifically designing the electronic readout circuit (input-capacitance, shaping time, etc.). In general, increasing leakage currents and capacitances will enhance the noise level.

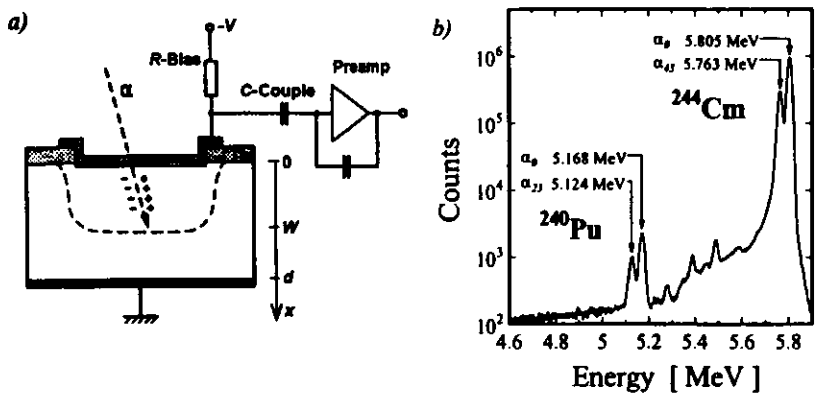

Fig. 2.1 Basic operation of a silicon detector. a) Schematic representation of the electronic readout and illustration of the electron-hole pair creation process in the depleted zone. b) Typical Multi Channel Analyzer (MCA) spectrum of a curium source recorded with a surface barrier detector (device 901G20, V_{bias} = 100 V, V_{dep} = 85 V, 62 hours measurement time). The source has an age approximately equal to the half-life of the ^{244}Cm nucleus (18.11 years), resulting in a significant activity of the daughter nucleus plutonium ^{240}Pu. The energy scale was calibrated employing the well known α-particle energies of these decays [LED78]. The other small peaks are related to impurities in the curium source [OSI95].

2.2 Structure of the Investigated Devices

2.2.1 Detector Grade Silicon

Virtually all properties of a semiconductor are related to imperfections of the crystal, i.e., to chemical impurities and lattice defects. Of major importance for the electronic device features are those imperfections forming quantum mechanical levels within the forbidden gap. For example, the detector grade silicon used in this work contains oxygen atoms on interstitial sites, O_i, and carbon atoms on substitutional sites, C_s, with concentrations of the order of a few times 10^{15} cm^{-3} [ZUL89,DRE90]. However, no electrical activity of these impurities has so far been observed, and the basic properties of the material resemble very much those of the perfect silicon crystal. On the other hand, only small concentrations of substitutional atoms from group III and V of the periodic table are required to dramatically change the resistivity of the material. It is therefore clear that the implications of additional energy levels in the forbidden gap can be various, and the efficacy of the one or the other crystal defect in modifying a particular property of the semiconductor will generally depend strongly on the energetic position and other quantities, as will be discussed extensively in Section 3.3.1.

The silicon employed for the manufacture of detectors is usually refined by the float zone process, resulting in dislocation free material of highest purity. The providers typically characterize the wafers at room temperature by the resistivity ρ and the minority carrier recombination lifetime τ_r. While the former can be controlled by intentionally doping the material, the latter crucially depends on the crystal growth and processing techniques. Incorporation of trace amounts of boron and phosphorus atoms results in either p- or n-type doping, i.e., either holes or electrons are predominantly found in the electrical

neutral material (majority carriers). The resistivity is related to the concentration of free electrons, n, and holes, p, by

eq. 2.2 $$\rho = \frac{1}{q_0\left(\mu_{0n} n + \mu_{0p} p\right)},$$

where μ_{0n} and μ_{0p} are the low field mobilities in the conduction and valence band, see Appendix A. In general, no specific assumption will be made about the composition of the doping atoms, and the net effect is visualized to arise from a concentration N_{eff} of ionized donors. Accordingly, p-type material is characterized by a negative value of N_{eff}. At room temperature the absolute value of N_{eff} is in practice always at least one order of magnitude larger than the intrinsic carrier concentration n_i (around 10^{10} cm^{-3}), which is the free carrier concentration in the undoped silicon. It is under these conditions justified to put n or p equal to $|N_{eff}|$ in n- or p-type material, whichever is the majority carrier. In the first approximation the corresponding minority carrier concentration can then be calculated by $n_i^2 / |N_{eff}|$.

The rate at which injected minority carriers recombine with the majority carriers is measured by the lifetime τ_r. Besides the small resulting diffusion currents this process would not affect the operation of a silicon detector. However, τ_r is related to the generation lifetime τ_g, i.e. the rate at which electron-hole pairs are generated in the depleted zone by thermal agitation. A small value of the lifetime is therefore very likely accompanied by a large reverse current, which indeed might deteriorate the detector performance.

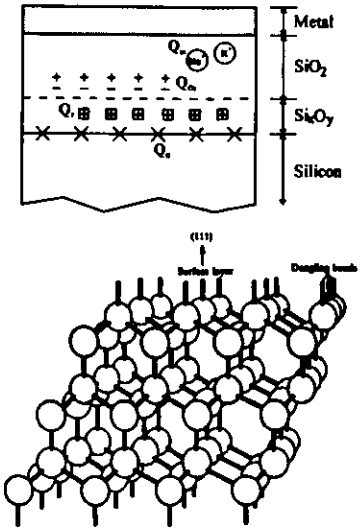

Fig. 2.2 Features of the thermal oxide and the interface between the oxide and the crystalline silicon, see [SZE81].

a) Charges in the silicon dioxide and interface region between the oxide and the silicon

Q_n : Interface-trapped Charge

Q_f : Fixed Oxide Charge

Q_m : Oxide-trapped Charge

Q_o : Mobile Ionic Charge.

b) One example for the origin of interface states are unsaturated dangling silicon bonds..

Almost all of the devices studied in this work were processed on (111)-oriented phosphorus doped float zone silicon wafers supplied by Wacker-Chemitronic [WAC]. The resistivities were mostly larger than 3 kΩcm, corresponding to $N_{eff} < 1.5\times10^{12}$ cm^{-3}, and the recombination lifetimes were quoted to be larger than 5 ms, which hardly gives rise to leakage currents. Moreover, also some p-type detectors and a few samples made from lower resistivity material were compared with the standard Wacker material in respect to their radiation hardness, see Section 3.2.5.

2.2.2 Oxide Passivation

It is not only the float zone technique, but also the high quality oxidation of the wafers which accounts for the superior properties of detector grade silicon. Usually a layer of amorphous SiO_2 around 200 nm (2000 Å) thick is thermally grown during several hours storage at approximately 1030°C in a dry O_2 gas stream, adding a small percentage of HCl or TCE (trichlorethylene). The wafer surfaces, which contain a huge number of electrically active interface states after the sawing and polishing, are largely passivated by this procedure. Fabrication of silicon detectors by the planar process, and the above oxidation scheme in particular, is traced back to J. Kemmer [KEM80].

The quality of the oxide is related to the number and the kind of the incorporated charges and the concentration of electrically active states remaining at the interface, see Fig. 2.2. There are various

sources for the former, which were classified by B.E. Deal in reference [DEA80]. Regarding the oxidation process, it is a particular problem to avoid the contamination with ions (sodium, potassium). Their charge is denoted by Q_m since they become mobile at elevated temperatures, a feature, which is exploited to detect them [GOR93]. Moreover, the dry thermal oxidation results in substoichiometric SiO_x according to the chemical reaction [DEV94]

eq. 2.3 $$O_3 \equiv Si - O - Si \equiv O_3 \xrightarrow[\text{Reduction}]{} O_3 \equiv Si - Si \equiv O_3 + O^{\uparrow} .$$

This so-called oxygen-vacancy complex may then permanently trap a hole, resulting in a positive charge, which is only one example for the origin of trapped oxide charges Q_{ot}

eq. 2.4 $$O_3 \equiv Si - Si \equiv O_3 + h^+ \rightarrow O_3 \equiv Si^{\circ} \; {}^{+}Si \equiv O_3 .$$

There is a pronounced substoichiometry of the SiO_x within a thin layer (few nanometers) underneath the interface, and a large concentration of related fixed positive charges Q_f is usually encountered there. Further, the interface between the silicon and the oxide gives rise to quantum mechanical states in the band gap of the silicon. Fig. 2.2 b) illustrates the commonly experienced dangling bonds, which however can be saturated by hydrogen atoms. Such interface states can act as surface recombination or generation centers, comparable to the previously discussed processes in the bulk characterized by the lifetimes τ_r and τ_g. Moreover, these states may be occupied with charges Q_{it}, depending on the electrical potential established at the interface under specific experimental conditions. Both the oxide and interface-trapped charges build up by the exposure to ionizing radiation. The corresponding radiation hardness considerations are the subject of Section 4.

2.2.3 Design Features

Two differently designed test structures have been investigated in this work, in the following referred to as surface barrier and ion-implanted devices. While the former were fabricated in the semiconductor lab of our group (Nukleare Meßtechnik, Universität Hamburg), the latter were provided by the semiconductor laboratory of the Max Planck Institut (MPI) München [MPI].

2.2.3.1 Surface Barrier Devices

The processing of the surface barrier detectors has been described in reference [FRE87], however, improvements were since achieved, compare for example [FRE90]. A side view of the device looks similar to the one illustrated in Fig. 2.1 a), a magnified view of the edge of the front electrode is presented in Fig. 2.3 a).

Starting with the oxidized wafers, openings for the front and rear contact metallizations are defined by a photo-lithographic step and subsequent etching. While the rear electrode usually is square shaped and covers most of the overall test structure area of 9.3×9.3 mm², the front contact can be a large circle, a small circle, a U-shaped electrode, and two narrow strips (see Fig. 2.3 b)). Correspondingly, the device name contains a K, G, U, and L or R for the left-hand or right-hand strip, respectively. Table 2.1 lists the electrode area and related dimensions of the various devices studied.

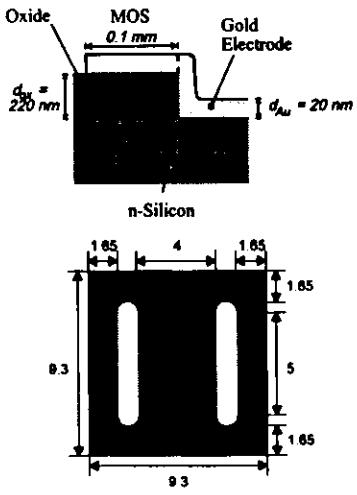

Fig. 2.3 Layout of surface barrier test structure. a) Magnified view of the edge structure. b) Top view of an L/R type detector, dimensions in mm.

The ohmic contact on the rear side is established by evaporation of 100 µg/cm² aluminum onto the naked silicon surface. A Schottky-barrier is fabricated on the front contact by deposition of a very thin gold layer (40 µg/cm²), allowing for the adsorption of pure oxygen at the end of the layer formation. A particular feature of these devices is the Metal Oxide Semiconductor (MOS) structure at the edge of the contact, which allows for the investigation of the oxide parameters. In regard to optical generation of free carriers it is noted that the approximately 20 nm thick gold layer is sufficiently transparent, whereas small circular openings had to be left in the rear contact for this purpose, see Appendix A. However, a thin layer of 4 µg/cm² Al was found to be inevitable to retain good ohmic properties.

2.2.3.2 Ion-Implanted Devices

Fig. 2.4 illustrates all important details of the ion-implanted test structures. Here the oxide is removed entirely from the rear side and selectively at the front side, such that the remaining passivation layer can serve as an implantation mask. The junction and the ohmic contact are established by exposure to boron and arsenic (nowadays: phosphorus) ions with kinetic energies of around 15 keV and 30 keV, respectively [KEM80]. In order to circumvent the problems arising from the high electric fields at the edge of the implanted junction, a so-called step oxide is employed to decelerate the impinging boron ions in a specifically thinned oxide region (50% of the full oxide thickness), such that their range in the silicon crystal is reduced significantly with respect to the ions entering through the oxide-free windows. A subsequent elevated temperature annealing is required to remove the displacement damage and to activate the implanted impurities.

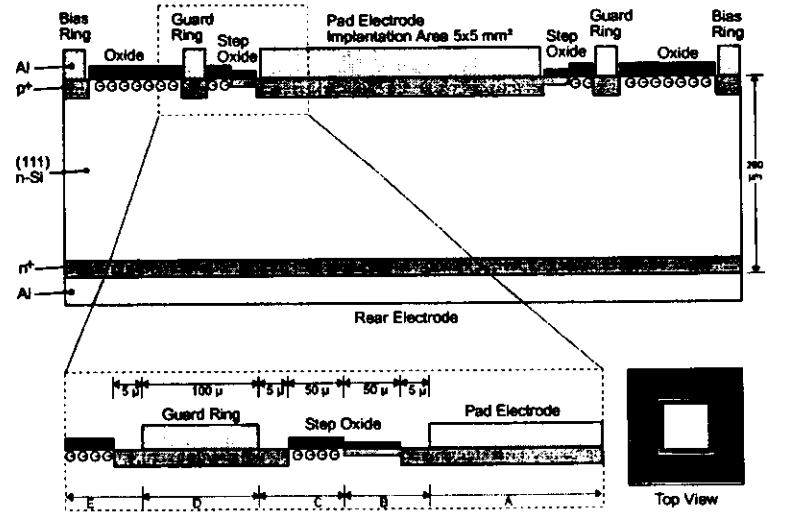

Fig. 2.4 Cross section of the ion-implanted test structures provided by the semiconductor laboratory of the MPI München. Top: full view, bottom: magnified view of the region between the guard ring and the pad electrode, the labels A - E indicate the regions studied with a proton micro-beam, see Section 2.4.3.

On the front side the implants are covered with an approximately 1 µm thick aluminum metallization. In addition to the pad electrode, whose implanted area is 25 mm², these devices are endowed with a guard and a bias ring. While the former is operated under the same bias voltage as the main electrode, and therefore is capable of sinking leakage currents generated at the edges of the depleted region, the latter is connected to the positive terminal of the bias supply. Accordingly, the p⁺n junction is operated in the forward direction and, except for the small voltage dropping across it, determines the electrical potential

of the undepleted bulk material. Thus, all connections required for testing can be accessed from the top side. However, the resulting contact resistances were found to be too large for high frequency measurements, and a reproducible ohmic contact could again only be accomplished by depositing a 100 μg/cm² aluminum layer onto the rear side n⁺ implant.

2.2.3.3 Sample Mounting

All investigated samples were mounted on an aluminum ceramics carrier of the dimension 2×2.5 cm². The fixture is supplied with five thin gold metallizations with a pitch of 2.54 mm, providing easy access to standard electronic equipment. The center strip contacts the rear electrode, and for most samples the front electrode was bonded to the leftmost gold strip by a copper whisker. Conductive silver glue has been employed to fix the sample on the mounting.

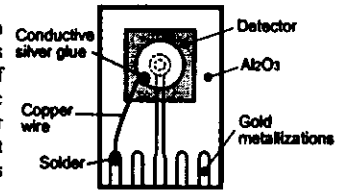

Fig. 2.5 Mounting and connection of a sample on the aluminum ceramics.

Table 2.1 Junction area, MOS area, and full sensitive area of the various devices studied. The latter was inferred from proton micro-beam measurements, see Section 2.4.4. The data for the surface barrier devices have been taken from reference [WUN92].

Device	Electrode Shape	Junction Area	MOS Area A_{ox}	Sensitive Area A
Ion Implanted	Square	0.25 cm²	0	0.275 cm² Floating 0.255 cm² Grounded
	Circle	0.25 cm²	0	0.272 cm² Floating 0.254 cm² Grounded
Surface Barrier	Large Circle (G)	0.385 cm²	0.027 cm²	0.442 cm²
	Small Circle (K)	0.126 cm²	0.017 cm²	0.160 cm²
	U-shaped (U)	0.149 cm²	0.042 cm²	0.232 cm²
	Two Strips (L/R)	0.058 cm²	0.018 cm²	0.093 cm²

2.3 The Electric Field Zone

The electric field zone has a major impact on the performance of the silicon detector. It is therefore worthwhile to examine, how the electric field distribution $E(x)$ is related to the externally applied reverse bias and the doping concentration. These subjects have extensively been treated in textbooks, see for example [SZE81]. Only the most important results will thus be recalled here. However, they are written in a form suitable for the further use in this work.

2.3.1 Abrupt Junction

For the sake of convenience, the junction is thought to be established by a thin and heavily doped p-type layer on a lightly doped n-type substrate. Regarding the depletion zone this treatment is appropriate for both surface barrier and ion-implanted devices. As the extent of the electrode is large compared with the detector thickness, it will be assumed that a one-dimensional modeling is sufficient.

Fig. 2.6 a) depicts the electrical charge density ρ_{el} encountered for a specific reverse bias voltage V. While outside the field region the free majority carriers neutralize the ionized doping atoms, a high negative and a small positive space charge concentration is emerging on the p⁺ and on the n side of the

junction. As the overall charge must be equal to zero, it is clear that the field zone chiefly penetrates into the weakly doped region (abrupt junction), which therefore will be the only objective in the following. Moreover, the so-called depletion approximation will be employed, i.e., ρ_{el} is assumed to be constant in the range $0 < x < W$, although the diffusion of electrons from the n-type bulk into the depleted region is known to result in a smooth distribution of the electrical charges around $x = W$. The value of ρ_{el} in the space charge region is given by $q_0 N_{eff,SCR}$, where $N_{eff,SCR}$ denotes the effective concentration of ionized donors in the field zone.

Given the above suppositions, the mathematical treatment, i.e. solution of the Poisson equation, is straight-forward. The first integration yields a linearly graded electric field and the second integration a parabolic electron potential energy*, see Fig. 2.6 b) and c). However, two boundary conditions need to be satisfied. Firstly, the electric field strength is equal to zero in the neutral bulk region, furnishing $E(W) = 0$. Secondly, the separation of the Fermi levels E_{Fp} and E_{Fn} in the neutral p⁺ and n region is equal to the potential energy difference $q_0 V$ maintained by the external bias supply. The total change in the electron potential energy $\int dx\, E(x)$ in the range $0 < x < W$ is therefore given by $q_0(V+V_{bi})$. This circumstance is indicated at the intrinsic Fermi level E_i in Fig. 2.6 c), which is a suitable reference level located approximately in the middle between the conduction and valence band energies E_C and E_V, compare [SZE85]. The so-called built-in voltage V_{bi} accounts for the existence of an electric field zone even under zero bias. It arises from the different work functions in the two materials brought into intimate contact. Let ΔE_{Fp} and ΔE_{Fn} be the energetic differences between the conduction band energy E_C and the Fermi level in the p⁺ and n region, respectively. Then the built-in voltage is given by $V_{bi} = (\Delta E_{Fp} - \Delta E_{Fn})/q_0$. The same holds for a surface barrier detector if ΔE_{Fp} is identified with the barrier height $q_0\phi_{B0}$. In an ion-implanted p⁺ layer the Fermi level is very close to the valence band, such that in the first approximation ΔE_{Fp} can be set equal to the band gap energy $E_g = E_C - E_V$.

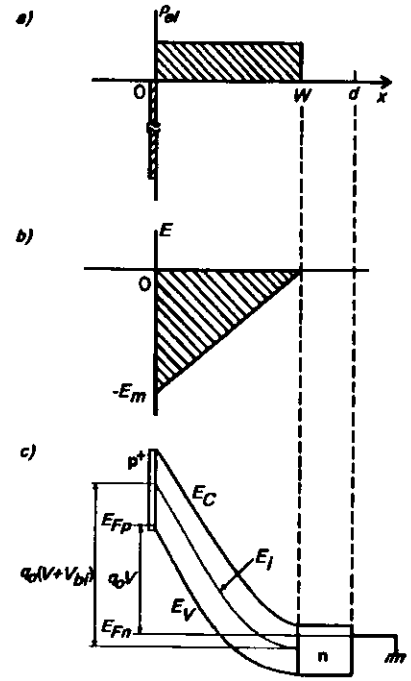

Fig. 2.6 Graphical solution of the Poisson equation for a one-sided abrupt junction. a) electrical charge density, b) electric field strength, and c) electron potential energy.

It is now easy to write down some important relations by mere inspection of the graphical construction presented in Fig. 2.6. The maximum field strength E_m at the junction is given by

$$\text{eq. 2.5} \qquad E_m(V) = 2\frac{V+V_{bi}}{W(V)},$$

and the width W of the depleted zone can be written

$$\text{eq. 2.6} \qquad W(V) = d\left(\frac{V+V_{bi}}{V_{dep}+V_{bi}}\right)^{1/2}.$$

The abbreviation V_{dep} has been introduced to account for the density of the space charges

* The electron potential energy is equal to the electron charge $-q_0$ times the electrical potential. Contrary to the electron potential energy the electric potential is thus becoming more positive towards the back plane contact.

eq. 2.7 $$V_{dep} = \frac{q_0}{2\varepsilon\varepsilon_0} d^2 |N_{eff,SCR}| - V_{bi}.$$

Here $\varepsilon\,\varepsilon_0$ denotes the permittivity of silicon (ε = 11.9). Evidently, eq. 2.7 furnishes the particular reverse bias under which the field zone reaches through all of the detector ($W = d$), and therefore is called depletion voltage. Regarding a typical wafer thickness of 300 µm it is clear that $|N_{eff,SCR}|$ must not be larger than a few 10^{12} cm^{-3} in order to allow for a full activation of the sensitive volume by a reasonable reverse bias, say less than 200 V. Compared with typical impurity concentrations this is however just a trace amount, emphasizing the importance of high purity material for this specific application.

If one does not rely on the depletion approximation, V_{bi} must be replaced with $V_{bi} + k_B T/q_0$ in all of the above equations, compare for example [SZE81]. However, practical values of V and V_{dep} are frequently found to be one order of magnitude larger than V_{bi}, and thus it is often justified to put $V_{bi} \approx 0$. If the reverse bias is larger than the full depletion voltage, it can no longer be exploited that the electric field is equal to zero at a certain position. It is then necessary to deduce the overall electric field from the superposition principle, which is however left for Section 2.6.2. Here it will be enough to note that under these conditions the depleted width is equal to the detector thickness and does not depend on the reverse bias anymore,

eq. 2.8 $$W(V \geq V_{dep}) = d.$$

Finally it is noted that the above relations may equally as well be applied to n$^+$-p junctions, since only the absolute value of $N_{eff,SCR}$ has been used. If the n$^+$ layer is located at $x = d$ the depleted zone will grow from the right-hand to the left-hand side for increasing reverse bias voltages V, which is applied the same way as before, i.e., a positive voltage is connected to the right-hand electrode and a negative voltage to the other one. Accordingly, the electric field remains negative, since positive charges always have to flow from the right-hand to the left-hand side. For example, radiation damage can change the sign of the space charge from positive to negative, accompanied by a movement of the junction from the front ($x = 0$) to the rear ($x = d$) contact of the detector.

2.3.2 MOS Diode

Regarding the field zone at the edge of the junction of the surface barrier devices it is instructive to recall the situation in a Metal Oxide Semiconductor (MOS) structure. A schematic representation is given in Fig. 2.7, where ψ_s and ϕ_B are the surface band bending and the bulk potential, introduced for the characterization of the various situations established at different bias voltages. A particular feature of MOS diodes is that virtually no current is flowing since the oxide is a very good insulator. Consequently, the Fermi level in the semiconductor is flat, irrespective of the bias voltage applied. In thermal equilibrium electrons are usually attracted from the n-type bulk towards the oxide-semiconductor interface, forming a very thin accumulation layer ($0 < \psi_s$). Accordingly, there is no depleted zone below the interface, and a negative voltage has to be connected to the front (gate) electrode in order to repel the electrons. For sufficiently large reverse bias voltages ($-\phi_B < \psi_s < 0$) the distribution of the electrical charges and the electron potential energy as depicted in Fig. 2.7 is obtained. Now, the states at the interface can act as current generation centers, provided the current can be collected by an adjacent electrical contact. If for larger bias voltages the intrinsic Fermi level E_i at the interface becomes larger than the Fermi level E_{Fn} ($\psi_s < -\phi_B$), an inversion

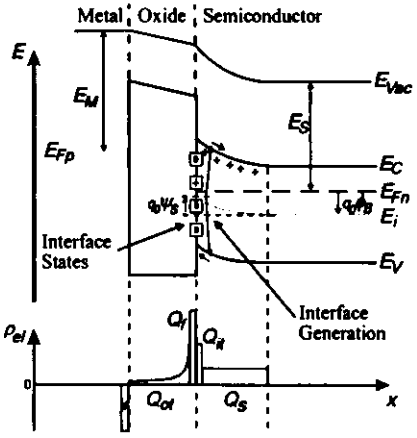

Fig. 2.7 Electron potential energy and electrical charges in an MOS diode, compare Fig. 2.2 b).

layer about 10 nm thick builds up. That is, free holes, which are the minority carriers in the n-type silicon substrate, are predominantly found at the interface. For very large values of the reverse bias the valence band comes close to the Fermi level, resulting in strong inversion ($-2\phi_B < \psi_s$). A further expansion of the depleted zone is then inhibited by the dramatically increasing concentration of holes in the inversion layer.

Special interest will be devoted to the specific reverse bias, under which the transition from accumulation to inversion takes place. Since the electrons are neither repelled nor attracted to the interface under this experimental condition, Q_I is zero and the electron potential energy must be constant throughout the semiconductor. Accordingly, the voltage in question is named flat-band voltage V_{fb}. It can be deduced that it is ([SZE81])

eq. 2.9 $$V_{fb,0} = (E_S - E_M)/q_0 + \frac{Q_{ox}}{C_{ox}} \frac{x_0}{d_{ox}},$$

where E_S and E_M denote the work function of the semiconductor and the metal, respectively. Q_{ox} is the sum over all charges related to the oxide and x_0 is the corresponding center of gravity. C_{ox} is the oxide capacitance of the MOS diode, which is measured in the accumulation condition,

eq. 2.10 $$C_{ox} = \varepsilon_{ox}\varepsilon_0 \frac{A_{ox}}{d_{ox}}.$$

A_{ox} and d_{ox} are the area of the oxide covered with the gate electrode and the oxide thickness, and the relative permittivity of dry oxide is ε_{ox} = 3.9. Substituting typical values of the work functions into eq. 2.9 shows that the usually observed positive flat-band voltages require positive oxide charges to exist in the processed devices.

Finally it will be noted that in general the overall positive oxide charge is a function of the applied reverse bias. If for example the Fermi level at the interface changes from a value close to the conduction band towards the valence band energy for increasing reverse bias voltages, the overall number of interface states occupied with electrons is diminishing. Accordingly, Q_{ox} is progressively increasing, resulting in a smooth transition from accumulation to inversion.

2.4 Probing the Depletion Region with a Proton Micro-Beam

2.4.1 Measurement Basics and Experimental Procedure

Proton micro-beam measurements provide an *in situ* visualization of the extension of the electric field zone in a silicon detector. The key element of this technique is a low energy proton beam which can be scanned over a large area, typically 1.55×0.77 mm^2 has been used here. Suitable energies should be chosen such that the proton penetrates significantly into the silicon but does not travel through all of the detector. Here 2 MeV protons from a Van-de-Graaff accelerator were utilized, which otherwise is employed by the group around Dr. Niecke (Arbeitsbereich Umweltanalytik, I. Institut für Experimentalphysik, Universität Hamburg) for spatially resolved PIXE measurements (Proton-Induced X-ray Emission). The energy dE lost by a proton of a certain energy E on the distance dx is related to the stopping power S by

eq. 2.11 $$-\frac{dE}{dx} = \rho S(E),$$

where ρ denotes the density of the ionized medium, and in silicon it is ρ = 2.33 g/cm^3. An integration of eq. 2.11 gives an average range of 2 MeV protons in silicon of 47 µm, employing the stopping power data compiled by J.F. Ziegler [ZIE77]. Since above 100 keV the ionization cross section is found to be increasing for decreasing proton energies, most of the ionization is produced at the end of the range. This relation between the ionization and the range is known as the Bragg curve.

Given the proton comes to rest within the depleted zone of the detector, all the generated electron-hole pairs are collected, and accordingly the signal detected reflects the total initial proton energy. If now the ionization chiefly takes place in the zero field region, the signal is significantly reduced. A two dimensional map of the electric field zone can thus be obtained by plotting the detected energy versus the position at which the proton intruded the detector. Fig. 2.8 displays the number of hits falling into a specific range of the detected energy and of the projected x coordinate of the scanned area. The scan regions have always been arranged in such a way that the symmetry of the investigated test structures allowed for this projection in order to reduce the complexity of the measured data. It would also have been possible to experimentally scan the proton beam along one line. However, then local proton damage would have become a major concern. For the same reason, and in addition to avoid pile-up effects in the readout electronics, the beam current was chosen orders of magnitude smaller than for typical PIXE measurements by narrowing the beam slits, resulting in only a few hundred recognized hits per second.

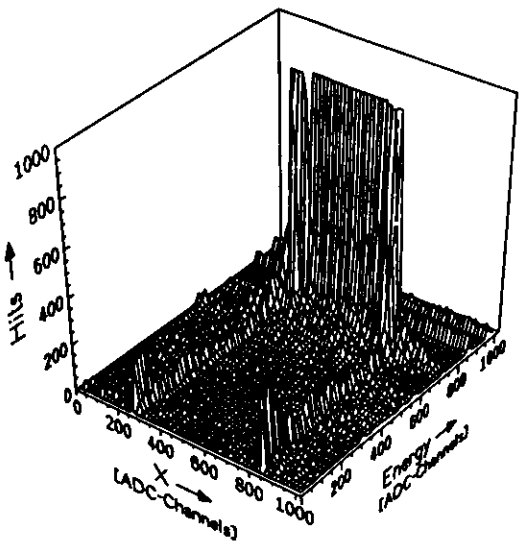

Fig. 2.8

Left: Number of hits as function of the projected x coordinate and the detected energy (device 932R28, V_{dep} = 88 V, reverse bias 80 V, 500 ns shaping time).

Bottom: Top view of the investigated surface barrier detector and indication of the scan region in conjunction with the corresponding coordinate system.

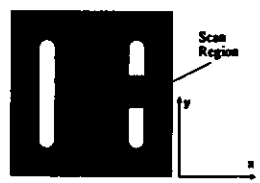

All measurements were carried out at room temperature in an evacuated sample chamber. A block diagram of the electronic readout and the proton micro-beam control is shown in Fig. F.1 of Appendix F. The energy ADC channels were scaled to a well defined electronic input signal by means of a test pulse generator, compare the two lines at about 900 channels in Fig. 2.8. Absolute energy calibration of the electronics was accomplished by the signal from the 2 MeV protons and by the additional acquisition of the spectrum of a ^{244}Cm source, emitting α-particles of very accurately known energies, see Fig. 2.1 b). Also the beam position information furnished by the micro-beam controlling system is an arbitrarily scaled ADC channel number. The required calibration of the spatial distances was attained by probing a hexagonal metallic grid with a specified lattice constant (63.5 µm), also used to focus the proton beam. An absolute assignment of the beam position with respect to the investigated device was then possible by inspection of the features of the measured data which unambiguously could be related to the known detector surface structure. Moreover, the samples were mounted on a mobile table that could be moved very accurately by means of stepping motors, thus providing an additional tool for the position calibration. While the minimum beam focus attainable is around 1 µm, a spatial resolution of 6 µm in the x and y direction has been employed. Finally it is noted that it also was possible to expose the back plane contact of the test devices to the proton beam, giving additional clues regarding the field extension.

2.4.2 Surface Barrier Devices

Computer programs were developed to extract the crest line produced by the proton signals in measurements like Fig. 2.8 which furnishes the detected energy as function of the projected coordinate. Mainly these so-called energy profiles will be discussed in the following. They are presented in Fig. 2.9 as function of the reverse bias voltage applied to a surface barrier detector. With respect to the signal caused by the protons impinging onto the central region of the junction electrode, evidently even under zero bias electron-hole pairs are collected due to the electric field arising from the built-in voltage V_{bi}, compare eq. 2.6. Moreover, for bias voltages larger than 5 V always the full proton beam energy is measured, indicating that the width of the depleted zone is larger than the proton range of 47 µm. Below this voltage it is possible to infer the width of the depleted layer from the signal height by exploiting the knowledge about the energy lost by the intruding proton on a certain distance which can be deduced from eq. 2.11. However, it is inevitable to take into account the shaping time of the electronic readout, i.e., the time during which charge is recognized. The chief problems arise from the ionization that takes place close to the edge of the depletion region, where the electric field is low, resulting in slow charge collection. Moreover, minority carriers created in the zero field region can, due to the large recombination lifetimes, easily diffuse into the field region and thus contribute to the overall signal. Employing the 2D-device simulation program ToSCA, the latter could be shown to result in an overestimation of the depleted width of around 1.5 µm and 15 µm for 100 ns and 500 ns shaping times, respectively [WUN96].

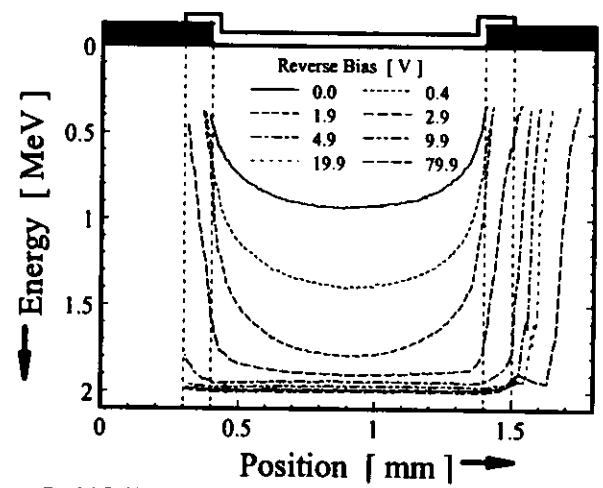

Fig. 2.9 Field zone in a surface barrier detector probed by protons impinging onto the front plane. The surface layout is depicted on the top of the diagram, compare Fig. 2.3 (device 932L10, 100 ns shaping time, V_{dep} = 81 V, V_{fb} = 1.8 V).

Concerning the edges of the investigated junction it is noticed that at bias voltages around 1.9 V the sensitive region expands significantly in the horizontal direction. In particular, virtually no signal is seen underneath the MOS region below 1.9 V, in agreement with the flat-band voltage V_{fb} of 1.8 V determined from the CV curve, see Section 2.5.3. For the largest reverse bias presented in Fig. 2.9, which is close to the full depletion voltage, a small portion of the proton energy is lost at a position around 1.5 mm. Now, the corresponding investigations employing protons intruding from the back side do not show this feature. It must therefore be concluded that an insensitive region evolves at the oxide-silicon interface. A likely explanation is that the transversal electric field component becomes very small at that position, allowing for the formation of a hole inversion layer. Next to the gold-silicon interface this would not be expected to exist, because there the inversion carriers are drained into the junction contact.

2.4.3 Ion-Implanted Devices with Floating and Grounded Guard Ring

Similar measurements have been performed on an ion-implanted device with either the guard ring short circuited to the pad electrode (Fig. 2.10 a)) or left floating (Fig. 2.10 b)). With respect to the behavior observed below the main electrode (region A), arguments equal to those mentioned for the surface barrier detector hold. The differences in the detected energies noticed in a) and b) arise from the different shaping times. However, yet a larger signal is observed in the thin oxide region B, located next to the main pad metallization, which is due to the energy lost by the protons in the aluminum contact layer. Indeed, employing the corresponding stopping power data, the thickness of the metallization could be deduced from this observation to be around 1.2 μm [OSI95].

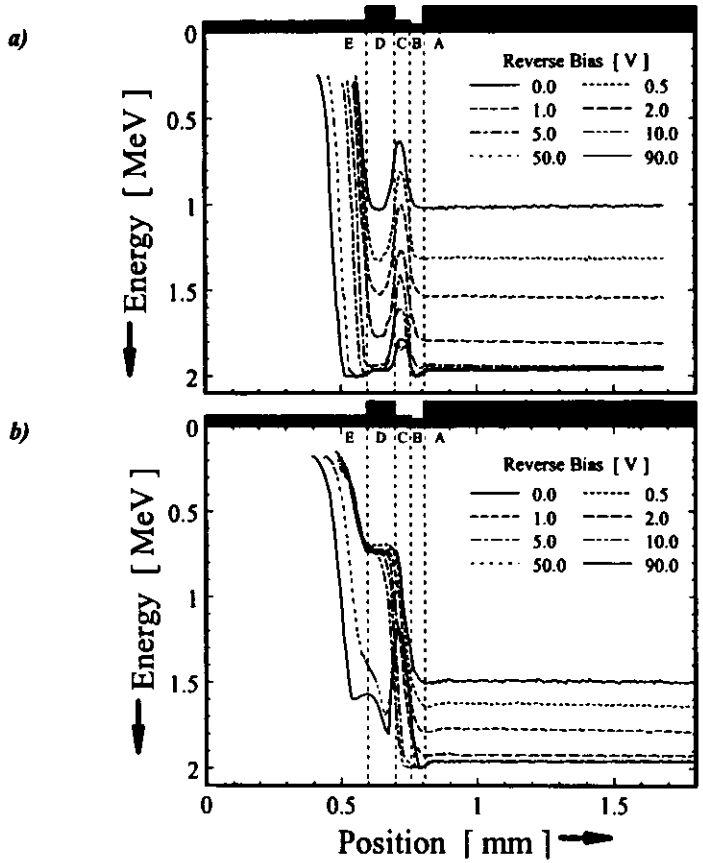

Fig. 2.10 Field zone in an ion-implanted detector (device M10911, V_{dep} = 86 V). In regard to the surface design and the labeling A - E of the different regions compare Fig. 2.4.

a) Guard ring short circuited to the pad electrode, 100 ns shaping time.

b) Guard ring floating, 500 ns shaping time.

Now, in the region D of Fig. 2.10 a), i.e. underneath the short-circuited guard ring, the field zone expands similarly to the main electrode. Below the thick oxide region C, a fraction of the proton energy is lost due to the electron accumulation layer at the silicon-oxide interface. Evidently the layer does not disappear even for the largest reverse bias voltages, indicating a local electron potential minimum essentially controlled by the number of oxide charges. Here it is important to recall that the measurements were performed in an evacuated chamber, while in normal air atmosphere the front electrode potential might be conducted to the oxide surface by the humidity. These considerations essentially determine the type of the boundary condition, Dirichlet or Neumann, that needs to be applied on top of the oxide surface in order to study the field zone with a device simulation program [RIC96]. As for the surface barrier detector, a lateral extension of the field-zone is observed in region E. Correspondingly, the depleted zones evolving below the main electrode and the guard ring would be expected to be merged at a reverse bias of around 10 V, where the lateral extension in region E is approximately half the distance between the pad and the guard.

If the guard ring is left floating the extension of the depleted zone displays markedly different features, see Fig. 2.10 b). For reverse bias voltages smaller than 10 V, a signal independent of the bias is detected below the guard ring in region D originating from the built-in electric field. The signal is however reduced with respect to the value observed underneath the main electrode at zero bias, because the guard is only loosely coupled to the electronic readout by the capacitance between the pad and the guard. Between 10 V and 50 V a considerable growth of the signal is observed, arising from the lateral extension of the electric field zone under the main electrode, which again leads to the merging of the separated depleted zones. With the shielding undepleted layer removed, the potential of the pad can be induced onto the guard through the electric field, which is known as punch-through biasing [KEM88]. However, as the distance between the electrodes in question is very large, the biasing mechanism is not very effective. For instance at 90 V the signal observed in the region D roughly equals the one underneath the main pad at 1 V reverse bias. It is interesting to note that after the punch-through has occurred the detected energy in the thick oxide region C is reduced, indicating the formation of a local electron potential minimum at the interface which allows for the development of an electron accumulation layer.

2.4.4 Lateral Extension of the Electric Field Zone

The proton micro-beam measurements can be employed to determine the sensitive volume of the detectors with regard to the lateral extension over the junction area. In order to allow for a quantitative evaluation, the lateral extension has been defined to be given by that specific position, where half of the energy compared with the center of the main pad is observed. The corresponding data obtained on the ion-implanted device already encountered in Fig. 2.10 are presented as function of the reverse bias voltage in Fig. 2.11. Protons were either impinging on the rear or the front side and the guard ring was either connected to the main pad electrode or left floating. Moreover, all measurements have been performed with two shaping times, 100 ns and 500 ns, demonstrating that the differences resulting from slow charge collection and minority carrier diffusion effects are small. It will be recalled that the lateral extension is probed at around the proton range of 47 μm below the contacts.

A very smooth curve is observed for the short-circuited guard ring below the front side corresponding to region E in Fig. 2.10 a). For the floating case the punch-through, which is indicated in Fig. 2.11, results in a more unsteady behavior. In any case the lateral extension below the rear contact is smaller, illustrating that the depleted zone is not growing like a rectangular box, but rather like a bulb. Of chief interest is the sensitive volume in the fully depleted state accomplished under a reverse bias of 86 V, as was inferred from CV measurements, see the following Section. With the guard ring floating the lateral extension measured with respect to the edge of the front electrode p' implant is around 200 μm at the front side and around 40 μm at the rear side, which gives an average of 120 μm. Thus the total sensitive area has been quoted to be 0.524×0.524 cm^2 on the square-shaped device and a corresponding value for the circle, see Table 2.1. If the guard ring is properly grounded the sensitive area assigned to the pad electrode extends laterally only half of the distance between the implants of the main junction and the guard ring. Accordingly the square-shaped sensitive area is then given by 0.505×0.505 cm^2.

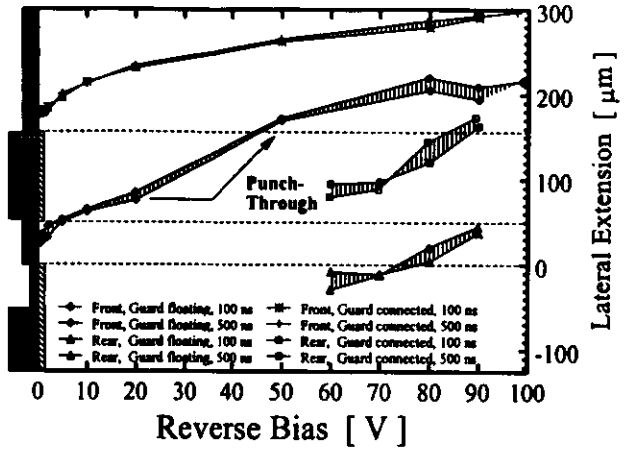

Fig. 2.11 The lateral extension of the depletion region as function of the reverse bias deduced from proton micro-beam measurements, compare Fig. 2.10.

2.5 Capacitance and Current under Reverse Bias

2.5.1 Equations for the Individual Capacitance and Current Contributions

There are several contributions to the capacitance and current measured under reverse bias which will be addressed individually in the following. For purpose of orientation the reader may notice the typically encountered characteristics presented at the end of the section which were obtained on a surface barrier (Fig. 2.15) and an ion-implanted detector (Fig. 2.16).

2.5.1.1 Junction Capacitance

The evolution of the depletion zone as function of the reverse bias is connected with an corresponding change in the dynamic junction capacitance C_j. For an idealized case, omitting the influence of deep trap levels, it can be shown that C_j is related to the width W of the depleted region by [SZE81]

eq. 2.12 $$C_j(V) = \varepsilon\varepsilon_0 \frac{A}{W(V)}.$$

That is, the device behaves like a regular parallel plate capacitor whose electrodes of area A are displaced by W. Since for sufficiently large reverse bias voltages V the depletion width is approximately proportional to the square root of V, plotting the capacitance versus the corresponding voltage in a double logarithmic scale gives a straight-line with slope -1/2. However, for $V > V_{dep}$ the depleted width is equal to the device thickness and remains a constant, as does the capacitance. Under zero bias, C_j depends only on the built-in voltage V_{bi} .

2.5.1.2 Additional Capacitance from the MOS Region

While the junction capacitance explains sufficiently well the total capacitance C observed on ion-implanted devices, the gold electrode overlapping the oxide around the junction of surface barrier devices causes a contribution C_{MOS}, that needs to be added to C_j . As long as the electron accumulation

layer exists underneath the oxide-silicon interface, C_{MOS} is equal to the oxide capacitance C_{ox} (eq. 2.10), see Fig. 2.12.

As the oxide is very thin compared with the width of the depleted region, the oxide capacitance, which is independent of the bias voltage, typically predominates and brings about a more or less constant total capacitance below the flat-band voltage V_{fb}. Upon depleting the silicon below the interface, the contribution vanishes abruptly and C is in the first approximation merely given by the junction capacitance. A minor modification of the effective junction area above that point was assumed to absorb the remaining capacitance C_{MOS}. Now, for purpose of evaluation of the flat-band voltage V_{fb} it has been exploited that in the flat-band condition C_{MOS} can be written [NIC82]

eq. 2.13 $$C_{MOS}(V_{fb}) = \frac{C_{ox}}{1 + \frac{\varepsilon_{ox}}{\varepsilon}\frac{\lambda}{d_{ox}}},$$

where ε_{ox} and ε are the relative permittivities of the dry oxide (3.9) and crystalline silicon (11.9), respectively, and λ denotes the extrinsic Debye-length

eq. 2.14 $$\lambda = \sqrt{\frac{k_B T}{q_0}\frac{\varepsilon\varepsilon_0}{q_0 |N_{eff,SCR}|}}.$$

The thickness of the oxide d_{ox} as certified by the oxidation laboratory has been used, and in conjunction with the known MOS area (Table 2.1) numerical values of C_{ox} and $C_{MOS}(V_{fb})$ were obtained.

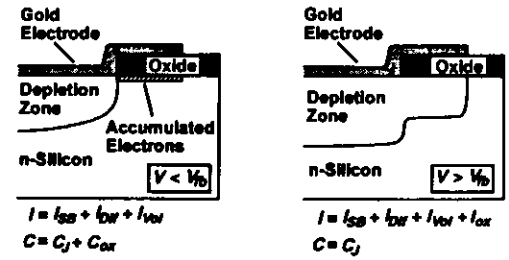

Fig. 2.12 Illustration of the capacitance and current contributions arising from the MOS region of the surface barrier devices.

2.5.1.3 Surface Barrier Current

The junction of surface barrier detectors is established by a metal-semiconductor contact, also called a Schottky diode, given the resulting device has rectifying properties. Contrary to diffusion currents, which predominate in ion-implanted devices, the current is carried by majority carriers. That is, for an n-type substrate the reverse current is constituted by electrons thermionically emitted from the metal into the semiconductor. This process requires an energetic barrier to be overcome, given by the difference $q_0\phi_{Bn}$ between the semiconductor conduction band energy and the metal Fermi level (compare Fig. 2.6 c)). Since the emission process is thermally activated, the saturated surface barrier current $I_{SB,sat}$ obtained under a large reverse bias can be written

eq. 2.15 $$I_{SB,sat} = AA^{**}T^2 \exp\left(-\frac{q_0\phi_{Bn}}{k_B T}\right).$$

Here A^{**} is the effective Richardson constant and ϕ_{Bn} denotes the actual barrier height, which is slightly decreasing for increasing reverse biases with respect to the zero field value ϕ_{B0} due to the Schottky effect [SZE81]. The total leakage current, and thus the quality of a surface barrier detector, depends critically on the obtained barrier height. For the devices produced according to the Hamburg group process values for A^{**} of the order of 100 $AK^{-2}cm^{-2}$ and particularly large barrier heights of around 0.92 eV are

typically observed*. Much smaller values are usually reported in the literature, emphasizing the role of the surface states at the junction for the particular fabrication process employed [SZE81]. The variation of the surface barrier current with the bias voltage, which is of interest only for $V < 3k_BT/q_0$, is given by

eq. 2.16 $$I_{SB}(V) = I_{SB,sat}\left(1 - \exp\left(-\frac{q_0 V}{k_B T}\right)\right).$$

2.5.1.4 *Diffusion Current*

Both surface barrier and ion-implanted devices exhibit, when operated under reverse bias, a contribution to the total current caused by the diffusion of minority carriers from the undepleted bulk region into the electric field zone. The bias dependence is given by the Shockley equation, similar to eq. 2.16. However, due to the different origin, the saturated current $I_{Dif,sat}$ is related to other quantities.

For the sake of conciseness the following relations will be given only for holes in an n-type substrate. The diffusion current is limited by the rate, at which the holes are extracted from the bulk region, depending on the efficacy of the processes aiming at the restoration of the thermal equilibrium situation. On the one hand, holes are homogeneously controlled in the bulk by generation/recombination, characterized by the minority carrier recombination lifetime for holes τ_p. On the other hand, minority carriers can be injected from the rear plane contact with an effective recombination velocity S. Fig. 2.13 shows three important special cases of the full solution of the problem presented by K.J. Rawlings [RAW87]. L_p denotes the diffusion length, which is related to the hole diffusion constant D_p (of the order of 10 cm^2s^{-1} at room temperature [SZE81]) and the lifetime τ_p by $L_p = (D_p/\tau_p)^{1/2}$.

a)	$L_p < d-W$	$I_{Dif,sat} = q_0 A p_{n0} \frac{L_p}{\tau_p}$	W E_V d p_{n0}
b)	$L_p >> d-W,\ S >> D_p/(d-W)$	$I_{Dif,sat} = q_0 A p_{n0} \frac{D_p}{d-W}$	p_{n0}
c)	$L_p >> d-W,\ S << D_p/(d-W)$	$I_{Dif,sat} = q_0 A p_{n0} \frac{d-W}{\tau_p}$	$\left(\frac{d-W}{L_p}\right) p_{n0}$

Fig. 2.13 Three important special cases regarding the origin of the diffusion current.

Given a short recombination lifetime, such that the hole diffusion length is much smaller than the width of the undepleted region, only τ_p determines the diffusion current (Fig. 2.13 a)). While this situation will in general be encountered on radiation damaged devices, the supplied float zone silicon has lifetimes of the order of several milliseconds, resulting in diffusion lengths of the order of millimeters. Then either case b) or c) shown in Fig. 2.13 applies, whichever is the value of S. Given S is large (injecting contact), the diffusion current evidently grows significantly when W approaches d. The equation in Fig. 2.13 b) does however not hold in that instance, but rather is the maximum current that can be injected from the back plane equal to $q_0 A p_{n0} S$.

2.5.1.5 *Volume Current*

The reverse current arising from the steady state generation of electron-hole pairs in the electric field zone is typically predominating in silicon detectors because of the large depleted volumes. The latter is also the reason for the large radiation sensitivity of the total leakage current, inasmuch as the radiation damage creates defect levels in the forbidden gap of the semiconductor, promoting the generation of electron-hole pairs significantly. The volume leakage current I_{Vol} is related to the generation lifetime τ_g by

eq. 2.17 $$I_{Vol}(V) = q_0 A n_i \frac{W_g(V)}{\tau_g},$$

* Average value of the devices 912G02, 912G04, and 912G06 in reference [ALS93].

where W_g is the so-called generation width [RAW87]. It is not justified to put W_g equal to the depleted width W, because then a volume leakage current would be flowing even under zero bias, see eq. 2.6. However, at reverse bias voltages much larger than the built-in voltage V_{bi} the values of W and W_g are equal to within a few per cent, and I_{Vol} is growing as the square root of V. A more detailed description of the relation between W_g, the defect level causing the leakage current, and the reverse bias voltage can be found in Section 3.3.1.6.

The ratio between the volume current at the temperature T and a certain reference temperature T_R is given by ([SZE81])

eq. 2.18 $$R(T) = \frac{I_{Vol}(T_R)}{I_{Vol}(T)} = \left(\frac{T_R}{T}\right)^2 \exp\left(-\frac{E_g}{2k_B}\left[\frac{1}{T_R} - \frac{1}{T}\right]\right).$$

This equation has been employed for the normalization of the experimental leakage current data to the reference temperature T_R = 20°C, using an effective energy gap E_g equal to the dielectric energy gap at room temperature (1.12 eV). The relation presupposes a dominant generation center* close to the intrinsic Fermi level E_i. Given the generation center is displaced from E_i, a larger effective energy gap would be resulting (compare Section 3.3.1.6). However, as the temperature was always very close to 20°C (± 2 K), an error in E_g would hardly affect the results. On the other hand, if eq. 2.18 is extrapolated towards low temperatures, a closer inspection is necessary (see Section 5.1.2).

2.5.1.6 *Interface Generation Current*

Closely related to I_{Vol} is the interface generation current arising from the electron-hole pair generation at the oxide-silicon interface, see Fig. 2.7,

eq. 2.19 $$I_{ox} = q_0 A_{ox} n_i S_0.$$

The generation process is active only on the depleted interface, thus I_{ox} contributes to the current only for reverse bias voltages larger than the flat-band voltage, see Fig. 2.12. As holds true for the analogous processes in the bulk, I_{ox} is related to levels in the forbidden gap of the semiconductor. Although these levels may have a certain energetic distribution, only their overall action will be taken into account here in terms of the surface recombination velocity S_0. For purpose of temperature normalization again eq. 2.18 can be employed, however, the exponent of (T_R/T) now must be put equal to three rather than two† [NIC82].

2.5.1.7 *Edge Effects*

So far it has always been asserted that the one-dimensional modeling of the devices is sufficient. Indeed, the departures from the ideal behavior are minor effects, inasmuch as the electrode dimensions are large compared with the sample thickness. However, regarding the dynamic capacitance the lateral bounds of the depleted zone cause an internal stray capacitance. This is expected to be the larger, the closer these bounds are located to the junction contact. This is because the capacitance is a monotonic function of the reciprocal distance between the considered electrodes. A lateral extension of the electric field zone should therefore in the first approximation reduce the total capacitance.

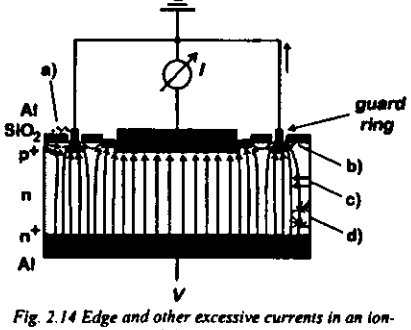

Fig. 2.14 Edge and other excessive currents in an ion-implanted diode and the operation of the guard ring. For the individual current contributions see text.

Also the leakage currents are typically observed to be larger than what would be expected from the sum of the previously discussed contributions. Fig. 2.14 shows some sources for excessive leakage currents. a)

* It will be shown in a late section that the dominant generation centers are in fact singled out by their neighborhood to this outstanding energetic position. Note that also the capture cross sections σ for electrons and holes are assumed to be equal.

† This relation assumes the surface states to be distributed homogeneously throughout the band gap.

illustrates the effect of humidity or moisture which conducts the pad electrode potential to the outer regions of the passivating oxide layer. Accordingly, the semiconductor electrons are repelled from the interface and a depleted surface (inversion) channel emerges, allowing for injection of free carriers generated at the numerous crystal imperfections at the sawing edge of the device. b) indicates the point of the largest electric field strength that might give rise to internal field emission (avalanche breakdown). c) refers to the diffusion of minority carriers into the field region, also taking place at the lateral bounds of the depleted zone. Finally, d) indicates the possibility of sawing cracks reaching into the field zone. However, usually the depletion region is sufficiently remote from the device edges to inhibit this process. In addition to a more precisely controlled sensitive volume, connection of the guard ring sinks most of the above excess currents. A particular difficulty is met with inverted detectors operated with a floating guard ring. Since the field zone then grows from the rear plane contact, which is not protected by a surrounding passivation layer, processes similar to a) should greatly enhance the overall leakage current. However, the effect of large concentrations of radiation damage-induced defect levels appears to prevent this potential failure mode [ERE96].

2.5.2 Experimental Techniques

Experimentally the measurement of current-voltage (IV) and capacitance-voltage (CV) data is straightforward. The employed equipment and the electrical connections can be found in Fig. F.2 of Appendix F. Virtually all measurements have been performed in the dark and in normal air atmosphere at room temperature. If not stated otherwise, the guard ring of the ion-implanted devices was left floating. Reverse bias characteristics were typically recorded by ramping the voltage from small to large values within a few minutes, allowing the sample and the instruments to settle at a given point for a sufficiently long time. CV data have always been recorded in the parallel readout mode of the LCR meter, i.e., the phase angle and the signal attenuation have been assumed to be due to a capacitor switched in parallel to a resistor, yielding the corresponding parallel capacitance C and the resistor conductance G. The oscillator frequency was usually 10 kHz and its amplitude V_{osc} was chosen as small as possible, typically 50 mV, but frequently noisy signals required larger levels of up to 1 V. Different values of V_{osc} do however hardly affect the measurement, contrary to the frequency f which on irradiated devices might severely influence the capacitance data at small reverse bias voltages. On the one hand, this is due to the damage-induced deep levels that, depending on their energetic position, can follow the oscillations and thus contribute to the dynamic capacitance only at sufficiently small frequencies [LI91]. On the other hand, the series resistance R_S, related to the undepleted bulk, can become significant, falsifying the real device capacitance C_{real} according to [GOR93]

$$\text{eq. 2.20} \qquad C = \frac{C_{real}}{1 + \left(2\pi f R_S C_{real}\right)^2} .$$

However, concerning reverse bias voltages close to the full depletion voltage V_{dep}, whose extraction often is the chief objective of CV measurements, the effect of eq. 2.20 is of minor importance.

2.5.3 Analysis of IV and CV Curves

The presentation of the different contributions to the dynamic junction capacitance and the leakage current given in the beginning of this section shows the detailed understanding about these basic device characteristics. Accordingly, the various parameters determining the peculiarities of the IV and CV curves can be extracted with high accuracy, as will be discussed in this section for both surface barrier and ion-implanted devices.

2.5.3.1 Evaluation of V_{dep}

It was stated previously that the junction capacitance C_J becomes a constant at the full depletion voltage V_{dep}, which is demonstrated in Fig. 2.15. However, frequently a slight reduction even beyond full depletion is observed, chiefly arising from the lateral expansion of the electric field zone. Therefore, the intersection of two straight-line fits to the CV data, one in the range $V > V_{dep}$, and the other one below V_{dep}, extended towards smaller bias voltages as long as the included points are in agreement with the

straight line model, is the usual praxis to obtain a reproducible numerical value for V_{dep}. Since the capacitance values might sometimes be affected by a small additive capacitance C_{stray} arising from an insufficient calibration of the LCR-meter, the CV curves have in this work been plotted into a C versus $V^{1/2}$ coordinate system, which also gives a straight-line. In contrast to the double-logarithmic plot, C_{stray} does then not influence the evaluation of V_{dep}. However, the differences are almost negligibly small.

2.5.3.2 Leakage Current at Full Depletion $I(V_{dep})$

Next the leakage current at full depletion $I(V_{dep})$ is determined by simply interpolating the IV data at the previously obtained V_{dep}. If volume current predominates the leakage current becomes more or less flat above full depletion. On the as-processed surface barrier detector shown in Fig. 2.15 the further increase is assumed to be due to minority carrier injection from the rear contact, electric field dependent lowering of the Schottky barrier, or other excessive leakage currents previously discussed. However, even very small bulk damaging particle fluences introduce a lot of efficient generation centers, such that these currents are in practice always screened by the volume current contribution.

2.5.3.3 Flat-Band Voltage V_{fb}

Flat-band voltages V_{fb} were extracted from the CV curves as illustrated in Fig. 2.15. In a log-log plot a straight line was fitted to the isolated junction capacitance C_J data observed in the range $V_{fb} << V << V_{dep}$, in order to allow for an extrapolation into the lower reverse bias range. Subtraction of C_J from the total capacitance signal separates the contribution $C_{MOS}(V)$ arising from the MOS region around the junction. Looking up the reverse bias at which this contribution equals the value yielded by eq. 2.13 provides a reproducible measure of the flat-band voltage V_{fb}.

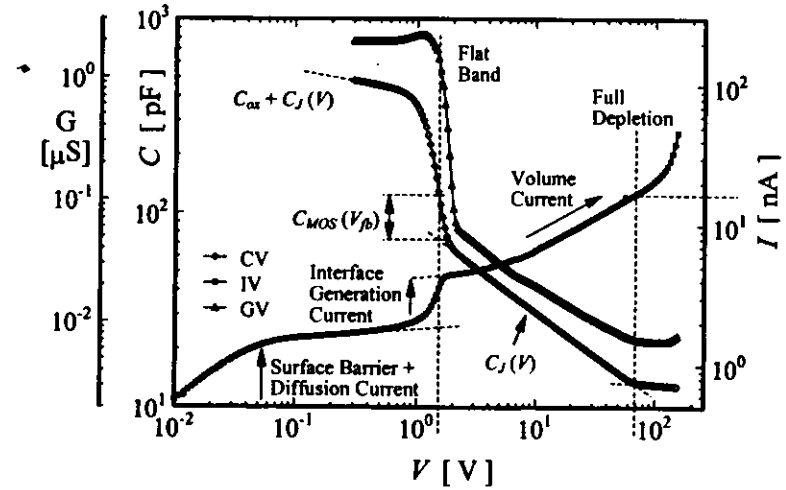

Fig. 2.15 Illustration of the evaluation of the flat-band voltage, the interface generation current, the full depletion voltage, and the corresponding full depletion leakage current on a surface barrier device, see text (device 932G30).

2.5.3.4 Interface Generation Current I_{int}

Firstly, a straight line is fitted to the total leakage current I measured well below the flat-band voltage in order to account for both the approximately constant offset comprised of the surface barrier and diffusion current and the slight increase attributed to the volume current. Secondly, a straight line is fitted to a small voltage range above V_{fb}, where the interface generation current has emerged and a further slight variation is seen. Now, I_{int} was taken as the difference between these two lines at V_{fb}. Regarding the latter

straight-line fit, it is noted that for increasing reverse bias voltages the total current might either be found to be continuously increasing, indicating a predominating volume current contribution properly accounted for by the above procedure, or to be decreasing, which then gives a local maximum in the IV curve, the so-called overshoot [FRE90]. In these instances the peak current was used instead of the straight-line fit extrapolation.

This phenomenon is typically observed when I_{ss} predominates and therefore reflects a voltage dependent reduction of the electron-hole pair generation rate at the oxide-silicon interface. Now, the generation is most efficient at those particular interface states for which emission of both electrons and holes takes place at a high rate, compare Fig. 2.7. Hence, an optimum surface generation center exhibits a level close to the middle between the valence and conduction band. Further, the average occupation with electrons is close to 1/2, that is, the surface Fermi level is close to the considered level. As the surface Fermi level sweeps from the conduction towards the valence band during the transition from the accumulation to the inversion, a maximum generation rate is expected at an intermediate reverse bias voltage: $V_{fb} + (E_{Fn} - E_i)/q_0$. The latter term depends on the effective doping concentration and is of the order of 0.1 V for the material used in this work. It must however be born in mind that the considered MOS structure is not isolated but rather electrically connected to the junction of the diode. It is therefore not justified to determine the occupation of the surface states by means of a surface Fermi level, since such a quantity exists only as long as no current is flowing. Still the above arguments might serve for a qualitative understanding of the effect.

2.5.3.5 Conductance

Conductance (GV) data have always been recorded, but were not evaluated quantitatively. Given the assumed equivalent circuit comprised of a capacitance in parallel with a resistance is correct, the low frequency limit of the GV-curve should be equal to the derivative of the IV curve dI/dV. Therefore, in the first approximation the conductance should depend on the bias voltage as does the dynamic capacitance, and this behavior is indeed observed in Fig. 2.15.

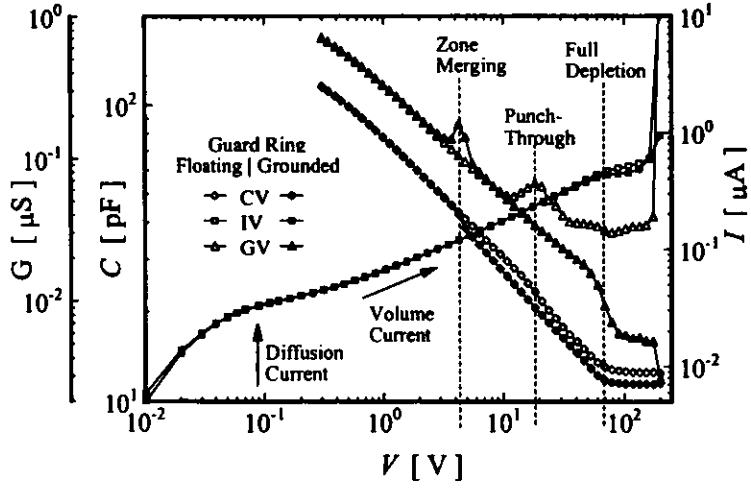

Fig. 2.16 IV, CV, and GV characteristics measured with either a floating or a grounded guard ring on an ion implanted detector (device M20812 stored for one run period in the PLUG calorimeter of H1 at HERA which produced bulk damage corresponding to an equivalent 1-MeV neutron fluence of around 10^{12} cm^{-2}).

2.5.3.6 Characteristics of an Ion-Implanted Device

Fig. 2.16 shows the IV, CV, and GV curves obtained on an ion-implanted device. All curves have been recorded with either a floating or a properly connected guard ring. The corresponding differences are related to specific extent of the field zone, see Section 2.4.3. Regarding the capacitance measured with a grounded guard ring, a sudden reduction is observed at around 4 V which must be concluded to be due to the merging of the depletion zones underneath the guard and the main pad, resulting in a decrease of the internal stray capacitance. Similarly a weak reduction is observed at around 20 V in the floating configuration, related to the occurrence of the punch-through. It will be noted that in both cases the conductance data exhibits a peak which, although it is not understood in detail, appears to be a fingerprint of these situations. With respect to the capacitances attained in the fully depleted state, the difference between the two modes of guard ring operation is, on the one hand, due to the different sensitive areas that need to be taken into consideration (see Table 2.1) and, on the other hand, due to the remaining internal stray capacitances in the floating configuration. In any case the depletion capacitance is larger than the value of around 10 pF expected for the given sample geometry according to $\varepsilon\,\varepsilon_0 A/d$. Finally, it will be noted that on this sample the proper connection of the guard ring helps in reducing the total current, not only because of the smaller sensitive area, but also due to the absorption of excessive leakage currents, as can be observed in the breakdown region around 200 V.

2.6 Laser-Induced Current Pulse Shapes

Current pulse signals measured at the terminals of a detector depend on the distribution of the electric field strength in the device. It is therefore possible to deduce the concentration of space charges $N_{eff,SCR}$ experimentally by intentionally inducing the current pulse and investigating it with an oscilloscope. This method has been introduced around 30 years ago, see for example reference [FRE70], and is now often referred to as TCT (Transient Current Technique). Regarding $N_{eff,SCR}$ it provides a critical cross-check to the otherwise used values inferred from CV curves. Moreover, based on this method an interesting tool for the microscopic investigation of defect levels has recently emerged (see Section 3.3.5). The various peculiarities of the current pulses and the procedures employed for the extraction of $N_{eff,SCR}$ will be discussed in the following.

2.6.1 Measurement Principle

2.6.1.1 Origin of the Current Signal

In the following the front and rear electrodes of the considered detector will be assumed to be connected to a negative and a positive terminal, respectively, such that electrons drift from the front to the rear contact and holes in the opposite direction. In addition the x axis of the employed coordinate system is always supposed to originate in the front contact and to point towards the rear electrode, which thus is located at $x = d$, so that the previous statement is equivalent to a negative value of the electric field strength E. If now N electron-hole pairs are created in the direct vicinity of the front or rear contact of a fully depleted detector, as e.g. in Fig. 2.17 by a laser, only either electrons or holes will travel through all of the detector, while accordingly either the holes or the electrons are collected immediately by the adjacent electrode. These two situations will therefore be called electron or hole injection. Now, with respect to Ramo's theorem eq. 2.1, the current signal $I_{n,p}(t)$ induced during the drift of either carrier (n or p) reflects its drift velocity $v_{dr,n,p}$ at a certain time t of the charge collection process,

eq. 2.21 $$v_{dr,n,p}(t) = \frac{d}{N_{n,p}(t) q_0} I_{n,p}(t) .$$

Corresponding experimental data are given by the transit regions of the current pulse shapes displayed in Fig. 2.18 a) and b) for electron and hole injection, respectively. The electron drift velocity is large in the beginning and decreases towards the end of the full collection time. In contrast to this, the holes drift but slowly in the beginning and are significantly accelerated during their passage through the detector. It is however well known that over a wide range of temperatures the drift velocity of both carriers in (111)-oriented silicon is an increasing function of the absolute value of the electric field strength, see Appendix A. In particular at low fields it is $v_{d,n,p} = \mu_{e,n,p} |E|$, and at high field strengths $v_{d,n,p}$ approaches a certain saturation value $v_{s,n,p}$. The measurements in Fig. 2.18 do therefore indicate a larger value of $|E|$ underneath the front electrode than below the rear electrode, as it is expected for an undamaged n-type detector exhibiting a positive space-charge, compare Fig. 2.6 b). Hence, one of the main benefits of the current pulse measurement is the direct evidence of the sign of the space charge. Further, it is clear that an increased reverse bias voltage results in a larger electric field strength, and accordingly the current signal is growing. Generally the full collection time of the injected electrons is approximately three times smaller than the one of the holes, in agreement with the ratio between the corresponding drift velocities.

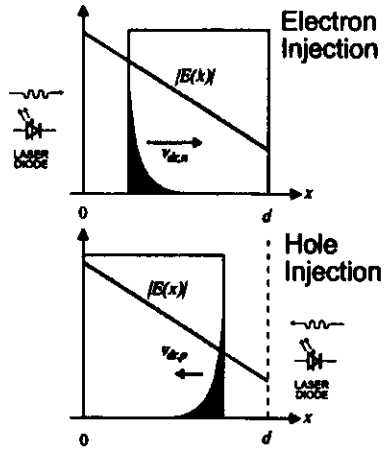

Fig. 2.17 Schematic illustration of the origin of the current pulse shapes.

Finally it will be noted that the total number of drifting electrons or holes $N_{e,p}$ is steadily decreasing during the charge collection process. This effect is due to the trapping at defect levels, resulting in an exponential decay of the number N of initially created pairs according to

eq. 2.22 $$N_{e,p}(t) = N \exp\left(-t/\tau_{tr,n,p}\right)$$

Here $\tau_{tr,n,p}$ denotes the trapping time constants for electrons and holes.

2.6.1.2 *Experimental Procedure*

Regarding the other features of the measured curves in Fig. 2.18, for instance those in the leading and trailing edge regions, it is necessary to have a closer look at the experimental procedure employed to record the current pulse shapes. The basic set-up of the measurement is identical to the time-of-flight experiment described by C. Canalli et al., who have studied the drift velocity $v_{d,n,p}$ of electrons and holes as function of the electric field strength and the temperature. However, they chiefly aimed at a constant $v_{d,n,p}$ and evaluated the duration of the current pulse, while here it is important to accurately measure the overall shape containing the information concerning the electric field profile.

The key element is a Tektronix TDS 540 sampling oscilloscope, providing a maximum of 1 Gigasamples per second and an analog band-width of 500 MHz, see the block diagram of the experimental set-up in Fig. F.4 in Appendix F. The current signal of the detector is transmitted via a coupling capacitor from the front contact electrode to the oscilloscope input connector, which is terminated by a 50 Ω resistor. Accordingly, the voltage measured by the oscilloscope is related to the current signal by $50\,\Omega \times i(t)$. Free carriers are generated underneath the sample electrodes by illumination with a short (< 1 ns) light pulse emitted from a low power semiconductor laser diode. A Hewlett Packard pulse generator is used to drive the laser electronically and also provides an accurate trigger signal, employed to initiate the recording of a waveform into the oscilloscope. Since typically a few hundred current pulse shapes need to be averaged in order to improve the signal to noise ratio, the external triggering is inevitable to avoid a broadening of the resulting waveform by a time jitter. However, the pulse generator introduces a lot of electronic interference, spoiling the recorded signals unless the light pulses are optically delayed by a several meters long glass fiber.

The leading and trailing edges of the pulse are affected by the total system risetime which, on the one hand, is determined by the analog bandwidth of the oscilloscope and, on the other hand, by the sample capacitance of around 10 pF and the oscilloscope input impedance of 50 Ω, resulting in a $2.2RC$ (10% to 90% risetime) of around 1 ns.

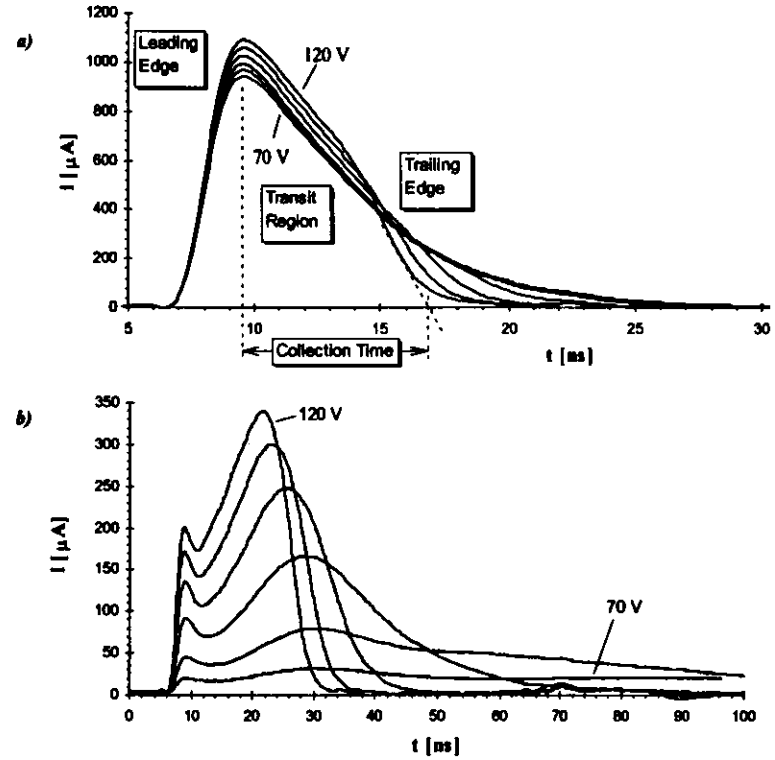

Fig. 2.18 Current pulse shapes measured on an undamaged ion-implanted device as function of the reverse bias voltage which was varied between 70 V and 120 V using 10 V increments. Free carriers were generated by a short (< 1 ns) 830 nm laser light pulse. a) Electron injection at the front electrode. b) hole injection at the rear electrode (device M21012, $V_{dep} = 84.7$ V)

2.6.1.3 *Closer Inspection of the Features of the Current Pulse Shape*

Now, the free carriers are not generated on a negligibly small distance but rather exhibit an exponential distribution,

eq. 2.23 $$n(x,t=0) = p(x,t=0) = N\frac{\alpha}{S}\begin{cases} \exp(-\alpha x) & \text{electron injection} \\ \exp(-\alpha(d-x)) & \text{hole injection} \end{cases}, \quad x \in [0\ldots d].$$

Here S is the illuminated area and α denotes the absorption constant, whose dependence on the wavelength λ and temperature T is explored in Appendix A. Typically a laser with $\lambda = 830$ nm has been used, penetrating around 10 µm into the silicon substrate at room temperature. Thus, in the beginning of

the current pulse shape presented in Fig. 2.18, which shows the total current $i = I_n(t) + I_p(t)$, an additional signal arises from a few holes and electrons drifting back to the illuminated electrode for the case of electron and hole injection, respectively. However, the holes are producing a comparatively small current signal due to their lower drift velocity and are therefore hidden under the predominating electron signal in Fig. 2.18 a). Moreover, the trailing edge of the current pulse shapes essentially reflects the progressing collection of the broad distribution of free carriers arriving at the collecting electrode*.

Usually the illuminated area S was around 0.01 cm², and the total number of electron-hole pairs N was of the order of 10^7. In conjunction with the above quoted penetration depth it can be concluded from eq. 2.23 that the initial concentration of free carriers generated at the illuminated electrode is of the order of 10^{12} cm^{-3}. As this value is similar to the effective doping concentration, the electric field is initially screened, known as plasma effect and resulting in a further deterioration of the signal risetime.

If the reverse bias is smaller than the full depletion voltage, an undepleted region evolves at the rear contact. Given the space charge is positive the electrons injected at the front contact travel towards the low field region with a continuously reduced velocity†, causing the long tail observed in Fig. 2.18 a). In contrast to this, a large portion of electron-hole pairs is created within the bulk region if the laser-light impinges onto the rear contact. Still, a regular current pulse shape is observed in Fig. 2.18 b) due to the exponential tail of the generated free carriers (eq. 2.23) which in part reaches into the field region. Minority carriers created in the bulk region diffuse into the field zone which is a comparatively slow process and therefore gives rise to the long tail encountered in Fig. 2.18 b).

2.6.2 Analysis of Current Pulse Shapes

2.6.2.1 Deduction of the Entire Field Profile E(x)

In the following it will be assumed that the current pulse shape is arising from the drift of an infinitely small layer of either N electrons or holes created in the direct vicinity of the contact electrodes. Given an experimental current pulse shape $i(t)$, one can calculate the drift velocity $v_{dr,n,p}$ corresponding to the time t during the collection process with eq. 2.21. Further, there is a unique relation between $v_{dr,n,p}$ and the absolute value of the electric field strength $|E|$ (see Appendix A) such that one equally well can plot E versus t. In order to convert the t axis into a spatial coordinate, it is necessary to deduce the position $x_{n,p}$ of the drifting electrons or holes at the time t. Now, the differential equation governing the motion of the free carriers is simply given by

$$\text{eq. 2.24} \qquad \frac{d\,x_{n,p}}{dt} = \pm v_{dr,n,p}(t).$$

The ± sign accounts for the fact that electrons/holes are drifting towards increasing/decreasing values of the x-coordinate ($v_{dr,n,p}$ is a positive number). The solution is obtained by integration

$$\text{eq. 2.25} \qquad x_{n,p}(t) = x_{n,p}(0) \pm \int_0^t dt'\, v_{dr,n,p}(t'),$$

where $v_{dr,n,p}(t)$ needs to be substituted from eq. 2.21, and the initial values of the carrier positions are $x_n(0) = 0$ and $x_p(0) = d$.

For the calculation of numerical values of the drift velocity by eq. 2.21, evidently the number $N_{n,p}$ of electrons or holes is required, which however is not known a priori, but can be calculated as follows. Given the trapping time constants are sufficiently large, such that the number of the drifting electrons/holes is essentially constant and equal to N, it can be exploited that after the so-called collection time $t_{c,n,p}$ all electrons or holes have passed through the detector, that is,

* These features are also illustrated in Fig. 2.22, the result of the numerical simulation of the corresponding processes.

† Indeed, in the simple physical modeling their collection time diverges, i.e., they never reach the undepleted bulk region.

$$\text{eq. 2.26} \qquad \begin{aligned} x_n(t_{c,n}) &= d = x_p(0) \\ x_p(t_{c,p}) &= 0 = x_n(0) \end{aligned}.$$

Substituting eq. 2.21 into eq. 2.25 and evaluating the resulting expression at $t = t_{c,n,p}$ gives

$$\text{eq. 2.27} \qquad \pm\frac{x_{n,p}(t_{c,n,p}) - x_{n,p}(0)}{d} N q_0 = \int_0^{t_{c,n,p}} dt'\, I_{n,p}(t').$$

This relation was written in a more general form in order to calculate the contribution of N electrons or holes created at an arbitrary position $x_{n,p}(0)$ in the detector to the externally detected signal. Since electrons and holes are always created in pairs, it is instructive to consider the sum of the two corresponding signals $\int dt' I_n(t') + \int dt' I_p(t')$: it is always equal to Nq_0. Furthermore it can be concluded that the full integral over the current pulse shape always gives Nq_0, irrespective of the initial spatial distribution of the ionized free carriers.

2.6.2.2 Extraction of the Space Charge Concentration

According to the procedure outlined above, the full electric field profile and therefore inhomogeneous distributions of the space charges can in principle be extracted from the current pulse shape. However, in practice deviations from a linearly graded electric field are hardly encountered, and methods assuming such a distribution of the electric field are commonly employed because they provide an easy tool to determine V_{dep}. A graphical construction of the electric field in a fully depleted detector is presented in Fig. 2.19. It has been exploited there that the electric field obeys the superposition principle, i.e., $E(x)$ can be written as the sum of the field strength established in the fully depleted detector and the constant field arising from the overbias $V - V_{dep}$ dropping over the full detector thickness d. $E(x)$ can suitably be written in the following form

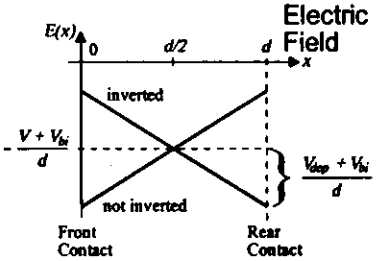

Fig. 2.19 Graphical construction of the electric field strength in a fully depleted detector.

$$\text{eq. 2.28} \qquad E(x) = -\frac{1}{d}\left[\left(V + V_{bi}\right) + k\left(1 - \frac{x}{d/2}\right)\left(V_{dep} + V_{bi}\right)\right],\ V \geq V_{dep},$$

where $k = \text{sign}(N_{eff,SCR})$ denotes the sign of the space charges that can be deduced from the shape of the current pulse directly. Once the full depletion voltage has been determined, $N_{eff,SCR}$ follows immediately from eq. 2.7.

The Collection Time

It will now be investigated which time expires during the drift of the free carriers from the place of their origin to an other position in the detector. Again the relation follows from the differential equation eq. 2.24. However, here the drift velocity is considered as function of the distance,

$$\text{eq. 2.29} \qquad t = \pm \int_{x_{n,p}(0)}^{x_{n,p}(t)} dx' \frac{1}{v_{dr,n,p}(|E(x')|)}.$$

Given an experimental value of the collection time $t_{c,n,p,exp}$ for either electron or hole injection has been extracted from a current pulse shape measured on a detector of known thickness d and at a certain reverse bias V. It is then possible to find a unique value of the full depletion voltage V_{dep}, determining the dependence of the electric field strength on the distance in eq. 2.28, such that the collection time

calculated according to eq. 2.29 equals the experimental value. The built-in voltage V_{bi} will be assumed to be equal to zero. For the purpose of numerical evaluation eq. 2.29 is approximated by a sum*

eq. 2.30 $$t_{c,n,p,exp}(V_{dep}) = \sum_i \frac{\Delta x_i}{v_{dr,n,p}(|E(x_i)|)}, \qquad d = \sum_i \Delta x_i ,$$

where $v_{dr,n,p}$ needs to be taken from Appendix A at the temperature of the specific measurement in question, and the electric field strength has to be calculated by eq. 2.28.

The procedure outlined above is the so-called t_c -method of the determination of the full depletion voltage. It is however not straight-forward to extract an experimental value of the collection time from the current pulse shape since, on the one hand, the drifting carriers are a broad distribution rather than an infinitely thin layer of charges and, on the other hand, the leading and trailing edges are affected by the system risetime. Fig. 2.18 a) illustrates a heuristically developed routine which was found to give depletion voltage data in agreement with those obtained from CV measurements, at least on undamaged devices (compare Fig. 2.20). One reference point in time is given by the first maximum of the current pulse shape and the second one by the intersection of the baseline with a straight-line fit to the trailing edge of the pulse. It will be noted that trapping effects hardly affect the evaluation unless significant portions of the drifting carriers are removed, such that the current signal fades before the collection process is completed.

The Transit Time Constant

An other evaluation method analyzes the shape of the current pulse in the transit region and will be called the τ -method. It is necessary to assume a constant mobility, i.e.,

eq. 2.31 $$v_{dr,n,p}(|E|) \approx \mu_{c,n,p}|E| ,$$

since then eq. 2.29 can be solved analytically by substituting the electric field strength E for the spatial coordinate x and employing the relation $dE/dx = 2k(V_{dep} + V_{bi})/d^2$. The result is the electric field at the position $x_{n,p}$ of the drifting particles, where they arrive at the time t ,

eq. 2.32 $$E(x_{n,p}(t)) = E(x_{n,p}(0))\exp\left(-\frac{t}{\pm k\tau_{n,p}}\right).$$

Here the transit time constant $\tau_{n,p}$ is given by

eq. 2.33 $$\tau_{n,p} = \frac{d^2}{2\mu_{c,n,p}(V_{dep} + V_{bi})} = \frac{\varepsilon\varepsilon_0}{q_0\mu_{c,n,p}}\frac{1}{|N_{eff,SCR}|}.$$

The expression on the right-hand side must not be confused with the dielectric relaxation time that is obtained by replacing the constant mobility with the zero field mobility $\mu_{0,n,p}$ and the absolute value of the effective doping concentration $|N_{eff,SCR}|$ with the concentration of free carriers in the not depleted bulk region which especially in radiation-damaged devices can largely deviate from $|N_{eff,SCR}|$. Now, the field strength according to eq. 2.32 can be substituted into eq. 2.31 to give the drift velocity which further can be used in the Ramo's theorem to equate the observed current signal

eq. 2.34 $$I_{n,p}(t) = \frac{Nq_0\mu_{c,n,p}}{d}|E(x_{n,p}(0))|\exp\left(-t\left[\frac{\pm k}{\tau_{n,p}} + \frac{1}{\tau_{tr,n,p}}\right]\right).$$

Here also the possible loss of carriers due to the trapping has been accounted for by eq. 2.22. Accordingly, a plot of the natural logarithm of the current signal $I_{n,p}$ versus the time t gives a straight-line with slope

eq. 2.35 $$\tau_{eff}^{-1} = \frac{\pm k}{\tau_{n,p}} + \frac{1}{\tau_{tr,n,p}}.$$

* Earlier works have equated the drift velocity by $v_{dr} = \mu_0(1 - aE)E$, which allows for an analytical solution of the integral. However, the actual field dependence of v_{dr} is more complicated, resulting in a higher accuracy of the numerical approach.

Provided the trapping can be neglected or is estimated from experimental data, the transit time constant can be calculated from eq. 2.35 and may be used in conjunction with eq. 2.33 to determine $|N_{eff,SCR}|$. In this work the constant mobility has always been derived from the drift velocity data presented in Appendix A at the average electric field strength V/d , compare Fig. 2.17,

eq. 2.36 $$\mu_{c,n,p} = \frac{v_{dr,n,p}(V/d)}{V/d}.$$

Comparison with CV Data

Finally it will be demonstrated that on undamaged devices the two methods described above give depletion voltages in agreement with the corresponding data obtained from CV measurements. For this purpose CV curves and current pulse shapes were measured on a set of 22 undamaged detectors exhibiting a wide spread in the initial doping concentration. In some cases hole injection at the rear plane contact was not possible due to the aluminum metallization. Fig. 2.20 displays the good correlation with the CV reference data. It is noted that the t_c -method gives more reliable data than the τ -method which tends to underestimate the depletion voltage. The error in the τ -method is increasing with V_{dep} because the collection times are decreasing, resulting in a serious influence of the system risetime on the shape of the current pulse signal in the drift region. This effect is a particular difficulty met with the pulses induced by electron injection. It is noted here that the trapping effects in the undamaged devices can be neglected and would not affect the evaluation.

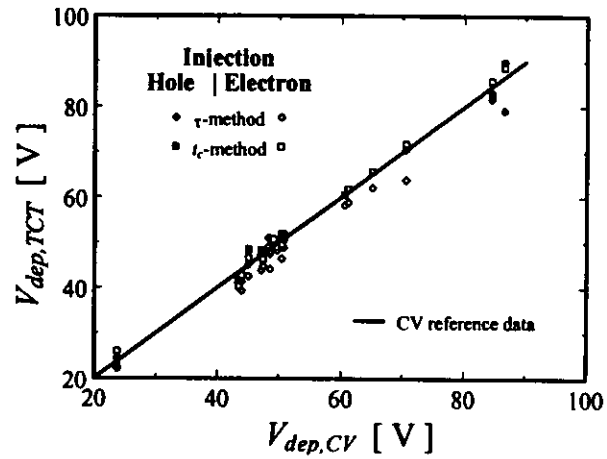

Fig. 2.20 Depletion voltages $V_{dep,TCT}$ determined from current pulse (TCT) measurements on a couple of undamaged devices by either the τ- or the t_c-method, see text. For comparison the data are plotted as function of the according $V_{dep,CV}$ extracted from capacitance voltage characteristics.

2.6.2.3 Simulation of Current Pulse Shapes

All methods for the analysis of current pulse shapes described so far did not take into account the initial distribution of the carriers generated by the laser light pulse, the deterioration by the system risetime, and other effects like for instance the broadening of the drifting carrier distribution arising from their diffusion. The most general way to examine the pulse shape data is to make a certain assumption about

the electric field distribution, i.e. $N_{eff,SCR}$, and to numerically simulate the current signal. Fitting the simulated to the experimental data should then give an optimum value for $N_{eff,SCR}$. This approach has been worked out with the aid of V. Eremin [ER196,GER96].

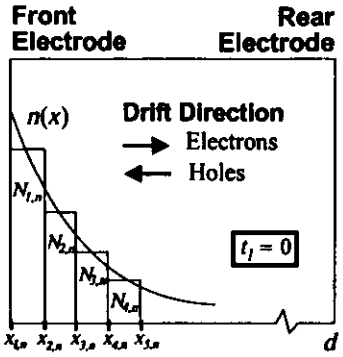

Fig. 2.21 Subdivision of the initial electron distribution n(x) generated by a laser light pulse impinging onto the front electrode.

Numerical Approach

The initial exponential distribution of the free carriers is subdivided into two sets of J layers, typically $J = 35$, each layer containing either $N_{j,n}$ electrons or $N_{j,p}$ holes, as illustrated in Fig. 2.21. Further, a discrete spatial coordinate $x_{j+1,n,p}$ is assigned to the boundary between the layers, such that the initial $N_{j,n,p}$ can be deduced from integration of eq. 2.23. For the case of electron injection, i.e. laser light impinging onto the front electrode, this gives

eq. 2.37 $$N_{j,n,p} = N\left[\exp\left(-\alpha x_{j,n,p}\right) - \exp\left(-\alpha x_{j+1,n,p}\right)\right]$$

and a similar result can be obtained for hole injection at the rear electrode. Now, the evolution of these layers is followed in time by solving the motion equation eq. 2.25 for each coordinate $x_{j,n,p}$ numerically employing a constant time step Δt, i.e. $t_k = k\,\Delta t$, where Δt usually was equal to 0.1 ns,

eq. 2.38 $$x_{j,n,p}(t_{k+1}) = x_{j,n,p}(t_k) \pm v_{dr,n,p}(|E(x_{j,n,p}(t_k))|)\Delta t\,.$$

Here, the drift velocities $v_{dr,n,p}$ were taken from the approximation to the experimental data published by C. Canalli, see Appendix A. The electric field strength is given by eq. 2.28, however, the built-in voltage V_{bi} has always been neglected. It is noted that the discrete points are not equidistant unless $v_{dr,n,p}$ is constant throughout the detector. The iterative procedure defined by eq. 2.38 is repeated until all carriers have arrived at the correspondingly collecting electrode. Application of Ramo's theorem, eq. 2.1, yields the current produced by the j^{th} layer at the time t_k,

eq. 2.39 $$I_{j,n,p}(t_k) = N_{j,n,p} q_0 \frac{v_{dr,n,p}(|E(x_{j,n,p}(t_k))|) + v_{dr,n,p}(|E(x_{j+1,n,p}(t_k))|)}{2d}\,.$$

Note that the average value of the drift velocity for the layer in question has been used. Since the carrier concentrations are supposed to be sufficiently small such that they do not screen each other, the total current produced by either electrons or holes at a specific time t_k follows from

eq. 2.40 $$I_{n,p}(t_k) = \sum_{j=1}^{J} I_{j,n,p}(t_k)\,.$$

The external current signal is given by the sum of both electron and hole current $I(t_k) = I_n(t_k) + I_p(t_k)$.

One particular result of such a simulation is presented in Fig. 2.22 for either injection of carriers at the front a) or rear electrode b). For both cases the relative contribution of the electrons and the holes to the total current signal has been indicated. A thickness of 300 µm and a positive space charge concentration (n-type) of 10^{12} cm^{-3} was assumed, giving a full depletion voltage V_{dep} of around 65 V. Moreover, the temperature, the reverse bias, and the laser wavelength were presupposed to be 300 K, 100 V, and 830 nm, respectively.

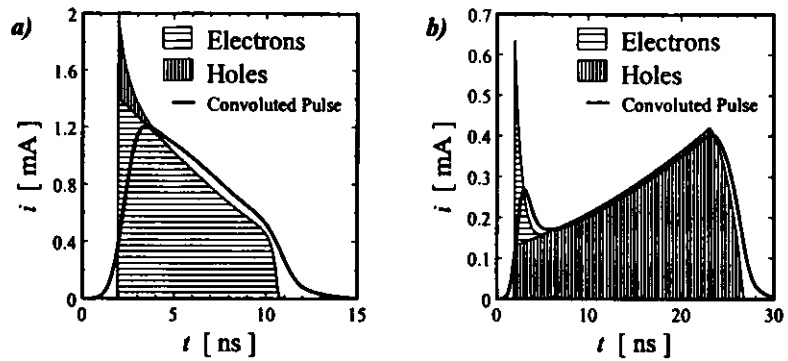

Fig. 2.22 Electron and hole components of the simulated current pulse shapes and the influence of the convolution with the system function. a) Front electrode, b) rear electrode illumination, regarding the parameters of the simulation, see text.

Diffusion and Trapping

In this numerical treatment longitudinal diffusion effects can in the first approximation be taken into account by the following procedure*. The $N_{j,n,p}$ have to be related to the corresponding free carrier concentrations n' and p' per distance by normalization to the appropriate layer width $x_{j+1,n,p} - x_{j,n,p}$. A gradient of this concentration results in a particle diffusion current $-D_{n,p}\,\partial\{n',p'\}/\partial x$, where in a semiconductor the diffusion coefficient $D_{n,p}$ is related to the low field mobility by

eq. 2.41 $$D_{n,p} = \frac{k_B T}{q_0}\mu_{0,n,p}\,.$$

Now, the continuity equation can be employed to obtain the temporal variation of the carrier concentrations due to the diffusion $\partial\{n',p'\}/\partial t = D_{n,p}\,\partial^2\{n',p'\}/\partial x^2$. Multiplying the latter with the time increment Δt does therefore furnish the change in the concentration that needs to be taken into consideration for one time step. Given the second derivative of the carrier concentration has been determined with an appropriate numerical method, the evolution in time of the number of carriers in the j^{th} layer can be written

eq. 2.42 $$N_{j,n,p}(t_{k+1}) = \left[N_{j,n,p}(t_k) + \left(x_{j+1,n,p} - x_{j,n,p}\right) D_{n,p} \frac{\partial^2\{n',p'\}}{\partial x^2}\Delta t\right] \exp\left(-\Delta t/\tau_{tr,n,p}\right)$$

Here the factor on the right-hand side accounts for the reduction of the carriers due to trapping (eq. 2.22).

The above program to represent the carrier diffusion is considered to be a first order approximation. A more rigorous derivation of the problem should start from the continuity equation, accounting for drift and diffusion simultaneously. However, for sufficiently small time steps Δt eq. 2.42 is expected to give reasonable numerical results. The corresponding evolution of the carrier distribution during the drift through the detector is shown in Fig. 2.23. While this affects the current pulse shapes only slightly in the trailing edge region, the system risetime, which will be discussed in the following, strongly distorts the pulse shape. Therefore, the numerically cumbersome calculation of the diffusion effects has always been omitted in the later analysis.

* Transversal diffusion does not affect the simulation result since the problem is tackled in a unidimensional picture.

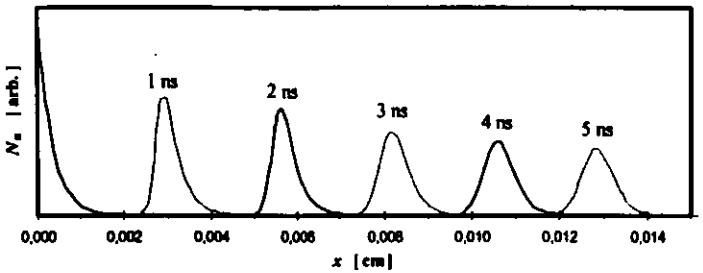

Fig. 2.23 Evolution of the distribution of the injected electrons during their passage through the detector showing the effect of diffusion (V_{bias} = 150 V, T = 300 K, λ = 830 nm).

Influence of the System Risetime

The current signal $I(t)$ resulting from the simulation could in an idealized case be measured directly at the electrodes of the detector. However, the electronic circuit attached to the detector feeding the current into the oscilloscope transforms the original signal, and some of the responsible sources have already been discussed in Section 2.6.1.2. This circumstances can appropriately be accounted for by the system impulse response $h(t)$ which is the output signal of the electronic circuit in question when the input has been stimulated by a delta-peak at $t = 0$. Then the output current $i(t)$ observed for an arbitrary input $I(t)$ is given by

eq. 2.43 $$i(t) = \int_{-\infty}^{+\infty} d\tau\, I(\tau) h(t-\tau).$$

It is therefore desirable to know the system impulse response, which is however hampered by the experimental difficulty to establish a delta peak-like input signal. If however $I(t)$ is a step function, whose derivative is a delta-peak, it can be shown that the derivative of the resulting output signal $i(t)$ also gives the impulse response. Now, in the first approximation a step-like current signal can be generated in the detector by simply employing a very long laser light pulse, since the corresponding photo-current rises very swiftly and remains very closely a constant afterwards. The numerical differentiation of the leading edge of a correspondingly recorded waveform is displayed in Fig. 2.24. For the further evaluation, the experimentally determined impulse response was parametrized by the sum of a Gaussian contribution and an exponential tail,

eq. 2.44 $$h(t) = \frac{a}{\sigma_h\sqrt{2\pi}} \exp\left(-\frac{t^2}{2\sigma_h^2}\right) + \frac{b}{\tau_h}\left(t/\tau_h\right)^2 \exp(-t/\tau_h)\,\theta(t),$$

where $\theta(t)$ is Heavyside's step function, and the normalization requires $a + 2b$ to be equal to unity. In order to gain this representation, the data were shifted by 7.9 ns on the t axis, such that the outstanding maximum is located at $t = 0$. The solid line in Fig. 2.24 is the corresponding fit obtained with the parameters $a = 0.82$, $\sigma_h = 0.7$ ns, $b = 9.0\times10^{-2}$, and $\tau_h = 0.89$ ns.

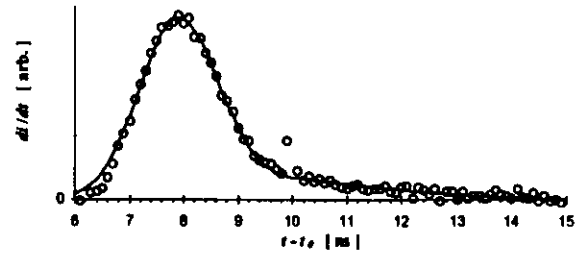

Fig. 2.24 The circles are the derivative of the initial rise of a measured current pulse shape that was induced by a long (> 15 ns) pulse of laser light on a detector reverse biased with 150 V. The solid line is the fit, furnishing the system pulse response in a suitable analytical form for a shifted time scale, see text.

Numerical convolution of the simulated current pulse shapes $I(t)$ was done according to eq. 2.43, employing the data as presented in Fig. 2.24 in the range from around 6 ns to 13 ns. The effect is shown in Fig. 2.22, emphasizing the role of the system risetime for the actual shape of the signal. It is noted that the previously discussed τ - method for the evaluation of the effective doping concentration can thus be afflicted with a serious systematic error, especially if it is applied to the short pulse shapes observed after electron injection at the front electrode.

2.7 Summary of the Basic Features of Silicon Detectors

- The operational principle of silicon detectors, the features of the float zone silicon substrate and the thermal oxide surface layer, and the design of the devices studied was presented. The one-dim. treatment of the electric field zone for an abrupt junction and a MOS diode was developed.

- The extension of the depleted zone was probed with spatially resolved proton micro-beam measurements on surface barrier and ion-implanted devices with floating and grounded guard ring. The lateral extension in the fully depleted state was found to be 120 μm for the floating guard ring set-up.

- The peculiarities of capacitance and current-voltage characteristics on surface barrier and ion-implanted devices were explained based on the proton micro-beam results.

- The theory of laser-induced current pulse shapes was developed focusing on the extraction of the space charge concentration. A comparison with CV data on unirradiated devices showed a good agreement. Methods based on the collection time rather than on the transit time constant were found to be more reliable and to be more robust in the presence of trapping centers and significant system risetimes. The simulation of pulse shapes was outlined accounting for electric field and temperature dependent drift velocities, diffusion, trapping, and the system risetime.

3 Bulk Damage Effects

Contrary to the oxide surfaces of silicon devices, electron-hole pairs created by an ionizing particle in the crystalline silicon bulk do not cause any permanent damage. Rather does the performance of a silicon detector, which predominantly is determined by the bulk properties, suffer from the displacement of silicon host atoms. A natural distinction is therefore given between surface damage effects, depending on the ionization dose (see Section 4), and bulk damage effects that will be discussed in the following.

3.1 The NIEL* Hypothesis

Displacement damage occurs if the interaction of an impinging particle of energy E_p transfers sufficient kinetic energy E_R to a specific silicon atom such that it is removed from its regular lattice site. This particular atom is then called the PKA (Primary Knock-on Atom), or recoil atom. As it takes at least a displacement threshold energy of approximately E_d = 25 eV to be overcome, it is often instructive to consider the maximum energy $E_{R,max}$ that can be imparted to the recoil by elastic scattering†,

eq. 3.1 $$E_{R,max} = 4\frac{m_p M_{Si}}{(m_p + M_{Si})^2} E_p .$$

This is around $4E_p m_p/M_{Si}$, provided the mass m_p of the damaging particle is much smaller than the one of the silicon nucleus (around 28 u). For neutrons or protons, both approximately 1 u, the energy must be greater than 175 eV, while for electrons the approximate relativistic relation $E_{R,max} = 2E_p(E_p+2m_0c^2)/(M_{Si}c^2)$ must be used and requires E_p to be larger than 260 keV to dislodge one host atom. Here it is also interesting to note the mechanism causing the displacement damage by exposure to ^{60}Co-gamma rays, which have also been used in this work. The average energy of the two emitted photons is E_γ = 1.25 MeV producing energetic electrons in silicon chiefly by the Compton effect. A continuous distribution of electrons is resulting, exhibiting an upper kinematic limit of $E_\gamma/(1+0.5m_0c^2/E_\gamma)$, i.e., approximately 1.0 MeV [CAH59]. Regarding the above mentioned displacement threshold, the vast majority of all ^{60}Co-gamma interactions displace only very few atoms.

In this work it will however mainly be dealt with high energetic particles situated orders of magnitude above these displacement thresholds. The recoil energy is then so large that the PKA starts moving through the lattice, continuously displacing further atoms, which again might be sufficiently energetic to initiate subcascades. During this process also a significant amount of the recoil energy is lost in ionization, i.e., only a portion $P(E_R)$ of E_R contributes to displacements, named Lindhard partition function. A more detailed discussion of these subjects can be found in reference [WUN92]. Now, the basic assumption of the NIEL hypothesis is that any displacement damage-induced change in the material properties scales with the amount of energy imparted in displacing collisions, irrespective of the spatial distribution of the introduced displacement defects in one PKA cascade, and irrespective of the various annealing sequences taking place after the initial damage event. While it will therefore be explored in the following, how the absorbed displacement energy is related to the interaction cross section and the differential particle flux spectrum, consideration of the microscopic details gives important clues regarding the chemical composition of the damage-induced defects and is left for Section 3.3.1.

Given several types of interactions between a particle of energy E_p and the silicon nucleus, whose relative efficacy is expressed by the corresponding cross sections‡ $\sigma_\nu(E_p)$. Moreover, for each let there be an energy distribution of the recoil $f_\nu(E_p, E_R)$ and a corresponding upper kinematic limit $E_{R,max,\nu}$. The displacement damage cross section $D(E_p)$, measured in MeVmb, is then usually defined by

* Non Ionizing Energy Loss.

† The derived displacement thresholds do not account for nuclear reactions, which for low energetic neutrons might cause damage due to neutron capture.

‡ Typical values are of the order of 100 mb. Note that as the total cross sections of fast neutrons is of the order of 1 b, the range in silicon is a few 10 cm, ensuring homogeneously distributed primary collision sites in the around 300 µm thick samples.

eq. 3.2 $$D(E_p) = \sum_\nu \sigma_\nu(E_p) \int_{E_d}^{E_{R,max,\nu}} dE_R \, f_\nu(E_p, E_R) P(E_R),$$

where the lower integration bound accounts for the circumstance that the partition function is assumed to be equal to zero below the displacement threshold, $P(E_R < E_d) = 0$.

Regarding a specific interaction, the integral on the right-hand side denotes the average value of the kinetic energy released to the crystal if one single interaction has occurred. In other words, the total displacement damage energy per volume deposited in a silicon crystal can be written

eq. 3.3 $$\rho_{dis} = \frac{8}{a^3} t_{exp} \int_0^\infty dE_p \, \phi(E_p) D(E_p),$$

where t_{exp} is the exposure time and $\phi(E_p)$ the differential particle flux spectrum. It was exploited here that the space density of the target nuclei is given by $8/a^3$, as eight silicon atoms are found in one cubic unit cell with a linear dimension of a = 5.43 Å [SZE81]. Now, according to the NIEL hypothesis any displacement damage-induced change in the material properties is proportional to ρ_{dis}. Fig. 3.0 displays the displacement damage cross section functions according to eq. 3.2 which have been used in this work for purpose of fluence normalization, see below. The neutron data have been taken from M.S. Lazo et al. below 18 MeV [LAZ87] and were extended towards higher energies with the results published by A. Van Ginneken [VGI89]. While the pion data were provided in numerical form by M. Huhtinen and P.A. Aarnio [HUH93], the proton damage function was also taken from [VGI89].

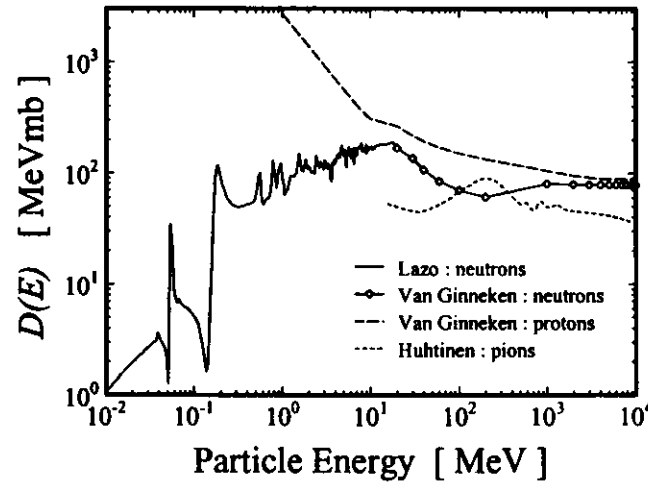

Fig. 3.0 Displacement damage cross sections for different particles as function of the particle energy.

Evidently the efficiency of introducing displacement damage into the silicon crystal depends on the particle type and on its energy. If therefore a sample has been exposed to a specific source for the time t_{exp}, and the particle fluence is quoted by

eq. 3.4 $$\Phi = t_{exp} \int_{E_{lo}}^{E_{hi}} dE_p \, \phi(E_p),$$

it is interesting to ask for the fluence required at an other source to introduce the same amount of displacement damage ρ_{dis}. If the damage is visualized to be arising from a monoenergetic 1 MeV neutron source, the corresponding equivalent fluence Φ_{eq} follows from

eq. 3.5 $$\rho_{dis} = \frac{8}{a^3} t_{exp} \int_0^\infty dE_p \, \phi(E_p) D(E_p) = \frac{8}{a^3} \Phi_{eq} D_n(1\,\mathrm{MeV}) .$$

It is possible to always compute the equivalent 1 MeV neutron fluence Φ_{eq} by

eq. 3.6 $$\Phi_{eq} = \kappa \Phi$$

if the so-called hardness factor κ of the source under consideration is defined by*

eq. 3.7 $$\kappa = \frac{1}{D_n(1\,\mathrm{MeV})} \cdot \frac{\int_0^\infty dE_p \, \phi(E_p) D(E_p)}{\int_{E_{lo}}^{E_{hi}} dE_p \, \phi(E_p)}$$

The bounds of the integral in the nominator are often identified with the energy cuts employed for the fluence measurement. However, typically no error is arising from this procedure because either the flux or the displacement damage cross section is negligibly small in the omitted energy range. On the other hand, in regard to wide spectrum neutron sources which at times can exhibit a huge particle flux in the thermal neutron range, considerable systematic errors can be introduced, e.g. 5% for CERN PSAIF as outlined in [ANG96].

Concerning the 1-MeV neutron displacement damage cross section D_n(1 MeV), a weighted least squares average value of 95±4 MeVmb was calculated from the various determinations of the displacement damage function, and this is currently the ASTM (American Society for Testing and Materials) standard [MES92].

Numerous sources will be encountered in this work, and their characteristics are compiled in Table 3.1. If no further reference is given, the hardness factor has been calculated according to eq. 3.7, employing the displacement damage cross section functions as shown in Fig. 3.0. While no energy cuts need to be taken into account for the monoenergetic sources, for ISIS E_{lo} and E_{hi} are 10 keV and 70 MeV, respectively.

Table 3.1 Characteristics of various irradiation sources.

Lab, Experiment	Particle	Spectrum	$\langle E_p \rangle$ [MeV]	κ
RAL[a], ISIS	spallation neutrons	[EDW90]	1.0	1.02
PTB[b], ^{9}Be(d,n)	generator neutrons	[BRE89]	5.3	1.45[k]
CERN[c], PSAIF	spallation neutrons	[FLO93]	1.0	0.78[g]
UKE[d], T(d,n)	generator neutrons	monoen.	14.1	1.88
CERN, PS	proton beam	monoen.	2.4×10^4	0.93
LAMPF[e]	proton beam	monoen.	647.0	1.12
	proton beam	monoen.	800.0	1.08
Lowell[f] ^{7}Li(p,n)	generator neutrons	[KEG96]	1.06	0.90[l]
PSI[g], πE1	pion beam	monoen.	65.3	0.56
	pion beam	monoen.	104.3	0.74
	pion beam	monoen.	147.2	0.86
	pion beam	monoen.	191.7	0.94
	pion beam	monoen.	236.3	0.93
	pion beam	monoen.	280.7	0.86
	pion beam	monoen.	330.5	0.76
BNL, ^{60}Co	γ	{1.17, 1.33}	1.25	0.0064[j]

[a] Rutherford Appleton Laboratory, United Kingdom.
[b] Physikalisch-Technische Bundesanstalt, Braunschweig, Germany.
[c] Conseil Europeen pour la Recherche Nucleaire, Swiss.
[d] Universitäts-Krankenhaus Eppendorf, Hamburg, Germany.
[e] Los Alamos (Clinton P. Anderson) Meson Physics Facility, USA.
[f] Lowell University, USA.
[g] Paul-Scherrer Institut, Switzerland.
[j] [BÖT97], quoted for a deuteron energy of E_d = 13.26 MeV.
[k] [VAS97], CERN PSAIF: κ' for a 140 keV low energy cut.
[l] [SUM93], displacement threshold E_d = 21 eV.

* Note that this is already the practical value of the hardness factor, as opposed to its thorough metrologic definition, where the lower and upper bounds of all integrals are 0 and ∞, respectively, see [ANG96].

3.2 Changes in the Macroscopic Detector Properties

3.2.1 Review of the Current Bulk Damage Models

After an introduction into the basic relation between damage-induced defect levels and the deterioration of the detector performance, the currently accepted models describing the changes in the macroscopic detector properties as function of fluence, annealing time, and temperature are reviewed. In this field a huge amount of experimental data has been reported in the literature by various groups, and the data measured and shown in this work are presented mainly for purpose of illustration. The corresponding numerical values of the parameters in the model equations have been compiled in a global survey (see Section 5) and are given in Table E.7.

3.2.1.1 Basic Defect Action

Radiation damage introduces a manifold of defect levels, and their basic action in the silicon detector is schematically illustrated in Fig. 3.1. Process a) is the carrier removal effect, also referred to as the compensation for the shallow doping impurities. Free carriers are trapped here into deep levels and can not participate in the conduction process anymore. This will for example increase the series resistance of a detector, that is not fully depleted. Process b) results in increased rate of recombination of excess carriers, which is not detrimental to the operation of the silicon detector. All diffusion currents, e.g., the forward current in an ion-implanted detector, will however be enhanced. Fig. 3.1 c) displays the two chief considerations deciding on the successful operation of silicon detectors in an environment with high radiation levels. Firstly, in the reverse biased device, deep levels, especially those close to the middle of the band gap, can generate excessive leakage currents that lead to noisy signals and, what turns out to be even worse, an increased power dissipation. Secondly, the defects introduced by the radiation damage may become charged in the depleted region and therefore contribute to the effective doping concentration. When, as is the case, the overall electrical charge becomes progressively negative, the external bias eventually fails to fully deplete the detector, or would have to be chosen so high that excessive break-down currents would prevent a reliable operation. Finally, Fig. 3.1 d) shows, how the free carriers generated by the passage of an ionizing particle through the detector can get trapped at defect levels during the charge collection process and thus escape the detection. Although the trapped carriers would be released later, they would probably not be taken into account since the charge collection needs to be completed within a short time, related to the high bunch crossing rate of future HEP colliders.

3.2.1.2 Effective Doping Concentration

The radiation damage-induced changes in the effective doping concentration can most instructively be illustrated by the corresponding variations of the CV curve, as for example in Fig. 3.2. These particular measurements have been carried out on an ion-implanted device in the course of a irradiation with fast neutrons from the Be(d,n) generator at the PTB, see Table 3.1. Evidently the full depletion voltage is decreasing for the first two exposures, while fluences in excess of around 10^{13} cm^{-2} are resulting in growing V_{dep} values. This was observed by various groups and it was concluded that the initially positive space charge, determining the full depletion voltage according to eq. 2.7, is continuously decreasing until the inversion of the sign of the space charge takes place and $N_{eff,SCR}$ becomes an increasingly negative number [WUN91,EDW91,ZIO91,PIT92,LEM92]. Further, one observes a flattening of the CV curve at small reverse bias voltages which in part is due to a growing series resistance of the undepleted bulk material, compare eq. 2.20.

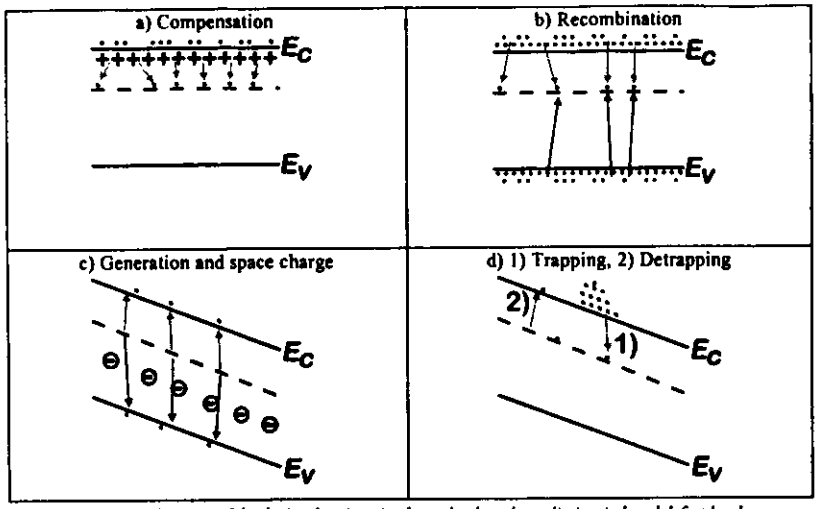

Fig. 3.1 Mechanisms of the device deterioration brought about by radiation-induced defect levels. Processes c) and d) are of superior importance for silicon detectors. E_C and E_V denote the electron energy in the conduction and valence band, respectively.

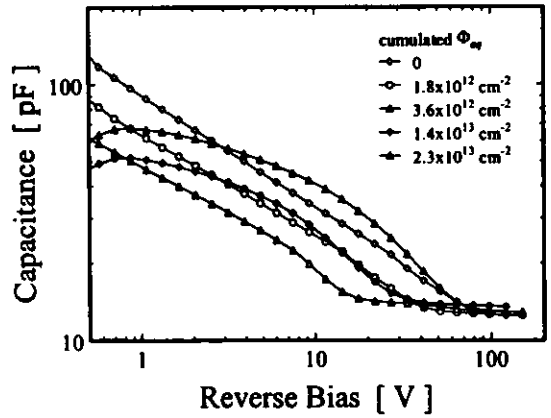

Fig. 3.2 Changes in the CV curves observed during an irradiation with fast neutrons (device M10609, d = 274 µm, total exposure time 2 hours at PTB Be(d,n), f = 10 kHz).

As outlined in the references [ER295,ANG95] direct evidence of the inversion of the sign of the space charge can be provided by current pulse shape measurements, and an example for this statement is presented in Fig. 3.3. The electric field strength sensed by the injected electrons below the front contact (beginning of the pulse shape) is larger than close to the rear contact (end of the pulse shape) before irradiation and after exposure to a small fluence Φ_{eq}. Now, the gradient of the electric field is changing the sign at an intermediate fluence Φ_{eq} accumulated during the irradiation, indicating a negative space charge and a junction located at the rear plane contact. Note that the length of the current pulses is

essentially determined by the employed bias voltage V_{bias} which, in order to facilitate the evaluation of the data, was always chosen closely above the actual full depletion voltage V_{dep}.

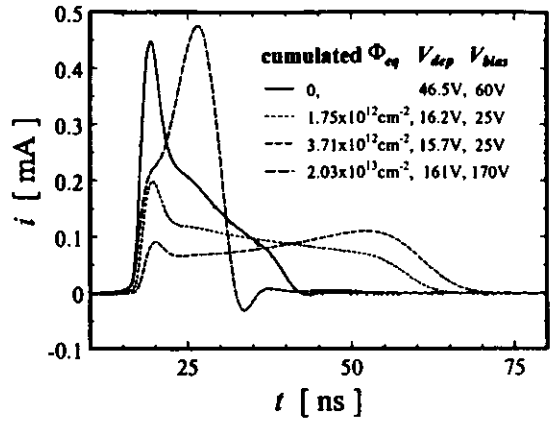

Fig. 3.3 Transformation of the current pulse shapes induced by electron injection at the front contact during an irradiation (device 942G21, d = 386.8 µm, total exposure time around two hours).

The change in the effective doping concentration will always be referred to $N_{eff,0}$, the value of $N_{eff,SCR}$ measured before irradiation, by

eq. 3.8 $$\Delta N_{eff}(\Phi_{eq},t) = N_{eff,0} - N_{eff,SCR}(\Phi_{eq},t),$$

since with respect to the above experimental observations this always gives a positive number. It is noticed that in eq. 3.8 the change in $N_{eff,SCR}$ does not only depend on the absorbed particle fluence Φ_{eq}, but also on the time of annealing elapsed since the irradiation. This circumstance is illustrated in Fig. 3.4, where the left-hand side shows the room temperature annealing period and the right-hand side the long term processes accelerated by storing the devices at 50°C.

Now, numerous experimental data (see Section 5.1.1) from systematic studies on this subject matter have been found to be in agreement with the following model. The total damage effect can be split into three portions by [FEI93,ZIO94,FRE94,BAT94]

eq. 3.9 $$\Delta N_{eff}(\Phi_{eq},t) = N_a(\Phi_{eq},t) + N_c(\Phi_{eq}) + N_Y(\Phi_{eq},t),$$

which distinguishes the

- short term annealing $N_a(\Phi_{eq},t)$,
- a stable damage component $N_c(\Phi_{eq})$,
- and the long term reverse annealing $N_Y(\Phi_{eq},t)$,

with annealing rates depending on the temperature T. With respect to the beneficial short term annealing, it appears to be difficult to reconcile the observations made on differently manufactured detectors with a universal behavior, and hardly any significant annealing steps were so far recognized [SCH95]. Due to the lack of a clear universal picture the process is then visualized to be arising from the decay of a set of radiation damage-induced acceptor-like impurities, and according to the considerations in Appendix C this results in an approximation of the annealing curve by a sum of exponentials [WUN92]

eq. 3.10 $$N_a(\Phi_{eq},t) = \Phi_{eq}\sum_i g_{a,i}\exp\left(-k_{a,i}(T)t\right).$$

That is, all acceptor concentrations are introduced proportional to the fluence at individual rates $g_{a,i}$ and display a simple first order decay with temperature dependent annealing rate constants $k_{a,i}(T)$. For practical applications, e.g. at LHC, short term annealing needs not to be taken into account because the exposure times are much longer than the typically encountered annealing time constants. Even if it is argued that low temperature operation would effectively freeze the beneficial annealing, the anticipated maintenance periods would be sufficient to allow for a considerable annealing. In any case could such a problem be overcome by intentionally warming up the silicon detectors.

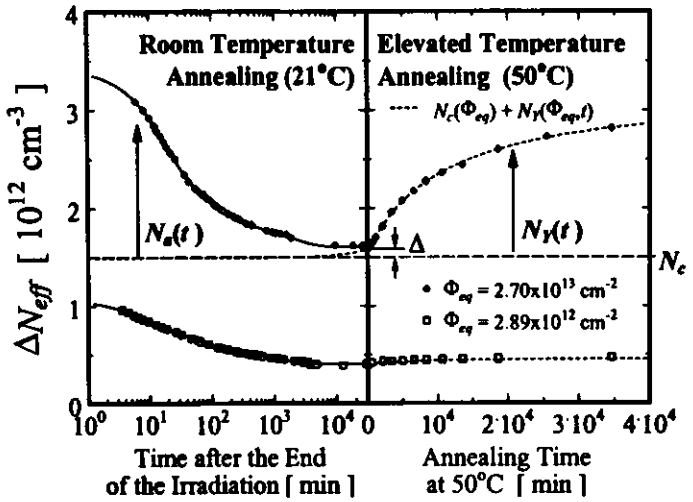

Fig. 3.4 Annealing behavior of the radiation damage-induced change in the effective doping concentration (ion-implanted devices M10708 and M10812, $N_{eff,0} \approx 1.4\times10^{12}$ cm^{-3}, exposure time/fluence 2 min/2.89×10^{12} cm^{-2} and 18 min/2.70×10^{13} cm^{-2}).

The plateau value reached at an intermediate stage of the annealing (around 2 weeks at room temperature) is quite close to the stable damage, which is the portion of the overall change in $N_{eff,SCH}$ that does not depend on the annealing time. A satisfying parametrization of the experimental data concerning the variation with the fluence is given by [FEI93,SCH94]

eq. 3.11 $$N_c(\Phi_{eq}) = N_{c0}\left(1-\exp(-c\Phi_{eq})\right) + g_c\Phi_{eq}.$$

While the term on the right-hand side again implies the introduction of acceptor-like states in proportion with the fluence, an additional contribution arises from the exhaustion of donor-like states whose initial concentration is N_{c0}, and accordingly c is called the donor-removal constant [FRE90]. However, care must be taken if N_{c0} is identified with the initial phosphorus concentration N_P since, on the one hand, from the microscopic understanding of the damage processes there is only a small chance to remove the trace amounts of phosphorus (see Section 3.3.1) and, on the other hand, experimental data on N_{c0} are typically found to be much smaller than N_P. For sufficiently large fluences ($\Phi_{eq} > c^{-1}$, i.e. usually Φ_{eq} in the 10^{13} cm^{-2} range or above) the exponential term can be neglected and it is approximately

eq. 3.12 $$N_c(\Phi_{eq}) \approx N_{c0} + g_c\Phi_{eq}$$

With respect to the room temperature annealing, following the minimum reached after around two weeks the ΔN_{eff} is found to be increasing very slowly with a time constant of the order of years. Since in inverted detectors the full depletion voltage increases correspondingly, and the reliable long term

operation (10 years) of such devices in future experiments for a given maximum operational voltage may not be guaranteed then, this so-called anti- or reverse annealing has become a major issue. Systematic studies investigating the annealing kinetics at elevated temperatures have suggested that the reverse annealing function can be written [FEI93,FRE94]

eq. 3.13 $$N_Y(\Phi_{eq},t) = N_{Y,\infty}(\Phi_{eq})\left(1-\frac{1}{1+N_{Y,\infty}(\Phi_{eq})\,k_Y(T)\,t}\right),$$

where the reverse annealing amplitude is proportional to the irradiation fluence

eq. 3.14 $$N_{Y,\infty}(\Phi_{eq}) = g_Y\Phi_{eq}.$$

In eq. 3.13 it is implicitly assumed that an acceptor-like state Y is created by a bimolecular reaction, where the temperature dependent reverse annealing rate constant obeys an Arrhenius-relation $k_Y(T) = k_0 \exp(-E_a/(k_B T))$, compare Appendix C. While eq. 3.13 has been accepted in this work as a good approximation of the reverse annealing curve employing a minimum number of free parameters, serious objections will be raised against the implied microscopic interpretation in Section 3.2.6.

Regarding the evolution of ΔN_{eff} observed during the isothermal elevated temperature annealing, as for example shown on the right-hand side of Fig. 3.4, it is evident that eq. 3.9, omitting the short term annealing N_a, can be fitted very reasonably to the experimental points by a least-squares method (solid line) when eq. 3.13 is substituted for N_Y. This gives unique estimates of N'_c, $N'_{Y,\infty}$, and k_Y. A correction for the amount of reverse annealing Δ taking place during the extended room temperature storage period Δt preceding the elevated temperature annealing* can be obtained from the approximation of eq. 3.13

eq. 3.15 $$N_Y(t) \approx k_Y(T) N^2_{Y,\infty} t,$$

which is valid as long as $k_Y(T) N_{Y,\infty} t$ is much smaller than unity. Now, $N_{Y,\infty}$ is not known and it will thus be assumed for the calculation of Δ that $N_{Y,\infty} \approx N'_{Y,\infty}$, introducing only a small error as Δ is small compared with $N_{Y,\infty}$. Therefore, in the first approximation

eq. 3.16 $$\Delta \approx k_Y(T_R) N'^2_{Y,\infty} \Delta t,$$

which then is used to obtain $N_c = N'_c - \Delta$ and $N_{Y,\infty} = N'_{Y,\infty} + \Delta$. For these corrections $k_Y(T_R = 20°C) = 1.55\times10^{-20}$ cm^{3}s^{-1} has been employed, the result of the global survey of this constant, see Section 5.1.1.

Provided data obtained on several annealed samples are taken into consideration it is possible to systematically study N_c and $N_{Y,\infty}$ as function of the fluence Φ_{eq} and k_Y as function of the annealing temperature T. While the former yields values of the damage constants N_{C0}, c, g_C, and g_Y (see eq. 3.11/eq. 3.12 and eq. 3.14), the latter gives E_a and k_0 in the Arrhenius-relation for $k_Y(T)$ as outlined in Section C. In this work this procedure has been exploited for the investigation of devices manufactured on materials with various initial resistivities and for the comparison of the damage-induced by different irradiation sources.

3.2.1.3 Leakage Current

The IV curves as function of the irradiation dose as typically observed by many experimenters is illustrated by an example in Fig. 3.5, compare the corresponding CV curves in Fig. 3.2. In addition to the changes in the full depletion voltage, which are indicated in the figure, there is a continuous increase of the leakage current. This is generally assumed to arise from volume generation centers introduced by the irradiation, in agreement with the approximate square-root like bias dependence, see Section 2.5.1.5. It will however be noted that, as reported in reference [WUN92], in the inverted detector ($\Phi_{eq} > 10^{13}$ cm^{-2}) a significant flattening of the characteristics is observed at bias voltages well below V_{dep}. As the generation centers are expected to be introduced homogeneously, this effect is believed to be related to a peculiarity of the field zone, which however so far is not understood. Still it is a common praxis to take the total leakage current at the full depletion voltage, inferred from CV measurements, as a measure of

* Although the short term annealing might not be completed within the period Δt in question, the extracted parameters N'_c, $N'_{Y\infty}$, and k_Y are hardly affected because, in respect to the least-squares fitting, they are chiefly determined by the experimental data points obtained on a very long time scale, whereas the short term annealing will have reached its final value already within a very short time of the elevated temperature annealing.

the number of the generation centers introduced in the overall sensitive volume. Accordingly, the change ΔI in the leakage current at V_{dep} should be normalized to the area A and the thickness d in order to reflect the bulk concentration of the generation centers, see eq. 2.17. The variation of this quantity with fluence is expressed in terms of the current related damage constant α, and at room temperature T_R it is

eq. 3.17 $$\frac{\Delta I}{Ad}(\Phi_{eq}, t, T_R) = \alpha \Phi_{eq} g(t),$$

where g is the normalized annealing function, i.e., $g(0) = 1$.

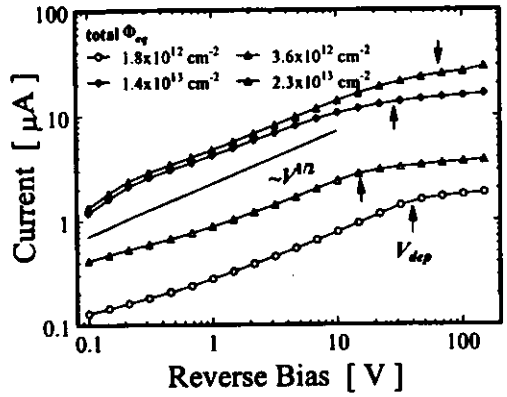

Fig. 3.5 IV curves as function of the irradiation fluence, compare the corresponding CV curves in Fig. 3.2. The IV data before irradiation is in the nA range and not shown here for the sake of the clarity of the figure.

Fig. 3.6 shows experimental leakage current data normalized to room temperature by $R(T)$ (see eq. 2.18 in Section 2.5.1.5) and to the irradiation fluence, i.e. $\alpha\, g(t)$, as function of the annealing time (compare the corresponding ΔN_{eff} data in Fig. 3.4). A strong beneficial annealing of the leakage current occurs, however, with different features in inverted and not inverted devices. The two corresponding sets of annealing functions have already been determined by R. Wunstorf [WUN92]. As in the case of the annealing portion N_a of the effective doping concentration, a certain number of individual contributors to the current have been presupposed, all annealing with a characteristic rate constant $1/\tau_i$ with first order kinetics, compare Appendix C. Correspondingly, the annealing function is given by

Table 3.2 Parameters of the leakage current annealing curve as determined by R. Wunstorf [WUN92].

Inverted		Not Inverted	
τ_i [min]	a_i	τ_i [min]	a_i
1.35×10^{1}	0.197	1.78×10^{1}	0.156
8.43×10^{1}	0.300	1.19×10^{2}	0.116
1.55×10^{3}	0.121	1.09×10^{3}	0.131
8.74×10^{3}	0.139	1.48×10^{4}	0.201
∞	0.243	8.92×10^{4}	0.093
		∞	0.303

eq. 3.18 $$g(t) = \sum_i a_i \exp(-t/\tau_i) \quad \sum_i a_i = 1,$$

and the parameters found in reference [WUN92] are cited in Table 3.2. These two functions have been plotted into the left-hand side of Fig. 3.6, selecting the value of the damage constant α such that the curves fit the experimental data.

As there is a good agreement regarding the shape of the annealing curve, no efforts have been made to fit the annealing parameters a_i and τ_i. The exposure times were particularly small (see caption of Fig. 3.4), such that only in the first minutes small differences arise from the annealing taking place during the

irradiation, which was not corrected for in the experimental data in Fig. 3.6, whereas the parameters in Table 3.2 are only valid for an infinitely short irradiation. Since there are no clear annealing stages which unambiguously can be related to the annealing of a certain defect*, eq. 3.18 is considered to be just a parametrization in which the fitted parameters are mainly determined by the density of the experimental data points and other numerical considerations. The agreement observed in Fig. 3.6 is concluded to be due to the similarity of the leakage current annealing processes taking place in the ion-implanted devices used here and the surface barrier detectors employed in [WUN92], reassuring that the leakage current is in fact related to the bulk damage in the float zone silicon substrate rather than to the device design. Also in agreement with [WUN92] the damage constant α is found to be larger in inverted detectors, as opposed to the similar behavior observed on the two samples after around one day of annealing.

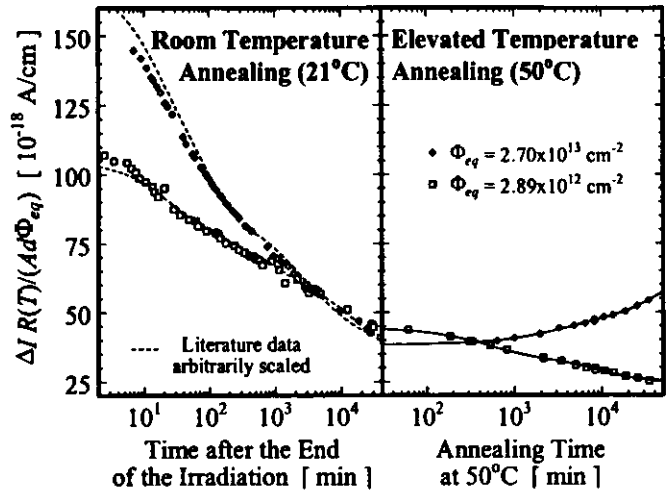

Fig. 3.6 Annealing of the reverse current for two differently irradiated devices, compare Fig. 3.4 (A = 0.275 cm^2, d = 280 μm). The room temperature annealing data were taken from reference [WUN92].

It is not easy to determine the leakage current related damage constant α experimentally, as this requires a very short irradiation and/or corresponding annealing corrections. The author has therefore suggested in reference [CHI95] to refer to the well annealed value of the leakage current, which according to the longest time constant given in Table 3.2 is reached after a few months of storage at room temperature,

eq. 3.19 $$\alpha_\infty = \frac{\Delta I(\Phi_{eq}, \infty, T_R)}{Ad\Phi_{eq}} = \alpha\, g(\infty).$$

Now, pertaining to the elevated temperature annealing displayed on the right-hand side of Fig. 3.6, a further continuous reduction is observed on the not inverted device while an increase is found on the heavily damaged sample. Regarding the latter no systematic dependence on the fluence but rather a large variation between different samples was found [SCH95]. If it is recalled that the depletion zone is growing from the back plane contact after inversion of the sign of the space charge allowing for the extension of the electric field region right to the device sawing edges, it appears more likely that the leakage current increase is related to the increasing full depletion voltages during the reverse annealing in heavily damaged samples, giving rise to a pronounced influence of high field and edge currents, rather than to the growth of an efficient bulk leakage current generation center. However, for a more general conclusion more systematic studies are necessary.

* On weakly damaged devices the annealing curve is strikingly well proportional to $\log(t)$ in the long term.

It must therefore be stated that there actually is no physical basis for the assumption that the leakage current reaches a plateau value after long annealing times as suggested by the mathematical description of the annealing curve by eq. 3.18. The quantity α_∞ introduced by eq. 3.19 is however valuable for pragmatic reasons. On the one hand, contrary to α it can easily be extracted from annealing curves even if only few points have been measured and, on the other hand, it represents the annealing state on a time scale typically encountered in practical applications of silicon detectors. In fact it provides an upper limit of the leakage current increase to be expected on an even longer time scale. In this context it is noted that for inverted devices the minimum value of the annealing curve has been associated with α_∞, also giving an upper limit of what might be observed on a suitably processed device that does not exhibit a long term increase of the overall leakage current.

In addition to the intrinsic dependence of the volume leakage current on the temperature, accounted for by the scaling factor $R(T)$ (eq. 2.18), also the rate of the annealing depends on the temperature. However, the annealing kinetics have so far not been studied in detail. As the parameters in Table 3.2 reflect only an approximation of the actual annealing curve by exponential functions and hardly can be ascribed to individual defects contributing to the leakage current, the author has further suggested in reference [CHI95] to account for the dependence of the annealing rate on the temperature by a scaling factor $\theta(T)$ applied to the time axis and which is unity at room temperature: $\theta(20°C) = 1$. Then the full expression for the leakage current can be deduced from eq. 3.17 and is written

$$\text{eq. 3.20} \qquad \frac{\Delta I}{Ad}(\Phi_{eq}, t, T) = \frac{\alpha_\infty}{g(\infty)} \Phi_{eq} R^{-1}(T) g(\theta(T)\, t),$$

where also α has been replaced utilizing eq. 3.19. In regard to the scaling factor $\theta(T)$ it has been exploited that according to Appendix C the differential equation eq. C.1 governing the annealing processes can always be written as function of a normalized 'time' $k(T)\,t$. Given only one particular microscopic defect governs the leakage current generation, then the annealing curve in fact is a function of $k(T)\,t$, irrespective of the relation between the measured leakage current and the concentration of the defects which might not simply be a proportionality. The scaling factor with respect to the reference temperature T_R is then just the ratio $\theta(T) = k(T)/k(T_R)$ which according to the Arrhenius-relation eq. C.2 depends only on the activation energy E_I characteristic of the annealing kinetics of the defect in question,

$$\text{eq. 3.21} \qquad \theta(T) = \exp\left(\frac{E_I}{k_B}\left[\frac{1}{T_R} - \frac{1}{T}\right]\right).$$

3.2.1.4 Charge Collection Deficiency

Employing α particles for the generation of a well defined number of electron-hole pairs, it has been demonstrated by R. Wunstorf in reference [WUN92] that for increasing fast neutron fluences a growing portion of the charge collected within the shaping time of the electronic readout is lost due to carrier trapping*. As the free carriers were created closely below the electrodes, it was possible to study the trapping time constants separately for electrons and holes, compare Section 2.6. The following parametrization of the functional dependence on the fluence has been found [WUN92]

$$\text{eq. 3.22} \qquad \tau_{tr,n}^{-1}(\Phi_{eq}) = \tau_{tr,n0}^{-1} + \begin{cases} \gamma_n \Phi_{eq} & \Phi_{eq} < \Phi_{eq}^* \\ \gamma_n^* (\Phi_{eq} - \Phi_{eq}^*) + \gamma_n \Phi_{eq} & \Phi_{eq} > \Phi_{eq}^* \end{cases},$$

$$\tau_{tr,p}^{-1}(\Phi_{eq}) = \tau_{tr,p0}^{-1} + \gamma_p \Phi_{eq}$$

where Φ_{eq}^* is the inversion fluence and $\tau_{tr,n0}$ is the trapping time constant extrapolated to $\Phi_{eq} = 0$, i.e., in the undamaged n-type float zone material. The physical model behind eq. 3.22 is that trapping centers are introduced in proportion with the fluence, for the electron trapping even at a higher rate after inversion of the space charge sign has occurred. The resulting collection deficiency $\Delta Q/Q_0$ depends on the applied bias voltage, the maximum collection time, and other experimental conditions. For the

* In general the overall trapping effect depends on the shaping time due to the detrapping, see Section 3.4.3.

situation of electron-hole pair generation by a mip, an approximate formulae can be found in Section 5.2.3.

3.2.2 Verification of the $N_{eff,SCR}$ Data Obtained from CV Curves by the Analysis of Current Pulse Shapes

As outlined in Section 2.6, the analysis of current pulse shapes (TCT) provides an alternative tool to CV measurements for the determination of the concentration of charges in the depleted zone, $N_{eff,SCR}$. It is therefore worthwhile to check, whether the two methods give compatible results on irradiated detectors, while a good agreement has already been demonstrated on undamaged samples in Fig. 2.20. In order to cover a wide fluence range, current pulse shapes and CV curves have been recorded on 4 devices (see Table 3.3) during an irradiation experiment with a total exposure time of around two hours at the Be(d,n) neutron generator of the PTB (compare Table 3.1). The corresponding differences between $N_{eff,SCR}$ taken from the CV curves ($N_{eff,CV}$) and by the t_c-method from the current pulse shapes induced by hole injection ($N_{eff,TCT}$) are plotted in Fig. 3.7 as function of the accumulated neutron fluence.

Table 3.3 Devices used for the comparison between CV and TCT data on $N_{eff,SCR}$ as function of the irradiation fluence, see text.

Device	942G21	942G30	M10510	M10511
Type	surface barrier	surface barrier	ion-implanted	ion-implanted
$N_{eff,0}$	0.417×10^{12} cm^{-3}	0.427×10^{12} cm^{-3}	1.53×10^{12} cm^{-3}	1.53×10^{12} cm^{-3}
d	386.8 µm	386.8 µm	274 µm	274 µm

As only the absolute values of $N_{eff,SCR}$ are considered here, the data suggest that irrespective of the sign of the space charge the CV method underestimates $|N_{eff,SCR}|$. Similar results were also obtained with the t_c-method for electron injection and the τ - method for hole injection. Respecting the τ - method, eq. 3.22 has always been used to correct for the influence of the trapping. Still, on pulse shapes induced by electron injection the method gives results which are not in agreement with all other methods. However, this problem has already been identified in Section 2.6 on the undamaged samples and is related to the short collection times for electrons, in particular if the full depletion voltages are large, e.g., in the high fluence range. All other methods are roughly in agreement with the form

$$\text{eq. 3.23} \qquad \left|N_{eff,CV}\right| - \left|N_{eff,TCT}\right| \approx -1\times10^{-2}\,\text{cm}^{-1}\times\Phi_{eq}.$$

Furthermore it has to be ascertained, how this discrepancy behaves during the annealing and reverse annealing in $N_{eff,SCR}$. In this respect Fig. 3.8 shows room temperature annealing data on an inverted detector. Depletion voltages V_{dep} were either inferred from CV curves or from current pulse shape measurements, evaluated with various methods. Evidently the difference stays more or less constant, i.e., it is in the first approximation justified to always apply eq. 3.23. Indeed eq. 3.23 might therefore be visualized as an estimate of the systematic error in the damage constant g_c, the introduction rate of stable acceptor-like defects.

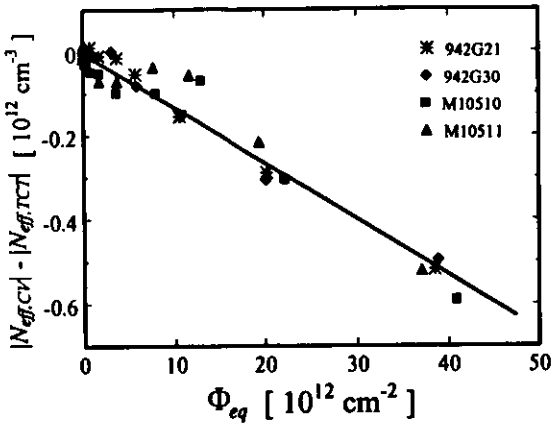

Fig. 3.7 Difference between the absolute value of the concentration of space charges obtained either from CV curves or by means of the t_c method employed for the analysis of current pulse shapes (TCT) induced by hole injection. The measurements were carried out in the course of an irradiation at the PTB Be(d,n) neutron generator, and the total exposure time was around two hours.

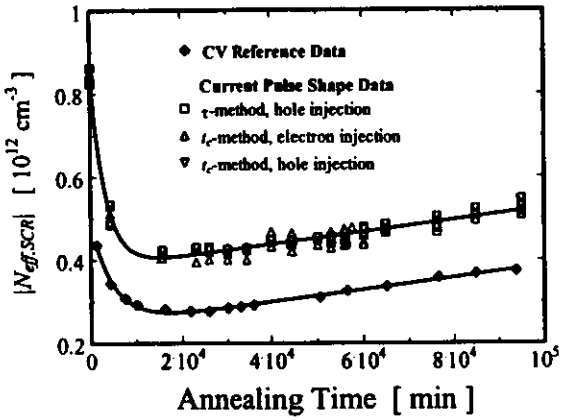

Fig. 3.8 Room temperature annealing of the doping concentration inferred from either CV curves or current pulse shape measurements (TCT), employing various methods for the analysis of the latter (device 937G01, Φ_{eq} = 1.90×10^{13} cm^{-2}, $N_{eff,0}$ = 0.205×10^{12} cm^{-3}, d = 390 µm, compare Table 3.4).

3.2.3 Isochronous Annealing Experiments

Using isochronous annealing one can comparatively quickly asses the thermally activated processes influencing the device properties in a wide range of activation energies, compare Appendix C. The experiments presented in the following were chiefly designed to enable the correlation of the changes in the macroscopic device properties with the corresponding variations on the microscopic scale. The latter was achieved by TSC spectra, which are presented separately in Section 3.3.3.6.

3.2.3.1 Experimental Procedure

Table 3.4 contains crucial information in regard to the state of the three examined devices prior to the annealing experiment. Note that one of the two ion-implanted detectors was not irradiated beyond the fluence required to invert the sign of the space charge. It was therefore possible to directly compare the different annealing processes taking place in weakly and heavily damaged samples. For each annealing step the samples were kept at the elevated temperature in normal atmosphere for a time period Δt of around 90 min and subsequently were rapidly cooled down to room temperature for the measurement of IV, CV, and current pulse shape (TCT) characteristics. The isochronous annealing procedure started at 50°C and the temperature increments ΔT were chosen as indicated in the last row of Table 3.4.

Table 3.4 List of the devices used for the annealing experiments. $N_{eff,0}$ and $N_{eff,1}$ denote the effective doping concentration prior to the irradiation and the first elevated temperature annealing, respectively.

Device	M20609	M20708	937G01
Type	ion-implanted	ion-implanted	surface barrier
$N_{eff,0}$	1.39×10^{12} cm^{-3}	1.26×10^{12} cm^{-3}	0.205×10^{12} cm^{-3}
d	280 µm	280 µm	390 µm
A	0.275 cm^2	0.275 cm^2	0.442 cm^2
Source	PTB Be(d,n)	PTB Be(d,n)	UKE T(d,n)
Φ_{eq}	9.76×10^{11} cm^{-2}	3.82×10^{13} cm^{-2}	1.90×10^{13} cm^{-2}
T_a storage	420 d	405 d	65 d
$N_{eff,1}$	1.20×10^{12} cm^{-3}	-1.46×10^{12} cm^{-3}	-0.555×10^{12} cm^{-3}
ΔT	20 K	20 K	5 K

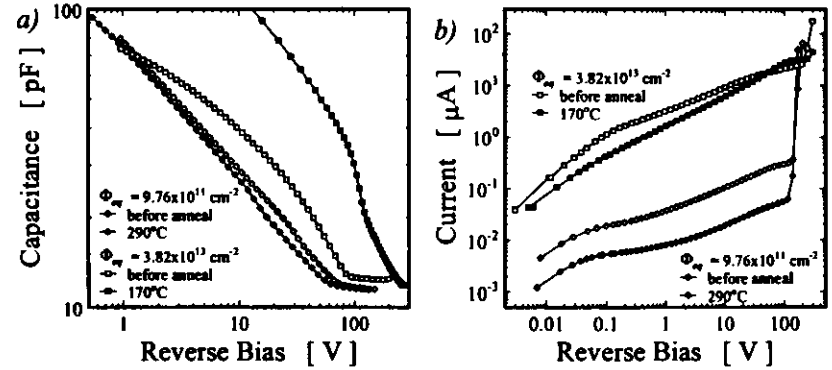

Fig. 3.9 CV a) and IV b) curves before the first annealing step and at a later stage of the annealing study.

Fig. 3.9 displays the CV and IV data obtained on the ion-implanted devices in the unannealed state and at the indicated stage of the annealing experiment. A breakdown occurs around 100 V for the not-inverted detector and around 200 V for the other sample. Since the full depletion voltage was increasing very much in the latter case, reasonable values of the leakage current at full depletion could only be derived up to the annealing step at 130°C, whereas V_{dep} could be determined by an extrapolation method up to the 210°C step. Evidently, the shape of the IV and CV curves of the heavily damaged sample undergo a pronounced evolution. In particular a kink is emerging under a reverse bias voltage of around 120 V, above which the capacitance starts descending more steeply than the ideal $1/V^{1/2}$ behavior. Contrary, the leakage current is staying at a constant level in this bias range, despite the apparent widening of the depleted zone. So far no explanation of this contradicting observations can be given. However, the unique field zone in inverted detectors, whose junction is situated at the unprotected rear electrode contact, is likely playing a role. In this context it is important to note that the current pulse shapes

obtained on the surface barrier detector were always in reasonable agreement with a linearly graded electric field, i.e., homogeneously distributed space charges. Unfortunately the sensitive Schottky-barrier was destroyed by the 100°C anneal, such that the further evolution of the field gradient is not known.

3.2.3.2 *Changes in $N_{eff,SCR}$ and I_{vol}*

The evaluated concentration of space charges $N_{eff,SCR}$ has been referred to the value $N_{eff,i}$ measured prior to the first annealing which results in an increasingly positive number when negative space charges are introduced. After normalization to the appropriate fluence, the data were plotted as function of the isochronous annealing temperature in Fig. 3.10 a), revealing the several stages of the reverse annealing, already noticed in reference [FRE94]. The first stage, which has been encountered within the isothermal annealing experiments presented in the previous sections and which is of prime importance for the long term operation of silicon detectors, is indicated at the data measured on the heavily damaged samples. The amplitude of this isolated annealing stage, as plotted in Fig. 3.10 a), gives the reverse annealing introduction rate g_Y, however, only if virtually no annealing has beforehand occurred at room temperature. This circumstance accounts for the obvious difference in the amplitudes observed on the two heavily damaged samples, since the storage periods at room temperature were much different, see Table 3.4. Moreover, the smaller increment ΔT realized for the surface barrier detector shifts the corresponding annealing data slightly towards smaller temperatures. No corresponding annealing stage can be identified for the weakly damaged sample, rather do the data presented in Fig. 3.10 a) provide evidence for markedly different annealing kinetics to prevail in the low fluence range.

The radiation damage-induced increase in the leakage currents plotted in Fig. 3.10 b) have been corrected to equivalent 20°C values and were normalized to both the sensitive volume A times d and the irradiation fluence Φ_{eq}. While the currents obtained on the weakly damaged device show beneficial annealing only, the accordingly awaited reduction on the inverted device is screened by excessive edge leakage currents occurring as a consequence of the growing full depletion voltage. Thus, only the data measured on the weakly damaged device is believed to reasonably well represent the annealing of bulk leakage current generation centers.

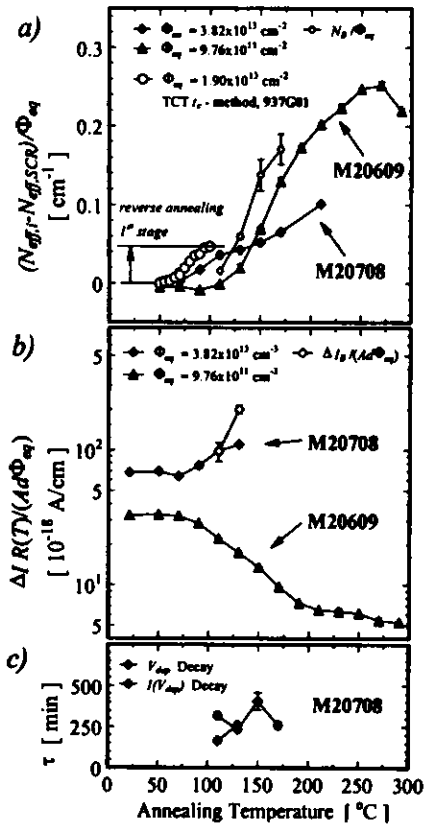

Fig. 3.10 Fluence normalized values of the effective doping concentration a) and the leakage current at full depletion per volume b) as function of the annealing temperature. N_B and ΔI_B are the concentration and the corresponding leakage current increase after excitation of the bistable defect which is decaying with the time constant plotted in c), see text.

3.2.3.3 *Evaluation of the Reverse Annealing Rate Constant*

By virtue of the small temperature increment ΔT of 5 K, the $N_{eff,SCR}$ values measured on the surface barrier detector can be exploited to evaluate the rate constant of the first stage of the reverse annealing with a reasonable accuracy according to the program outlined in Appendix C. As so far only $N_{eff,SCR}$ data inferred from CV curves have been employed for this purpose, one gains a critical test of the proposed reverse annealing function and an estimate of the systematic errors in the constants k_a and E_a derived from the Arrhenius-relation eq. C.2. Of special interest in this context is the observation that during all of the isochronous annealing experiment a constant difference of around 15 V persisted between the V_{dep} data inferred from the current pulse shapes (TCT) and CV curves, compare eq. 3.23.

The procedure developed in Appendix C requires the monitoring of the concentration of a defect that is destroyed by the annealing. However, N_Y is annealing in, and the analysis must therefore be applied to the difference between the saturation value of $N_{eff,SCR}$ reached on top of the annealing stage and the preceding values. As it is not always possible to unambiguously determine the plateau value, a large systematic error is introduced, as opposed to the isothermal annealing experiments, which are much more accurate in this respect. Here the $N_{eff,SCR}$ established after the last annealing step at 100°C has been employed, which by optical inspection is found to be sufficiently close to the saturation value. The resulting Arrhenius-plot in conjunction with the straight-line fit is displayed in Fig. 3.11. T_i denotes the temperature of the isochronous annealing step and $Y_{2,i}$ is given by eq. C.11. The overall agreement confirms that eq. 3.13 furnishes a reasonable approximation of the reverse annealing function. Further, within the experimental errors the evaluated parameters E_a = 1.36 eV and k_a = 4×10³ cm³/s match the numbers found in reference [MOI95] in a similar experiment, however, using CV curves rather than TCT. Those values are cited here for comparison: E_a = 1.34 eV, k_a = 1.1×10³ cm³s⁻¹.

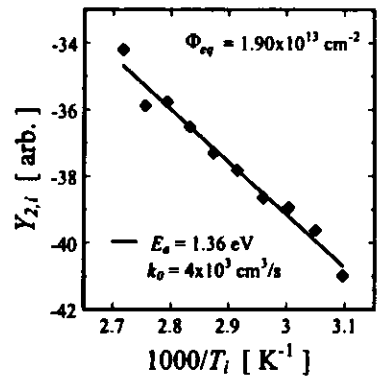

Fig. 3.11 Evaluation of the reverse annealing rate constant from $N_{eff,SCR}$ data obtained with the t_r-method on current pulse shapes (TCT), compare Fig. 3.10 a) (device 937G01).

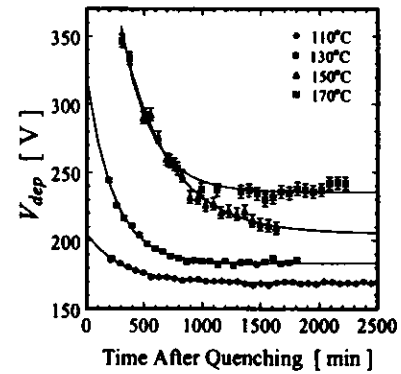

Fig. 3.12 Transient effect observed on the depletion voltage after quenching the sample M20708 from the indicated annealing temperature to room temperature (solid lines: fit).

3.2.3.4 *Bistable Defect Reactions*

Besides the overall variations of the doping concentration and the bulk leakage current there is also a transient effect arising from the elevated temperature annealing in inverted detectors, manifested by a decay of the depletion voltage from an excited value, observed right after quenching the sample to room temperature, towards a steady state value. Corresponding observations were made on the sample M20708, see Fig. 3.12. This subject has previously been studied in detail in reference [MOL95], and was discussed there in terms of a bistable defect reaction, as illustrated in Fig. 3.13. Prolonged annealing at temperatures greater than 80°C introduces a bistable complex defect with the two states A and B. The transformation from A to B can be achieved by forward current injection, illumination, or thermal

agitation, and thus state B is prevailing during the elevated temperature annealing. Examination of the functional dependence of the decay rate from state B to A on temperature has shown that the rate constant is in agreement with a simple dissociation process, see Appendix C. Further, the formation of state B appears to be a diffusion limited second order process. Therefore, state A may be visualized to consist of two components, A1 and A2.

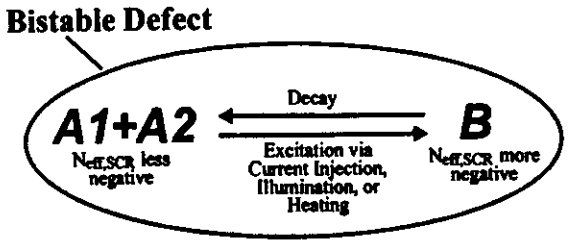

Fig. 3.13 Schematic illustration of the features of the bistable defect generated in heavily damaged samples by elevated temperature annealing.

The amplitudes, the time constants, and the steady state values of the depletion voltage transients seen in Fig. 3.12 were determined by fitting an exponential decay model to the data where the time scale was set to zero at the end of the preceding annealing step. For annealing temperatures in the range from 110°C to 170°C the concentration N_B of generated bistable defects in the state B was calculated from the voltage amplitude using eq. 2.7 and plotted into Fig. 3.10 a) after normalization to the fluence. Also the IV data exhibit a transient decay. It is however not clear, whether this excess leakage current reflects a midgap generation center related to state B of the bistable defect, or if one just observes edge currents related to the V_{dep} decay. The amplitude ΔI_B of the declining current has been determined using the same fitting procedure as for the depletion voltage, see Fig. 3.10 b). With respect to the observations made after the 170°C annealing step it will be noted that the device characteristics were already significantly distorted. In particular a current breakdown was reached at the largest reverse bias voltages of the IV and CV measurements. As this injects free carriers and thus might reverse the decay, the systematic investigation is difficult at these annealing stages.

An other striking feature of the bistable defect is that the decay from state B to A virtually does not take place in the depleted zone of a detector. This fact has been exploited in reference [MOL95] to demonstrate that the defect in question is homogeneously distributed throughout the bulk by storing a sample in which state B was excited under several reverse bias voltages. After state B has decayed within the undepleted bulk region, a step function like distribution of space charges was found to be established, as could be confirmed by the peculiarities of the corresponding CV curves.

Here a corresponding examination has been carried out with current pulse shape measurements providing information regarding the electric field distribution more directly. Fig. 3.14 shows the current pulse shapes induced by hole injection at the rear electrode of an inverted detector annealed at 140°C immediately after excitation of state B and after a long storage period at room temperature under a reverse bias voltage of 80 V. Underneath the rear electrode, where the electric field existed during the reverse bias storage, the current signal resulting from the holes drifting from the rear to the front electrode is virtually unchanged. Only after an intermediate position in the detector the field gradient is found to be reduced, indicating a decrease in the number of negative space charges with respect to the value observed before.

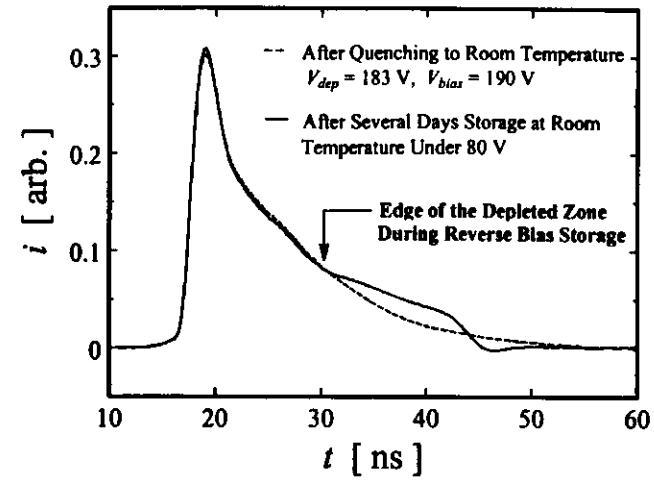

Fig. 3.14 Current pulse shapes induced by hole injection at the rear electrode before and after reverse bias storage (device 942G19, d = 386.8 µm, Φ_{eq} = 1.01×10^{13} cm^{-2} from the PTB Be(d,n) source, $N_{eff,0}$ = 0.548×10^{13} cm^{-3}, annealed at 140°C).

Evidently the bistable defect provides an easy tool to change the concentration of space charges experimentally by simply injecting a forward current, which will be successfully applied in Section 3.3.3.6 in order to provide evidence for the correlation of a specific defect level with the observed increase in the negative space charge. Moreover, a suitable sequence of forward current injections and reverse bias storage sequences allows one to tailor the electric field profile, which might serve as a calibration tool for the determination of the entire field profile from current pulse shape measurements.

3.2.4 Comparison between Various Particle Types

3.2.4.1 The Pion Damage Function

Experimental studies of the damage caused by high flux pion irradiations were carried out within the SIRAD collaboration at the Paul Scherrer Institute (PSI, Villigen, CH). The experiments were designed to examine the resonant behavior (Δ resonance) of the pion displacement damage function predicted in reference [HUH93] (compare Fig. 3.0) and to provide long term damage constants for fluences up to 10^{14} cm^{-2}. As at LHC a major fraction of the damage is caused by pions, in particular in the innermost regions of the tracker, it was an urgent task to examine the hypothesized enhancement of the damage at an energy of around 200 MeV. For this purpose the πE1 beamline at PSI was tuned to produce positive pions with energies ranging from 65 MeV to 331 MeV (energy scan). Moreover, a single extended irradiation was performed with 236 MeV negative pions to exclude a charge sign dependence.

For a PSI cyclotron proton beam intensity of 800 µA the positive pion flux is of the order of 5×10^8 cm^{-2}s^{-1} at around 200 MeV and falls off by a factor of 5 to the upper and lower energies [FUR95]. Due to the limited experimental time it was thus impossible to scan the pion beam at more than five different energies, and also the fluence per energy point in a single exposure had to be chosen as low as about 10^{12} π /cm^2. In that fluence range the change in the effective doping concentration is not a suitable measure of the non-ionizing energy loss (NIEL), because the change is not growing in proportion with the particle fluence, but rather exponentially due to the donor removal effect, compare eq. 3.11. On the other hand, the leakage current is increasing proportional to the fluence, and hence a plot of the change in

the current normalized to the pion fluence Φ (not normalized to equivalent 1 MeV neutrons!) versus the pion energy should reveal the predicted Δ resonance. However, the complex annealing behavior of the leakage current makes this straight-forward approach difficult. It has therefore been assumed here that the annealing curve on pion damaged devices is similar to the one reported after neutron damage, which has been confirmed by the RD2 Collaboration [BAT96]. It is then possible to rearrange eq. 3.20 according to

eq. 3.24 $$\alpha'_{\infty i} = \frac{\Delta I(t_i)}{Ad\Phi}\frac{R(T)}{}\frac{g(\infty)}{g(t_i)},$$

so that the current related damage constant α'_∞ can be calculated from each measurement of the leakage current $\Delta I(t_i)$ after an arbitrary room temperature annealing time t_i. Moreover, if N measurements are available, the overall average $(\Sigma\alpha'_{\infty i})/N$ yields an optimum value for α'_∞. As the devices considered here were damaged just weakly, the annealing parameters valid for the fluence range below inversion of the sign of the space charge have been employed, see Table 3.2.

The detectors used for the experiment were made from Wacker n-type silicon with an initial doping concentration ranging between 0.1 and 0.5×10^{12} cm^{-3}. Table 3.5 lists the geometry of the devices, the pion momentum p and kinetic energy E_p, and the pion fluence Φ inferred from aluminum foil activation measurements with an accuracy of 5% (reaction ^{27}Al(π^+,xN)^{24}Na) [FUR95]. The room temperature current annealing data was gathered within a time period of 200 days. The first IV and CV curves were recorded 15 days after the irradiation due to the transportation of the devices. About 20 current damage constants per device were averaged to get the α'_∞ data and the corresponding standard deviation σ_1 shown in table 3. While σ_1 represents the deviation from the assumed annealing curve, the error σ_2 is arising from the uncertainty in the fluence.

Table 3.5 Devices used for the pion energy scan: 937KXX : Surface barrier detectors. MUEBXX : Micron ion-implanted diodes provided by [MIC]. Regarding the calculation of the error bar, see text.

Device	d [μm]	A [cm^2]	N_{eff0} [10^{12} cm^{-3}]	p [MeV/c]	E_p [MeV]	Φ [10^{12} π /cm^2]	$\alpha'_\infty, \pm\sigma_1, \pm\sigma_2$ [10^{-18} A/cm]
937K09	390	0.16	0.18	π^+ 300	192	2.50	32.4, ±1.0, ±1.6
937K29	390	0.16	0.23	π^- 350	236	3.08	27.4, ±1.4, ±1.4
MUEB01	312	0.25	0.34	π^+ 300	192	2.50	27.4, ±0.5, ±1.4
MUEB02	312	0.25	0.36	π^+ 150	65	1.26	21.1, ±0.5, ±1.1
MUEB03	310	0.25	0.33	π^+ 350	236	2.48	26.0, ±0.6, ±1.3
MUEB04	310	0.25	0.46	π^+ 250	147	1.90	33.2, ±2.4, ±1.7
MUEB05	295	0.25	0.08	π^+ 400	281	1.90	37.7, ±1.1, ±1.9

Finally, Fig. 3.15 presents a plot of α'_∞ versus the pion energy with error bars calculated by adding σ_1 and σ_2 in quadrature. The pion damage function from reference [HUH93] was scaled to the data in order to illustrate the predicted behavior. Although systematic errors due to the beam divergence and surface components of the leakage current have been neglected, it must be stated that the agreement is not convincing. Regarding the device used at the highest energy, the large deviation might be related to the much lower initial doping concentration which could give rise to systematic errors in the assumed volume of the depleted region. In conclusion, the theoretical dependence of the displacement damage effects on the pion energy is too weak, as that evidence for the resonant behavior could be provided within this experiment. In the same sense, no significant difference is seen in the damage from positive and negative pions.

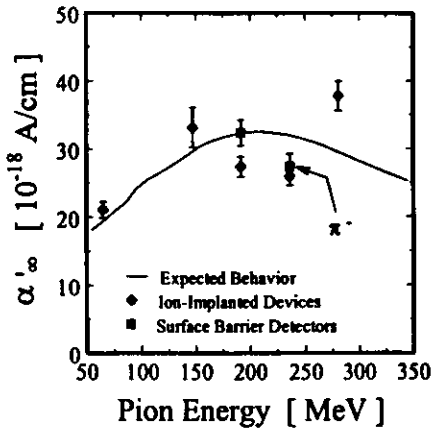

Fig. 3.15 The current related damage constant after complete annealing as function of the pion energy.

3.2.4.2 Comparison between Neutron, Proton, and Pion Damage

Surface barrier detectors were exposed to high fluences ($\Phi_{eq} > 10^{13}$ cm^{-2}) of 5.3 MeV neutrons from the PTB Be(d,n) generator, 24 GeV protons from the CERN PS, and 236 MeV pions at PSI (see Table 3.1) in order to compare the long term behavior. The chief objective of the study were the damage constants in the model equations for the doping concentration (g_c, N_{c0}, and g_Y) and for the leakage current (α_∞). All 17 devices under test were processed from the same wafer (identifier 935, d = 329 μm, N_{eff0} = 0.45×10^{12} cm^{-3}). Thus, effects related to the influence of different starting materials were avoided (compare next section).

Isothermal annealing was done in normal air atmosphere, mostly at a slightly elevated temperature of 49.5°C. In the course of the annealings that were extended up to a cumulated tempering time of several days the devices were cooled down to room temperature (around 21°C) as often as 20 times in order to record IV- and CV-curves. Some hundred characteristics were gathered to obtain accurate data on the doping concentration and the leakage current as function of the annealing time. Extraction of the parameters N_c, N_{Ya}, and k_Y from the individual annealing curves was performed as outlined in Section 3.2.1.2. An example for the accuracy of the least-squares fitting procedure is given in Fig. 3.16, where for this purpose the evolution of the full depletion voltage has been plotted versus a logarithmic time scale. According to the discussion given in Section 3.2.1.3, the leakage current increase ΔI corrected to 20°C and normalized to the sensitive volume (Ad) was taken from the minimum of the leakage current annealing curve. Except for the reverse annealing rate constants, all evaluated data are plotted in Fig. 3.17 versus the equivalent 1 MeV neutron fluence, compare the hardness factors κ in Table 3.1.

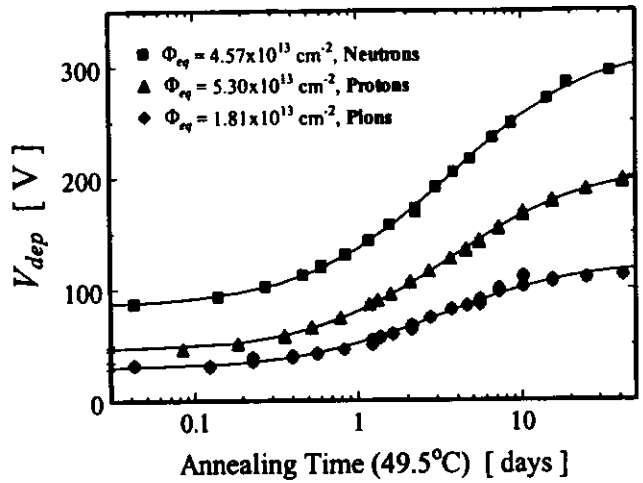

Fig. 3.16 Isothermal reverse annealing curves and corresponding least-squares fits (solid lines) for three surface barrier detectors damaged with either neutrons, protons, or pions.

The determination of the reverse annealing generation rate g_γ and the current related damage constant α_∞ for every particle source is illustrated in Fig. 3.17 a) and c), respectively. For both cases the damage constant, summarized in Table 3.6, was calculated by averaging the individual ratios between $N_{y\infty}$ or $\Delta I\,R(T)/(Ad)$ and the corresponding fluence Φ_{eq}. The error quoted in Table 3.6 is the error in the average value, compare Appendix D. It will be noted that the errors in the individual data points in Fig. 3.17 a) and c) are implicitly assumed to scale with the fluence. Regarding the portion of the stable damage N_c shown in Fig. 3.17 b) it has been exploited that according to eq. 3.12 the data should fall onto a straight-line in the considered fluence range. The solid lines in Fig. 3.17 b) display the corresponding fits, furnishing optimized N_{C0} and g_c values and their errors, both given in Table 3.6. For the sake of convenience it has implicitly been assumed here that, contrary to the determination of g_γ and α_∞, the error in the individual N_c data points assigned to one straight-line fit is a constant.

The α_∞ for pions quoted here differs significantly from 3×10^{-17} Acm^{-1}, which is the approximate value following from the α'_∞ quoted in Table 3.5 for a fluence of around 10^{12} π /cm^2 if a hardness factor close to unity is taken into account. It has however already been discussed in Section 3.2.1.3 that the method employed for the extraction of the leakage current increase in heavily damaged samples does only provide an upper limit for the current related damage constant. Anyway, since the devices used for the present study were processed from the same wafer and the current damage data were only taken from devices with identical geometry, a comparison between the results from different particle types is still justified. In this context it is noted that accordingly only those four pion irradiated devices exhibiting the large circle geometry (type G, compare Table 2.1) could be taken into consideration. In fact always a pair of K-type and G-type detectors have been exposed in order to determine the influence of the electrode geometry. While no differences were seen in the data related to the effective doping concentration in the space charge region, the leakage current increase normalized to the sensitive volume was found to be systematically larger for the K-type devices. The latter indicates an underestimation of the sensitive volume after the inversion of the space charge sign. This is conceivable if it is recalled that the area of the front electrode was assumed to determine the sensitive area, whereas in the inverted detectors the junction is growing from the rear plane contact which for both designs extends close to the sawing edges of the devices.

While the agreement between the damage constants found for neutron and pion damage is very good, the results for the 24 GeV proton irradiations are always found to be significantly smaller. This would not have been expected as only equivalent 1 MeV neutron fluences were used, see Section 3.1. Provided the proton fluence determination is correct this would mean that the used proton damage function ([VGI89]) yields a too large hardness factor at the energy 24 GeV. This is imaginable as the inelastic interaction between a 24 GeV proton and a silicon atom results in residual nuclei whose energy has a Maxwellian type distribution with an average in the 10-20 MeV range, and which renders the calculation of the damage function more difficult [VGI89]*. Moreover, in general departures from the NIEL hypothesis need to be taken into account if the spatial distribution of the radiation damage-induced crystal defects plays a role [VLI87]. The latter would however only be expected if the average energy imparted to the PKA is less than around 5 keV (see Section 3.3.1.1) which is not accomplished for the particles studied here. This is also confirmed by the ratios between two damage constants shown in Table 3.6, which are assumed to be directly related to the introduction rate of microscopic crystal defects. As the ratios do not depend on the fluence calibration, they should be similar for all particle sources. The quoted error follows from standard error propagation, see Appendix D. Only for the protons is a slight elevation of the g_γ/α_∞ value noticed, which however with respect to the omission of systematic errors is found to be insignificant. It will be noted that the above ratios also exclude a contribution from impurities created in nuclear reactions (see Section 3.3.1.1) to the macroscopically observed damage effects, which is also not accounted for by the NIEL hypothesis.

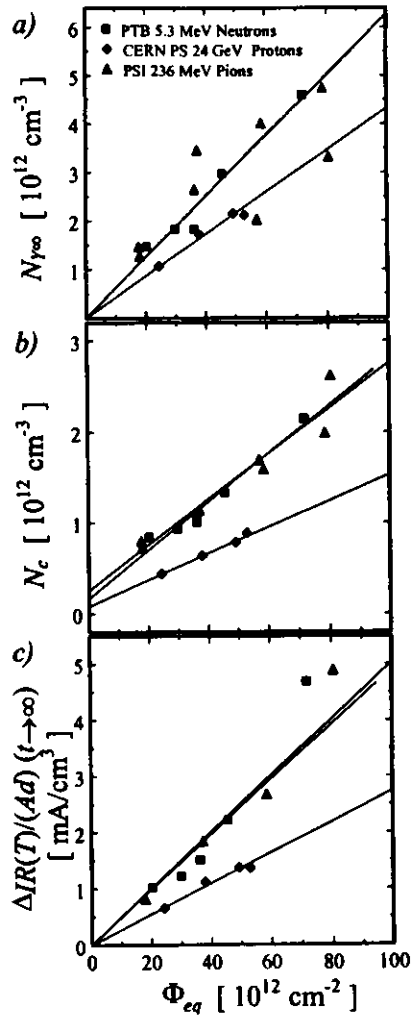

Fig. 3.17 Extracted parameters of the isothermal annealing curves as function of the equivalent 1 MeV neutron fluence. The solid lines are fits to the data for purpose of evaluation of the damage constants for each particle source.

In conclusion it is found that with the hardness factor and fluence determination currently employed for the 24 GeV proton beam, the quoted Φ_{eq} is not equivalent to 1 MeV neutrons. Therefore, experimental values of the hardness factors were determined from the presented data. The damage constants g_c, g_γ, and α_∞ obtained for the protons and pions without normalization to equivalent 1 MeV neutron data were divided by the corresponding values found at the PTB Be(d,n) neutron generator as given in Table 3.6. The weighted average of these ratios is

* It is noted that depending on the mass of the fragments their range might become of the order of the device thickness, such that a fraction of the imparted energy might be transported out of the considered silicon material.

$\kappa_{exp,CERN\ PS} = 0.582 \pm 0.028$ and $\kappa_{exp,PSI\ 236\ MeV} = 0.928 \pm 0.067$.

As previously stated, within errors the quoted pion fluences can be regarded as equivalent to 1 MeV neutrons, whereas the proton values are seriously in error, see Table 3.1. In this context it is noted that as opposed to the Van Ginneken data ([VGI89]) used in this work, the proton damage function presented in reference [HUH93] furnishes a hardness factor for 24 GeV protons much closer to the experimental value found here.

Table 3.6 Number of samples investigated and summary of the average 1 MeV neutron equivalent damage constants and the corresponding errors found for neutrons, protons, and pions. Note that these data depend on the used hardness factors (Table 3.1) and are restricted to a specific material (wafer 935).

Particle Type	Neutrons	Protons	Pions
Number of Devices	5	4	8
N_{eff0} [10^{12} cm^{-3}]	0.16±0.13	0.06±0.05	0.24±0.15
g_c [10^{-2} cm^{-1}]	2.66±0.30	1.51±0.11	2.54±0.28
g_I [10^{-2} cm^{-1}]	6.25±0.35	4.32±0.11	6.27±0.64
α_∞ [10^{-17} Acm^{-1}]	4.92±0.44	2.74±0.08	5.03±0.36[a]
g_c/α_∞ [10^{15} A^{-1}]	0.54±0.08	0.55±0.04	0.50±0.07
g_I/α_∞ [10^{15} A^{-1}]	1.27±0.13	1.58±0.06	1.25±0.16

[a] Only 4 devices were taken into account, see text.

3.2.4.3 ^{60}Co Gamma Irradiations

Three surface barrier detectors and one ion implanted device, all fabricated from n-type float zone material, have been exposed to ^{60}Co gamma radiation at the Brookhaven National Laboratory (BNL). In order to observe changes in the macroscopic device properties, irradiation doses D of up to 5 MGy were chosen. The dose rate was either 1.5 or 5 kGy per hour, i.e., it took around 40 days to obtain the highest dose. Only a cursory check of the annealing curve has been performed during the several months of storage at room temperature following the irradiation. The leakage current increase, corrected to 20°C and normalized to the sensitive volume, and the change in the concentration of space charges ($\Delta N_{eff} = N_{eff,0} - N_{eff,SCR}(D)$) as inferred from IV and CV curves is plotted in Fig. 3.18 a) and b), respectively. Except for some minor variations, which are most likely related to the annealing of the positive charges and interface states of the seriously damaged oxide passivation (see Section 4), neither annealing nor reverse annealing similar to the effects found for heavy particle-damaged samples are observed. Accordingly, it is justified to equate the average for each device, depicted by the solid lines in Fig. 3.18. These averages are in addition plotted as function of the irradiation dose in Fig. 3.19.

It should be noted that due to the damaged oxide the leakage currents are composed of bulk and surface generation currents. Only the ion implanted device was supplied with a guard ring, which however was left floating. Proper contacting of the guard ring, sinking most edge and surface currents, was done only once and has reduced the overall current by a factor of two. In the surface barrier detectors the relative contribution would be expected to be even larger. The effective doping concentration is found to become more negative, and also the sign of the space charge is observed to be inverted, as could be confirmed by TCT measurements, see Section 3.3.5. Moreover, in the dose range studied a significant removal of the phosphorus dopants has to be envisaged, accounting for the observation that the change in $N_{eff,SCR}$ is larger for the ion-implanted device manufactured on lower resistivity material.

Since in the first approximation both quantities, $\Delta I\ R(T)/(Ad)$ and ΔN_{eff} appear to be increasing proportional to the dose, the data have been normalized with respect to D and averaged afterwards, resulting in the damage constants and the standard deviation error presented in Table 3.7. Finally the ratio between the two damage constants is quoted in the bottom row of Table 3.7, which has to be compared with the corresponding values found after heavy particle damage in Table 3.6. Bearing in mind the immense surface current contribution, it is noted that for ^{60}Co-gamma damage the ratio is at least one order of magnitude larger, indicating the expected breakdown of the NIEL hypothesis, compare Section 3.1.

Table 3.7 Damage constants and the corresponding standard deviation errors for ^{60}Co-gamma irradiation.

$(\Delta I\ R(T)/(Ad))/D$	$(3.9\pm1.5)\times10^{-11}$ Acm^{-3}Gy^{-1}
$\Delta N_{eff}/D$	$(2.4\pm0.7)\times10^{5}$ cm^{-3}Gy^{-1}
$\Delta N_{eff}/(\Delta I\ R(T)/(Ad))$	6×10^{15} A^{-1}

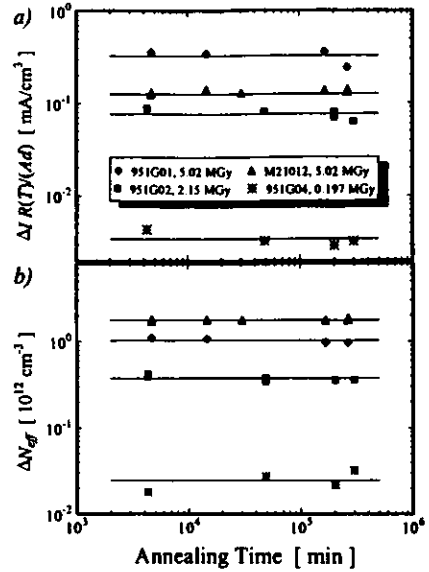

Fig. 3.18 Annealing curves after high dose ^{60}Co gamma irradiation. a) Leakage current increase, b) change in the concentration of space charges.

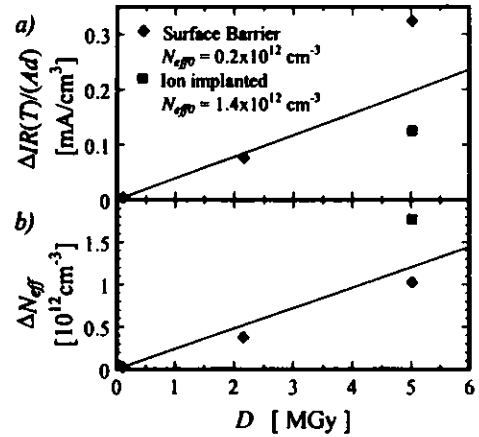

Fig. 3.19 Leakage current increase a) and change in the effective doping concentration b) observed after ^{60}Co-gamma irradiation as function of the irradiation dose D.

3.2.5 Influence of the Starting Material

Five different starting materials with average initial doping concentrations ranging from 0.6×10^{12} cm^{-3} (p-type) to 2.5×10^{12} cm^{-3} (n-type) were investigated with respect to the long term damage constants related to the doping concentration. Because errors from the fluence normalization had to be avoided (compare the previous section), all devices were exposed at the same source, namely, the Be(d,n) neutron generator at the PTB (compare Table 3.1), which allows easy access and a fluence determination with an accuracy of better than 5% [BRE89].

In order to extract the damage constants with some significance in terms of the statistics, at least 4 detectors for any given starting material were irradiated, each material type covering a wide range of equivalent 1 MeV neutron fluences up to 8×10^{13} cm^{-2}. All devices were subjected to isothermal annealing in normal air atmosphere, typically at 49.5°C, and the analysis of the accomplished ΔN_{eff} annealing curves and the subsequent extraction of the damage constants for each material type was essentially equal to the procedure employed in the previous section. The corresponding $N_{y\infty}$ and N_c data are plotted in Fig. 3.20 a) and b) respectively, and the resulting average damage constants and the corresponding errors are given in Table 3.8.

Table 3.8 Main processing characteristics, number of samples analyzed, and average values of the damage constants with the corresponding error found for the devices made from different starting materials. For $N_{eff,0}$ the standard deviation error has been quoted. All devices were exposed at the PTB Be(d,n) source, and the accordingly small error of about 5% in the fluences was neglected.

Devices	Material, Manufacturer	Type	d [µm]	$N_{eff,0}$ [10^{12} cm^{-3}]	#	N_{c0} [10^{12} cm^{-3}]	g_c [10^{-2} cm^{-1}]	g_Y [10^{-2} cm^{-1}]
935	Wacker, Hamburg	surface b.	329	0.453±0.03	5	0.16±0.13	2.66±0.30	6.25±0.35
936	Wacker, Hamburg	surface b.	299	-0.563±0.10	4	0.00±0.23	1.63±0.58	5.36±0.22
934	Wacker, Hamburg	surface b.	505	0.441±0.04	4	0.24±0.05	2.58±0.21	5.62±0.29
BRBI	Tesla, Bratislava	ion-impl.	375	2.46±0.33	4	0.75±0.55	2.94±0.85	5.69±0.15
M1, M2	Wacker, MPI München	ion-impl.	274, 280	1.42±0.08	11	0.60±0.14	3.07±0.27	5.95±0.62[a]

[a] Only three devices from wafer M1.

Regarding the reverse annealing amplitude $N_{y\infty}$, the proportionality presupposed in eq. 3.14 evidently holds over the full range of the investigated fluences, i.e., no tendency of saturation at high Φ_{eq} is noticed, which has been proposed in reference [WU196]. Further, within the experimental errors the introduction rate g_Y is found to be the same, irrespective of the initial resistivity. It is therefore reasonable to quote the corresponding weighted average,

$$\bar{g}_{Y,PTB\ Be(d,n)} = (5.66 \pm 0.11)\times10^{-2}\ \text{cm}^{-1},$$

which due to the fluence normalization problems has been restricted to the particular irradiation source used. The given uncertainty should be considered as the lower limit of the statistical error in the average value of g_Y, because not all of the individual g_Y's in Table 3.8 are fully compatible with this average in regard to their 1-σ errors.

The same arguments may equally as well be applied to the introduction rate of the stable acceptor-like states g_c, which has the overall weighted average

$$\bar{g}_{c,PTB\ Be(d,n)} = (2.68 \pm 0.14)\times10^{-2}\ \text{cm}^{-1}.$$

Only for the initial p-type material is the g_c not in accord with this average. However, bearing in mind the small number of investigated devices, the deviation has not been considered to be significant.

While due to the covered fluence range mostly the simplified relation eq. 3.12 has been employed for the fitting of the dependence of the stable damage as function of fluence, sufficient data were available for the devices provided by MPI München, allowing for the least-squares fitting of all parameters in eq. 3.11. The so-called donor removal constant could therefore be derived on these samples, however, only with a considerable uncertainty,

$$c_{MPI} = (2.4\pm1.4)\times10^{-13}\ \text{cm}^2.$$

The parameter N_{c0} is expected to exhibit a correlation with the initial doping concentration $N_{eff,0}$, which is explored in Fig. 3.21. The indicated straight-line fit has the form

$$N_{c0}(N_{eff,0}) = (0.3 \pm 0.1)N_{eff,0} + (0.1 \pm 0.07)\times10^{12}\ \text{cm}^{-3}.$$

In a simple approach N_{c0} may be regarded as a specific fraction of all donors with total concentration N_D which can be removed permanently by not further specified processes related to the radiation damage events. The initial doping concentration usually is composed of donors and acceptors $N_{eff,0} = N_D - N_A$, for instance phosphorus and boron. It will be assumed here that the degree of the compensation is very small, i.e., the boron concentration is much smaller than the one of phosphorus, such that $N_{eff,0} \approx N_D$. Since according to the obtained relation it is always $N_{c0} < N_{eff,0}$ for initial n-type material, it must be concluded that not all donors of the initial material become electrically inactive after high fluence irradiation.

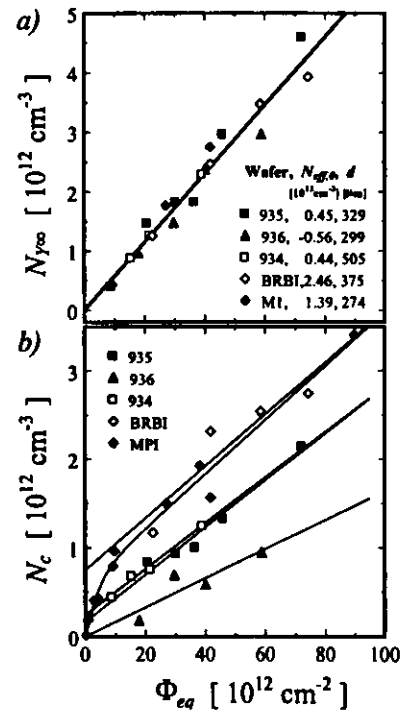

Fig. 3.20 Extraction of the long term damage constants of the radiation damage-induced changes in $N_{eff,SCR}$ on devices fabricated from materials with various initial resistivities. a) Amplitude of the reverse annealing, the solid line depicts the overall weighted average. b) Portion of the stable damage and the corresponding fits, see text.

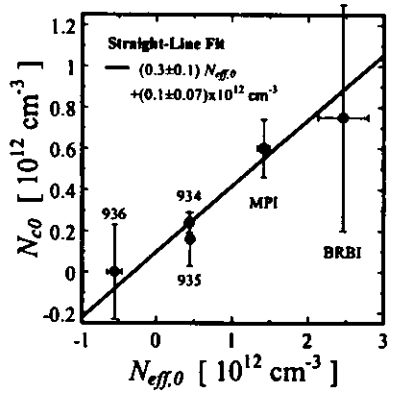

Fig. 3.21 Correlation between the parameter N_{c0} and the initial doping concentration $N_{eff,0}$. The solid line is a straight-line fit, weighted with the errors in the N_{c0} data as given in Table 3.8. The standard deviation error bars supplied to the $N_{eff,0}$ values illustrate the variation of the initial resistivity on the wafers.

It will however be noted that these results were obtained from short term high flux irradiations, whereas long exposure times at a low flux might remove all donors. The latter statement is based on the microscopic model that the donors are deactivated by two competing processes and only one of the reaction products exhibits a short term annealing, resulting in the recovery of a fraction of the donors. However, equally well the initial overall donor concentration could be composed of two portions of which only one is removed. Further studies are therefore needed to resolve this ambiguity.

In addition it can be deduced from the

comparison of the data obtained on the devices 934 and 935 in Table 3.8, which are fabricated from almost identical material that the damage constants do not depend on the device thickness. This would have been awaited if the device surfaces were acting as effective sinks for migrating complex defects [LUT95]. Moreover, particularly noteworthy is the qualification of the long term damage model equations also for the BRBI devices, which are not made from Wacker material.

3.2.6 Comment on the Reverse Annealing Model

A plot of all reverse annealing rate constants determined at 49.5°C in the studies presented in Section 3.2.4 and Section 3.2.5 versus the corresponding equivalent 1 MeV neutron fluence is shown in Fig. 3.22. Evidently $k_Y(49.5°C)$ can not reasonably be assumed to be a constant, but rather is in agreement with a $1/\Phi_{eq}$ dependence. Earlier studies have not reported this relation because the measurements were carried out in a limited range of fluences, on the one hand, to avoid exceedingly large full depletion voltages at large Φ_{eq} and, on the other hand, to circumvent the difficulties met with samples irradiated close to the point of inversion ($\Phi_{eq} \approx 10^{13}$ cm^{-2}). In regard to the significant spread in the rate constants noticed in Fig. 3.22 it is thus not surprising that only now, with a larger number of samples, the variation of k_Y with fluence could be assessed more clearly.

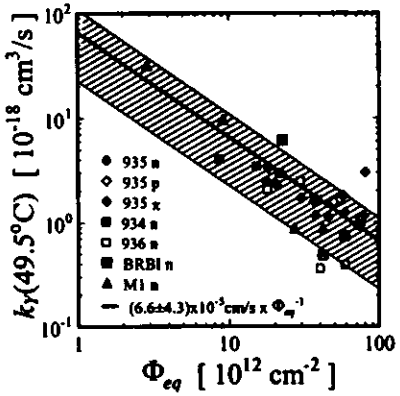

Fig. 3.22 Reverse annealing rate constant at 49.5°C as function of the fluence as determined on various wafers and different particle types, see text.

A dependence proportional to $1/\Phi_{eq}$ is motivated by the idea that the reverse annealing is a composition of essentially first order annealing processes as proposed by Z. Li in reference [LI295], and that the currently used reverse annealing curve is just a suitable parametrization, giving a good fit to the experimental data while employing a minimum number of parameters. In fact, also a sum of two exponential terms $a_1\exp(-t/\tau_1) + a_2\exp(-t/\tau_2)$ fits the reverse annealing data equally well, however, requiring four parameters to be adjusted. Such a model has not been used as the fitted parameters would be strongly correlated and hardly could be determined unambiguously.

Now, if the differential equation for the defects Y accounting for the negative charge is identified with a term reflecting an overall average first order reaction with the rate constant k_{Y1},

eq. 3.25 $$\frac{dN_Y}{dt} = k_Y\left(N_{Y\infty} - N_Y\right)^2 \approx k_{Y1}\left(N_{Y\infty} - N_Y\right),$$

where k_{Y1} is considered to be independent of the irradiation fluence, and if $N_{Y\infty}/2$ is accepted as an average value of $(N_{Y\infty} - N_Y)$, then k_Y would be expected to vary with fluence as

eq. 3.26 $$k_Y(\Phi_{eq}) \approx \frac{2k_{Y1}}{g_Y}\Phi_{eq}^{-1},$$

where eq. 3.14 has been used for $N_{Y\infty}$.Correspondingly, the rate constants k_Y depicted in Fig. 3.22 have been multiplied with the appropriate fluences Φ_{eq} in order to obtain the average value and the standard deviation error of the constant $2k_{Y1}/g_Y$, see the legend of Fig. 3.22. If it is further asserted that the overall average first order rate constant k_{Y1} exhibits the same thermal activation characteristics as k_Y, it is possible to evaluate the frequency factor k_{01} of k_{Y1} in the Arrhenius-relation eq. C.2 in Appendix C. If the global averages E_a = 1.31 eV and $g_Y \approx 5\times10^{-2}$ cm^{-1} are employed, compare Section 5.1.1, one gets $k_{01} = 5\times10^{14}$ s^{-1}. While, as was noticed earlier in reference [FEI93], the k_0 typically quoted for the reverse annealing rate constant k_Y is orders of magnitudes larger than what can be expected from the microscopic

understanding of a second order process developed in Appendix C, the value found for k_{01} is in reasonable agreement with the most abundant phonon frequency $k_B T/h$, bearing in mind the various simplifications utilized.

Besides the dependence on Φ_{eq} observed here, further experimental evidence for the underlying first order kinetics was indirectly provided by the failed efforts to out-diffuse the defects X which according to the original suggestion of the second order model combine to form the electrically active Y-defect. These ideas were based on the derivation of the diffusion constant of the defects X from the numerical value established for k_0 [LUT95]. Since according to the above statements k_0 can not be given a sound physical meaning, the diffusion constant and thus the efficacy of the out-diffusion process was significantly overestimated.

In order to calculate the parameter k_Y in the reverse annealing function eq. 3.13 at an arbitrary irradiation fluence and annealing temperature based on the results reported here, the global average E_a = 1.31 eV can be used as the thermal activation energy of the process. Then it is

$$k_Y(\Phi_{eq}, T) = k_0(\Phi_{eq})\exp\left(-\frac{1.31\,\text{eV}}{k_B T}\right) \quad \text{with} \quad k_0(\Phi_{eq}) = (1.9 \pm 1.2)\times10^{16}\ \text{cm/s}\times\Phi_{eq}^{-1},$$

as can be deduced from eq. 3.26 and the numerical value of $2k_{Y1}/g_Y$ given in Fig. 3.22.

Finally it will be noted that for the device plotted at $\Phi_{eq} \approx 3\times10^{12}$ cm^{-2} in Fig. 3.22 the reverse annealing introduction rate g_Y was found to be 2.41×10^{-2} cm^{-1}, i.e., around half of the world average (see Appendix E). Further, on the even more weakly damaged sample examined by isochronous annealing in Fig. 3.10 the first reverse annealing stage could not be observed at all. In conclusion this indicates a variation of the reverse annealing introduction rate g_Y with fluence. In this context it is important to realize that so far no dependence of the considered annealing process on the type of free carriers (electrons or holes) predominating in thermal equilibrium was observed. For example, the parameters evaluated for the most weakly damaged sample from the BRBI wafer ($\Phi_{eq} \approx 2\times10^{13}$ cm^{-2}) studied in Section 3.2.4 fit well the expected behavior, although by virtue of the low initial resistivity it was never inverted to p-type. Further systematic studies on reverse annealing in the low fluence range are inevitable to gain a deeper insight.

3.2.7 Summary of the Changes in the Macroscopic Detector Properties

- The currently accepted models describing the damage-induced doping changes, leakage current increases, and charge collection losses due to trapping as function of fluence and annealing time were reviewed and illustrated by experimental examples.

- A difference of approximately 10^{-2} cm^{-1} $\times$ Φ_{eq} was observed between the absolute values of the space charge concentration $N_{eff,SCR}$ inferred from CV curves and from TCT measurements. This result was found to hold in a wide range of fluences (Φ_{eq} < 5×10^{13} cm^{-2}) and, in the first approximation, to be independent of the room temperature annealing time (< 10^5 min).

- Isochronous annealing
  - Three neutron-damaged devices were subjected to isochronous annealing and data were shown on the evolution of the doping changes and the leakage current.
  - Using $N_{eff,SCR}$ values derived from TCT measurements, the thermal activation energy of the rate constant of the first stage reverse annealing was determined to be 1.36 eV.
  - It was confirmed by TCT measurements that the bistable defect accounting for the decay of the depletion voltage observed after quenching the sample from the annealing temperature is distributed homogeneously throughout the bulk.

- Comparison between particle types
  - Pion irradiations have shown no significant enhancement in the damage effects around the Δ resonance energy at approximately 200 MeV.
  - Long term damage constants were compared between fast neutrons (PTB Be(d,n)), 236 MeV pions (PSI), and 24 GeV protons (CERN PS) using devices fabricated from the same wafer. For the proton damage at the CERN PS an experimental hardness factor of $\kappa_{eff,CERN\ PS}$ = 0.582±0.028 was found, which deviates significantly from the value currently used for the normalization to equivalent 1 MeV neutron data (0.93).
  - High fluence ^{60}Co-gamma irradiations were found to introduce bulk leakage current generation centers and negative space charge (also inversion of the space charge sign). No annealing effects were observed.

- Influence of the starting material
  - Damage constants for the damage-induced changes in the doping concentration were studied on materials of various initial resistivities (0.6×10^{12} cm^{-3} p-type to 2.5×10^{12} cm^{-3} n-type) using fast neutrons from the PTB Be(d,n) generator.
  - Negative space charge was found to be introduced at a rate independent of the initial resistivity, both in the stable and the reverse annealing portion.
  - Only about 30% of the initial doping was found to be removed at high fluences, indicating a 'reservoir of non removable donors'.

- The first stage reverse annealing rate constant was found to vary with fluence as $1/\Phi_{eq}$, and an explanation was given based on underlying first order processes.

3.3 Microscopic Defect Studies

As noted in the beginning of Section 3.2.1, the changes in the macroscopic device properties of the silicon detectors are explained in terms of electrically active defect levels which are generated by the interaction of high energetic particle radiation with the silicon atoms. A deeper understanding of the complex macroscopic behavior can thus only be gained by microscopic investigations of these defects using spectroscopic methods. This approach is now being pursued by several groups active in the field of radiation damage studies on silicon detectors [BIG95, ERE95, LI196, WAT96]. However, a conclusive explanation of the radiation damage-induced device deterioration based on a microscopic model is not yet available.

In the following it will therefore briefly be reviewed, which knowledge about radiation damage-induced defects regarding their origin and their electrical activity in the semiconductor has so far been gathered in the literature. A compilation of all impurities and defects encountered in radiation damaged silicon is given in Appendix B*. Thereafter the formal theory underlying the measurement of Thermally Stimulated Currents (TSC) will be developed from first principles, explicitly taking care of the peculiarities that one faces in heavily damaged, high resistivity samples. The TSC method, which has been used in particular by the group around E. Borchi for a long time [BO191], will then be employed extensively for the characterization of defect levels, their concentrations, and their annealing behavior (Section 3.3.3). Since the silicon studied here is clearly distinct from standard electronic material, it is not surprising that spectroscopic methods have now emerged which otherwise are rarely used or which in fact are new developments. While the former refers to the optical defect filling and current based Deep Level Transient Spectroscopy (I-DLTS) adopted in the pioneering work of Z. Li [LI394], the latter concerns the measurement of laser-induced current pulse shapes (Transient Current Technique TCT) at cryogenic temperatures, which was put forward by V. Eremin [ER295]. Both methods have been applied in this work for the determination of deep level parameters and will be presented in the Sections 3.3.4, and 3.3.5.

3.3.1 Radiation Damage-Induced Defect Levels in Silicon Diodes

3.3.1.1 The Origin of the Defects

Nuclear Reactions

Suppose a cross section $\sigma(E)$ characteristic of a nuclear reaction between a particle with energy E and a silicon isotope ^{X}Si resulting in a specific nucleus, and let $\sigma(E)$ be sufficiently small such that the reaction products are distributed homogeneously throughout the material under study. Then the introduction rate g of the new nucleus can be written as the product of $\sigma(E)$ and the density of the target atoms. In a silicon crystal this refers to the lattice sites occupied with the considered isotope, and if it is recalled that the cubic silicon unit cell has the linear dimension a = 5.43 Å and contains eight atoms, it is

eq. 3.27 $$g = f\,\sigma(E)\,8/a^3$$

Here f denotes the natural abundance of ^{X}Si being 92.21%, 4.7%, and 3.09% for ^{28}Si,^{29}Si, and ^{30}Si, respectively. If the particle source under consideration is not monoenergetic, eq. 3.27 needs to be integrated over E employing the normalized differential flux spectrum as a weighting function.

A very popular example is the neutron capture reaction ^{30}Si(n,γ)^{31}Si $\rightarrow$ ^{31}P + β^- which frequently is used to obtain n-type doping of highest homogeneity [MEE79]. However, the thermal neutron flux of the sources studied in this work is too small as that measurable amounts of phosphorus could be generated. Further, for particle energies greater than certain threshold values additional reaction channels are open, e.g. for neutrons†, ^{28}Si(n,p)^{28}Al (> 4 MeV), ^{28}Si(n,d)^{27}Al (> 10 MeV), and ^{28}Si(n,α)^{25}Mg (> 3 MeV) [ANG96]. While ^{28}Al decays according to ^{28}Al $\rightarrow$ β^- + ^{28}Si with a half-life of 2.3 h, ^{25}Mg is a stable nucleus. The corresponding cross sections for the interaction with pions and 24 GeV protons (below 2.6

* Regarding a description, how the dominant displacement damage defects have in the past been identified, compare [SCH95].

† The threshold values quoted are only approximate.

GeV see [MIC95]) are not well known, however, for suitable neutron energies $\sigma(E)$ becomes as large as 300 mb (see e.g. reference [MCL88]) which then yields maximum introduction rates g_{Al} and g_{Mg} of the order of 0.01 cm^{-1}.

Although this is a small value compared with displacement damage defects, these reactions are noteworthy as Al and Mg introduce shallow impurity levels, either donors as interstitial atoms or acceptors on substitutional lattice sites, see Appendix B. Regarding the dependence of the cross section for the reaction $^{28}Si(n,\alpha)^{25}Mg$ on the neutron energy shown in reference [MCL88], it is clear that measurable concentrations of the stable ^{25}Mg nucleus would only be expected to be produced by one particular source studied in this work, namely the 14.1 MeV neutron generator at the UKE Hamburg, compare Table 3.1. Interest should be devoted to the fact that interstitial magnesium can donate two electrons and, due to the reduced core charge compared with silicon, would be expected to accept two electrons on the substitutional position. Only one acceptor state has however been observed so far. The reconfiguration from an interstitial to a substitutional defect or vice versa, which might be connected with a characteristic annealing temperature, would therefore be at least threefold active in terms of the density of space charges and thus could easily be detected by the corresponding change in the full depletion voltage. In this context it must be born in mind that the nucleus in question will be the Primary Knock-on Atom (PKA) and therefore has a high chance to come to rest on an interstitial site in the vicinity of various other defects, see below.

Displacement Damage Defects

The defects usually encountered in displacement-damaged silicon are stable complexes of impurities and lattice vacancies emerging after a variety of annealing processes (see Fig. 3.23), as will be discussed in the following, compare [VLI87] and [ASO87]. The initial damage consists of several Frenkel-pairs created along the tracks of the primary (PKA) and secondary recoil atoms as they move through the crystal. Also direct creation of higher order intrinsic point defects, e.g. divacancies VV, is anticipated given the considered recoil is sufficiently energetic compared with the single atom displacement threshold of around 25 eV. While initially chiefly decelerated by ionization the differential displacement cross section caused by elastic scattering of the recoils is increasing, such that below approximately 5 keV a disordered region (or terminal cluster) appears at the end of every cascade. It contains higher concentrations of intrinsic defects exhibiting a mutual interacting through the resulting lattice strain. The extent of such a region is of the order of 10 nm. Before thermal rearrangements take place the total number of displaced atoms is approximately equal to the nonionizing energy of the PKA (compare Section 3.1) divided by 50 eV ([VLI87]).

Now, the self interstitial Si_i which is known to diffuse very easily even at low temperatures will recombine with nearby vacancies, especially all close-pairs will be lost. The recombination rate within the disordered regions is as large as 75-95% [SHI90]. As only around 5 keV / 50 eV = 100 or less displaced atoms are associated with a disordered region, only of the order of 10 intrinsic displacement defects constitute its final state. These are most likely few divacancies or other higher order intrinsic point defects in the vicinity of each others lattice strain since isolated interstitials and vacancies will not persist. If the energy initially imparted to the PKA is smaller than approximately 5 keV the number of displacements in the terminal region will be decreased accordingly. Here it is interesting to note that for a PKA energy of less than 1 keV in respect to the previously mentioned recombination rate only a single defect would be left, that is, no lattice strain interaction between defects would be expected to be remaining. In this respect an extreme situation is met with ^{60}Co-gammas, as only few atoms can be displaced, compare Section 3.1. In particular the direct creation of a divacancy or any other higher order intrinsic point defect is very unlikely. On the other hand, for average recoil energies larger than around 5 keV merely the number of subcascades is growing as function of the PKA energy, and the structures produced in the cascade terminals are virtually the same*.

Interstitials escaping the recombination will kick out substitutional impurity atoms according to the Watkins replacement mechanism. Due to the large abundance, carbon is considered to be the main sink: $Si_i + C_s \rightarrow C_i$. Proceeding further in time, the silicon vacancies will start migrating and combine with the dominant sink O_i to form the A-center VO_i. Although there are other impurities available to

* In this sense, except for the ^{60}Co-gamma irradiations, all sources investigated in this work are expected to give a similar composition of the displacement damage-induced defects, compare Section 3.1.

complex with the vacancy, for example substitutional phosphorus P_s resulting in the E-center VP_s, such processes are not very effective in high resistivity material since the concentration is very small compared with interstitial oxygen (so-called vacancy sharing). As outlined in reference [SU90], the ratio between the A-center and E-center concentration is in the first approximation about 350 for the particular example of $[O_i] = 5\times10^{15}$ cm^{-3} (see Section 2.2.1) and $[P_s] = 10^{12}$ cm^{-3}. In this respect also the reaction $V + V \rightarrow VV$ is not very effective, unless there is a locally increased vacancy concentration, as for example close to the cascade terminals, compare [SVE92].

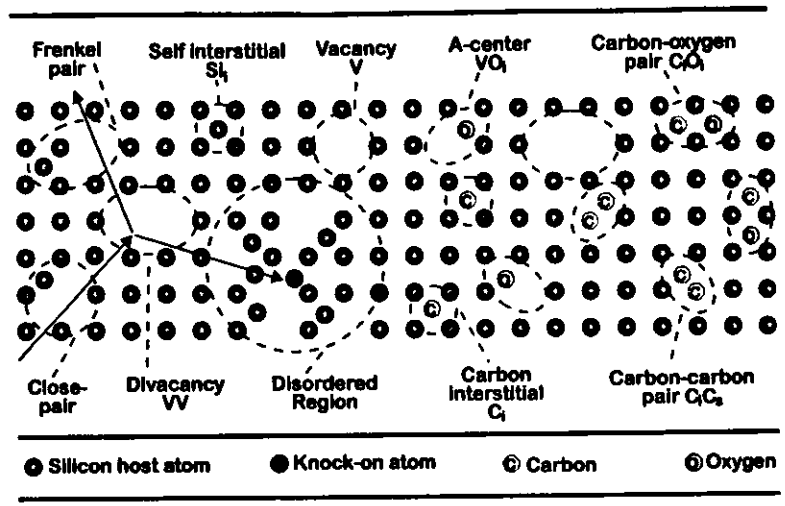

Fig. 3.23 Schematic representation of the crystal defects originating from displacement damage. The time is considered to proceed from the left to the right-hand side, arriving at a situation essentially stable at room temperature.

The final mechanism to form the stable situation takes place with a time constant of the order of several hours at room temperature and is initiated by the migration of the previously released interstitial carbon C_i. These atoms chiefly get trapped at interstitial oxygen atoms (C_iO_i) or substitutional carbon (C_iC_s). Again the formation rate of C_iP_s is relatively small, similar to VP_s [ASO87].

There is still a controversy whether the carbon oxygen complex can be formed in float zone silicon. However, as outlined by C.A. Londos [LON90], the following arguments lead to the decision in favor of the existence of C_iO_i: The composition first proposed for the defect was C-O-V, called the K-center [MOO77]. The formation would therefore require an A-center to react with a migrating interstitial carbon atom. In Czochralski silicon, where oxygen is more abundant than carbon by two orders of magnitude [ZUL89], the created A-centers could compete with the substitutional carbon for the capture of the migrating C_i. Still, in float zone silicon an electrically active defect level similar to the K-center has commonly been observed. Consequently, many authors have assigned the C_iC_s complex to this level, although Song et al. [SO290] have provided strong evidence for a much different position of the C_iC_s levels in the band gap (see Appendix B). It must therefore be argued nowadays that the trapping of C_i at O_i does not require a vacancy, which is in agreement with the structure of the C_iO_i defect proposed in reference [JON92].

3.3.1.2 Classification of Defect Levels

According to their particular influence on the electrical device properties the defects are classified in several ways. Firstly a distinction is made between point defects and clusters, where the latter are

regarded as the stable state of the disordered regions. The cluster model was first proposed to account for the very high minority carrier recombination rates observed after damaging the samples with heavy particles in contrast to electron or photon radiation damage [GOS59]. While the conclusions of that model do only apply to the neutral bulk, their action within the space charge region was not further specified and a distinction from the point defects seemed not to be justified until the recent ideas of B.G. Svensson [SVE91] and S. Watts et al. [WAT96].

Other classification schemes for the defect levels in the gap do also originate from the behavior under a particular experimental condition (Fig. 3.24). The terms defect level and trap, which frequently will be used interchangeably, basically mean the same thing. While the first relates to the chemical origin of the quantum mechanical level, the latter expresses the fundamental ability to remove a free carrier from the conduction or valence band, regardless of the time that the corresponding carrier stays in the trap.

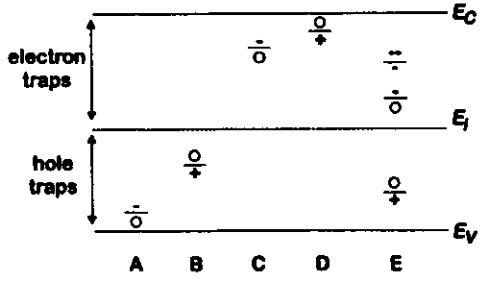

Fig. 3.24 Classification of levels in the forbidden gap.

A: shallow acceptor, e.g. B_s
B: deep donor, e.g. C_iO_i
C: deep acceptor, e.g. VO_i
D: shallow donor, e.g. P_s
E: amphoteric level, e.g. VV

An electrically neutral defect from which an electron can be excited into the conduction band is called a donor. The corresponding energy level is introduced at $E_t = E_C - \Delta E_n$, where ΔE_n denotes the required electron ionization energy. In the thermal equilibrium the ionization state is governed by the Fermi level E_F relative to E_t, i.e., if $E_F > E_t$ the donor is neutral and if $E_F < E_t$ it is positive, which explains the symbols depicted in Fig. 3.24. Likewise, an acceptor level is realized if a free hole can be excited into the valence band leaving behind a negatively charged defect.

Next, a distinction is made between electron and hole traps, which is a misleading name, since all defect levels can trap both carriers, electrons and holes. However, in experiments using a junction space-charge technique (DLTS, TSC, etc.), levels located in the upper or the lower half of the gap can only be detected if the corresponding level has been prepared such that it is occupied with an electron or hole*. Accordingly, the energetic position is measured relative to the conduction and valence band for all electron and hole traps, respectively, regardless whether it is a donor or acceptor. Furthermore, an acceptor level in the lower half and a donor level in the upper half of the gap will sometimes be called shallow since these levels contribute to the space charge in the depleted region†. Among them are the hydrogenic levels introduced by B_s and P_s.

Finally, sometimes amphoteric defects are anticipated exhibiting both donor and acceptor states. Analogous to this are defects with multiple ionization states, being able to bind more than one single elementary charge, see [BLA74]. For most of the experimental conditions the corresponding levels can be treated as being isolated from each other. The only requirement is that the concentrations assigned to those levels should be identical.

Metastability

Since the binding forces between the constituents of a complex defect are basically electromagnetic, it is clear that the minimization of the total energy may sometimes require the structure and the bonds to

* A thorough definition could be made in terms of the emission rates for electrons and holes e_n, e_p. For electron traps $e_n > e_p$ and for hole traps $e_n < e_p$.

† This feature is also related to the rates at which carriers are emitted from the trap level into the conduction or valence band by thermal agitation. The notion shallow is in the literature often used for traps that are ionized at a certain temperature, irrespective of the position of the trap level in the gap. Such a definition is however ambiguous as it depends on temperature, doping, and compensation level.

rearrange if the charge state of the defect under consideration is changed. Moreover, upon reorientation also the quantum mechanical levels are expected to be altered. This so-called metastability has now been observed for a number of defects in silicon and will be illustrated here for the example of the C_iC_s pair, which is one of the prominent defects in irradiated float zone silicon.

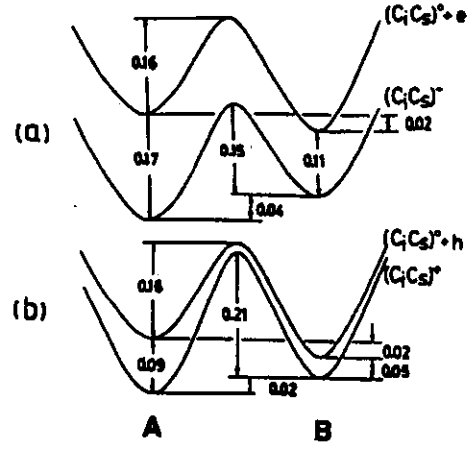

Fig. 3.25 Configurational coordinate diagram of the C_iC_s pair as presented in [SON88]. The defect has two stable configurations, A and B. The figure gives all reorientation and ionization energies for a) the acceptor level, and b) the donor level.

In the work of L.W. Song et al. [SON88] all of the relevant energies and barriers for each of the three charge states of the defect have been determined. As stated there this is believed to be „the first bistable defect in any solid for which such detailed information has been obtained". The situation is sketched schematically in the configurational coordinate diagram in Fig. 3.25. The two stable configurations are assigned an A and a B on the left and right-hand side, respectively. For every charge state the potential energy is plotted as function of a reorientation parameter, which is introduced for purpose of illustration and must not be confused with the distance of the carbon atoms. Fig. 3.25 a) compares the neutral (top) and negative (bottom) defect whereas Fig. 3.25 b) represents the neutral (top) and positive (bottom) defect, i.e., the upper curves are identical in a) and b). In every case will the C_iC_s pair favor the configuration exhibiting the smallest total energy. It is apparent from Fig. 3.25 that this will be state B for the neutral and state A for the positively and negatively charged defect. However, the reorientation requires an energetic barrier to be overcome. Thus, at low temperatures the defect can be frozen in the non-optimum configuration*. For example, if the defect is prepared in state B and is allowed to capture free electrons at low temperature, the reorientation into the favorable state A takes place with a time constant τ_w given by

eq. 3.28 $$\tau_w^{-1}(T) = 1.4 \times 10^{12}\,\mathrm{s}^{-1} \exp\left(-\frac{0.145\mathrm{eV}}{k_B T}\right).$$

Note that the activation energy in this relation, which has been determined by G.E. Jellison in the range from 77 K to 125 K [JEL82], was quoted to be 0.15 eV in Fig. 3.25. Moreover, it is noteworthy that the frequency factor is of the order of the most abundant phonon frequency k_BT/h, indicating a single jump process, compare Appendix C. It will be shown later, how a specific charge state is prepared and which of the configurations are expected under different experimental conditions. In this regard it is mentioned

* Generally, the ratio of defects present in the configurations B and A is given by a Boltzmann term [B]/[A] = $\exp(-(E_B - E_A)/k_BT)$, where E_B and E_A denote the minimum energies of Fig. 3.25. Since the energetic differences $E_B - E_A$ are small (0.04, -0.02, and 0.02 eV for the negative, neutral, and positive charge state, respectively) significant portions of both configurations are anticipated at high temperatures, e.g. room temperature.

here that at 50 K eq. 3.28 yields a characteristic time constant of about 300 s and much larger values at lower temperatures. Further, the defect introduces an amphoteric level scheme into the band gap for both configurations, see Appendix B. The corresponding deep donor and acceptor levels are close to the valence and conduction band, respectively. In Fig. 3.25 the vertical lines indicate the corresponding electronic transitions between the different charge states of the defect.

3.3.1.3 Occupation Statistics for Traps in the Thermal Equilibrium

In a semiconductor the state of thermal equilibrium is adequately characterized by the existence of a unique electrochemical potential for the electrons, also often referred to as Fermi level E_F, which is a constant all over the region of interest. As a parameter within the Fermi distribution function

eq. 3.29 $$F(E) = \frac{1}{1 + \exp\left(\frac{E - E_F}{k_B T}\right)},$$

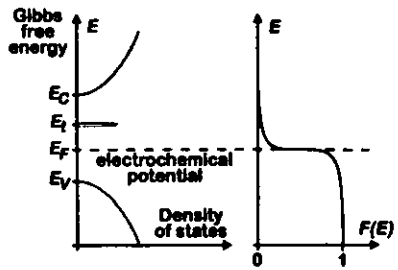

Fig. 3.26 Occupation of energy levels in the thermodynamic equilibrium via the Fermi distribution function.

E_F determines the occupation of all quantum mechanical states at an energy E with electrons (Fig. 3.26). It should be born in mind that E is a Gibbs free energy in the thermodynamic sense [ENG83]. Within the effective mass approximation, and when E_F is not too close to the conduction and valence band energies E_C and E_V (non-degenerate situation), it follows from eq. 3.29 that the concentrations of free electrons in the conduction band, n, and free holes in the valence band, p, are given by (see [SZE81])

eq. 3.30 $$n, p = N_{C,V} \exp\left(\pm \frac{E_F - E_{C,V}}{k_B T}\right).$$

Here, the effective density of states N_C and N_V in the bands are related to the corresponding Density-Of-States (DOS) masses $m^*_{dC,V}$ via

eq. 3.31 $$N_{C,V} = 2\left(2\pi m^*_{dC,V} k_B T / h^2\right)^{3/2}$$

In silicon the constant energy surfaces of the conduction band in k-space are six equivalent ellipsoides. This leads to the expression

eq. 3.32 $$m^*_{dC} = 6^{2/3}\left(m_l^{*2} m_t^*\right)^{1/3}$$

with transverse and longitudinal effective masses m_t^* and m_l^*. On the other hand, the valence band is spherical at $k = 0$ and consists of two degenerate subbands. Accordingly, two different effective hole masses (light and heavy) exist, which combine to

eq. 3.33 $$m^*_{dV} = \left(m_{lh}^{*\,3/2} + m_{hh}^{*\,3/2}\right)^{2/3}.$$

In this expression the spin-orbit split off band has been neglected. Substituting m_t^*, m_l^*, m_{lh}^*, and m_{hh}^* as given by [SZE81] gives the numerical values of the DOS masses relative to the electron rest mass m_0

eq. 3.34 $$m^*_{dC} / m_0 = 1.08 \text{ and } m^*_{dV} / m_0 = 0.549.$$

These values will be used for the evaluation of deep level parameters in this work. It is however known that the data in reference [SZE81] is not consistent regarding the relation between the effective density of states and the intrinsic carrier concentration. This subject has recently been reviewed by M.A. Green, who discusses the dependence of the DOS masses on temperature [GRE90].

Now, consider a trap at the Gibbs free energy E_t and of concentration N_t and let the fractions n_t and p_t of N_t be occupied with electrons and holes such that the totality condition is fulfilled,

eq. 3.35 $$N_t = n_t + p_t.$$

Regarding an arbitrary number of traps this leads to the general definition of the effective doping concentration N_{eff} (shallow doping, e.g. phosphorus, and radiation damage-induced levels),

eq. 3.36 $$N_{eff} = \sum_{donors} p_t - \sum_{acceptors} n_t.$$

N_{eff} thus denotes the total density of electrical charges trapped into defect levels. Application of eq. 3.29 gives n_t and p_t in the thermal equilibrium*

eq. 3.37 $$\{n_t, p_t\} = N_t \frac{1}{1 + \exp\left(\pm \frac{E_t - E_F}{k_B T}\right)}$$

The energy E_t could for instance be determined with an optical technique. However, such data are rarely found in the literature. As will be seen in the following section, electrical techniques like TSC and DLTS measure, either for electron (n) or for hole (p) traps, the enthalpy $\Delta H_{n,p}$ with respect to the conduction/valence band and the corresponding entropy factor $X_{n,p}$. It will be shown that this follows from the thermodynamic relation between the Gibbs free energies and the enthalpies

eq. 3.38
$$E_C - E_t = \Delta H_n - k_B T \ln(X_n) \quad \text{e - traps}$$
$$E_t - E_V = \Delta H_p - k_B T \ln(X_p) \quad \text{h - traps,}$$

where the entropy factors $X_{n,p}$ originate from the total entropy change $\Delta S_{n,p}$ encountered when an electron/hole is excited from the defect into the conduction/valence band†

eq. 3.39 $$X_{n,p} = \exp\left(\Delta S_{n,p} / k_B\right) = \frac{g^*}{g} \exp\left(\Delta S_{vib,n,p} / k_B\right)$$

As outlined in [LOW80], it is only when no complicated vibrational (dynamic Jahn-Teller) interaction exists that the total entropy change can be split into the two parts on the right-hand side of eq. 3.39. They account for the change in the electronic degeneracy of the defect, g^*/g, and the change in the vibrational frequencies of the crystal, $\Delta S_{vib,n,p}$. Therefore, the rearrangement in eq. 3.39 has to be taken with some care, but it is a very useful notation since numerical values of g and $\Delta S_{vib,n,p}$ can often be estimated qualitatively.

The two electronic degeneracy factors g and g^* reflect the number of quantum mechanical electron states equal in energy for the case that the trap is occupied with an electron or hole and for the case that the corresponding carrier is excited from the trap, respectively. While for example the electron bound to a hydrogenic donor is twofold spin degenerate ($g = 2$), there is no degeneracy when the donor is ionized ($g^* = 1$). Correspondingly ionized hydrogenic acceptors also have $g^* = 1$, however, due to the two-fold degenerate valence band a bound hole results in $g = 4$. Regarding complex defects, it is necessary to know the bonding structure which for instance can be ascertained with EPR measurements‡. If the total core charge is an even number the neutral state is usually found to be not degenerate, compare for example reference [BRO82] for VO_i, VV, and VP_s.

By considering the localization of bound carriers around a defect center, it is found in [VEC76] that the change in the vibrational entropy $\Delta S_{vib,n,p}$ due to the ionization of electrons/holes from hydrogenic

---

* It is noted that the Fermi-distibution function is not modified here with the defect electronic degeneracy factors, as is done in [BLA74], rather are those factors incorporated into the correct definition of the free energy of the defect level (cf. Appendix A of [VEC76]). Moreover, according to [BLA74], eq. 3.37 can be serious in error since excited states of the trap level have been neglected. For example, at low temperatures a considerable deviation from eq. 3.37 is caused by the crystal field splitting of the phosphorus ground state.

† The entropy changes can also be regarded as the sum of the corresponding free carrier formation entropy in the bands and the reorientation entropy of the defect [VEC76].

‡ Electron Paramagnetic Resonance.

donors/acceptors like e.g. phosphorus/boron is very close to zero because the considered carrier is delocalized before and after the ionization, so that the vibrational modes of the crystal remain unchanged. Moreover, it is argued there that the ionization of a vacancy from its neutral to either its negative (hole excitation, $\Delta S_{vib,p}$) or positive (electron excitation, $\Delta S_{vib,n}$) state is essentially equivalent to the creation of a free electron-hole pair, which changes the entropy by ΔS_{CV}.

Now, for any defect level successive emission of an electron and a hole creates a free electron-hole pair and the overall effect upon the vibrational lattice modes is indistinguishable from the direct pair creation across the gap. Therefore, it is

eq. 3.40 $$\Delta S_n + \Delta S_p = \Delta S_{vib,n} + \Delta S_{vib,p} = \Delta S_{CV},$$

and accordingly the removal of an electron/hole from the negative/positive vacancy towards the neutral state takes place virtually without change of the vibrational entropy.

Further, following from the thermodynamic definition the entropy change can be shown to simply reflect the variation of the Gibbs free energy with temperature

eq. 3.41 $$\Delta S_n = -\frac{\partial (E_C - E_t)}{\partial T},\ \Delta S_p = -\frac{\partial (E_t - E_V)}{\partial T},\ \text{and}\ \Delta S_{CV} = -\frac{\partial (E_C - E_V)}{\partial T}.$$

Consequently, e.g. the phosphorus donor level as well as the vacancy acceptor level are both virtually pinned to the conduction band. That is, their Gibbs free energy levels relative to E_C vary only weakly with temperature due to the electronic degeneracy factors. In the same sense the boron acceptor level and the vacancy donor level are virtually pinned to the valence band. These considerations may equally be applied to other vacancy related defects. It is this measure which should be taken if no value of $X_{n,p}$ is on hand, rather than fixing the level energy relative to the intrinsic Fermi level E_i, defined below. It will be seen in Section 3.4 that the macroscopic device properties at room temperature, as inferred from microscopic defect parameters obtained at low temperature, crucially depend on the correct notion of the defect level energy.

It is now instructive to calculate the state of occupation of the traps in the electrical neutral bulk as function of temperature. Some extrinsic Debye-lengths away from the contacts, where no electric field exists, the sum of all charges cancels out. Therefore, in the neutral region it is

eq. 3.42 $$0 = (p - n) + N_{eff}.$$

Substituting eq. 3.30 and eq. 3.36 in conjunction with eq. 3.37 into eq. 3.42 yields a unique solution for the Fermi level E_F at any temperature T, given numerical values of E_t and N_t for every trap involved.

Fig. 3.27 shows the result of such a calculation assuming a constant background doping of 10^{12} cm^{-3} substitutional phosphorus atoms (P_s) and equal concentrations of divacancies (VV), A-centers (VO_i), and C_iO_i, all varying from 10^{11} cm^{-3} to 10^{15} cm^{-3} (see caption). In addition, an acceptor level Y arbitrarily placed at 0.2 eV above the valence band, whose concentration is 10% of the previously mentioned defects, was introduced for purpose of illustration and accounts for the type inversion effect. The level parameters $\Delta H_{n,p}$ and $X_{n,p}$ as given in Appendix B were used to determine E_t employing eq. 3.38, except for P_s and Y, whose entropy factors were calculated from the appropriate degeneracy factors, see above. The donor state of the divacancy $VV^{(+/0)}$ has not been taken into account since it would not affect the calculation. It is interesting to note the crossing of the Gibbs free energy of the $VV^{(-/-)}$ level and the A-center around 250 K predicted by this set of level parameters.

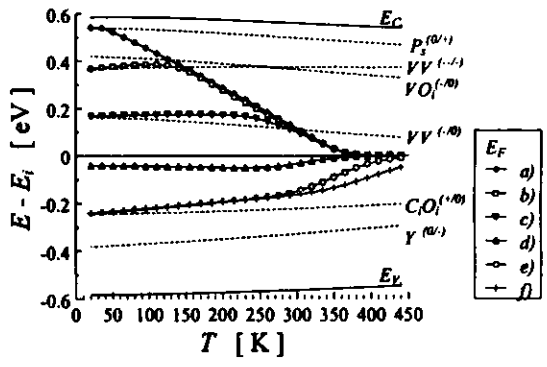

Fig. 3.27 Gibbs free level energies and Fermi level E_F plotted in the band gap as function of the temperature for a fixed amount of phosphorus $[P_s] = 10^{12}$ cm^{-3} and various concentrations of VV, VO_i, C_iO_i, and an acceptor level Y arbitrarily placed at E_V + 0.2 eV (see text).

$[VV] = [VO_i] = [C_iO_i] =$

a) 10^{11}, b) 5×10^{11}, c) 10^{12},

d) 10^{13}, e) 10^{14}, f) 10^{15} cm^{-3},

and $[Y] = 0.1\times$[e.g. VV].

All energies are given relative to the intrinsic Fermi level E_i, which is the position of the Fermi level in the instance of $n = p$. From eq. 3.30 and eq. 3.31 it can be inferred that

eq. 3.43 $$E_i = \frac{E_C + E_V}{2} - \frac{1}{2}k_B T \ln(N_C/N_V) = \frac{E_C + E_V}{2} - \frac{3}{4}k_B T \ln(m^*_{dC}/m^*_{dV}).$$

The common value of n and p is given by

eq. 3.44 $$n_i = (N_C N_V)^{1/2} \exp(-E_g/2k_B T),$$

which is the so-called intrinsic carrier concentration. $E_g = E_C - E_V$ denotes the band gap energy. The notation relative to E_i is a common praxis as most expressions are largely simplified. For example, one can write

eq. 3.45 $$\{n, p\} = n_i \exp\left(\pm\frac{E_F - E_i}{k_B T}\right),$$

so that the mass action law $n\,p = n_i^2$, which always holds in thermal equilibrium, now is verified very easily. Because of the higher accuracy, and in order to comply with the evaluation of level parameters in reference [HAL96], the data for the DOS masses and the temperature dependent energy gap were taken from reference [GRE90] and literature cited there.

The general behavior of the Fermi level that is seen in Fig. 3.27 can be described as follows. At high temperatures E_F settles close to the middle of the band gap because free carriers thermally excited across the gap dominate over the carriers excited from defect levels. Therefore, $n \approx p$, i.e. $E_F \approx E_i$. At intermediate temperatures the semiconductor becomes extrinsic, that is, one type of free carriers is more abundant than the other in order to cancel out the overall electrical charge on the ionized traps. As long as this charge is approximately constant it can be seen from eq. 3.30 that the Fermi level must vary more or less linearly with temperature (N_C and N_V do not exhibit a strong T dependence). Due to this variation, E_F can cross trap levels and change their occupation with electrons for decreasing temperatures. However, at a specific level this will cancel out all electrical charges on the traps and free carriers are no longer necessary to maintain the charge neutrality. At the corresponding temperature the free carriers will freeze and the Fermi level E_F is said to be pinned. These considerations are for example very helpful in understanding TSC spectra that have been obtained after filling trap levels by cooling the sample under zero bias (see Section 3.3.3).

The concentration of free electrons (n), holes (p), and of ionized traps as function of temperature is illustrated in Fig. 3.28. The calculation corresponds to curve a) in Fig. 3.27, which is the case of the smallest total trap concentrations. As argued above, deep levels (VV and VO_i) are completely occupied with electrons at low temperatures due to the Fermi level crossing. Eventually E_F pins at the phosphorus level whose degree of ionization, and consequently also the free electron concentration, levels off around

40 K in this example. At high temperatures, encountered for example within annealing experiments, all deep traps become partly ionized due to the broadening of the Fermi distribution.

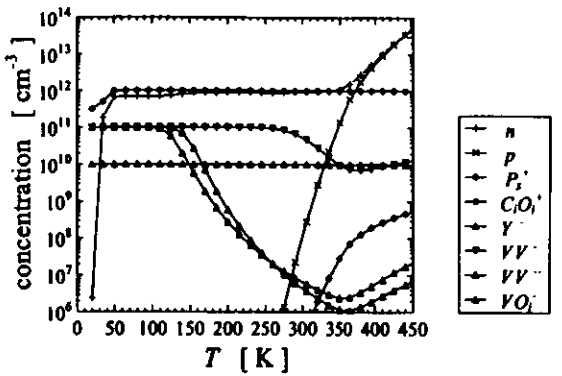

Fig. 3.28 Variation of the free carrier (electrons n, holes p) and ionized trap concentrations with temperature for the case a) displayed in Fig. 3.27. Below 350 K holes are minority carriers and vary with T as n_i. The free electrons cancel out the charge on the ionized phosphorus atoms. Freezing of the free carriers and of the phosphorus ionization (Fermi level pinning) starts around 40 K.

3.3.1.4 Interaction of Traps with the Conduction and Valence Band

So far the processes which change the occupation of a trap with electrons have not been further specified. Fig. 3.29 shows the transitions at work as originally proposed by W. Shockley, W.T. Read [SHO52], and R.N. Hall [HAL52].

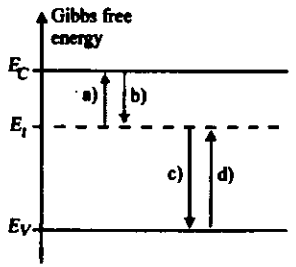

Fig. 3.29 Electron and hole transitions taking place at a trap positioned at an energy E_t in the forbidden gap.

a) electron emission

b) electron capture

c) hole emission

d) hole capture

In this model free carriers can either be captured from (b and d) or be emitted to (a and c) the conduction and valence band. Therefore, the differential equation for n_t is written

eq. 3.46 $$\frac{\partial n_t}{\partial t} = -\underbrace{e_n n_t}_{a)} + \underbrace{c_n n p_t}_{b)} + \underbrace{e_p p_t}_{c)} - \underbrace{c_p p n_t}_{d)}.$$

In this work a transition, typically an emission process, will be denoted by the defect introducing the considered level and the associated initial and final charge state. That is, e.g. $C_iO_i^{(+/0)}$ for the hole emission from the C_iO_i donor level, as compared to $B_s^{(0/-)}$ for the hole emission from the boron acceptor.

The Thermal Emission Rate

The emission rates $e_{n,p}$ and capture coefficients $c_{n,p}$ are introduced to account for the efficacy of the four mechanisms a)-d). In thermal equilibrium the detailed balance principle requires the processes a) and b) as well as c) and d) to operate at the same rate. From this it follows that

eq. 3.47 $$e_{n,p} = c_{n,p} N_{C,V} \exp\left(\pm\frac{E_t - E_{C,V}}{k_B T}\right) = c_{n,p} n_i \exp\left(\pm\frac{E_t - E_i}{k_B T}\right).$$

Here eq. 3.37 has been substituted for n_i or p, and either eq. 3.30 or eq. 3.45 has been employed for the free carrier concentration in thermal equilibrium. From the previous section it is clear that the Gibbs free energy of the trap, E_t, measured with respect to E_C or E_V will vary with temperature when the emission process is accompanied by an entropy change. In order to eliminate this implicit dependence on temperature eq. 3.38 needs to be substituted into eq. 3.47, which yields

eq. 3.48 $$e_{n,p} = X_{n,p} c_{n,p} N_{C,V} \exp\left(-\frac{\Delta H_{n,p}}{k_B T}\right).$$

Since spectroscopic methods like DLTS and TSC measure the dependence of the emission rate on the temperature, it is apparent from eq. 3.48 that the characteristic energy observed is an enthalpy. A trap is fully characterized when both capture coefficients c_n and c_p, which in general are depending on temperature, and either X_n and ΔH_n,or X_p and ΔH_p are determined from the experiment*. The latter parameters are then used to calculate the free energy E_t according to eq. 3.38. For a particular trap level E_t can further be used in eq. 3.47 to calculate both emission rates, for electrons and holes.

Although the previously stated procedure is clearly desirable, most experiments do not measure the capture coefficients. Rather is the following relation employed to define an (emission) cross section $\sigma_{n,p}$ that is assumed to be a constant in the temperature range in which the analysis of the level parameters is performed, (compare eq. 3.48)

eq. 3.49 $$X_{n,p} c_{n,p} = \nu_{thC,V} \sigma_{n,p}.$$

The parameter $\nu_{thC,V}$ is calculated according to

eq. 3.50 $$\nu_{thC,V} = \left(\frac{3 k_B T}{m^*_{dC,V}}\right)^{1/2}.$$

It is noted here that eq. 3.50 must not be confused with the real thermal velocities of the free carriers in the conduction and valence band (see [GRE90]). It is merely introduced analogous to a thermal velocity in order to get a concise equation for the emission rate, which is now obtained by combining eq. 3.31, eq. 3.48, eq. 3.49, and eq. 3.50

eq. 3.51 $$e_{n,p}(T) = B\left(\frac{m^*_{dC,V}}{m_0}\right)\sigma_{n,p} T^2 \exp\left(-\frac{\Delta H_{n,p}}{k_B T}\right).$$

This relation is used for the evaluation of spectroscopic experiments in this work. B is a constant

$$B = 2\sqrt{3}\, k_B^2 \left(2\pi/h^2\right)^{3/2} = 3.256 \times 10^{21}\ \mathrm{K^{-2} cm^{-2} s^{-1}},$$

and $m^*_{n,p}/m_0$ is given by eq. 3.34. Only when the capture coefficient does not depend on the temperature will eq. 3.51 furnish the correct enthalpy value $\Delta H_{n,p} = \Delta H'_{n,p}$.

Electric Field Enhancement of the Emission Rate

In the presence of an electric field the emission rate can be substantially increased. An overview of the subject and a detailed calculation for various non-Coulombic defect potentials has been given by P.A. Martin et al. [MAR81]. Basically three different processes need to be taken into account, either phonon-assisted or pure tunneling and the Poole-Frenkel effect, see Fig. 3.30.

* It is noted here that there is no easy way to measure both emission processes a) and c) for a particular trap separately since one of the emisssion rates always predominates.

For a typical space charge density of around 10^{12} cm^{-3} and a reverse bias voltage of 10 V, eq. 2.5 yields a maximum field strength of the order of 10^3 V/cm. Now, pure tunneling becomes important only at around 10^7 V/cm, and thus is not anticipated in the high resistivity material studied in this work. Still significant effects can arise from phonon assisted tunneling for typical short-ranged deep level potentials, and Poole-Frenkel enhanced emission for long range Coulombic potentials. However, at the smallest electric field strengths only the latter is noteworthy. Therefore, if a field enhanced emission is noticed in this work the corresponding defect level is most likely a shallow donor or acceptor, both leaving a charged defect upon emission of the trapped carrier.

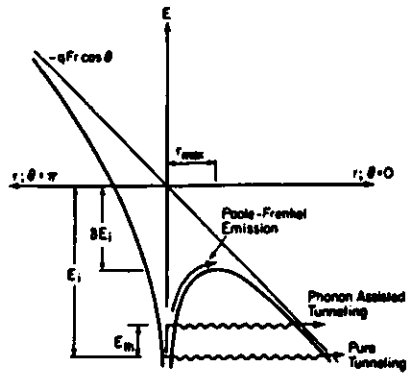

Fig. 3.30 Three mechanisms of field enhanced emission for a Coulombic potential, from P.A. Martin et al. [MAR81].

According to Fig. 3.30 the Poole-Frenkel effect can be regarded as a lowering of the ionization energy E_i, which is equal to $E_C - E_i$ and $E_i - E_V$ for shallow donors and acceptors, respectively. Given a constant electric field F aligned in the - z direction, the radius of the local potential maximum is given by

eq. 3.52 $$r_{max} = \sqrt{q_0 / \left(4\pi\varepsilon\varepsilon_0 F\cos(\theta)\right)},$$

which is around 35 nm for $F = 10^3$ V/cm and $\theta = 0$. The corresponding change in the potential barrier is

eq. 3.53 $$\delta E_i(\theta) = -q_0\sqrt{\frac{q_0 F\cos(\theta)}{\pi\varepsilon\varepsilon_0}},$$

yielding - 7 meV for the above example. A three-dimensional averaging of the spatially varying emission enhancement factor $\exp(-\delta E_i(\theta)/k_B T)$ results in

eq. 3.54 $$e_{n,p}(F)/e_{n,p}(0) = \gamma^{-2}\left[(\gamma-1)\exp(\gamma)+1\right]+1/2,$$

where $\gamma = -\delta E_i(\theta = 0)/(k_B T)$. For $\delta E_i(\theta = 0) = -7$ meV and at $T = 100$ K this gives a factor of 1.4, as compared to the one-dimensional approximation $\exp(\gamma) = 2.3$, which largely overestimates the correct value.

The Capture Coefficients

Depending on the underlying process the capture coefficients should generally exhibit a characteristic variation with temperature. Different modes of energy dissipation are illustrated in Fig. 3.31, for a full discussion see [BRA79]. The multi-phonon process as originally proposed by [HEN77] has been widely applied for capture experiments in large band gap materials. As a main feature the capture cross section would be expected to show an exponential dependence on the temperature, reflecting an energetic barrier E_b that needs to be overcome by thermal activation,

eq. 3.55 $$\sigma = \sigma_\infty \exp\left(-E_b/k_B T\right).$$

However, for deep levels in silicon originating from radiation damage the capture exhibits a much weaker temperature dependence and the excitonic Auger mechanism would appear to be more likely [HAL96].

As outlined in [LOW80] in general the capture cross section σ is small if the emission enthalpy ΔH is large, and vice versa,

eq. 3.56 $$\sigma = \sigma(0)\exp(-\alpha\Delta H),$$

provided the capture mechanism occurs by a smoothly varying process of energy dissipation. The examination of experimental values in [LOW80] suggests that electron traps similar to the A-center are reasonably well described by $\sigma(0) = 4.1\times10^{-13}$ cm^2 and $\alpha = 14$ eV^{-1}. If no experimental value is available σ can crudely be estimated from eq. 3.56.

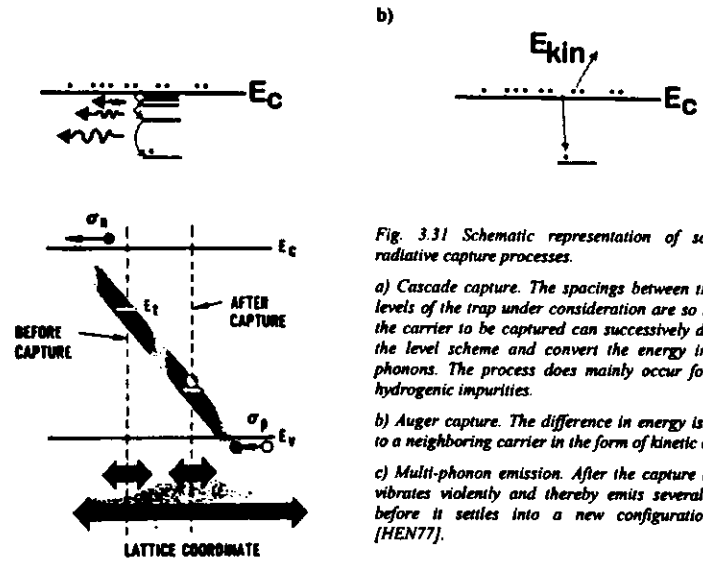

Fig. 3.31 Schematic representation of some non-radiative capture processes.

a) Cascade capture. The spacings between the excited levels of the trap under consideration are so small that the carrier to be captured can successively drop down the level scheme and convert the energy into single phonons. The process does mainly occur for shallow hydrogenic impurities.

b) Auger capture. The difference in energy is imparted to a neighboring carrier in the form of kinetic energy.

c) Multi-phonon emission. After the capture the defect vibrates violently and thereby emits several phonons before it settles into a new configurational state [HEN77].

Basic Equations with Defects

As a groundwork for the following sections it is shown here, how an arbitrary number of traps enters into the basic semiconductor equations in one dimension. Firstly, the continuity equations for electrons and holes are written

eq. 3.57 $$\frac{\partial\{n,p\}}{\partial t} = G_{ext} \pm \frac{1}{q_0}\frac{\partial j_{n,p}}{\partial x} - \{n,p\}\sum_{traps} c_{n,p}\{p_t,n_t\} + \sum_{traps} e_{n,p}\{n_t,p_t\}.$$

The electrical current densities $j_{n,p}$ are composed of drift and diffusion terms. Making use of the Einstein relation, which relates the diffusivity and the zero field mobility $\mu_{0n,p}$, gives

eq. 3.58 $$j_{n,p} = q_0\left(\{n,p\}\mu_{n,p}(E)E \pm \frac{k_B T}{q_0}\mu_{0n,p}\frac{\partial\{n,p\}}{\partial x}\right).$$

Here E denotes the electric field strength and $\mu_{n,p}$ is the field dependent drift mobility, see Appendix A. The total current, which must be solenoidal, is the sum of j_n, j_p, and the displacement current originating from the temporal variations of the electric field E

eq. 3.59 $$j_{tot} = j_n + j_p + \varepsilon\varepsilon_0\frac{\partial E}{\partial t} \quad \text{and} \quad \frac{\partial j_{tot}}{\partial x} = 0.$$

Finally, the Poisson equation is written

eq. 3.60 $$\frac{\partial E}{\partial x} = \frac{q_0}{\varepsilon\varepsilon_0}\left(p - n + N_{eff}\right)$$

employing the general definition of N_{eff} presented in eq. 3.36. Given a set of appropriate boundary conditions, simultaneous solution of eq. 3.57, eq. 3.60 , and eq. 3.46 for every trap under consideration will provide a full characterization of the particular situation studied.

3.3.1.5 The Space Charge Region

When a diode is reverse-biased, a region W devoid of free carriers evolves such that the ionized traps within this region account for the band bending required to maintain the potential difference q_0V (Fig. 3.32). Since this is not a thermal equilibrium condition, eq. 3.37 can not be used to calculate the occupational state of the traps. However, it is $n \approx p \approx 0$, thus capture of free carriers in the space charge region can be neglected and only emission processes of electrons and holes from the traps into the conduction and valence band need to be taken account. Therefore, eq. 3.46 reduces to

eq. 3.61 $$\frac{\partial n_t}{\partial t} = -e_n n_t + e_p p_t$$

In the steady state it is $\partial n_t / \partial t = 0$ and the occupation of a trap with electrons n_t^* or holes p_t^* is

eq. 3.62 $$\left\{n_t^*, p_t^*\right\} = \frac{N_t}{1 + \left(e_n/e_p\right)^{\pm 1}} = \frac{N_t}{1 + \left(\frac{c_n}{c_p}\right)^{\pm 1} \exp\left(\pm 2\frac{E_t - E_i}{k_B T}\right)}.$$

Provided the capture coefficients c_n and c_p are of the same order of magnitude, it is evident that in the first approximation only levels below the intrinsic Fermi level are occupied with electrons, whereas all other levels are empty. In addition it can be concluded that only those acceptor levels located in the lower half of the band gap and only those donor levels in the upper half can contribute to the space charge under these conditions. Thus, in the space charge region the effective doping concentration is approximately given by

eq. 3.63 $$N_{eff,SCR} \approx \sum_{\substack{donors \\ with\ E_t > E_i}} N_t - \sum_{\substack{acceptors \\ with\ E_t < E_i}} N_t .$$

It will be noted that the above statements do not hold at the edge regions λ and μ of the depleted zone, as displayed in Fig. 3.32. These regions are defined for each trap by the intersection of the quasi Fermi levels for electrons and holes, E_{Fn} and E_{Fp}, and the energy level E_t. Within those edge regions the occupation function is given, like in the neutral bulk region, by the thermal equilibrium Fermi distribution, however, replacing the Fermi level E_F by either E_{Fn} or E_{Fp}. An active depletion width W_g can therefore be defined by $W_g = W - \lambda - \mu$.

It will now be studied, which currents flow in the space charge region when the occupation of a single discrete trap relaxes from a previously prepared excited state to the steady state value given by eq. 3.62. The result will be the total external current $j_{tot}(t)$ at a specific time t . Especially no supposition is made here neither for the state of occupation at that time nor for the way by which this state was arrived at. Consider the deep donor level in Fig. 3.32 that changes its state of occupation via emission of holes in the range from x_0 to $x_0 + W_g$. Also electrons will be emitted from this trap level, though at a much smaller rate. Anyway, the treatment that follows also holds without modification for any trap, irrespective of the position in the band gap. Due to the electric field the emitted holes and electrons are swept to the left and right-hand side of this region rather quickly. Hence, the free carrier concentrations n and p can be set equal to zero and consequently the continuity equations for electrons and holes, eq. 3.57, are reduced to

eq. 3.64 $$0 = \frac{1}{q_0}\frac{\partial j_n}{\partial x} + e_n n_t, \quad 0 = -\frac{1}{q_0}\frac{\partial j_p}{\partial x} + e_p p_t .$$

From eq. 3.64 the electron and hole current density j_n and j_p can easily be found by integration, making use of the boundary condition that according to the direction of the electric field no electrons flow through the edge on the left-hand side at x_0 and no holes flow through the edge on the right-hand side at $x_0 + W_g$. That is, the corresponding currents are equal to zero at these points, and subsequently

eq. 3.65 $$j_n(x) = -q_0 e_n n_t (x - x_0) \text{ and } j_p(x) = -q_0 e_p p_t (W_g - (x - x_0)).$$

For the coordinate system chosen, the electric field has a negative value which requires the currents to be negative. In eq. 3.65 it was assumed that the occupation of the trap under consideration is homogeneous throughout W_g. However, no assumption was made about the background doping or the spatial variation of the electric field strength. According to eq. 3.59 the total current can be calculated at any position x as the sum of electron (j_n), hole (j_p), and displacement current (j_{dis}), see Fig. 3.32. j_{tot} is now integrated over x in the region W_g, exploiting that the total current must not vary with distance,

$$W_g j_{tot} = \int_{x_0}^{x_0+W_g} dx \left(j_n + j_p + \varepsilon\varepsilon_0 \frac{\partial E}{\partial t}\right)$$

eq. 3.66
$$= \int_{x_0}^{x_0+W_g} dx \left(j_n + j_p\right) + \underbrace{\frac{\partial}{\partial t}\int_{x_0}^{x_0+W_g} dx\, E}_{=0} + \varepsilon\varepsilon_0 \underbrace{\left(E(x_0)\frac{\partial x_0}{\partial t} - E(x_0+W_g)\frac{\partial (x_0+W_g)}{\partial t}\right)}_{\approx 0}.$$

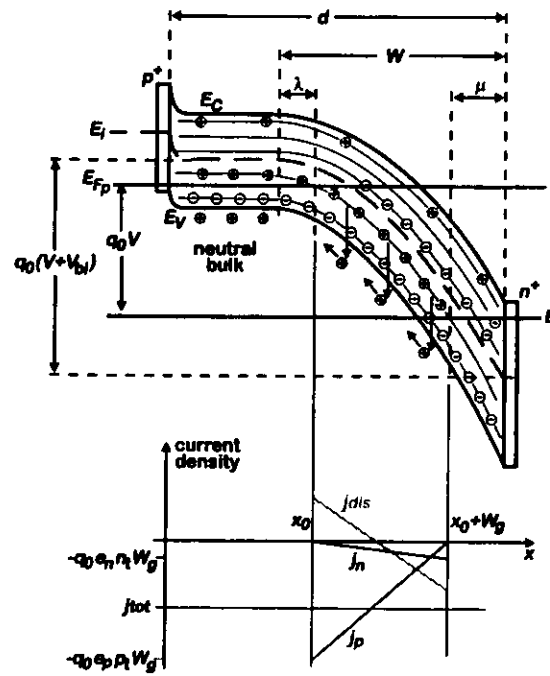

Fig. 3.32 Band structure of a reverse-biased diode with traps at an intermediate low temperature. Some of the deep levels are assumed to be filled due to a preceding filling pulse. Levels from E_C to E_V are: a shallow donor, a deep acceptor, a deep acceptor filled with electrons, a deep donor during emission, and a shallow acceptor. For purpose of illustration the shallow doping has been chosen to be p-type (in analogy to an inverted detector). The currents in the space charge region are:

j_n: electron drift current,

j_p: hole drift current,

j_{dis}: displacement current.

As the external bias is kept constant, the second term on the right-hand side must be equal to zero. However, to isolate this boundary condition the successive order of integration and differentiation of the electric field needed to be exchanged. Since in the general treatment the bounds of the integral have to be considered as function of time, the last term on the right-hand side is introduced. Now, for the situation of a fully depleted detector, the bounds x_0 and $x_0 + W_g$ correspond fairly well to the front and back plane contact, which makes them constant in time. If, on the other hand, one of the bounds corresponds to the edge of the depleted zone and thus is left free to vary, the electric field must have a value close to zero at that position. In conclusion it can be shown that the last term is small compared with the first term on the right-hand side of eq. 3.66, given the active depletion region W_g is larger than the edge regions λ and μ. This can always be achieved by using a reverse bias larger than E_0/q_0, which will be the standard procedure in this work. A more rigorous description of the problem appropriate for small reverse bias voltages is possible in terms of the so-called Grimmeis D-factor, compare [MEI92].

The final result is obtained by performing the integration of the electron and hole currents over distance, using the relations given in eq. 3.65. Bearing in mind the above approximations, the total current at a specific time t can be written in a very general form,

$$\text{eq. 3.67} \qquad j_{tot} = -q_0 \frac{e_n n_t + e_p p_t}{2} W_g .$$

All quantities in this expression are considered to be functions of the time t, i.e., the relation also holds true if the active depleted width W_g is not constant during the emission of carriers.

The dependence of the trap occupation n_t on time can be determined from the differential equation eq. 3.61. A general solution in the space charge region can be found by integration,

$$\text{eq. 3.68} \qquad n_t(t) = n_t^*(t) + \left[\left(n_t(0) - n_t^*(0) \right) - \int_{n_t^*(0)}^{n_t^*(t)} dn_t^{*\prime} \exp\left(\int_0^{t'(n_t^{*\prime})} dt'' (e_n + e_p) \right) \right] \exp\left(-\int_0^t dt' (e_n + e_p) \right).$$

Although the solution is frequently found with an other arrangement of the terms, the above expression is especially suitable for numerical integration, irrespective of whether electron emission, e_n, or hole emission, e_p, dominates. Basically eq. 3.68 says that at any time t, n_t is given by the steady state value n_t^* at that time (eq. 3.62) plus an exponential decay of the initial perturbation at $t = 0$, $n_t(0) - n_t^*(0)$, to which the temporal variation dn_t^* of the steady state value supplies a correction.

Having established all trap concentrations, the active depletion width W_g must be chosen in accord with the boundary conditions of the problem, typically as a function of the reverse bias. For the case of one single trap level with small concentration, such that the effective doping concentration $N_{eff,SCR}$ may be assumed to be constant all over the depleted region W, it is possible to derive expression for λ, μ, and W_g [RAW87]. The separation of the trap energy from the bulk Fermi level is denoted by

$$\text{eq. 3.69} \qquad \Delta_t = \begin{cases} (E_{Fn} - E_t)/q_0 & N_{eff} > 0 \\ (E_t - E_{Fp})/q_0 & N_{eff} < 0 \end{cases}.$$

Moreover, for the sake of conciseness, the effective doping concentration is accounted for by the full depletion voltage V_{dep}

$$\text{eq. 3.70} \qquad V_{dep} = \frac{q_0}{2\varepsilon\varepsilon_0} d^2 |N_{eff,SCR}| - V_{bi} .$$

Then, for $V < V_{dep}$ it is

$$\text{eq. 3.71} \qquad W = d \left(\frac{V + V_{bi}}{V_{dep} + V_{bi}} \right)^{1/2},$$

$$\text{eq. 3.72} \qquad \lambda = d \left(\frac{\Delta_t}{V_{dep} + V_{bi}} \right)^{1/2} = \text{const} , \text{ and}$$

$$\text{eq. 3.73} \qquad \mu = W \left[1 - \left(1 + \frac{\Delta_t - V_{bi}}{V_{dep} + V_{bi}} \right)^{1/2} \right].$$

Now, if significant concentrations of defects are present, which will often be the case in this work, the compensation effect will result in a Fermi level close to the intrinsic Fermi level in the neutral bulk. Thus, the λ-region is more or less meaningless. Also, it is in general not possible to make a reasonable supposition for the built-in voltage V_{bi}. Therefore, if nothing else is stated, the built-in voltage and the edge regions will just be neglected and the following, much simplified expression is used for the calculation of the active depletion width

$$\text{eq. 3.74} \qquad W_g \approx \sqrt{\frac{2\varepsilon\varepsilon_0 V}{q_0 |N_{eff,SCR}|}} .$$

A more detailed expression for the variation of the total current j_{tot} with time would require the temporal variations of the emission rates, i.e., the temperature T as function of the time t, to be further specified. This course will be followed twice, for the thermally stimulation of currents in Section 3.3.3 and for the isothermal current decay in Section 3.3.4.

A special solution is given for the case that the steady state condition specified by eq. 3.62 is reached. That is, eq. 3.68 is considered on a time scale large compared with the characteristic time constant $(e_n + e_p)^{-1}$. The evaluation gives the leakage current related to a specific defect level,

$$\text{eq. 3.75} \qquad j_{tot}^* = -q_0 \frac{e_n e_p}{e_n + e_p} W_g N_t = -q_0 n_i \tau_g^{-1} W_g .$$

The generation lifetime τ_g in eq. 3.75 is given by

$$\text{eq. 3.76} \qquad \tau_g^{-1} = \frac{e_n e_p}{e_n + e_p} \frac{N_t}{n_i} = \frac{c_n c_p N_t}{c_n \exp\left(\frac{E_t - E_i}{k_B T} \right) + c_p \exp\left(-\frac{E_t - E_i}{k_B T} \right)} .$$

Plotting eq. 3.76 as function of E_t gives a very narrow peak around E_i (provided the capture coefficients c_n and c_p are of the same order, compare [SZE85]). This demonstrates that trap levels close to E_i are singled-out by eq. 3.76 as efficient leakage current generation centers. Finally it will be noted that if a set of discrete levels exists in the sample, the total current simply consists of the sum of the currents from each trapping level.

3.3.2 Experimental Set-Up for Microscopic Defect Studies

As outlined in the previous section, the most important parameters of a deep level, the enthalpy and the cross section, are intimately connected with the dependence of the emission rate eq. 3.51 on the temperature. It is therefore common to most spectroscopic methods that a specific electrical property, related to the emission rate, is measured as function of a varying the cryogenic temperature. Since the quality and the reproducibility of the results depends very much on the accuracy of the measured temperature, considerable experimental efforts have often to be made in order to optimize the particular experimental set-up. Thus, in the following, the two cryostats used in this work will be described in detail. All electronics issues have been compiled in the form of block diagrams in Appendix F and will be discussed in the sections dealing with the particular experiments.

3.3.2.1 The I-DLTS and TSC Set-Up

TSC and DLTS measurements can provide valuable spectroscopic information for temperatures as low as 10 K and have therefore been built on top of the 2nd stage cold station of a closed-cycle helium refrigerator which is housed in an evacuated cryostat chamber, see Fig. 3.33. The circular high-purity copper plate (hot-stage) is separated from the coldest point of the refrigerator via sapphire rods (high thermal conductivity). This is a design feature of the original DLTS system and was introduced in order

to overcome the limit arising from the highest temperature allowed for the 2nd stage cold station [COH]. However, because of the relatively small band gap energy this is not a difficulty met with defect studies on silicon*. Indium foils were used at various places to improve the thermal contact. A cylindrical 30 Ω resistor is located in the middle of the hot-stage and provides a heating power of 30 W when the maximum current of 1 A is supplied from the temperature controller. TSC measurements have profited from the hot-stage set-up inasmuch as the large heat capacity of the cold-stations is decoupled by the sapphire rods, allowing for comparatively high heating rates (1 K/s).

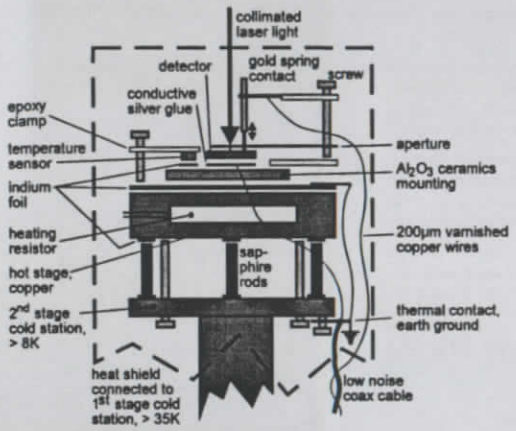

Fig. 3.33 Exploded side view of the mechanical set-up constructed on top of the 2nd stage cold station of a closed-cycle helium refrigerator (CTI Cryogenics Model 22C, operated at 50 Hz). The outer cryostat chamber walls are not shown.

The samples, as mounted on the ceramics support, were clamped very tightly on top of the hot-stage. In order to ensure maximum accuracy of the temperature, the silicon diode sensor was always placed on top of the sample ceramics support in very close proximity to the detector. Although worse than e.g. sapphire, the heat conductivity of the Al_2O_3 ceramics was found to be sufficient to allow fast cooling. Below around 30 K the cooling rate is increasing due to the reduced heat capacity of copper. At temperatures smaller than 20 K the heat conductivity is reduced (e.g. in the sapphire rods) and heat transport to the hot-stage set-up by radiation from the heat shield becomes important. Although the cooling rate is significantly reduced then, temperatures of around 15 K could easily be attained within around one hour.

The electrical connections have been optimized with respect to both the heat leakage from the external connectors and the two main noise sources, namely, microphonic interference, caused by the helium gas pumping at a rate of around 1 Hz, and RF. Very good results were achieved using a soft coax cable for the supply of a positive reverse bias voltage to the rear contact of the detector. A thermal connection at the 2nd stage cold station blocks most of the heat leakage. Moreover, thin copper whisker wires with small thermal conductivity were used to bridge the final distance to the sample connectors. The RF is largely blocked by the cryostat housing, so that an unshielded wire was sufficient for the connection of the low potential side.

For the instances where optical filling was used (I-DLTS), an aperture was placed closely above the sample in order to confine the weakly collimated laser light to a narrow spot. The laser diodes and the collimator were mounted outside the cryostat housing at a fixed distance above the hot-stage and could be adjusted with respect to the X and Y position. The light was transmitted through one of the quartz glass windows of the cryostat. Moreover, an alternate heat shield providing a small passage ($\varnothing \approx 5$ mm) for the light was necessary. The latter is a source of infrared stray light, which adds up to the black body

* Even trap levels close to mid-gap exhibit an emission time constant in the order of ms around 300 K, which is the lower limit for the rate-window in a typical DLTS measurement. Whether a temperature is useful or not does however depend on the particular spectroscopic method in use.

radiation field that exists in the entire set-up due to the relatively warm (> 35 K) heat shield. The corresponding photon energy would according to a first order estimate be able to depopulate occupied trap levels with small ionization energies. This is probably the reason why, using this set-up, the shallow levels introduced by phosphorus and boron could not be detected in TSC measurements, whereas these levels were seen by groups using a liquid helium cryostat which of course provides a more efficient shielding [BAL93,BIG94]. Finally, it is noted that because of its easy and reliable operation the set-up described above has at times also been applied to study the variation of IV and CV curves with temperature.

3.3.2.2 The TCT Set-Up

Also laser-induced current pulse shapes can be studied at lower temperatures, which has recently given significant new insights into the field of radiation-induced deep levels in silicon detectors (see Section 3.3.5). The set-up has to be designed for high frequency operation (ns time resolution) and has to provide a means for laser light illumination on the front and rear side of a cooled detector. Only few set-ups fulfilling these requirements have so far been constructed, basically all by V. Eremin [ER295].

Fig. 3.34 illustrates the principal arrangement and sketches the cooling mechanism. The detector is mounted directly on a high quality circular copper plate which is connected to the earth ground. A bronze clamp is used to establish the front contact and to put pressure on the sample to improve the thermal contact. The temperature sensor again is placed in the direct vicinity of the sample. Heating power is supplied by a circular shaped, approximately 25 Ω heating resistor glued to the bottom side of the copper slab. All electrical connectors and also the two glass fibers for front and rear side illumination are lead into the aluminum housing through a brass tube from the top. At the end of the fibers the cladding has been removed. The unfocused laser light illuminates a spot whose extent can crudely be adjusted by manipulating the distance between the fiber ends and the detector surfaces.

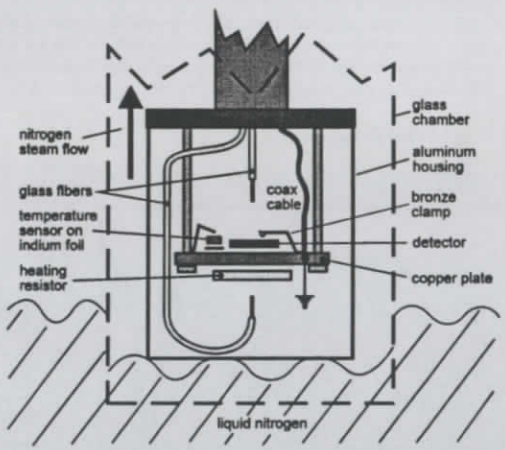

Fig. 3.34 Side view of the mechanical set-up constructed by V. Eremin [ER295] for the study of laser-induced current pulse shapes and transformations of the electric field due to the trapping of the optically generated free carriers into deep traps.

The whole apparatus is then placed into a bottle-like glass chamber whose bottom has been removed (compare Fig. 3.34). A rubber ring is used to tightly close the neck. In order to initiate the cooling process, the level of liquid nitrogen, which is continuously evaporating, is raised. Within the glass chamber the level is regulated by the pressure of the nitrogen steam which passes the aluminum housing and leaves the top valve (not shown) at a limited rate, i.e., the valve actually controls the cooling rate.

3.3.3 Detailed Studies on Damage-Induced Defect Levels Using TSC

The measurement of thermally stimulated currents (TSC) provides a means for the study of defect levels in semiconductor diodes. This technique has been widely used for the investigation of radiation damage effects in silicon detectors since it is easy to set up and, in contrast to the well established C-DLTS technique (compare Section 3.3.4), remains applicable even for the highest fluences [HEI76,BOR91, LI395]. In addition to the TSC spectrum, which is a unique representation of the deep level energies associated with the defects present in the sample, concentrations and spectroscopic information like emission enthalpies and cross sections can be obtained.

The basic measurement scheme is illustrated in Fig. 3.35, and the corresponding electrical set-up used 0in this work is shown in Fig. F.3 of Appendix F. The devices have typically been cooled down under a reverse bias (a). At the lowest temperature (T_{meas}) a sufficiently large forward bias (-100 V) was applied for a certain time (t_{fill} > 1 s), whereby the injection current was limited by a series resistor R (b). Immediately following the trap filling period the reverse bias is reestablished. After an initial delay period (t_d) the temperature is raised at a constant heating rate β and the TSC data are recorded (c). At a certain temperature characteristic of a particular defect level the trapped carriers are emitted into the valence or conduction band, which is detected as a current signal. If not otherwise stated, the heating rate was 220 K in 20 min*, that is, β = 0.183 K/s.

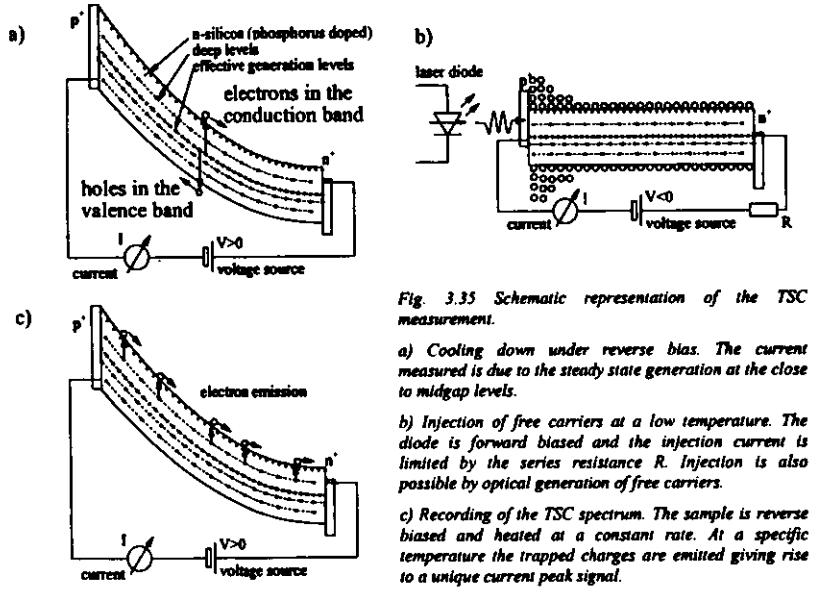

Fig. 3.35 Schematic representation of the TSC measurement.

a) Cooling down under reverse bias. The current measured is due to the steady state generation at the close to midgap levels.

b) Injection of free carriers at a low temperature. The diode is forward biased and the injection current is limited by the series resistance R. Injection is also possible by optical generation of free carriers.

c) Recording of the TSC spectrum. The sample is reverse biased and heated at a constant rate. At a specific temperature the trapped charges are emitted giving rise to a unique current peak signal.

Fig. 3.36 shows typical TSC spectra for a set of reverse bias voltages measured on a device irradiated by a large fluence (Φ_{eq} = 3.82×10^{13} cm^{-2}). Above around 180 K the steady state leakage current predominates the overall signal. The high resolution of this measurement allows an unambiguous assignment of peak labels, which are introduced here in order to facilitate the discussion in the following sections.

* Regarding a discussion of the experimental considerations leading to this choice compare the variation of the heating rate method in Section 3.3.3.7.

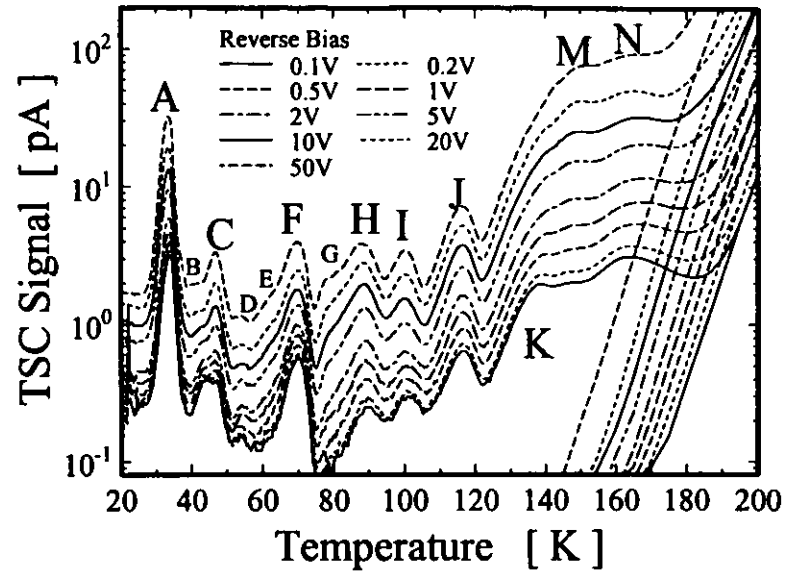

Fig. 3.36. Typical TSC spectra for a detector irradiated by a fluence of 3.82×10^{13} cm^{-2} (device M20708). The filling of the deep levels was achieved by injecting a forward current of I_{fill} = 1.7 mA at T_{fill} = 20 K. A heating rate of β = 0.183 K/s and different reverse bias values were used. The depletion voltage at 294 K was V_{dep} = 82 V after 1 year of room temperature annealing. The various emission peaks have been labeled with a capital letter.

It is noted here that in the early literature, when the TSC method has been used on low resistivity material, it was a common praxis to fill only majority carriers, preferably by cooling the sample in thermal equilibrium under a bias voltage of 0 V [SAH70,BUE72]. However, due to the Fermi level pinning illustrated in Fig 3.27 this is useful only when the deep level concentrations are small compared with the concentration of shallow dopants. For heavily damaged devices fabricated from high resistivity silicon this assumption is not generally valid. Thus, a significant occupation with electrons and holes is often possible only via injection of free carriers either by forward biasing or by means of optical excitation. The initial state of the defects is then not very well defined, and ambiguous results are obtained depending on the filling temperature and the length of the free carrier filling pulse or the ratio between deep center and shallow dopant concentrations, both complicating the derivation of deep level parameters from TSC spectra, especially the concentrations.

Therefore, systematic investigations exploring the dependence of the TSC spectra on the filling conditions and the applied bias voltages will be presented. Methods for the accurate extraction of concentrations will be applied to the predominant peaks found in the spectra. Further, two devices have been subjected to isochronous annealing which allows for the correlation of the evolution of the TSC spectra with simultaneously measured IV and CV data. Finally, deep level parameters will be determined using the variation of the heating rate and the delayed-heating method.

3.3.3.1 Useful Equations for the Analysis of TSC Signals

A very general expression for the currents originating from carrier emission in the space charge region has already been derived, namely eq. 3.67 in Section 3.3.1.5. Suppose a specific deep level whose concentration, energetic position, both capture coefficients, and initial occupation is known. Also let the size of the active volume be specified. Employing the variation of the temperature as function of time

that was realized in a particular TSC measurement, the corresponding current signal to be expected from this trap could be calculated numerically. While this shows the way, how to develop a most general fitting program that deconvolutes the entire TSC spectrum, it gives not much insight into the functional relation between the level parameters and the features of the corresponding TSC peak signal. Therefore, approximate analytical expressions will be derived in the following. It must however be born in mind that considerable simplifications are necessary, especially a temperature independent cross section, compare Section 3.3.1.4.

It will from now on be assumed that one of the emission rates dominates over the other, e.g., $e_n >> e_p$ for traps in the upper half of the band gap (electron traps)*. The positive electrical current measured in the external circuit I_{TSC} is given by the device area A times the simplified expression for the total current density j_{tot} deduced from eq. 3.67,

eq. 3.77 $$I_{TSC}(T(t)) = \frac{1}{2} q_0 A W_g e_{n,p}\{n_t, p_t\} = -\frac{1}{2} q_0 A W_g \frac{\partial \{n_t, p_t\}}{\partial t}.$$

As there is a unique relation between time and temperature, the TSC signal I_{TSC} can be regarded as function of both. Thus, from the rearrangement shown on the right-hand side, which follows from eq. 3.61 when the above presupposition is employed, it can be concluded directly that the integration of the TSC signal from one trap over the time, $Q = \int dt\, I_{TSC}(t)$, is related to the concentration of initially filled traps by [FOR71]

eq. 3.78 $$\{n_t(0), p_t(0)\} = 2\frac{Q/q_0}{A W_g}.$$

Moreover, the time at which the TSC signal has its maximum value can be found from eq. 3.77 by differentiation. It follows that the emission rate at that point obeys the differential equation $\partial e_{n,p}/\partial t = (e_{n,p})^2$. Since the emission rate is a function of the temperature, it is now necessary to assert that $T(t) = T_{max} + \beta \times t$, assuming an essentially constant heating rate β. Application of eq. 3.51 then yields for the temperature T_{max} of the current peak [BUE72]

eq. 3.79 $$T_{max} = \frac{\Delta H_{n,p}/k_B}{\ln\left(\frac{T_{max}^4}{\beta} \frac{B\sigma_{n,p} m^*_{dC,\nu}/m_0}{\Delta H_{n,p}/k_B + 2T_{max}}\right)}.$$

It is clear from this relation that the ionization enthalpy is more or less proportional to the corresponding peak temperature. For silicon, a heating rate of 0.183 K/s, and typical cross section values (10^{-15} cm^2) the enthalpy is in the first approximation given by $\Delta H'_{n,p} \approx 28\, k_B T_{max}$.

Finally, the full expression for the variation of the TSC signal with temperature can be deduced by substituting the concentration of occupied traps given by eq. 3.68 into eq. 3.77,

eq. 3.80
$$I_{TSC}(T) = \frac{1}{2} q_0 A \{n_t(0), p_t(0)\} W_g(T) e_{n,p}(T) \exp\left(-\frac{1}{\beta}\int_{T_{max}}^{T} dT'\, e_{n,p}(T')\right)$$
$$\approx \frac{1}{2} q_0 A \{n_t(0), p_t(0)\} W_g(T) e_{n,p}(T) \exp\left(-\frac{k_B T^2}{\beta\left(\Delta H_{n,p} + k_B T\right)} e_{n,p}(T)\right).$$

In accord with the initial assumptions it has been used in eq. 3.68 that n_t^* is equal to 0 or N_t for electron or hole traps, respectively. It should be noted that eq. 3.80 stays valid even if the depleted width W_g varies, provided the assumptions made in Section 3.3.1.5 hold true. The analytical approximation of the integral in eq. 3.80 has been taken from reference [SI271], where the weak T^2 dependence of the emission rates is neglected. Using that approximation it is further possible to derive an analytical expression for the peak current of the TSC signal

* All equations are written for both electron and hole traps. The reading, also in the {}-brackets, is from the left to the right and from the top to the bottom.

eq. 3.81 $$I_{max} = \frac{1}{2} q_0 A \{n_t(0), p_t(0)\} W_g(T_{max}) \frac{\beta \Delta H_{n,p}}{k_B T_{max}^2} \exp\left(-\frac{\Delta H_{n,p}}{\Delta H_{n,p} + k_B T_{max}}\right).$$

and the peak width at the points of inflection

eq. 3.82 $$\Delta T = 2 k_B T_{max}^2 / \Delta H_{n,p}.$$

ΔT corresponds fairly well to the width at half maximum of the TSC peak. Therefore, a very simple peak analysis would determine the width and the maximum temperature to get $\Delta H_{n,p}$ from eq. 3.82 and an estimate of the cross section $\sigma_{n,p}$ from eq. 3.79. Finally, the concentration of the filled traps can be inferred from the peak height using eq. 3.81. This analysis can give reasonable results only when the peak is clearly isolated. If the TSC signal constructed from the evaluated parameters does not fit the measured data, the investigated peak is likely to be composed of more than one level.

3.3.3.2 Defect Assignment

Radiation damage-induced defect levels have often been accurately characterized, and a compilation of the corresponding data selected from various literature references is given in Appendix B. Also it has been calculated there with eq. 3.79 at which temperature T_{max} the corresponding TSC peak is to be expected. The calculation holds for the heating rate normally employed in this work: β = 0.183 K/s. A straight-forward assignment of the chemical nature to the peaks observed in the TSC spectrum can therefore be done by just comparing the observed peak temperatures with those given in Appendix B. Ambiguities can furthermore be resolved by accounting for the fact that, as outlined in Section 3.3.1.1, there is a limited number of defects which are expected to predominate in neutron-damaged high resistivity silicon, namely VO_i, VV, C_iC_s, and C_iO_i.

Peak	T_{max} [K]	Type	Occurrence	Assignment
A	34.2	*e*	Fig. 3.54 c)	?
B'	39.6	?	Fig. 3.56 b)	?
C	48.0...47.1	*e*	Fig. 3.54 c)	$C_iC_s(B)^{(-/0)}$ ...?
F	70.0	*e*	Fig. 3.54	$VO_i^{(-/0)}$ ($+C_iC_s(A)^{(-/0)}$)
H	89.7	*h*	Fig. 3.56 b)	$VV^{(+/0)}$
H'	91.2	*e*	Fig. 3.54 b)	
I	95.6...99.1	*e*	Fig. 3.54 c)	$VV^{(-/-)}$
J	116.2	*h*	Fig. 3.54 c)	? ($C_i^{(+/0)}$)
J'	120.6	*e*	Fig. 3.54 a) ↑	?
Q	125.8	*h*	Fig. 3.54 c) ↑	?
K	137.3	*h*	Fig. 3.56 b)	?
L	≈ 135	*e*	Fig. 3.40	
L'	146.3	*e*	Fig. 3.54 a) ↑	?
M	147.2	*h*	Fig. 3.54 c)	$C_iO_i^{(+/0)}$
N	164.1	*e*	Fig. 3.54 a)	? + $VV^{(-/0)}$
N_s	167.2	*e*	Fig. 3.54 a)	$VV^{(-/0)}$
N_d	≈ 175	*h*	Fig. 3.54 c)↑	?
R	≈ 180	*h*	Fig. 3.40	

Table 3.9 Compilation of the peaks found in the TSC spectra (heating rate β = 0.183 K/s) and tentative assignment of their chemical nature by comparison of the observed peak temperature T_{max} with the values calculated from literature data according to eq. 3.79 (β = 0.183 K/s), see Appendix B. Some small peaks which were not clearly resolved in the spectra have not been taken into account (D, E, G, etc.). The arrow indicates that the peak emerges during isochronous annealing.

All peaks that have been observed in this work are listed in Table 3.9. In addition to the measured maximum temperatures T_{max} also the type (electron or hole trap) is given which, as will be shown in Section 3.3.3.4, could be inferred from TSC measurements applying special methods of trap filling. Most

peak temperatures were taken from the TSC spectra measured on a weakly damaged device during the isochronous annealing study (Section 3.3.3.6). Whether a certain peak is observed or not depends very much on the particular experimental conditions realized and on the annealing history. Reference is therefore given of the specific figure showing the peak.

The assignment of peak *J* to the C_i donor level is speculative, as the interstitial carbon anneals out rapidly at 300 K. As all samples studied were stored for an extended period at room temperature, $C_i^{(+/0)}$ should not be present in the measurements shown in this work. Further, a lot of peaks were discovered whose origin is not clear. On the one hand, this may be due to the distinct filling processes used for TSC, as compared to DLTS, which might bring to daylight yet unknown metastable defect levels. On the other hand, the absolute sensitivity of current based spectroscopic methods is very high [MEI92]. Thus, these levels may simply have been overlooked in other measurements up to now.

3.3.3.3 Variation of the Depletion Width

The analysis of experimental TSC data is straight-forward only if the width of the active region W_g is a constant, at least during the emission of carriers from the particular trap under study. The assumption to be fulfilled is that the concentration of the corresponding trap needs to be small compared with the total concentration of the remaining space charges. This is however only valid for small irradiation fluences, less than 10^{12} cm^{-2}, regarding typical values of the defect introduction rates (≈ 1 cm^{-1}) and initial doping concentrations ($\approx 10^{12}$ cm^{-3}). The particle fluences that the devices will be exposed to during the operation in a future high-energy physics experiment are however considerably larger. Therefore, the test structures used for TSC measurements in the literature are often found to not accomplish the above presupposition. It will thus be explored here, how the TSC spectrum is deteriorated by high defect concentrations and which way concentrations can still be derived correctly.

Fig. 3.37 shows simulation results of the TSC signal I_{TSC}, of the active depletion width W_g, and the effective doping concentration $N_{eff,SCR}$ as function of temperature, reflecting the major effects encountered in a more or less realistic situation. A certain amount of shallow phosphorus background doping and three filled defect levels, two deep acceptor electrons (F, N) and one deep donor (M) giving rise to the TSC peaks, were taken into account. The occupation of the three traps with electrons and holes as function of time was found from eq. 3.68 by numerical integration. The temperature was assumed to be increasing at a constant rate of 0.183 K/s. Moreover, the trap occupation was taken to be homogeneous, not only in the depleted region, but all over the sample thickness. This assumption is however almost certainly seriously in error since within the neutral bulk region, whose width also turns out to be temperature dependent, the carriers emitted from a particular trap are very likely to be retrapped into deeper levels. Taking the retrapping into account would however render the whole subject almost intractable. The effective doping concentration has therefore been calculated at every temperature by mere summation of all donors (phosphorus, M) occupied with holes, p_t, minus all acceptors (F, N) occupied with electrons, n_t, see eq. 3.36. Finally, the active depletion width was simply related to the effective doping concentration by eq. 3.74. In conclusion the peaks are found to be distorted due to the contraction and widening of the depleted zone during the emission. The deterioration is found to be enhanced for higher defect concentrations. It is worth noting that the effective doping concentration may even change the sign, i.e., the junction of the diode may switch from the front to the back plane and vice versa. Although the trap concentrations have intentionally been chosen to reflect this feature, the degenerate shape of some TSC peaks frequently observed on heavily damaged samples is concluded to arise from this phenomenon.

The deformation of peak shapes due to the variation of the depletion width can most instructively be illustrated by the reverse bias dependence of TSC spectra, as for instance the measurements performed on a weakly damaged device shown in Fig. 3.38 a). It is apparent from the saturation of the peak heights that the detector is more or less fully depleted for the largest reverse bias chosen. In the other curves, the temperature at which the current has its maximum appears to be shifted (peaks M and N). Consequently, the evaluation of level parameters, especially those derived from the peak shape or position, would be highly questionable. On the other hand, it is clear from the measurement obtained at 100 V that a large bias voltage can lead to excessive leakage currents spoiling the spectrum. Therefore, the experimenter is often forced to carefully chose a smaller reverse bias.

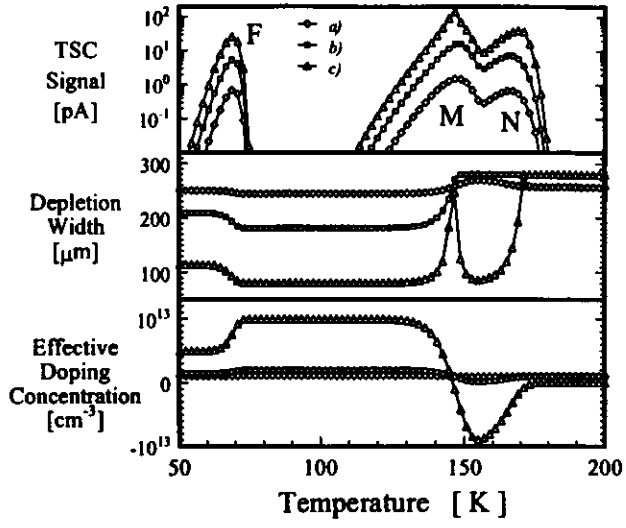

Fig. 3.37 Simulated TSC spectra and corresponding variation of the depletion width and the doping concentration during the measurement (heating rate 0.183 K/s, bias 50 V, area 0.25 cm², and thickness 280 μm). Level parameters (ΔH ,σ) of the peaks F, M, and N correspond to $VO_i^{(-/0)}$, $C_iO_i^{(+/0)}$, and $VV^{(-/0)}$, respectively.

N_P, $n_{t,F}$, $n_{t,M}$, $n_{t,N}$ were chosen to be

a) 10^{12} cm^{-3}, 5×10^{10} cm^{-3}, 2×10^{11} cm^{-3}, 10^{11} cm^{-3}

b) 10^{12} cm^{-3}, 5×10^{11} cm^{-3}, 2×10^{12} cm^{-3}, 10^{12} cm^{-3}

c) 0, 5×10^{12} cm^{-3}, 2×10^{13} cm^{-3}, 10^{13} cm^{-3}.

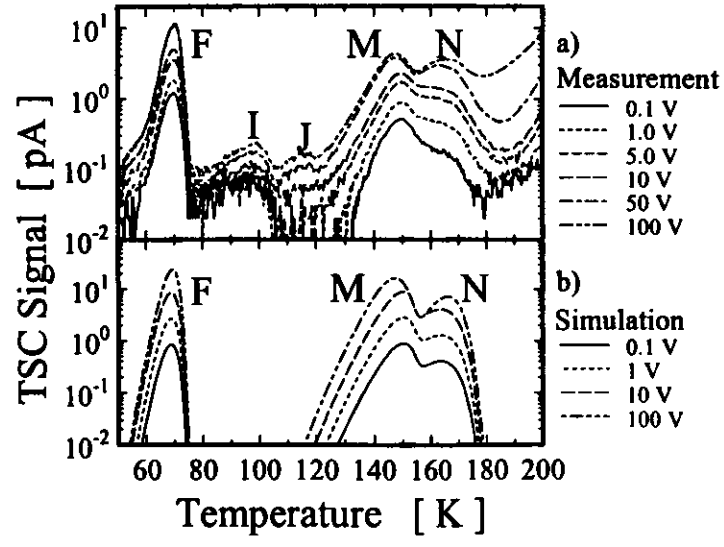

Fig. 3.38 a) Reverse bias dependence of the TSC spectra measured on a detector that was exposed to a neutron fluence of 9.76×10^{11} cm^{-2} (device M20609). Filling of the deep levels was achieved by injecting a forward current of 1.75 mA at 50 K for 30 s (heating rate 0.183 K/s). The full depletion voltage as determined from the room temperature CV curve was 72 V at the time of the measurement.

b) Corresponding results of a simulation reproducing all relevant features of the measurement, compare Fig. 3.37. N_P, $n_{t,F}$, $n_{t,M}$, $n_{t,N}$ were chosen to be 10^{12} cm^{-3}, 1.5×10^{12} cm^{-3}, 2×10^{12} cm^{-3}, and 10^{12} cm^{-3}, respectively.

The corresponding simulation results shown in Fig. 3.38 b) confirm that the shift of the peaks M and N can be explained in terms of the variation of the depletion width. From the concentrations chosen for the shallow doping and the three traps (see caption) it can be inferred that $N_{eff,SCR}$ changes from a positive value to almost zero during the emission of the hole trap M. Accordingly, the depletion width is growing, resulting in a TSC peak signal shifted to higher temperatures. Contrary, the depletion width shrinks during the emission of the electron trap N, which shifts the peak to lower temperatures. It is only when the applied reverse bias is sufficient to always fully deplete the device (100 V) that an undistorted peak shape is observed.

In conclusion, an overall reasonable agreement between measurement and simulation is found, justifying the models and assumptions of the computation. Therefore, in the following a procedure derived from those models will be presented, which can be used to obtain the concentrations of initially filled traps from TSC spectra measured on devices that not always were in the fully depleted state. At every temperature the effective doping concentration $N_{eff,SCR}$ is assumed to be given by the corresponding value $N_{eff,RT}$, determined at room temperature from a CV measurement, plus the concentrations of all hole traps and minus the concentrations of all electron traps still being occupied at that temperature, i.e., all traps exhibiting an emission peak at a higher temperature. On top of a particular peak the concentration of the very trap causing the peak is accounted for by the half of its own concentration, e.g., $N_{eff,SCR} = N_{eff,RT} - n_{t,N} + n_{t,M} - n_{t,F}/2$ on top of peak F in Fig. 3.38. The active depletion width W_a then is calculated from $N_{eff,SCR}$ by eq. 3.74. Finally, the initially filled concentration of the trap under consideration is given by eq. 3.78. The peak integrals Q of every trap are required as input data. Also it must be known, whether the peaks arise from electron or hole traps, which can however be guessed from TSC spectra when special modes of deep level filling are studied (see next Section). As the procedure involves all peaks of the spectrum at the same time, the solution can only be found by an iterative numerical calculation.

Application of the above program for the reconstruction of trap concentrations from the simulated TSC curves presented in Fig. 3.37 demonstrates an overall accuracy of better than 20% (Table 3.10). However, for high defect concentrations the algorithm does not find a unique solution, rather is there an unresolved ambiguity as to whether a small peak is originating from a small trap concentration or a small depletion width. Consequently, for heavily damaged devices ($\Phi_{eq} > 10^{13}$ cm^{-2}) there is no evident way to determine the concentrations of initially filled defects.

Table 3.10 Ratios between the reconstructed concentrations and the actual values used for the simulation a)-c) in Fig. 3.37.

Peak	a)	b)	c)
F	0.920	0.995	-
M	1.007	1.083	-
N	0.852	0.845	1.174

Regarding a device irradiated to 3.82×10^{13} cm^{-2}, the peak heights have been evaluated and are plotted as function of the reverse bias in Fig. 3.39 (compare the spectra displayed in Fig. 3.36). Bias voltages higher than 50 V could not be applied due to the resulting unstable current signals reflecting a breakdown behavior. A more or less square root like bias dependence is observed in Fig. 3.39 in agreement with a regular evolution of a space charge region and homogeneous trap distributions. In respect to small reverse bias voltages, all peak currents are significantly larger than would be expected from the simple dependence on the width of the active depletion layer. Therefore; it must be concluded that the current flow arises from

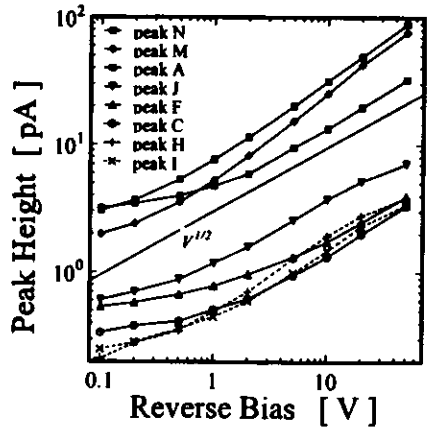

Fig. 3.39 Peak height as function of the reverse bias evaluated on the TSC spectra presented in Fig. 3.36 (device M20708, $\Phi_{eq} = 3.82\times10^{13}$ cm^{-2}).

diffusion and recombination processes, extensively studied in the literature in terms of the thermally stimulated conductivity [BRA79]. The concentrations can only be evaluated from such spectra if very much simplified physical models are assumed, being subject to the criticism raised in reference [BRA79]. However, for heavily damaged devices trap concentrations can hardly be determined anyway. Thus, for such devices the highly resolved spectra obtained at small reverse bias voltages, which appear to supply more information compared with spectra measured under larger bias values (see. Fig. 3.36), are a good choice to monitor the defect levels.

3.3.3.4 TSC Spectra for Various Irradiation Fluences and Filling Conditions

A set of 7 ion implanted detectors, listed in Table 3.11, has been used in order to study the TSC spectrum at various irradiation fluences ranging from 10^{11} cm^{-2} to 10^{14} cm^{-2}. Different modes of electrical trap filling were examined and will be presented in separate sections,

- cooling down under zero bias,
- switching to zero bias at low temperature, and
- injecting a forward current of around 1.7 mA at 25 K, 50 K, and 80 K.

The focus will be on the qualitative understanding of the different trap filling processes which is gained by a thorough discussion of the spectra. Chief considerations will be the decision, whether a particular peak arises from an electron or hole trap and the determination of defect concentrations.

If not otherwise indicated, leakage currents have been subtracted. The corresponding data were taken from dedicated TSC measurements obtained after intentionally omitting deep level filling*. This practice ensures reproducible thermal conditions, which is of prime importance as the leakage current exhibits a strong exponential dependence on the temperature. Data gathered during the cooling of the sample is, regarding the measured sample temperature, frequently found to be shifted with respect to the subsequent TSC scan. Making use of these data can therefore introduce large systematic errors. In order to allow for an easy comparison, the reverse bias was always chosen to be 50 V and the samples were always heated at a rate of 0.183 K/s.

Table 3.11 List of the devices exposed to different amounts of neutron radiation and studied with TSC. Except for M10610 all devices were irradiated at the PTB Be(d,n) source, compare Table 3.1.

Device	$V_{dep,0}$ [V]	d [µm]	Φ_{eq} [cm^{-2}]	inverted ?	RT anneal [days]	V_{dep} at TSC [V]
M20610	80.0	280	9.01×10^{10}	no	460	85.1 V
M10912	86.6	274	2.99×10^{11}	no	410	82.3 V
M20609	83.1	280	9.76×10^{11}	no	420[a)]	71.5 V
M10610	85.7	274	4.26×10^{12}	no	470	37.3 V
M20611	88.1	280	9.67×10^{12}	no	420	17.6 V
M20708	75.4	280	3.82×10^{13}	yes	365	81.9 V
M20710	81.7	280	8.96×10^{13}	yes	250	≈ 250 V

a) +90min 50°C

Cooling Down Under Zero Bias

First the filling of defects by cooling down under zero bias will be discussed (Fig. 3.40). The general behavior can readily be explained in terms of the Fermi level. For the two devices irradiated to the lowest fluence the obtained spectra look similar and the magnitude of the peak currents scales with the corresponding Φ_{eq}. As indicated by Fig. 3.27, for larger defect concentrations the Fermi level pins at some deep trap during cooling down under zero bias, e.g. level N in the case of the device M20609

* For the device M20710 the leakage current was not measured separately. Therefore the exponential temperature dependence of the steady state current at high temperatures was used to extrapolate the leakage current towards lower temperatures.

irradiated to a fluence of around 10^{12} cm^{-2}. Finally, at very high fluences (>10^{13} cm^{-2}), there appears to be one sole trap, peak R, located close to the middle of the gap that is filled under these conditions. This signal might be related to deep traps at around 0.5 eV observed in studies using TCT, see Section 3.3.5. It must however be born in mind that the peak is found only after subtracting a significant leakage current. From the corresponding data obtained on the devices M20708 and M20710 at around 180 K one may have objections to the validity of this method.

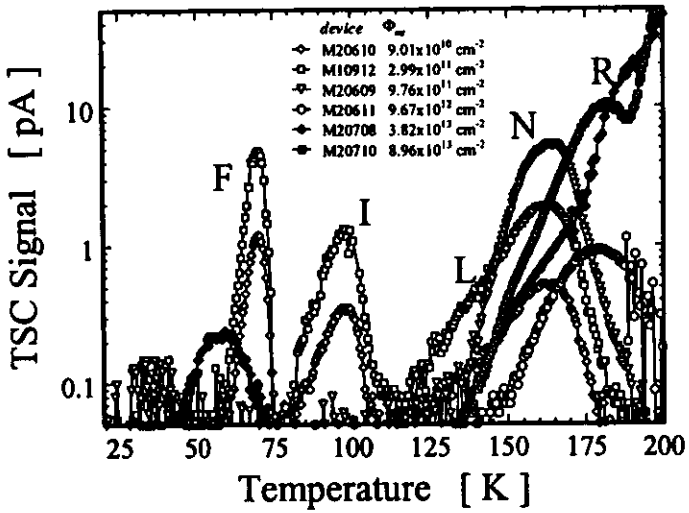

Fig. 3.40 TSC spectra measured after filling defects by cooling down under 0 V bias (thermal equilibrium). A heating rate β of 0.183 K/s and reverse bias voltage of 50 V was used, except for M20710 (80 V). For better clarity of the figure the M20710 curve has been shifted by 0.1 pA. The leakage current has always been subtracted, for more details compare Table 3.11.

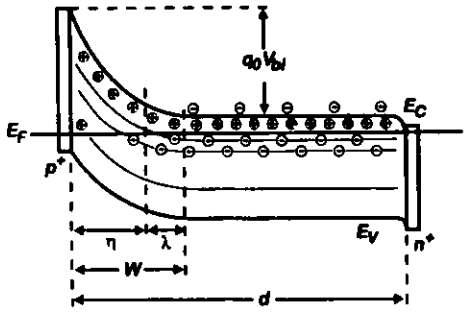

Fig. 3.41 Schematic representation of the bands and the trapped charges after the diode has been cooled down to low temperature under zero bias for the case that no Fermi level pinning at one of the defect levels under investigation has taken place. Except for the shallow donor close to the conduction band the levels in the upper and the lower half of the gap are assumed to be acceptors and donors, respectively. The built-in voltage V_{bi} is close to the upper limit (≈ E_g/q_0). In a more rigorous treatment the λ region would have to be defined for each defect level individually.

This mode of defect filling is suitable only for very low defect densities. However, it has the advantage of only filling majority carrier traps. Moreover, complete filling of a trap is achievable, provided the Fermi level crosses the corresponding level. Therefore, the concentrations of the electron traps F, I, and L+N (L is only a small contribution to N) can be determined very accurately from the spectra measured on the devices M20610 and M10912 by integrating the total charge emitted within those peaks (eq. 3.78). It is however necessary to exactly determine the active depletion layer width W_g, which is

different from the device thickness because the diodes were not biased to full depletion during the measurement, compare Fig. 3.32. In addition, the filling with electrons does not take place in the vicinity of the p$^+$-n junction because in this region a layer of width η virtually denude of free carriers exists due to the built-in voltage V_{bi}, see Fig. 3.41.

Fig. 3.41 illustrates how numerical values of η can be estimated. If no Fermi level pinning occurs, the built-in voltage V_{bi} approaches E_g/q_0 at low temperatures*. Given the charge trapped in the λ region is small compared with the effective doping concentration $N_{eff,SCR}$, the width W at zero bias can be calculated from eq. 3.71, giving approximately 30 μm. Moreover, for traps close to the conduction band the λ region is close to zero and becomes as large as 20 μm for a level in the middle of the gap, resulting in an average value of 10 μm for λ. Therefore an average value of η = W - λ = 20 μm has been used for the devices M20610 and M10912 in Table 3.12. Contrary, for the device M20609 the Fermi level pins at peak N (λ = 0) and according to the position of the level $VV^{-/0}$ in the gap, the built-in voltage at low temperature is approximately given by E_g-0.4 eV. It can be seen that then an edge region of around η = 30 μm has to be taken into account. Now, a total active width was defined by the particular region depleted by a reverse bias of 50 V according to the approximate expression eq. 3.74, minus η, minus the average width of the λ-region. The trap concentrations and the active depletion width as function of the temperature were determined by the iterative procedure introduced in Section 3.3.3.3, and the results are listed in Table 3.12.

Table 3.12 Evaluation of the concentrations of the peaks F, I, L+N filled by cooling down under zero bias. The effective doping concentration $N_{eff,ST}$ was derived from the depletion voltage measured at room temperature (compare Table 3.11). Special care was taken for the accurate determination of the active volume (see text). The introduction rates g_t were calculated using the fluence values given in Table 3.11.

Device	$N_{eff,ST}$ [10^{12} cm^{-3}]	η [μm]	$W(50\ V) - \eta - \lambda$ [μm]			n_t [10^{12} cm^{-3}]			g_t [cm^{-1}]		
			F	I	L+N	F	I	L+N	F	I	L+N
M20610	1.43	20	211	203	192	0.0910	0.0637	0.185	1.01	0.707	2.05
M10912	1.44	20	244	244	210	0.292	0.207	0.594	0.977	0.691	1.99
M20609	1.20	30	250	250	250	0	0	1.04	–	–	> 1.07

While introduction rates for all three peaks can be given in the low fluence range (devices M20610 and M10912), only a lower limit is available for the composite peak L+N for the case of the device M20609. Regarding the latter it is known that due to the Fermi level pinning the concentration of all trapped electrons, n_{L+N}, must equal the effective doping concentration measured at room temperature, $N_{eff,ST}$. Therefore, the accuracy of the above calculation can be assessed. The observed difference of about 15% can in part be explained by the implicit assumption made in Table 3.12 that the device is fully depleted during all of the emission period. This cannot be true as the depletion voltage measured at room temperature is more then 20 V larger than the applied reverse bias. The corresponding systematic error introduced by the temperature dependent width of the depletion layer is however assumed to be smaller for the other two devices. Here it is reassuring to note that the data found for M20610 and M10912 agree to within 3%, which is comparable to the accuracy of the irradiation fluence. In all cases the active area was assumed to be 0.275 cm^2 (floating guard ring) which might be in error since the value was obtained on an undamaged device at room temperature in the state of full depletion (see Section 2.4.4). The overall error can be estimated conservatively to be of the order of 20%.

Finally, the averaged data obtained on M20610 and M10912 can be discussed in the light of the chemical composition of the defects producing the TSC peaks F, I, and L+N (Table 3.13). First of all it is clear that, according to the findings of [SO290], peak F is a superposition of the well known A-center VO_i and the bistable state (A) of the carbon pair C_iC_s anticipated when the defect is allowed to capture electrons at sufficiently high temperatures (see Section 3.3.1.2). The bistable state (B) of this defect can only be prepared when the sample is cooled down under reverse bias or when minority carriers are injected at low temperature (see the following sections). Therefore, only the sum of the introduction rates of the two defects can be given. As argued in reference [FRE96], peak N is composed of the transition

* The small contribution from the ionization energies of phosphorus and boron has been neglected.

from the singly negative to the neutral divacancy and an additional unknown defect (compare Section 3.3.3.6). The introduction rate of the unknown component can be estimated to be the difference between L+N and I, which is 1.32 cm^{-1}. It is however assumed here that there is a one to one relation between the concentration of divacancies seen in peak I and the fraction within peak N. Recently Svensson and coworkers have provided evidence for the model that due to the influence of the lattice strain on the divacancy bond switching frequency the signal of the transition from the doubly charged to singly charged state is reduced compared with the deeper level $VV^{(-/0)}$ [SVE91,SVE93]. Consequently, the introduction rate given for peak I should be considered as a lower limit for the divacancy. Accordingly, 1.32 cm^{-1} is the upper limit for the introduction rate of the unknown component in peak N. Accounting for the small contribution given by peak L would further reduce this value.

Table 3.13 Best values of the introduction rates and the supposed chemical composition of the peaks studied. Following the irradiation, the devices were stored for around 400 d at room temperature.

Peak	Average Introduction Rate g_t	Chemical Composition
F	0.993 cm^{-1}	$VO_i^{(-/0)} + C_iC_s\ (A)^{(-/0)}$
I	0.699 cm^{-1}	$VV^{(-/-)}$
L + N	2.02 cm^{-1}	L = ?, N = ? + $VV^{(-/0)}$

Switching to Zero Bias

Cooling down the samples under 50 V reverse bias and switching to 0 V bias at 25 K results in the TSC spectra displayed in Fig. 3.42. For the weakly damaged samples the filling process can be visualized as follows. On a very short time scale after switching to zero bias a quasi-equilibrium condition will prevail stabilized by the fastest processes active, namely, capture and emission from the shallow phosphorus level. Evidently, as can be inferred by analogy from the calculations presented in Figs. 3.27 and 3.28, at 25 K the number of free electrons is already significantly reduced with respect to the total phosphorus concentration. On a larger time scale the remaining free carriers will then be shared according to the instantaneous trapping rate $c_n p_t$ of each electron trap present. Due to the trapping of electrons the phosphorus becomes compensated and the free carrier concentration n approaches zero. Initially all electron traps are empty, i.e., in the beginning of the process p_t equals N_t, but then levels off as does n. Hence, the trapping rate is time dependent and the mathematical analysis of the filling process is complicated. It is however qualitatively clear that the free carriers will predominantly go into the most abundant traps and into the levels exhibiting the largest capture cross sections. The latter are mainly found for small ionization enthalpies, compare eq. 3.56, i.e., the peaks on the left-hand side of the spectrum are filled predominantly.

Based on these arguments the following conclusions can be drawn from the data on the not inverted samples (M20610, M10912, M20609, $\Phi_{eq} < 10^{12}$ cm^{-2}) presented in Fig. 3.42. The peaks I and L are not filled here, in contrast to Fig. 3.40. Therefore, the corresponding capture cross sections are assumed to be rather small. It must however be born in mind that some of the deep levels, for example those of the divacancy, arise from motionally averaged states [SVE92]. It is thus not clear, whether the quantum mechanical states corresponding to peak I and L do actually exist at 25 K.

Moreover two new peaks, A and C, are observed to appear (see Fig. 3.42). These electron traps are however not seen in Fig. 3.40 although in respect to the $N_{eff,RT}$ value and defect concentrations given in Table 3.12 it is clear that after filling of peak F during cooling down under zero bias enough free carriers should be left, at least for one of the devices (M20610, M10912), to fill C and A. It is therefore argued here that peak A exhibits a similar metastable behavior as does peak C. The emergence of peak C under these filling conditions is in agreement with the previous assignment to the bistable state (B) of the C_iC_s pair. Peak C would be awaited to occur here because in the space charge region state (B) is the stable configuration which is frozen during the cooling under reverse bias. Accordingly, peak F is only due to

the A-center VO_i, i.e., in contrast to the 0 V cooling no C_iC_s in the state (A) is expected to add to the overall peak signal here.

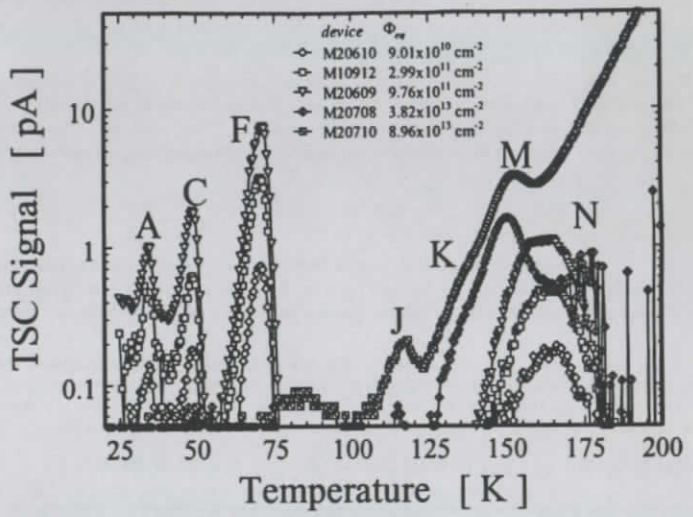

Fig. 3.42 TSC spectra measured after filling defects by cooling down under reverse bias and switching to zero bias at T_{fill} = 25 K (M20710 T_{fill} = 20 K) for 30 s. A heating rate β of 0.183 K/s and reverse bias voltages of 50 V was used, except for M20710 (80 V). The leakage current has always been subtracted, for more details compare Table 3.11. The data measured on device M20611 was omitted for purpose of clarity of the plot.

Concerning the inverted devices (M20708 and M20708, $\Phi_{eq} > 3\times10^{13}$ cm^{-2}) free holes rather than free electrons are captured at the filling temperature. In addition to the peak M, previously assigned to the donor level of C_iO_i, also the peaks J and K are thus clearly identified as hole traps. It will be noted that the negative space charge required for the hole trap filling does actually exist at low temperatures. Models requiring thermal activation for the negative charges to be established, e.g. by a leakage current, would therefore contradict the results found in Fig. 3.42.

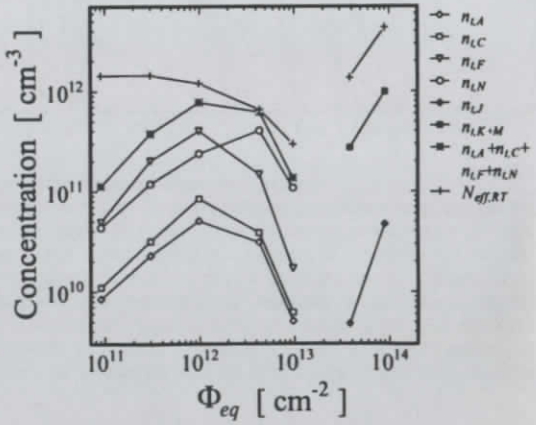

Fig. 3.43 Concentration of the filled defects evaluated from the spectra shown in Fig. 3.42.

Finally, the evaluated concentrations of filled defects are plotted versus the irradiation fluence in Fig. 3.43. The previously mentioned iterative procedure has been used to determine the active depletion layer, however, neither an edge region η during the filling nor a λ region during the measurement has been taken into account as

no reasonable assumption could be made about these quantities. As therefore the actual active depletion layer width is likely to be smaller than the assumed volume, all quoted concentrations are expected to be underestimated. Fig. 3.43 illustrates that at low fluences Φ_{eq} the concentrations of filled electron traps are increasing proportional to Φ_{eq}, as expected. At around 2×10^{13} cm^{-2} inversion of the sign of the space charge takes place, i.e. $N_{eff,ET} \approx 0$, and therefore one observes a related drop of the filled electron trap concentrations on the left, followed by an increase in the filled hole trap concentrations for larger fluences on the right-hand side.

As far as the devices M20610 and M10912 are concerned, the trap concentrations normalized to the fluence are more or less equal (Table 3.14). It is only for the device M20609 that the normalized concentrations level off significantly although the amount of free electrons available for trap filling as suggested by $N_{eff,ET}$ is not exhausted by the sum of all filled electron traps, see Fig. 3.43. This is however due to the previously mentioned freezing of the ionization of the phosphorus level at 25 K. It is therefore reasonable to average the data obtained on M20610 and M10912 in order to extract defect introduction rates, see Table 3.14. Now, the sum of C_iC_s (peak C) and VO_i (peak F) is found to be 0.115 cm^{-1} + 0.610 cm^{-1} = 0.725 cm^{-1} which is around 30% smaller than the more reliable data obtained in Table 3.13 (peak F). It must be concluded that this difference reflects the error in the assumed active volume. The ratio between the concentrations of C_iC_s and VO_i as given in Table 3.14 should however in the first approximation not be affected by the active volume and is therefore estimated to be $[C_iC_s] / [VO_i]$ = 0.19 for the particular samples studied here.

Table 3.14 Fluence normalized concentration of the electron traps filled by switching to zero bias at 25 K.

Peak	Evaluated Concentrations Normalized to the Irradiation Fluence				Chemical Composition
	M20610	M10912	M20609	(M20610+M10912)/2	
A	0.094 cm^{-1}	0.076 cm^{-1}	0.052 cm^{-1}	0.085 cm^{-1}	?
C	0.123 cm^{-1}	0.106 cm^{-1}	0.086 cm^{-1}	0.115 cm^{-1}	C_iC_s $(B)^{(-/0)}$
F	0.546 cm^{-1}	0.674 cm^{-1}	0.411 cm^{-1}	0.610 cm^{-1}	$VO_i^{(-/0)}$
N	0.480 cm^{-1}	0.395 cm^{-1}	0.243 cm^{-1}	0.438 cm^{-1}	? + $VV^{(-/0)}$

Injecting a Forward Current at 25 K, 50 K, and 80 K

Injection of a forward current at low temperature is probably the least understood mode of trap filling. However, it is commonly used in practice since for heavily damaged detectors only by this way a significant occupation of defect levels, regardless whether it is an electron or a hole trap, can be achieved.

Theoretical Background and Discussion of Forward IV Curves

Given the emission rates for electrons and holes of a particular trap level are sufficiently small at the filling temperature, such that the reemission of captured carriers is negligible during the trap filling pulse. This of course holds true for all defect levels that will give rise to a peak in the following TSC temperature scan. In the steady state condition the concentration of traps occupied with electrons or holes normalized to the total concentration (filling factor) can then be deduced by setting eq. 3.46 equal to zero

eq. 3.83 $$\frac{\{n_t, p_t\}}{N_t} = \frac{1}{1+\left(\frac{pc_p}{nc_n}\right)^{\pm 1}}.$$

The filling factors are therefore depending on the overall hole injection ratio p / n and the ratio between the capture coefficients for holes and electrons c_p/c_n, where the latter needs to be considered for each trap. To the experimental end p/n can be adjusted by realizing appropriate values of the injected current. Correspondingly, forward IV curves have been studied as function of temperature. They are presented in

Fig. 3.44 for an unirradiated control sample a), one weakly damaged b), and one heavily damaged device c).

According to the standard Shockley model of the diffusion diode, the current I can be written as function of the externally applied positive forward voltage V [SZE81],

eq. 3.84 $$I(V) = A\left\{p_{n0}, n_{p0}\right\}\sqrt{D/\tau_{rec}}\left[\exp\left(\frac{q_0(V - R(V)I(V))}{\eta k_B T}\right) - 1\right].$$

Here p_{n0} and n_{p0} denote the minority carrier concentrations in the n- or p-type bulk material, and free carriers are thought to be injected from either the p$^+$ or the n$^+$ contact. D and τ_{rec} mean the corresponding diffusion constant and minority carrier recombination lifetime. A series resistance R has to be taken into account, in particular as the radiation damage-induced deep levels compensate for the shallow doping*. Moreover, if the amount of injected minority carriers comes into the order of the majority carrier concentration, high-level injection takes over, which is easily accomplished in high resistivity material. This condition is represented by an ideality factor η of 2 which otherwise would be expected to be unity. Also then it is $n = p$ in the vicinity of the junction. In general it has to be taken into account that the free carrier concentration and also the hole injection ratio is varying with distance.

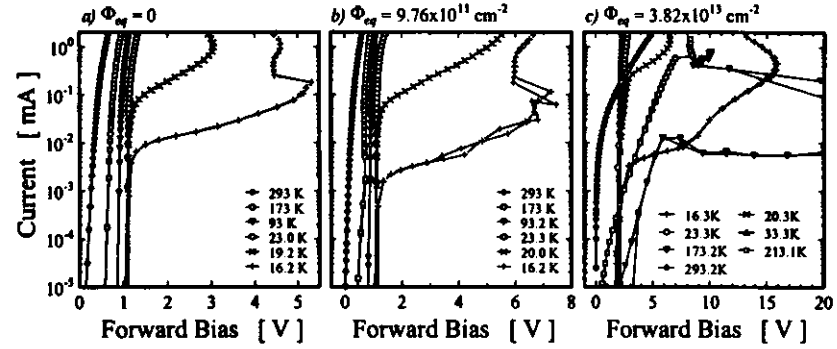

Fig. 3.44 Forward IV characteristics measured at several temperatures on devices that were not irradiated a) or exposed to a fluence of around 10^{13} cm^{-2} and 4×10^{13} cm^{-2} for b) and c), respectively (devices M10713 a), M20609 b), M20708 c)). It should be noted that all measurements have been ramped up and down in order to ascertain that the complex behavior represents a reproducible steady state condition.

Radiation damage-induced deep levels will mainly affect the recombination lifetime τ_{rec}. Assuming a capture coefficient c of 10^{-8} cm^3/s ($\sigma \approx 10^{-15}$ cm^2, $v_{th} \approx 10^7$ cm/s) and exploiting that τ_{rec} is approximately given by† $(c\,N_t)^{-1}$, the following relation is obtained

eq. 3.85 $$\tau_{rec} \approx \frac{10^8\ \text{scm}^{-2}}{\Phi_{eq}}.$$

It has been assumed here that the defect introduction rates are of the order of 1 cm^{-1}. For the example of a fluence of $\Phi_{eq} = 10^{14}$ cm^{-2}, eq. 3.85 yields $\tau_{rec} \approx 1$ µs, whereas in the undamaged devices τ_{rec} is of the order of several ms according to the certification of the Wacker float zone material [WAC]. In conjunction with eq. 3.84 it is then clear that the forward current is increasing very much as function of

* It proves however very difficult to determine a unique value of R because of its inherent dependence on the concentration of injected free carriers which, on the other hand, is a function of the bias V.

† Assuming an optimum recombination center, limited only by the trapping rate, compare eq. 3.46.

the irradiation fluence in the range of small forward bias voltages, where the series resistance effect can be neglected (less than approximately 0.5 V at room temperature)*.

An other characteristic quantity related to τ_{mr} is the recombination length $L = (D\,\tau_{mr})^{1/2}$. The diffusion coefficient D is different for electrons and holes and depends on the temperature. At room temperature D is of the order of 10 cm^2s^{-1}. Regarding lower temperatures, which is of chief interest for the TSC filling pulse, use of the Einstein-relation and a crude estimate of the mobility (5×10^4 $cm^2V^{-1}s^{-1}$ [SZE81]) gives a diffusion constant of around 200 cm^2s^{-1} at 50 K. Thus it is roughly

eq. 3.86 $$L(50\,\mathrm{K}) \approx \sqrt{2\times10^{10}/\Phi_{eq}}\,,$$

which shows that the injected carriers are expected to recombine on a distance of around 150 µm when $\Phi_{eq} = 10^{14}$ cm^{-2}. However, it will be shown below that the experimental data suggests recombination lengths one order of magnitude smaller than awaited from eq. 3.86. At times L can thus be found to be well below the device thickness, demonstrating that inhomogeneous filling of traps in general needs to be taken into account. It is noted that this problem may best be overcome by generating the free carriers optically with a suitably chosen wavelength, such that the light penetrates all through the device [LI395], compare Appendix A.

Now, application of eq. 3.84 is strictly valid only as long as L is smaller than the device thickness d. This is for example not true for the undamaged device or in the lower fluence range. In those cases the term $(D/\tau_{mr})^{1/2} = L/\tau_{mr}$ in eq. 3.84 should be replaced with d/τ_{mr}, where it is assumed that the width of the space charge region is zero and that the injected carriers are extracted completely after diffusing through the device thickness d [SZE81]. However, the recombination velocity at the back plane contact is very small as otherwise, upon full depletion, a large current would be injected, see Section 2.5.1.4. Thus, the free carriers injected during forward biasing will pile up, resulting in a minimum variation of their concentration with distance.

The Shockley model (eq. 3.84) would predict IV curves to be more or less straight lines (slope proportional to $q_0/(k_BT)$) when plotted in semi-logarithmic scales. A slight leveling-off at large currents due to the series resistance is however conceivable. Inspection of Fig. 3.44 reveals that this appears to be a reasonable description for all data measured on the undamaged device at temperatures greater than 23 K. Concerning the weakly damaged device (Fig. 3.44 b)), the IV curves resemble those of the control sample only when currents larger than 10^{-2} mA are injected. Now, at low temperatures all traps with negligible emission rates will assume a charge state according to eq. 3.83 upon the injection of free carriers. Moreover, there is obviously no significant voltage drop across the diode, that is, no electric extended field zone exists. Accordingly, the charges trapped in the defects have to be absorbed in the difference of the concentrations of free electrons and holes in order to maintain the approximate space charge neutrality [LAM62]. If it is possible to inject large amounts of free carriers compared with the deep level concentrations, a high injection condition with p/n equal to one is established. If on the other hand the free carrier concentrations are comparatively small, the electrons and holes trapped into the deep levels have to cancel each other, and p/n is unlikely to be unity. A dependence of the recombination lifetime on the injection level, as outlined in [LAM62], can then lead to a negative differential resistance and unstable oscillating currents. While the former can for example be seen on the 173 K data in Fig. 3.44 b), the latter was observed on the heavily damaged device in the range from 40 K to 150 K. To improve the visibility, the corresponding measurements were omitted in Fig. 3.44 c).

Further, it is noted that the Shockley model can then not be applied anymore, rather do the devices behave like p'-i-n' diodes in which simultaneous injection of holes and electrons from the p' and n' contact takes place (double-injection). Moreover, the forward current is mainly controlled by the recombination processes in the almost intrinsic bulk region. Since, on the one hand, the diffusion currents exhibit a much stronger temperature dependence than those due to recombination and, on the other hand, the compensation of majority carriers makes the bulk intrinsic, the p'-i-n' diode model is anticipated to take over at low temperatures. This can for example be observed on the heavily damaged device in Fig. 3.44 c) where only at the highest temperatures a reasonable agreement with the Shockley model is found.

* It is noted that in the presence of significant amounts of recombination centers η would be expected to be equal to two for the smallest bias voltages, compare [SZE81].

Neglecting the charges trapped into the deep levels, the current flow in a p'-i-n' diode can be deduced as for example outlined in [SZE81]. It is shown there that in the first approximation the voltage V_i dropping across the intrinsic layer i does not depend on the injected current

eq. 3.87 $$V_i \approx \frac{3k_BT}{8q_0}\begin{cases}\pi\exp(d/2L_a) & d > 2L_a\\ (d/L_a)^2 & d < 2L_a\end{cases}.$$

Furthermore, a distinction is made between so-called short and long p'-i-n' diodes, whichever is the value of the ambipolar* diffusion length L_a compared with the device thickness d. Additional voltage may drop across the resistance R_c of the contacts

eq. 3.88 $$V = V_i + R_cI\,.$$

The forward IV characteristic would then be expected to be a straight line intersecting the voltage axis at $V = V_i$ when extrapolated to $I = 0$. Fig. 3.45 demonstrates that this characteristic feature has actually been observed on a heavily damaged device at 50 K (M20708, $\Phi_{eq} = 3.82\times10^{13}$ cm^{-2}). The plot presents the diode voltage versus the corresponding filling currents averaged during a 20 s lasting TSC filling pulse. Evidently the contact resistance can be neglected, and the diode voltage V is always more or less equal to $V_i \approx 4$ V. For $V_i = 4$ V, eq. 3.87 gives an ambipolar diffusion length of 21 µm. Now, this is a factor of ten smaller than what would be expected from eq. 3.86, which is based on the approximate knowledge about defect concentrations and cross sections. The recombination of excess carriers appears to be enhanced with respect to the standard Shockley-Read-Hall treatment†.

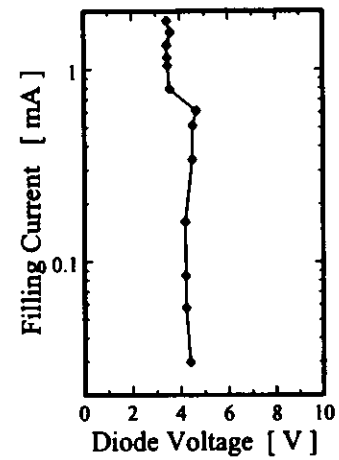

Fig. 3.45 The voltage drop across the diode plotted as function of the injected forward current (50 K, device M20708, $\Phi_{eq} = 3.82\times10^{13}$ cm^{-2}, $t_{fill} = 20$ s, $R_{fill} = 222$ kΩ, 3 month annealing at room temperature, $V_{dep} = 40$V, $V_{bias} = 43$ V).

It is moreover shown in [SZE81] that the current flowing through the p'-i-n' diode is proportional to both the injected free carrier concentration n' and the voltage V_i dropping across the intrinsic layer,

eq. 3.89 $$I \approx \frac{8}{3}\frac{A}{d}\frac{q_0^2}{k_BT}D_aV_in'\,.$$

It should however be noted that the derivation in [SZE81] assumes high injection, i.e., $n' = n = p$, and a spatially constant free carrier concentration n'. In the presence of large defect concentrations both presuppositions cannot be fulfilled. On the one hand, the recombination length becomes significantly smaller than the device thickness and, on the other hand, as previously stated the balance of the charges trapped into the defects will govern the injection ratio as long as the concentration of the injected free carriers is small.

Regarding the data presented in Fig. 3.45, eq. 3.89 yields a free carrier concentration of only about 2×10^9 cm^{-3} for $I = 1.7$ mA ($A = 0.275$ cm^2, $d = 280$ µm, $D_a(50\,\mathrm{K}) \approx 200$ cm^2s^{-1}). Despite the serious simplifications in the model, the value obtained for n' is in the right order of magnitude as will be confirmed in Section 3.3.3.5 by the dependence of the trap filling process on the duration of the filling pulse.

At the lowest temperatures ($T < 23$ K) there is a very large voltage drop across the diodes irrespective of the irradiation fluence (Fig. 3.44). Now it has to be recalled that even the shallow doping impurities would not be ionized at these temperatures. Concerning the defect free control sample it is clear that the

* L_a and D_a are special combinations of the corresponding recombination lengths and diffusion constants for electrons and holes, respectively. Since only the order of magnitude of those quantities is discussed in this section, they can be identified with the previously introduced L and D.

† This has frequently been reported in the literature on fast neutron-damaged devices and was explained there in terms of cluster type defects [VLI87].

bulk is virtually neutral and, accordingly, also there a p⁺-i-n⁺ diode like behavior is expected. The reduction of the voltage drop at larger forward currents can consequently be understood to follow from the injection level dependence of the recombination lifetime of the phosphorus donor level [LAM62]. Similar negative resistance curves have been reported very early by N. Holonyak et al. [HOL62]. It can however not be excluded here that both contacts become blocking and a space charge region is established. Further, it may happen that the current does not even flow through the bulk of the detector but rather along the edges.

Qualitative Discussion of the TSC Spectra

Fig. 3.46 displays the spectra measured on the samples listed in Table 3.11 (10^{11} cm^{-2} < Φ_{eq} < 4×10^{13} cm^{-2}). Traps have been filled by injecting a forward current of around 1.7 mA for 30 s at 25 K, 50 K, and 80 K in figure a), b) and c), respectively. Let us assume that large concentrations of free carriers are injected such that the injection ratio p/n is equal to unity. As outlined in the previous section this presupposition is expected to hold true only for devices irradiated by comparatively small fluences and at high temperatures. Then one can see from eq. 3.83 that effective filling of an electron or hole trap is only realized if $c_n >> c_p$ or $c_n << c_p$. However, inspection of data on the capture coefficients from the literature, as given by [HAL96] (Appendix B), suggests filling factors of around 7%, 0%, 4%, 0%, and 100% at 50 K and similar values at 25 K and 80 K for the charge states VO_i^-, VV^{--}, VV^-, VV^+, and $C_iO_i^+$, respectively. It is therefore not clear why other peaks than the one arising from the transition $C_iO_i^{+/0}$ (peak M) are seen in the spectra gathered on the weakly damaged devices at all. However, in [HAL96] the capture coefficients were measured with the C-DLTS technique, which fills the traps in-situ at temperatures much higher than the filling temperatures under consideration here. It is thus highly likely that the above estimates of the filling factors are not accurate, rather do the curves in Fig. 3.46 indicate largely different ratios between the capture constants at low temperatures.

It should be noted that the removal of the injection current and successive application of the reverse bias proceeds on a time scale of several 100 ms due to the RC-filter in the bias supply (Fig. F.3 in Appendix F). Therefore, on weakly damaged devices, where the damage-induced deep levels do not compensate for all of the shallow dopants, recombination of captured holes and additional electron trap filling may take place during the switching process because free electrons flood the diode when the bias is close to 0 V*. A corresponding examination in Section 3.3.3.5 will however show that this effect is almost negligible on a device irradiated by a fluence of around 10^{12} cm^{-2}. Regarding the heavily damaged devices, the total concentration of charges trapped into the defects, i.e. $N_{eff,SCR}$, was argued to be close to zero in the previous section because, compared to the defect densities, only small concentrations of free carriers can be injected. Accordingly, virtually no free carriers are available to alter the trap occupation during the switching process. Therefore, an influence of the switching time would only be expected to be active in the lowest fluence range (Φ_{eq} < 10^{12} cm^{-2}).

As for heavily damaged samples $N_{eff,SCR}$ is close to zero after the filling pulse, the depletion width extends all over the device thickness upon reverse-biasing the diode. This explains the dominance of the first peak in the spectrum (peak A in Fig. 3.46 a), peak F in Fig. 3.46 b)) inasmuch as it is during the emission of the first peak in the spectrum that the charge balance becomes distorted, which is accompanied by a reduction of the depletion layer width. Since both peaks, A and F, arise from electron traps, $N_{eff,SCR}$ will become a positive number during their emission. Therefore, in the high fluence range, all peaks at temperatures between the first peak and peak M appear to be reduced in height. M corresponds to the hole trap transition $C_iO_i^{+/0}$ and therefore releases positive charges. If this proceeds $N_{eff,SCR}$ is decreasing and thereby the depleted layer is widening. The resulting distortion of the peak shapes, especially M and N, has already been discussed in Section 3.3.3.3.

* For a concentration of free carriers of around 10^{13} cm^{-3} the capture time constant is of the order of only 100 µs given a capture cross section of 10^{-15} cm^2.

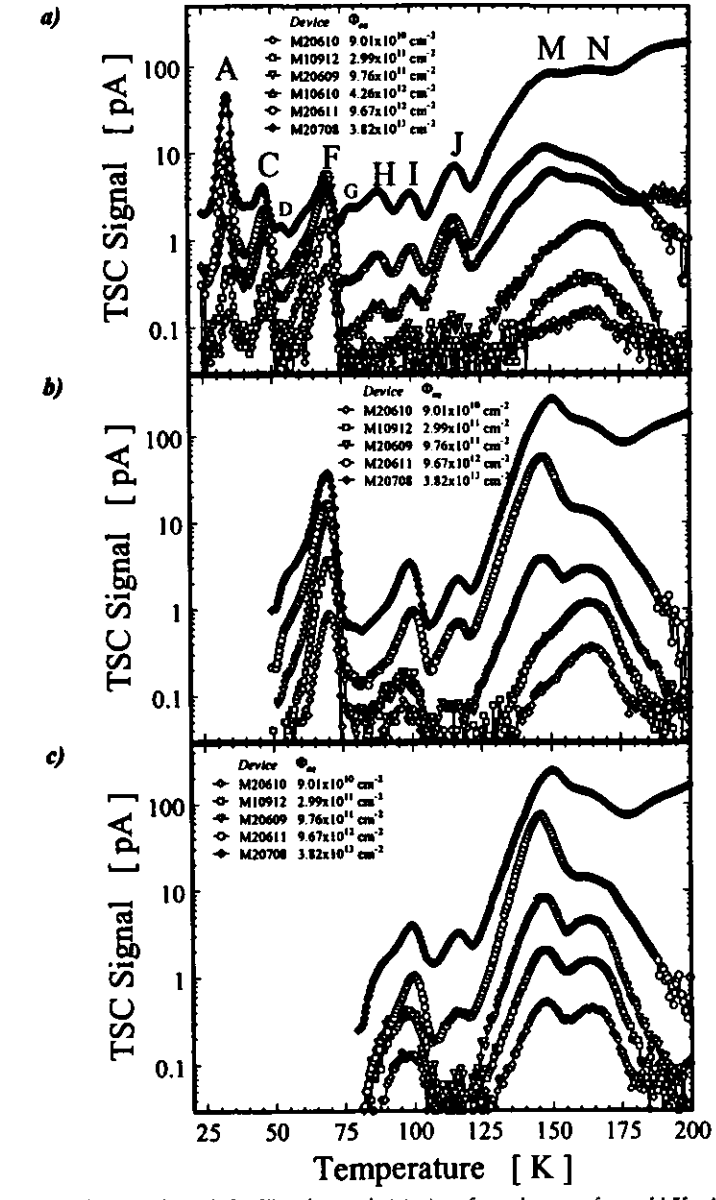

Fig 3.46 TSC spectra obtained after filling the traps by injecting a forward current of around 1.75 mA for 30 s (20 min in case of the device M20708) at 25 K a), 50 K b) and 80 K c). A heating rate β of 0.183 K/s and a reverse bias voltage of 50 V was used, except for M20609 in a) (75 V, 270 d annealing at room temperature). The leakage current has always been subtracted, for more details compare Table 3.11.

The C_iO_i donor level exhibits a particularly strong dependence of the hole capture coefficient c_p on the temperature, as will be shown in Section 3.3.3.5 which is devoted exclusively to this subject. This fact accounts for the improved filling of peak M at higher temperatures, e.g. 80 K, irrespective of the irradiation fluence. Further, at low temperatures the trap is not filled at all, and the p'-i-n' model governs the filling process with a small concentration of injected free carriers n'. As then the charges trapped in the defects have to cancel out and the only dominant hole trap is inactive, also electron traps can not be filled efficiently. Moreover, it would be expected in such a situation that the hole injection ratio p / n is becoming larger than unity in order to compensate for the diminished c_p of the dominant hole trap. In conclusion, at low temperatures the filling of some less abundant hole traps improves (peaks G, H, J), while the filling factor of the dominant traps is small.

Evaluation of Defect Concentrations

From the statements above it is evident that great care must be taken if concentrations of defects are derived from TSC spectra in which the traps have been filled with a forward injection current. Only in a few selected cases an evaluation has been tried (Fig. 3.47). The data on peak M and peak N were taken from the 80 K injection curves, in which they are always isolated so that a unique integration of the current is possible. The active depletion layer width was calculated by the iterative procedure described in Section 3.3.3.3. However, any edge or λ-regions were again neglected. The peaks A and F were investigated on the 25 K and 50 K injection spectra, in which they appear as first TSC signal. Therefore, it was assumed that N_{dTSC} is close to zero right after injection, see above. The effective doping concentration applied to calculate the depletion width from eq. 3.74 was therefore taken to be half of the concentration of the peak under consideration, again requiring an iterative numerical computation to get the final result. According to this procedure all devices would appear to be more or less fully depleted during the emission of the two peaks studied.

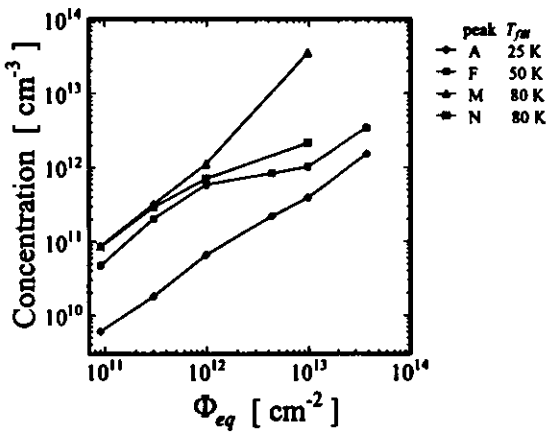

Fig. 3.47 Concentrations of selected peaks evaluated from the TSC spectra obtained after injecting a forward current at 25 K (peak A), 50 K (peak F), and 80 K (peaks M and N), compare Fig. 3.46. Different methods were used for the calculation of the active depletion width (see text).

Provided the assumptions made about the depletion width are correct, the results displayed in Fig. 3.47 indicate that the introduction of peak F levels off at fluences greater than 10^{12} cm^{-2}. Since there is no physical basis for a decreasing introduction rate of the A-center*, this observation is probably due to the hole injection ratio p / n (see eq. 3.83) which, as argued before, at low temperatures is expected to grow from unity to larger values as function of the fluence. Moreover, at higher fluences peak M seems to grow more rapidly at the expense of peak N. But the data has to be taken with care, as for example the algorithm used for the determination of the depletion width did not find a unique solution for the device irradiated to 3.82×10^{13} cm^{-2}.

* Only if a significant fraction of the interstitial oxygen concentration were exhausted would the A-center production be suppressed, which however requires fluences larger than 10^{13} cm^{-2}.

In order to avoid systematic errors due to the poorly defined depletion width, Table 3.15 presents concentrations normalized to the irradiation fluence only for the three devices exposed to less than 10^{12} cm^{-2}. The average is considered to be the lower bound of the introduction rate of the corresponding crystal defect, assigned in the last column. Peak F does not contain a contribution from the C_iC_s defect because injection of minority carriers should transform the defect into the bistable configuration B [SO290]*.

Table 3.15 Evaluated peak concentrations as shown in Fig. 3.47 normalized to the appropriate irradiation fluence.

Peak	Evaluated Concentrations Normalized to the Irradiation Fluence				Chemical Composition
	M20610	M10912	M20609	Average	
A	0.067 cm^{-1}	0.060 cm^{-1}	0.067 cm^{-1}	0.065 cm^{-1}	?
F	0.523 cm^{-1}	0.678 cm^{-1}	0.602 cm^{-1}	0.601 cm^{-1}	$VO_i^{(-/0)}$
M	0.967 cm^{-1}	1.07 cm^{-1}	1.14 cm^{-1}	1.06 cm^{-1}	$C_iO_i^{(+/0)}$
N	0.938 cm^{-1}	0.977 cm^{-1}	0.723 cm^{-1}	0.879 cm^{-1}	? + $VV^{(-/0)}$

The long switching time could strongly enhance the filling of the electron traps A and F since their small ionization energy is correlated with a large capture cross section, see eq. 3.56 (compare also the corresponding compilation in Appendix B). The data found for A and F do probably therefore resemble to the values found in Table 3.14. On the other hand, peak N is located deep in the forbidden gap and has a smaller capture cross section. Further, the C_iO_i level exhibits a remarkably small capture coefficient for electrons. Thus, the peaks M and N are concluded to be mainly filled by the free carriers supplied during the injection and are not affected by the switching process.

For the other peaks observed in Fig. 3.46 no reasonable assumption can be made for the depletion width W_g. Therefore, the data given in Table 3.16 were obtained by simply setting $W_g = d$. Thus, an ultimate lower limit of the introduction rates is obtained, given the traps are distributed homogeneously throughout the bulk. The data were moreover derived from that particular TSC spectrum, in which the peak in question exhibited the largest filling factor. Concerning peak C a continuous decrease of the normalized concentration as function of the fluence is observed, which is in agreement with the view that for heavily damaged devices the depletion width shrinks after the emission of the first peak in the spectrum.

Table 3.16 Normalized trap concentrations for the remaining peaks observed in Fig. 3.46. Since no other reasonable assumption was possible, the device thickness d has been assumed for the depletion width. Thus the ultimate lower limits of the corresponding defect introduction rates are represented.

Peak, T_{fill}	Evaluated Concentrations Normalized to the Irradiation Fluence						Chemical Composition
	M20610	M10912	M20609	M10610	M20611	M20708	
C, 25 K	0.101 cm^{-1}	0.058 cm^{-1}	0.057 cm^{-1}	0.021 cm^{-1}	0.013 cm^{-1}	0.006 cm^{-1}	$C_iC_s(B)^{(-/0)}$
H, 25 K	-	-	-	0.003 cm^{-1}	0.007 cm^{-1}	0.009 cm^{-1}	$VV^{(+/0)}$
I, 80 K	0.180 cm^{-1}	0.160 cm^{-1}	0.051 cm^{-1}	-	0.010 cm^{-1}	0.012 cm^{-1}	$VV^{(-/-)} \rightarrow C_iP_s III^{(0/+)}$?
J, 25 K	-	-	0.012 cm^{-1}	0.026 cm^{-1}	0.017 cm^{-1}	0.017 cm^{-1}	? ($C_i^{(+/0)}$)

Peculiarities of the Peak I

Regarding the origin of peak I, previously assigned to the transition $VV^{(-/-)}$, the transformation of the peak shape recognized at 50 K and 80 K injection suggests that for heavily damaged devices an other trap is emerging at the same temperature. This is supported by the fact that the energy levels of the

* Even if the concentration of injected holes were small and C_iC_s would therefore have a chance to reorient from state (B) to state (A), the time constant for this process at 50 K is around 300 s (Section 3.3.1.2). However, the filling pulse length was 30 s, so that only small concentrations of state (A) would exist.

divacancy arise from motionally averaged states, which do not exist below 25 K [SVE91]. Still a peak around 100 K is observed, which then is unlikely to be due to the divacancy.

Now, it has been found in C-DLTS measurements that the C_iP_s defect introduces a signal close to the doubly charged divacancy, compare for example the work of M.T. Asom et al. [ASO87]. Although the expected introduction rate is relatively small, see Section 3.3.1.1, significant concentrations of this complex defect of the order of several times 10^{11} cm^{-3}, reflecting the exhaustion of all substitutional phosphorus atoms, are anticipated in the most heavily damaged samples. Gürer et al. have shown that the C_iP_s pair exhibits a pronounced configurational metastability [GÜR92]. For purpose of clarity, only the two commonly encountered configurations, namely IA and III, have been cited in Appendix B. Great interest needs to be attributed to the finding that the state III can be prepared by injection of free carriers at low temperature. Regarding the mode of trap filling discussed here, it is clear that the corresponding transition at E_C - 0.23 eV should typically be observed. Further, since this essentially is the lowered shallow phosphorus donor level, the defect is positively charged after emission of the electron, allowing for a significant enhancement of the emission rate in the presence of an electric field by the Poole-Frenkel effect, compare Section 3.3.1.4.

The latter can then account for the observation made in Fig. 3.48 a), which shows the reverse bias dependence of the TSC spectrum measured on the most heavily damaged device studied. Obviously there is a shift of the maximum temperature of peak I, which has been evaluated and plotted versus the corresponding reverse bias voltage in Fig. 3.48 b). As outlined in Section 3.3.1.4, the Poole-Frenkel effect can be regarded as a reduction of the defect ionization energy, which according to eq. 3.79 would correspond to a peak temperature decreasing as function of the electric field strength.

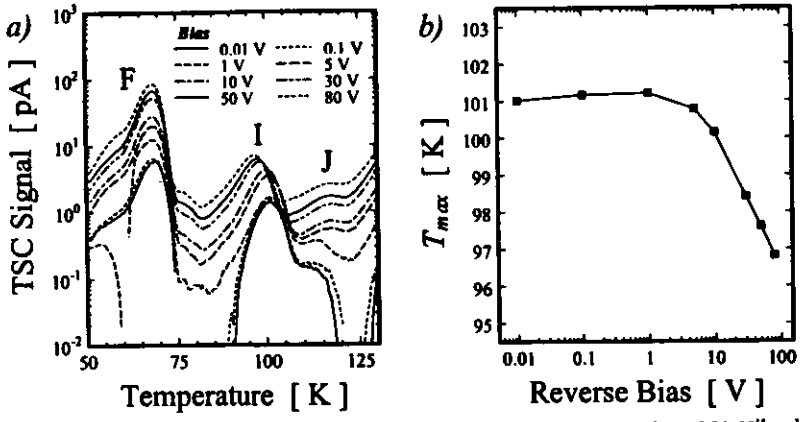

Fig. 3.48 The reverse bias dependence measured on a heavily damaged device (M20710, Φ_{eq} = 8.96×10^{11} cm^{-2}, 7 months annealing at room temperature). a) TSC spectra obtained after injecting 2.5 mA at 50 K for 30 s, heating rate β = 0.183 K/s. The sample was always cooled under 100 V. b) Maximum temperature of peak I versus the reverse bias voltage applied during the TSC temperature scan.

If it is recalled that the concentrations of the dominant defects are very large (of the order of 10^{14} cm^{-3}) and therefore significant space charge densities $N_{eff,SCR}$ are expected during the TSC temperature scan, it is reasonable that the electric field strength, which in the first approximation is proportional to the square-root of $|N_{eff,SCR}|$, was sufficiently large only in this particular sample, so that the peak shift could be noticed. From the first order approximation $\Delta H'_{\alpha,p} \approx 28\, k_B T_{max}$ derived in Section 3.3.3.1 it can be concluded that a shift of 4 K in T_{max} corresponds to a lowering of the ionization energy of around 10 meV. Regarding the numerical examples given in Section 3.3.1.4 this is compatible with the Poole-Frenkel effect.

It could be argued that the shift observed on peak I supports its assignment to the doubly charged divacancy. However, the trapping of the second electron at the singly charged divacancy requires a short range potential minimum, typical of deep defect levels, which however has a repulsive Coulombic character on the long range. In analogy to the examination presented by P.A. Martin et al. [MAR81], it is thus concluded to be unlikely that field enhanced emission could be observed on the transition $VV^{(-/-)}$.

However, the assignment of the transition $C_iP_s(III)^{(0/+)}$ to peak I is regarded as tentative as neither accurate data on the emission enthalpy and the cross section were available which could have allowed for a confirmation on the basis of the predicted TSC peak temperature, nor has any observation ever been made which were in agreement with the expected dissociation of the defect by forward current injection at room temperature.

3.3.3.5 The C_iO_i Donor Level - Detailed Studies on the Trap Filling Process

The TSC peak M, which was assigned to the transition $C_iO_i^{(+/0)}$, exhibits a pronounced dependence on the filling conditions. Of particular interest is the evolution of the TSC spectrum as function of the filling temperature T_{fill} shown in Fig. 3.49. For purpose of trap filling a forward current of around 1.75 mA was injected for 30 s. In particular one notes the marked growth of peak M for increasing T_{fill}. Corresponding observations have already been reported in the literature, for example [LI395] and [SCH95]. However, so far no explanation on a sound physical basis is available.

It will be argued below that the changes in the electron traps (peaks F, I, and N) are likely to be second order effects related to the improved filling of the C_iO_i donor. For the particular case of the C_iC_s pair it has however been held in earlier works that the transformation of the defect from the bistable configuration B, which is frozen during cooling under reverse bias, to the state A could account for the growth of peak F as function of T_{fill} [SCH95]. This argument follows from the evaluation of the thermal activation properties of C_iC_s by Jellison [JEL82], see eq. 3.28 in Section 3.3.1.2. This predicts the transformation time constant to be equal to t_{fill} = 30 s at 53.6 K. However, according to reference [SO290] injection of minority carriers inhibits the reconfiguration. Moreover, at 50 K, where the time-constant would be expected to be around 300 s, no corresponding dependence of the peak height could be observed as function of the duration of the injection filling pulse (1 s < t_{fill} < 1000 s) [HEY96].

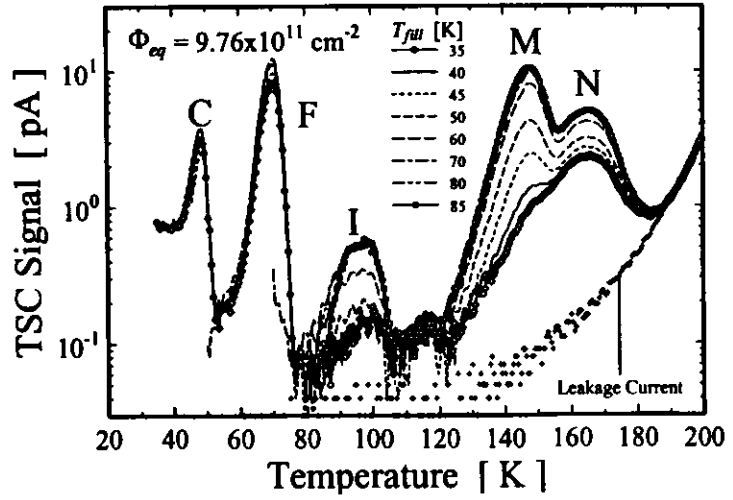

Fig. 3.49 Variation of the TSC spectrum as function of the filling temperature T_{fill}. I_{fill} = 1.75 mA, t_{fill} = 30 s, β = 0.183 K/s, bias = 75 V. V_{ann} = 72 V at room temperature after 6.5 months of annealing (device M20609).

Now, for the given fluence (Φ_{eq} = 9.76×10^{11} cm^{-2}), the concentration of deep levels present in the device studied is of the order of 10^{12} cm^{-3} (compare the defect introduction rates quoted in the previous section). Consequently, according to eq. 3.70 the applied reverse bias voltage of 75 V can reasonably well be assumed to always fully deplete the device and an otherwise possible variation of the depletion layer width would not affect the spectra shown in Fig. 3.49. Further, the recombination length can be estimated by eq. 3.86 to be of the order of 1.5 mm, that is, the trap filling will be assumed to be homogeneous throughout the detector*.

According to eq. 3.83 the dependence of the C_iO_i filling factor on T_{fill} observed in Fig. 3.49 can basically originate from the following two sources

- the hole injection ratio p / n (T_{fill}) and
- the ratio between the capture coefficients for electrons and holes c_n / c_p (T_{fill}).

In order to study the first item, the TSC spectrum has been recorded for various injection currents at T_{fill} = 50 K, see Fig. 3.50 a). For the smallest injection current it is $p / n \approx 0$, and the filling of the traps is similar to the filling achieved when switching to zero bias (see Fig. 3.42). As outlined in Section 3.3.3.4, complete filling of all electron traps can then not be achieved because their concentrations are larger than the density of positive space charges, $N_{eff,RT}$, frozen during the cooling. As long as the concentration of injected free carriers is comparatively small (small injection currents), the approximate space charge neutrality must be established. This promotes the filling of electron traps (e.g. peak N in Fig. 3.50 a)) upon a significant portion of the C_iO_i donors becomes occupied with holes. In analogy the filling of the electron traps improves when the occupation of C_iO_i varies as function of T_{fill} in Fig. 3.49.

For the largest filling currents realized a saturation of the filling factor of C_iO_i is noted in Fig. 3.50 a). Inspection of Fig. 3.46 b) reveals that for the particular device studied here this saturated filling factor is larger than the one obtained on the two more weakly damaged devices. As for the latter samples a high-injection condition of the diffusion currents with p / n = 1 is expected to be realized, the hole injection ratio must become larger than unity for the sample considered here (Φ_{eq} = 9.76×10^{11} cm^{-2}). This indicates that at 50 K the concentration of free carriers is not sufficient to achieve high-injection ($n = p \gg N_t$) rather is the forward current flow a mixture of p$^+$-i-n$^+$ diode like double-injection and hole diffusion.

So far we have $p / n > 1$ at 50 K. In order to show that $p / n \geq 1$ over the full range of filling temperatures studied in Fig. 3.49, the concentration of filled defects have been evaluated from the spectra. It was thus possible to calculate the total space charge density trapped into defects ($N_{eff,RT} + p_{fill} - n_{ef} - n_{tf} - n_{ff}$) as function T_{fill} (not shown). In the first approximation it was found that the charges cancel out only for $T_{fill} < 70$ K. Thus, this temperature marks the transition from p$^+$-i-n$^+$ diode to diffusion diode like behavior, i.e., below 70 K it is $p / n > 1$ and above 70 K it is p / n = 1.

As illustrated in Appendix F, different injection currents have always been realized by appropriate forward bias voltages in conjunction with a suitable resistor for current limitation. Now, the startling observation made in Fig. 3.50 a) is that the peak filling does depend on the forward bias voltage used for the filling pulse rather than on the injected current. For example, the same filling factors were achieved using a -100 V filling voltage although the correspondingly injected currents, 15 µA and 1800 µA, were not even of the same order. It is noted that it was possible to reproduce the experiment, indicating that it is a real effect [HEY96]. The observation does however contradict the physical understanding of the filling process developed above. That is, the 30 s long filling period does not govern the trap filling but rather do the switching processes at the beginning and at the end. For example, if the filling voltage is removed and the reverse bias is reestablished the diode voltage will sweep through 0 V at a rate determined by the RC filter in the bias line, see Fig. F.3 in Appendix F. In this particular moment free electrons might flood the device and significantly alter the trap occupation.

* However, as the experimental data suggested a ten times smaller recombination length, a slight variation of the initial trap occupation with distance might exist.

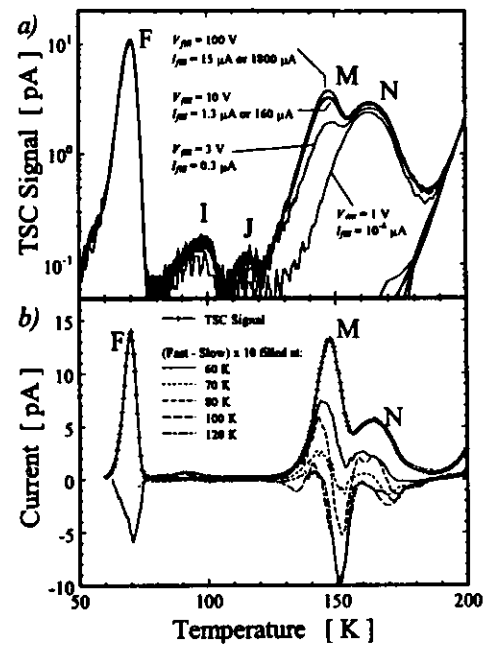

Fig. 3.50 a) Filling current/bias dependence, device M20609 (Φ_{eq} = 9.76×10^{11} cm^{-2}, 7 months room temperature storage, V_{dep} = 71 V) using various forward voltages and either a 56 kΩ or a 6.8 MΩ resistor for the limitation of the forward injection current. Using 30 V as filling voltage has given results similar to 100 V indicating a saturation. Thus the data have been omitted. The reverse bias and the heating rate were 74 V and 0.183 K/s, respectively. b) Differences in the peak filling arising from the switching speed (device M20812, V_{dep} = 68.4 V, $V_{dep,0}$ = 87.4 V, V_{bias} = 50 V, β = 0.183 K/s, t_{fill} = 30 s).

It has therefore been investigated whether enhancements of the C_iO_i filling with respect to the value obtained for the largest filling voltages in Fig. 3.50 a) can be achieved when the switching time is reduced. For this purpose traps have either been filled by application of a forward bias of 10 V without the RC filter and any other series resistor (fast), or by application of a forward bias of 100 V and limiting the current to 1.75 mA by a resistor of 57 kΩ using the standard electrical set-up (slow). In the former case the maximum current of around 2.5 mA is limited by the voltage source protection circuit (compare [SCH95] where this kind of filling has been used). The resulting differences in the TSC spectra are shown in Fig. 3.50 b). Evidently the filling is altered by less than 10% irrespective of the filling temperature. This suggests that the saturation value, which always was realized in Fig. 3.49, does not depend on the switching speed*.

In conclusion, only the dependence of the c_n / c_p on temperature can explain the variations of the C_iO_i filling factor. However, according to the recent measurements of Hallén et al. [HAL96], quoted in Appendix B, the ratio would be expected to be $c_n/c_p(T_{fill}) = 0.1\times(T_{fill}/ 300\ \mathrm{K})^{4.59}$, which due to the particularly small electron capture coefficient is only of the order of around 10^{-3} at 100 K and 10^{-4} at 10 K. This would suggest that, given $p \geq n$, all C_iO_i donors should be filled at all temperatures. However, C-DLTS has been used in that study and the capture coefficients could only be measured there in the range from 160 K to 238 K. It must thus be put in doubt that the extrapolation to lower temperatures is valid.

For purpose of quantitative evaluation, the height of peak M in Fig. 3.49 which is proportional to the initially filled concentration (eq. 3.81) has been plotted versus the corresponding filling temperature T_{fill} in Fig. 3.51. Integration of the current has not been tried as at the smallest T_{fill}, peak M is not very well resolved (Fig. 3.49). Corresponding results were obtained on the device examined in Fig. 3.50 b) and on a heavily damaged, inverted detector. In the latter case the C_iO_i donor was filled by switching to zero bias, see Fig. 3.52. This is noteworthy in particular, because the filling mode is very much different from the injection filling. Still a similar temperature dependent increase of peak M is observed. It should however be born in mind that in the presence of large defect concentrations the variation of the active

* It should however be noted that the device used for this cross check is not the same as the one studied in Fig. 3.50 a). However, as can be learned by comparison of the TSC spectra, the defect concentrations are almost similar and also the variation of the C_iO_i filling with temperature is identical (see below). The irradiation fluence is not exactly known because the device was placed for one run period as a control sample into the PLUG calorimeter, which is a part of the H1-experiment at HERA, DESY. Although no bulk damage effects had ever been expected in that position the shift in the depletion voltage and the leakage current increase suggest an equivalent 1 MeV neutron fluence of around 2×10^{13} cm^{-2}.

volume might distort the systematic dependence compared with the more weakly damaged samples (Fig. 3.51).

The data presented in Fig. 3.51 indicate that the ratio between the electron and the hole capture coefficient is much larger than unity at low temperatures. Now, the electron capture coefficient is known to increase as function of temperature in the range from 160 K to 238 K, and this trend is assumed to hold at lower temperatures. Thus, the hole capture would be required to exhibit an even stronger variation with temperature, which for example is anticipated in the multi-phonon emission model (Section 3.3.1.4). In this model an energetic barrier related to a change in the reconfiguration of the complex defect needs to be overcome before the capture of a free carrier can succeed. In analogy to eq. 3.55 the ratio between the capture coefficients was therefore assumed to be given by

eq. 3.90 $$\frac{c_n}{c_p} = a\exp(b/T).$$

Accounting for the current offset, which is noticed at the smaller filling temperatures in Fig. 3.51 and which arises from overlapping TSC peaks, the following parametrization can be given for the total peak height as function of the filling temperature (compare eq. 3.83)

eq. 3.91 $$I_M(T_{fill}) = Offset + Amplitude\frac{1}{1+a\exp\left(b/T_{fill}\right)}.$$

The variation of p/n with temperature discussed previously was assumed to be weak compared with the exponential term and has therefore been neglected. It was possible to fit eq. 3.91 to the data displayed in Fig. 3.51, finding an overall good agreement. The corresponding values found for the variable parameters are given in Table 3.17. The average energy barrier for the two weakly damaged devices (M20609, M20812), which appear to give more reliable data, is 35.1 meV. In the last column it has been calculated which ratio between c_n and c_p would be predicted at a temperature of 160 K applying eq. 3.91. This has to be compared to 5.6×10^{-3} which is the corresponding value deduced from the measurements of Hallén et al. at the lowest temperature (160 K) they have been investigating (see Appendix B). Especially the value obtained on the device M20609, which has given the most accurate fit, suggests that their results and those reported here match at a specific intermediate temperature.

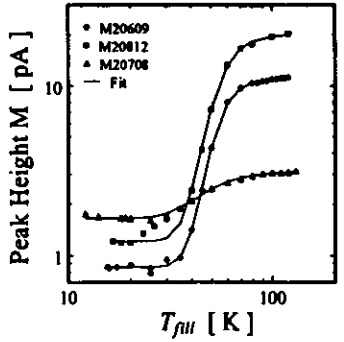

Fig. 3.51 The height of peak M as function of the filling temperature derived from TSC spectra measured after injecting a forward current (devices M20609 and M20812, compare Fig. 3.49 and Fig. 3.50 b)) or switching to zero bias (device M20708, compare Fig. 3.52). The solid lines are fits to the data, see text.

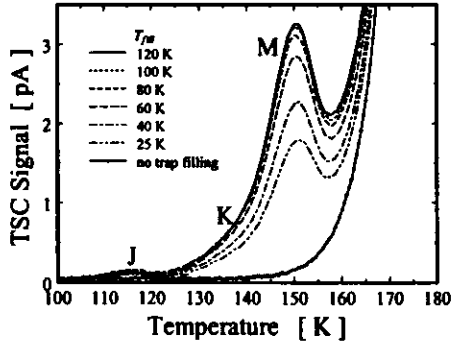

Fig. 3.52 TSC spectra measured on a heavily damaged device (M20708, $\Phi_{eq} = 3.82\times10^{13}$ cm^{-2}) as function of the temperature T_{fill} at which the reverse bias of 50 V was removed and 0 V were applied for 30 s. Since the space charge is negative, only hole traps are filled giving rise to the peaks J, K, and M.

Table 3.17 Parameters of the fit to the data displayed in Fig. 3.51.

Device	*Offset* [pA]	*Amplitude* [pA]	a	$b\times k_B$ [meV]	$c_n/c_p = a\exp(b/160\text{ K})$
M20609	0.855	10.4	3.43×10^{-4}	37.4	5.2×10^{-3}
M20812	1.21	19.2	1.07×10^{-3}	32.8	1.2×10^{-2}
M20708	1.65	1.56	1.49×10^{-2}	17.8	5.4×10^{-2}

If it is assumed that the electron capture coefficient of the C_iO_i donor as measured by Hallén et al. ($c_n(T) = 3.9\times10^{-10}\,(T/300\text{ K})^{-2}$ cm^{3}s^{-1}) were suitable even for low temperatures, then eq. 3.90 can be used to calculate the corresponding hole capture coefficient according to $c_p(T) = c_n(T)a^{-1}\exp(-b/T)$. At 50 K this gives $c_n = 3.5\times10^{-14}$ cm^{3}s^{-1} and $c_p = 1.7\times10^{-14}$, 1.6×10^{-14}, or 3.8×10^{-14} cm^{3}s^{-1}, whichever set of parameters is employed*. On the one hand, this indicates that in the steady state condition, which is established during the filling pulse, less than half of all C_iO_i defects are occupied with holes. On the other hand, both capture coefficients are very small and, as will be shown in the following, the time needed for reaching the steady state condition during the filling pulse becomes very large.

In order to determine the filling time constant of a particular trap, the rate equation eq. 3.46 has to be examined. It will be assumed that the temperature has a small value, such that the electron and hole emission rates (e_n, e_p) are both negligible. Given the concentrations of injected free electrons n and holes p are constant, an analytical solution is possible. Regarding the special situation that the trap is empty before the filling pulse, the result can be rearranged to give the hole filling factor (e.g. of the C_iO_i donor)

eq. 3.92 $$\frac{p_t}{N_t}(t_{fill}) = \frac{1}{1+\frac{n}{p}\frac{c_n}{c_p}}\left[1-\exp\left(-\left[nc_n+pc_p\right]t_{fill}\right)\right]$$

The filling factor approaches the steady state value eq. 3.83 with a characteristic time constant

eq. 3.93 $$\tau_{fill} = \left(nc_n + pc_p\right)^{-1}$$

which is of the order of 100 µs when a free carrier concentration of 10^{12} cm^{-3} and typical numbers for the capture coefficient ($v_{th} \approx 10^7$ cm/s, $\sigma \approx 10^{-15}$ cm^2) are used. Employing the above estimates of the capture coefficients of C_iO_i at 50 K would then however give a τ_{fill} of the order of ten seconds, which is already comparable to the commonly used filling time of 30 s.

Systematic variation of the duration of the free carrier injection pulse t_{fill} has only in one case been found to affect the TSC spectrum (Fig. 3.53). Similar observations were already reported in [SCH95]. Trap filling in this heavily damaged device was achieved by forward current injection at 50 K. Only for filling times of the order of

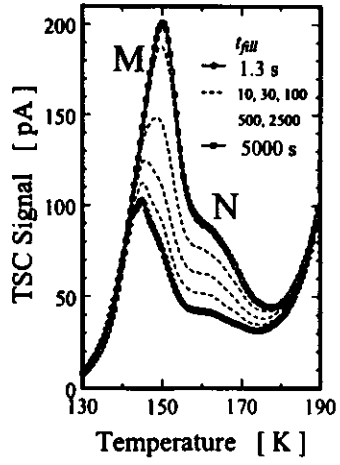

Fig. 3.53 Influence of the duration of the injection pulse t_{fill} on the TSC spectrum. $I_{fill} = 1.7$ mA, $T_{fill} = 50$ K, $\beta = 0.183$ K/s, bias = 50 V, $V_{dep} = 65$ V at room temperature after a 7.5 months annealing (device M20708, $\Phi_{eq} = 3.82\times10^{13}$ cm^{-2}). Only the temperature range in which changes could be observed is shown. The serious distortion and shift of the TSC signals is due to the variation of the depletion width, see Section 3.3.3.2.

* The corresponding capture cross sections would then both be of the order of 10^{-21} cm^2.

understood if the free carrier concentration during the filling period is of the order of 10^{10} cm^{-3}. Now, in the previous section a free carrier concentration of around 2×10^{9} cm^{-3} has been determined at 50 K and an injection current of 1.7 mA for the device considered in Fig. 3.53 (compare Fig. 3.45). Recalling the various simplifications which were necessary to obtain that result, it must be concluded that the two values are in reasonable agreement. Then, also a consistent picture concerning the dependence on the filling time emerges since the alteration of the spectrum in Fig. 3.53 does simply reflect the dependence of the number of C_iO_i donors occupied with holes on the filling time t_{fill} according to eq. 3.92. Due to the comparatively small concentration of injected free carriers the total trapped charge must be approximately zero. This requires more electrons to get trapped upon charging of the C_iO_i donor which then accounts for the simultaneous increase of peak N observed in Fig. 3.53. Moreover, it is noted that the variation with filling time was noticed only for a filling temperature of around 50 K but not at 20 K or 80 K. This is however in agreement with the above modeling. On the one hand, at 20 K the hole capture coefficient is so small that the hole filling factor would be expected to be close to zero, i.e., C_iO_i is not filled at all. On the other hand, at 80 K the hole capture coefficient is already quite large, which leads to comparatively short filling times (eq. 3.93).

3.3.3.6 Isochronous Annealing Study

Isochronous annealing has already been used in Section 3.2.3 for the investigation of the changes in the macroscopic properties. Regarding the description of the experimental procedure, the reader is referred to that section. For the two ion-implanted samples (M20609, M20708 see Table 3.4) it will now be discussed in detail which related processes could be detected on the microscopic scale using the TSC method. A correlation of these results with the macroscopic properties will be presented separately in Section 3.4.

Spectra Obtained on a Weakly Damaged Device (Φ_{eq} = 9.76×10^{11} cm^{-2})

As outlined in the previous sections, it must be born in mind that the filling conditions strongly influence the obtained spectra. In order to gain a comprehensive representation of all defect levels, various sets of measurement parameters have been applied (compare Section 3.3.3.4). Fig. 3.54 a) displays the observed variation of the TSC spectrum with the annealing temperature when electron traps were filled by cooling down under zero bias. In the early stages of the annealing experiment peak N always compensates for all of the positive space charges. Thus, no deep traps but those causing the TSC signal N were filled. After the 150°C annealing step, the left-hand side of the composed peak N started to anneal out and, following the 210°C anneal, the remaining fraction N_c was sufficiently isolated to allow for a thorough determination of the deep level parameters $\Delta H'$ and σ by the delayed heating method, see Section 3.3.3.7, which are in very good agreement with those well-known for the transition $VV^{(-/0)}$. The decomposition of peak N into two portions has originally been introduced in reference [FRE96], where similar annealing studies were presented, however, using the C-DLTS method. Finally, at the 290°C anneal, an electron trap causing a TSC peak at around 145 K emerges, which has been labeled L'. The annealing of peak N reduces the compensation and therefore enables the partial filling of traps further away from the middle of the band gap. Whichever are the concentrations of the deeper levels (L' and N), the heights of the peaks F and I are modified accordingly, which must not be confused with a real annealing effect.

For comparison Fig. 3.54 b) shows the corresponding spectra where the electron traps have been filled by switching to zero bias after cooling down under reverse bias. Several filling temperatures have been used and the curves presented in Fig. 3.54 b) were combined in such a way that the optimum filling of the deep levels is represented: A and C have been filled at 25 K, F at 50 K, and all others at 80 K. In addition to the more shallow peaks that were not filled in Fig. 3.54 a) it is worth noting the absence of peak L' under these conditions indicating either a small electron capture cross section, as compared for example to the doubly charged divacancy $VV^{(-/-)}$ (peak I), or a metastable behavior. Moreover, yet another electron trap, H', which anneals in is found on the left-hand side of peak I.

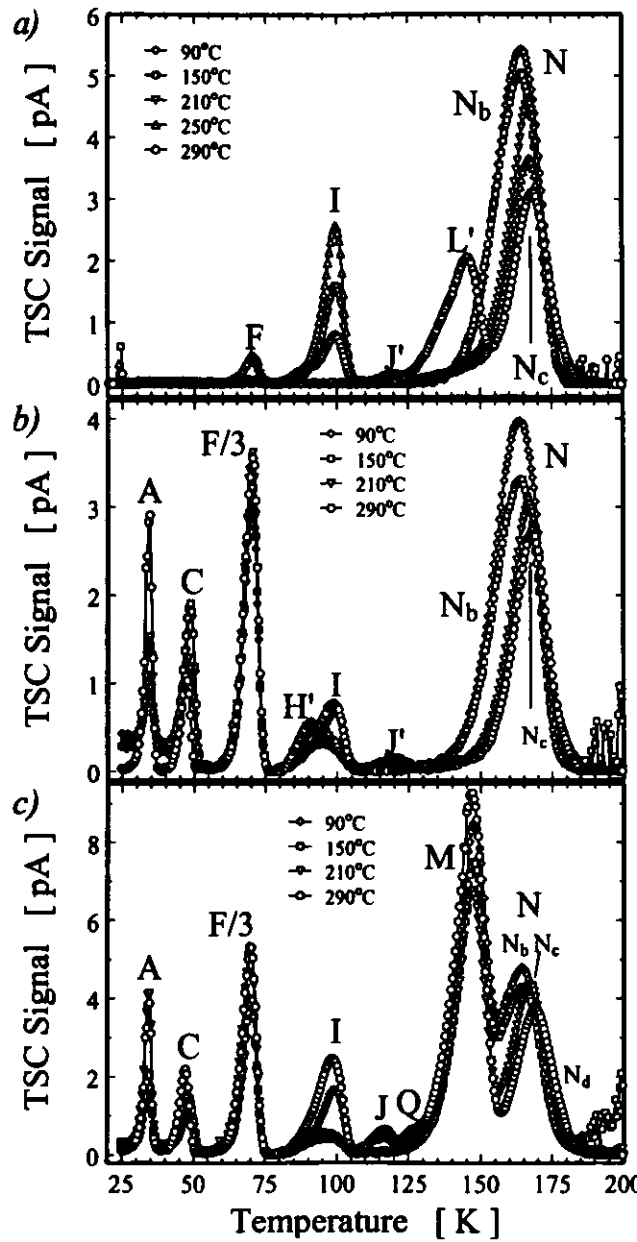

Fig. 3.54 Isochronous annealing of the TSC spectrum measured on the device M20609 (Φ_{eq} = 9.76×10^{11} cm^{-2}).

After filling electron traps by cooling down under zero bias. While the annealing of peak N and the emergence of peak L' is properly represented by this figure, the heights of the peaks F and I do in the first place reflect the varying filling factor arising from the different compensation conditions, see text.

Composite TSC spectra obtained after filling electron traps by switching to zero bias for 30 s at an appropriate temperature: 25 K for peaks A and C, 50 K for peak F, and 80 K for peaks H' through N. Peak F has been scaled down by a factor of 3 for better visibility.

Detection of electron and hole traps by applying a 30 s long injection pulse of 1.7 mA at low temperature. The spectra were composed the same way as noted under b).

Finally, electron and hole traps have been filled simultaneously by applying a forward injection current at low temperature, Fig. 3.54 c). Again the filling factor depends on the injection temperature and therefore the spectrum has been composed the same way as in Fig. 3.54 b). The filling of the hole traps J and Q, which are annealing in, is actually improved for 20 K injection, which has however not been included in the figure. It is noted that under these experimental conditions peak N shifts to higher temperatures during the isochronous annealing experiment than observed in Fig. 3.54 a) and b). It must therefore be concluded that a hole trap, N_d, grows on the right-hand side of N at the later annealing stages.

Evaluation of Defect Concentrations and Discussion

Concentrations of defect levels were derived from these TSC spectra by integrating the corresponding peak currents (eq. 3.78), however, omitting those peaks, which were not sufficiently isolated. Regarding the various filling modes, for each peak only one of them has been found to give the largest filling factor and was thus used preferentially. Accordingly, appropriate procedures were applied for the accurate determination of the defect concentrations. These have already been outlined in Sections 3.3.3.4 for the particular device under consideration. Here it should be noted that in order to avoid current injection from the back plane contact during the TSC measurement always a reverse bias of 50 V has been used which is closely below the full depletion voltage measured at room temperature. The evaluated data have been normalized to the irradiation fluence and are presented in Fig. 3.55 a) and b) as function of the temperature of the preceding annealing step. In some cases a significant shift of the peak temperature has been observed which implies that those peaks do not originate from a single defect, and that their composition is varying in the course of the annealing (Fig. 3.55 c)).

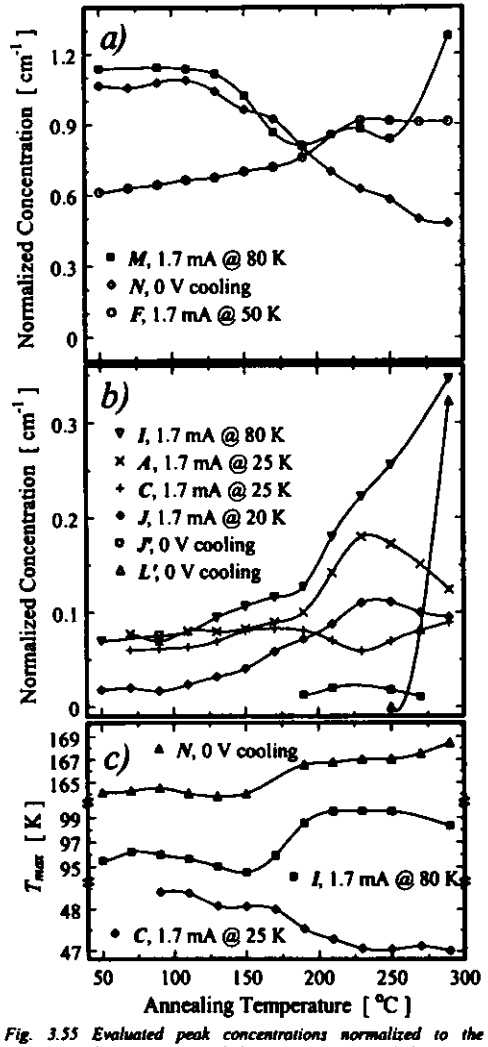

Fig. 3.55 Evaluated peak concentrations normalized to the irradiation fluence (open symbols: electron traps, filled symbols: hole traps): a) dominant peaks b) smaller peaks, various filling methods were applied as indicated. c) Temperature shift of the peaks N, I, and C.

The shift observed on peak N in Fig. 3.55 c) suggests that N_x anneals out at around 175°C. However, the sum of N_x and N_d is diminishing continuously without marked stages (above 100°C)*, in agreement

* Concerning peak N, as shown in Fig. 3.55 a), it will be noted that due to the compensation the concentration quoted for the first annealing temperatures reflects the lower limit.

with the observations made in reference [MOL96] using C-DLTS. Concerning the divacancy level $VV^{(-/0)}$ it has however often been argued in the literature that the corresponding peak appears to be broadened if the divacancies are located in strained lattice regions, i.e., in the vicinity of disorder which is predominantly introduced by heavy particle damage (compare Section 3.3.1.1). In this field the work of B.G. Svensson et al., who systematically studied the level as function of the energy and mass of the particles used for damaging the crystal, is noteworthy in particular [SVE93]. There are therefore serious objections to the view that peak N is composed of two different fractions (? + $VV^{(-/0)}$). In this picture the shift in the peak temperature, which also is observed on the $VV^{(-/-)}$ transition (peak I), could reflect a reduction of the lattice strain by suitable thermally activated rearrangements. Moreover, according to the model developed in [SVE91], lattice strain significantly reduces the rate of the bond-switching, which is crucial for the formation of the motionally averaged quantum-mechanical states of the VV constituting the energy levels in the forbidden gap. As the bond-switching is thermally activated this effect is more pronounced at low temperature, i.e., below a certain temperature the levels do not exist. In particular this accounts for the striking observation frequently made in C-DLTS studies that the concentration of the doubly charged divacancy appears to be smaller than that of the singly charged. In analogy, upon reduction of the lattice strain by the elevated temperature annealing, the apparent concentration of $VV^{(-/-)}$ would be expected to be growing until a one to one ratio with respect to $VV^{(-/0)}$ is accomplished. The changes observed in the concentration of peak I in Fig. 3.55 b) appear to be in agreement with this view.

As already discussed in the Section 3.3.3.4, the C_iC_s pair does not contribute to peak F for the specific filling conditions chosen. The growth of peak F observed in Fig. 3.55 a) does therefore indicate an increase in the $VO_i^{(-/0)}$ (A-center) concentration. It is thus highly likely that the annealing of peak N liberates vacancies which consequently are captured at the dominant sink, namely, interstitial oxygen. Peak M, which was assigned to the transition $C_iO_i^{(-/0)}$ exhibits a 25% reduction at around 150°C. As the annealing temperature of C_iO_i is much higher (see Appendix B), it is concluded that peak M is composed of $C_iO_i^{(-/0)}$ and another unknown transition. The marked increase in peak M at the end of the experiment can not be excluded to be due to the emergence of the overlapping peak L', since L' might become filled by the forward current injection.

The data on the smaller peaks in the spectrum have been compiled in Fig. 3.55 b). These are of particular interest as in terms of the defect concentrations the changes in $N_{eff,RT}$ were found to take place in the same order of magnitude (compare Section 3.2.3). Except for the peaks C and I, which tentatively were assigned to the transitions $C_iC_s(B)^{(-/0)}$ and $VV^{(-/-)}$, the chemical origin of the various TSC signals is not known. Among the defects anticipated in radiation damaged silicon the C_iC_s pair is one of the least stable and should anneal out at around 300°C (Appendix B). In fact, the annealing behavior observed on peak C in conjunction with the shift of the maximum temperature detected in Fig. 3.55 c) indicates a transformation of the defect close to 200°C.

Possible candidates for the defect giving rise to the peak L' which emerges at approximately 290°C would be higher order V_xO_y complexes. However, obviously there is no corresponding reduction of the VO_i or VV concentration, which should be noticed upon complex formation with interstitial oxygen. Since also none of the other peaks is annealing out, it is unlikely that the defect is arising from the reconfiguration of radiation damage-induced defects at all. Finally, it will be noted that the peak temperature of J' is similar to J, which implies that the concentration determined for J probably reflects the sum of both.

Spectra Measured on a Heavily Damaged Device ($\Phi_{eq} \approx 3.82\times10^{13}$ cm^{-2})

It has been discussed extensively in Section 3.3.3.4 that defect concentrations can hardly be determined from TSC measurements on heavily damaged devices. In addition one has to envisage large leakage currents deteriorating the spectra. However, the TSC method can still serve as a tool for monitoring the defects which then at least allows for the qualitative correlation with the macroscopic properties. These considerations are of particular interest since it has been found in Section 3.2.3 that the macroscopic annealing behavior is different for weakly and heavily damaged devices. It would therefore also appear to be difficult to predict the macroscopic properties, which are of practical interest chiefly in the high fluence range, from the results obtained on weakly damaged samples.

In inverted detectors one can exclusively fill hole traps when the negative space charge is frozen during the cooling and defects are filled at low temperature by switching to zero bias (compare Section 3.3.3.4). Corresponding spectra have been recorded in the course of the isochronous annealing

experiment (Fig. 3.56 a)). A comparatively large reverse bias voltage of 50 V had to be used in order to obtain TSC signals significantly larger than the system noise. A strong increase in the leakage current was noticed, and it was for example impossible to detect the $C_iO_i^{(*,0)}$ transition at the later annealing stages. Still peak H and peak J are sufficiently remote from the temperatures where the leakage current predominates and appear to grow. Here it needs to be recalled that also the negative space charge is found to increase (see Fig. 3.10 a)), which then, for the particular mode of trap filling discussed here, enhances the hole filling.

More reliable results were obtained when a 1.7 mA forward current was injected for 30 s at 20 K, see Fig. 3.56 b). A reverse bias voltage of only 0.1 V was chosen as it is suitable to overcome the problems arising from the leakage currents. Although leakage current data has thoroughly been subtracted, at the later annealing stages a useful spectrum is still observed only for measuring temperatures below 150 K. All peaks originating from hole traps (H, J, Q, and M) are growing in these spectra. It is of particular interest to note that the two peaks J and Q, whose concentrations are known to be comparatively small (see Fig. 3.54 c)), are becoming predominant regarding their peak heights. This feature, which must be related to the specific experimental conditions, is not understood. Nevertheless, at least in part would the growth of the peak heights be expected to reflect an increase of the corresponding defect concentrations.

It has been described in Section 3.2.3 that in inverted detectors elevated temperature annealing generates a bulk defect which can be cycled reversibly between its two bistable states. The excited state, which makes $N_{eff,SCR}$ more negative, can easily be prepared in the experiment by simply injecting free carriers. This provides a means to unambiguously detect the corresponding deep levels in the TSC spectrum: The sample in question has been stored at room temperature for at least one day after quenching from the isochronous annealing temperature. This allows for the settling of the depletion voltage, i.e., the de-excitation of the bistable defect, compare Fig. 3.12. After recording the TSC spectrum as described above, an excitation current of 1.7 mA was injected for 20 min at 290 K. According to the systematic investigation into the transformation kinetics in reference [MOL95], this procedure is sufficient to entirely excite the bistable defect. On the thus prepared sample the TSC measurement was repeated using identical experimental parameters.

Now, Fig. 3.56 c) shows the subtraction ΔI of the TSC spectrum gathered before excitation from the one after excitation. The above program was carried out successfully at the four annealing temperatures indicated. It is evident that only peak J responds to the preparation of the excited state. This particularly unique relationship between the change in a macroscopic property (e.g. $N_{eff,SCR}$) and a sole defect level will be discussed again in Section 3.4.

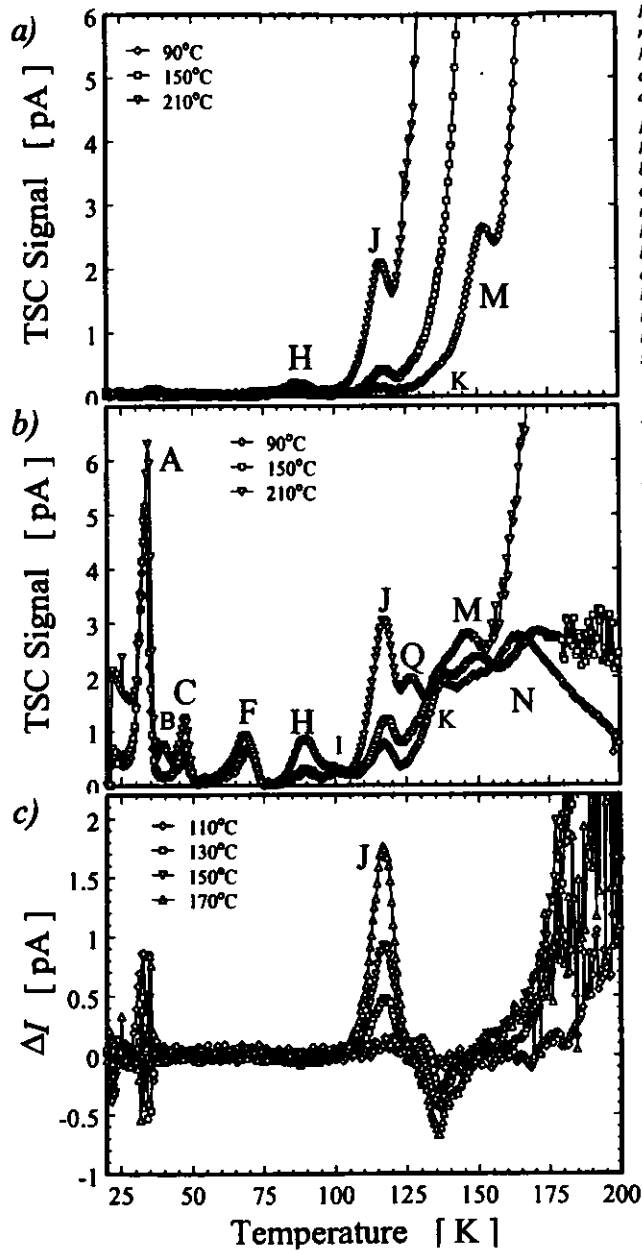

Fig. 3.56 TSC spectra measured on the device M20708 (Φ = 3.82×10^{11} cm^{-2}) after the indicated annealing step.

Defect filling was achieved here by switching to zero bias at 20 K for 30 s after cooling the sample under a reverse bias of 50 V. Only hole traps are filled because the frozen space charge is negative. The leakage current, which is increasing very much in this sample, was not subtracted.

A 1.7 mA forward current was injected for 30 s at 20 K prior to recording these TSC spectra using a reverse bias of 0.1 V. The leakage current has been subtracted.

Difference of the TSC spectrum measured before the excitation and the one measured afterwards. The parameters of the measurements were identical to b). The modified depletion width after excitation in conjunction with the large leakage currents cause the increase of ΔI above 160 K.

3.3.3.7 Determination of Level Parameters $\Delta H'$ and σ

Numerous methods designed for the analysis of TSC spectra have been reported in the literature. They are all aiming at the extraction of the characteristic parameters $\Delta H'$ and σ which for each defect level determine the variation of the emission rate with temperature (eq. 3.51)*. This is usually achieved by measuring the emission rate at various temperatures and plotting these data in semi-logarithmic scales as function of the inverse temperature (Arrhenius-plot). In general there is a trade-off between the accuracy of the obtained results and the required experimental effort. Here, the latter refers in particular to the number of spectra that need to be recorded, i.e., the total measurement time.

Among those methods requiring only a single spectrum is the one put forward by J.G. Simmons and G.W. Taylor [SI271], which was already sketched in Section 3.3.3.1. They simply make use of the maximum temperature and the peak width at half maximum. In addition the defect concentration can be inferred from the peak height. Moreover, frequently the so-called initial-rise method is used, which exploits that according to eq. 3.77 the detected current is proportional to the emission rate as long as the total number of emitted carriers is small compared with the defect concentration. An Arrhenius-plot can therefore be constructed from the left-hand side of the TSC peak signal under study. Only recently T. Schulz has suggested a refinement of this procedure, the integral analysis, in which he determines the concentration of yet occupied traps in eq. 3.77 by integrating the peak current [SCH95]. This then allows the extension of the Arrhenius-plot towards higher temperatures. Finally, it is worth mentioning the deconvolution method as described by M. Bruzzi in reference [BRU95]. Basically, the full equation derived for the TSC current signal, eq. 3.80, is fitted to the measured spectrum by simultaneous variation of $\Delta H'$, σ, and also the concentration of initially occupied traps. It is then possible to take into consideration several traps and to resolve complicated signals originating from overlapping TSC peaks.

It should however be born in mind that all these methods depend crucially on the shape of the TSC peaks which can be seriously distorted if for instance the depletion width is varying during the emission of the trapped carriers. Further, the initial-rise method is suitable only if current signals orders of magnitude smaller than the maximum peak current can be accurately measured. This is however often hampered by the system noise or a base-line signal. Regarding the deconvolution method it must be stated that the analysis of overlapping peaks cannot be done unambiguously, rather is it necessary to make some reasonable suppositions for the capture cross sections of the traps.

A natural shortcoming of the TSC method lies in the fact that the temperature is not a constant which renders the precise determination of the sample temperature very difficult (see Section 3.3.2). While also the variation of the heating rate, one of the two methods used in this work, suffers from this problem, the delayed-heating technique does not, and hence furnishes results of superior accuracy. Moreover, both methods do not rely on the peak shapes but require the recording of several spectra under specific experimental conditions, as will be described in the following.

Variation of the Heating Rate

This method is traced back to M.G. Buehler, who has pointed out in reference [BUE72] that the peak temperature T_{max} depends on the heating rate β, compare eq. 3.79. Minor rearrangements of the formula leads to

$$\text{eq. 3.94} \qquad \ln\left(\frac{T_{max}^4}{\beta}\right) \approx \frac{\Delta H'_{n,p}}{k_B}\frac{1}{T_{max}} + \ln\left(\frac{\Delta H'_{n,p}/k_B}{B\sigma_{n,p}\, m_{dC,V}^*/m_0}\right).$$

where it has been assumed that the correction $2T_{max}$ supplied to the term $\Delta H'_{n,p}/k_B$ can be neglected, since it arises from the weak T^2 dependence of the emission rate (eq. 3.51). If thus the temperature of a particular peak is considered in several TSC spectra measured with different heating rates, a plot of $\ln(T_{max}^4/\beta)$ versus $1/T_{max}$ is expected to give a straight line. Accordingly, the slope α_2 of a straight line $\alpha_1 + \alpha_2/T_{max}$ fitted to the data furnishes the emission enthalpy $\Delta H'$. This then needs to be combined with the constant α_1 in order to evaluate the emission cross section σ according to the term on the right-hand side of eq. 3.94.

* In order to apply the appropriate value of the effective mass one has to ascertain in advance, whether one is dealing with an electron or a hole trap.

Such experiments have also been conducted in this work, and Fig. 3.57 presents the corresponding spectra obtained on a heavily damaged device (M20708, $\Phi_{eq} = 3.82\times10^{13}$ cm^{-2}). The traps have been filled by a 30 s lasting injection of around 1.65 mA at 20 K. It was possible to vary the heating rate β over a wide range of two orders of magnitude. The upper limit of around 1 K/s is imposed, on the one hand, by the maximum heating power provided by the temperature controller and, on the other hand, by the heat capacity of the sample mounting. The latter is an increasing function of temperature, which accounts for the fact that the highest rate of around 1.4 K/s could not be obtained above 100 K. There are also two natural limits for the smallest feasible heating rate. While the first concerns the total measurement time, which for example was around five hours for the smallest β chosen, the second arises from the signal-to-noise ratio, as according to eq. 3.81 the TSC signal is in the first approximation proportional to β.

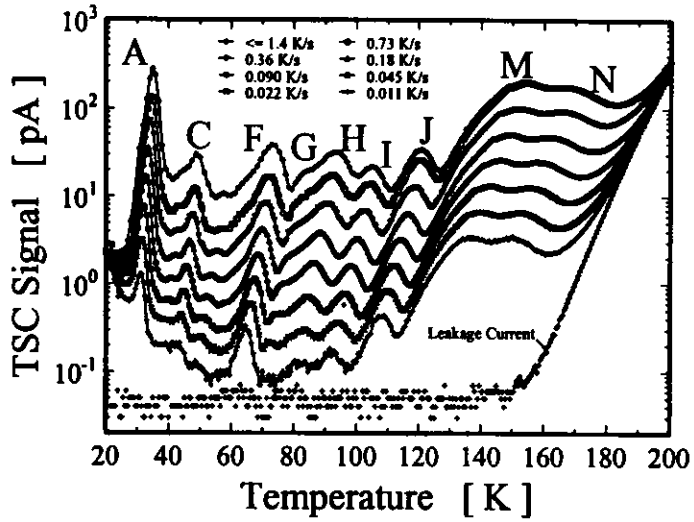

Fig. 3.57 A variation of the heating rate experiment conducted on a heavily damaged sample (M20708, Φ_{eq} = 3.82×10^{13} cm^{-2}, 6.5 months room temperature annealing, $V_{dep} \approx 65$ V, $V_{bias} = 50$ V). The various heating rates β are indicated in the figure. Trap filling was achieved by forward current injection at 20 K ($t_{fill} = 30$ s, $I_{fill} \approx 1.65$ mA).

Now, concerning all TSC signals for which an unambiguous determination of the peak temperature was possible, an analysis according to the aforementioned program has been tried, see Fig. 3.58. In addition to the data presented in Fig. 3.57, for the peaks F, I, and J also similar TSC measurements in which the traps have been filled at 50 K were taken into account. Moreover, some supplementary data points for peak F were obtained on a weakly damaged device*. It will be noted that the heating rate is not precisely a constant during all of the temperature scan. Therefore, it was necessary to determine appropriate values of β in the neighborhood of the particular peak under study. This can be done off-line, as both time and temperature are recorded.

The data plotted in Fig. 3.58 exhibit a significant scatter and deviations from the predicted straight line relation. Further, the evaluations of the peaks F and I were not very well reproduced with respect to the different sets of TSC spectra analyzed. It has therefore been tried here, to give a first order estimate of the statistical error for the individual data points. A chief source of uncertainty clearly must be sought in the sample temperature. The reproducibility of the temperature between two arbitrary TSC temperature scans has been assumed to be 1 K. This error is thought to arise from long term temporal variations in the temperature distribution of the whole experimental set-up (Section 3.3.2). In addition, it

* Device M20609, $\Phi_{eq} = 9.76\times10^{11}$ cm^{-2}, for details see [HEY96].

has been asserted that there is a disagreement between the temperature of the sample and the temperature sensor arising from the finite thermal conductivity of the mounting. Given the one is trailing the other during the TSC temperature scan, larger differences are expected at higher heating rates. It is arbitrarily put here that this error is 1 K for a heating rate 0.183 K/s, the value which typically has been used. Accordingly, the error $\sigma_{T_{max}}$ in the evaluated T_{max} data was calculated by $\sigma_{T_{max}} = 5.464\,s \times \beta + 1\,K$. Standard error propagation then yields the corresponding error in the quantity $\ln(T^4_{max}/\beta)$, which is depicted in Fig. 3.58.

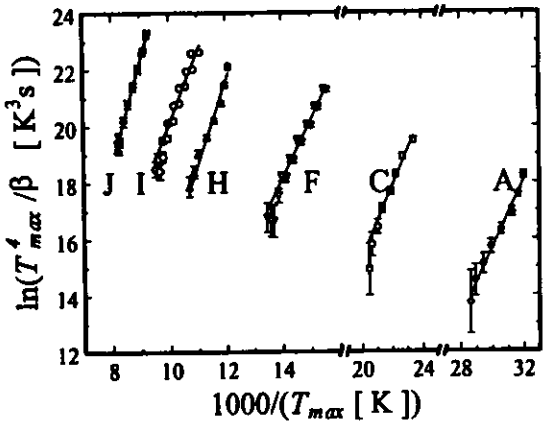

Fig. 3.58 Evaluation of the level parameters according to eq. 3.94 from the T_{max} data evaluated on TSC spectra that were obtained for various heating rates, compare Fig. 3.57. Concerning the error bars, see text.

Thus it was possible to make use of a weighted least-squares procedure for the calculation of the straight-line fit (Appendix D), and the results are listed in Table 3.18. In the last column the correspondingly minimized χ^2's normalized to the number of degrees of freedom (D.o.F) of the fit have been quoted. A value larger than one does therefore indicate that the errors in the individual data points have been underestimated. Accordingly, then also the errors given for the evaluated parameters are too small*.

Table 3.18 Level parameters evaluated with the variation of the heating rate method. σ_u and σ_l denote the upper and lower error bound of the cross section. Regarding the reliability of the estimated errors, see text.

Peak	Type	ΔH^* [meV]	σ_l, σ_{min}, σ_u [cm²]	χ^2 / D.o.F.	Transition
A	*n*	104±7	$(0.2, 2.4, 37)\times10^{-16}$	0.9	?
C	*n*	108±6	$(1.3, 5.8, 27)\times10^{-15}$	1.4	$C_iC_s(B)^{(-/0)}$
F	*n*	181±4	$(2.3, 4.4, 8.5)\times10^{-14}$	2.7	$VO_i^{(-/0)}$
H	*p*	260±7	$(1.4, 3.8, 10)\times10^{-13}$	10	$VV^{(+/0)}$
I	*n*	220±4	$(1.0, 1.6, 2.5)\times10^{-16}$	19	$C_iP_s(III)^{(0/+)}$?
J	*p*	321±4	$(0.9, 1.5, 2.3)\times10^{-15}$	1.6	?

In addition there are yet unrecognized systematic errors, which however have to be taken into account if the presented results are compared with literature data. For instance, the variation of the depletion width can shift a peak. For the given experimental conditions it is a specific difficulty met with peak A, compare Section 3.3.3.4. Further, the position of peak I was found to depend on the electric field

* In the first approximation a better estimate of the error in ΔH^* can be gained by multiplying the quoted value with the square-root of the given normalized χ^2.

strength, which accounts for the badly reproduced maximum temperatures of the two sets (20 K and 50 K injection) of spectra studied. Moreover, the data evaluated for the peaks C and H seem not to be in agreement with the assumed straight line model. The presented derivation of the level parameters appears to be appropriate only for the peaks F and J. Thus, the overall performance of the variation of the heating rate method is not convincing. Still, more reliable data would be awaited on weakly damaged devices. Finally, it is noted that the temperature range which can be exploited for the construction of an Arrhenius-plot is quite small, as for instance compared to DLTS, see Section 3.3.4. Consequently, it is very difficult to accurately determine cross sections using the variation of the heating rate method.

Delayed Heating

The most powerful recipe regarding the deep level characterization by the TSC technique has been put forward by J.C. Muller et al., who have described the method of delayed heating in reference [MUL74]. In a unique way they combine the advantages of an isothermal technique with the resolving power of TSC measurements. The basic idea lies in the modification of the trap filling pulse.

Consider the end of the filling period and assume that the filling factor is equal to one, i.e., $n_t(0)$ or $p_t(0) = N_t$, whichever is the type (electron or hole trap) of the deep level under study. Upon reverse biasing the diode the initial filling can evidently be altered in a very controlled fashion by simply retaining the sample at the low temperature T_d for a certain delay period t_d before the regular TSC temperature scan is initiated. The filled defects are therefore allowed to emit the trapped carriers which changes their initial occupation according to an exponential decay law

eq. 3.95 $$\{n_t(0), p_t(0)\} = N_t \exp\left(-e_{n,p}(T_d)t_d\right).$$

This relation follows directly from the solution of the rate equation eq. 3.68 when the temperature is assumed to be a constant (isothermal decay) and one of the emission rates predominates. The height of the peak under consideration, which is proportional to the initial occupation (see eq. 3.81), will thus be a function of the delay time t_d. This is demonstrated in Fig. 3.59 for the transition $C_iO_i^{(-/0)}$ (peak M), which among others has been studied here.

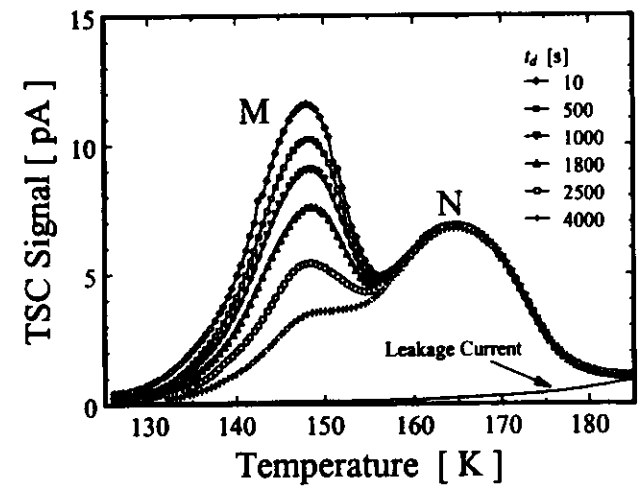

Fig. 3.59 Delayed heating measurement on the $C_iO_i^{(-/0)}$ donor level. The set of TSC curves shown was obtained for a delay temperature T_d = 126 K and for the delay times t_d (device M20609, Φ_{irr} = 9.76×10¹¹ cm⁻², 6 months room temperature annealing, V_{bias} = 74 V, I_{pol} = 1.7 mA, t_{pol} = 30 s, V_{dep} = 71 V, β = 0.19 K/s).

According to eq. 3.95 a semi-logarithmic plot of the peak height versus the delay time is supposed to give a straight line. Thus, $e_{n,p}(T_d)$ can be derived from an appropriate straight-line fitting procedure, which is presented in Fig. 3.60. The determination of the emission rate as function of temperature requires the recording of sets of TSC spectra like in Fig. 3.59 at various delay temperatures T_d. A conventional Arrhenius-plot can then be employed to determine the level parameters (Fig. 3.61).

Evidently, the delay temperature T_d, which has always been chosen equal to the filling temperature T_{fill}, must be sufficiently small compared with the peak temperature T_{max} in order to allow for an accurate assessment of the considered peak. For typical heating rates, of the order of 0.1 K/s, the emission time constants at the delay temperature $1/e_{n,p}(T_d)$ are then found to be much larger than one second. Delay times t_d should be chosen in the range from zero to few times the emission time so as to recognize the full exponential decay transient. In practice, delays ranging from 1 s to 10000 s (≈ 3 hours) were realized, where the lower bound is due to the assembly speed of the computerized set-up and the upper bound due to the total measurement time.

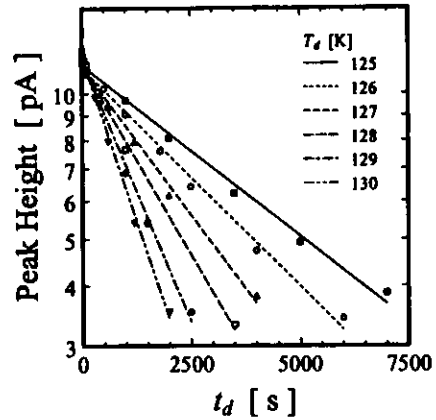

Fig. 3.60 Determination of the emission rate at various delay temperatures by means of a straight-line fit (compare Fig. 3.59).

Regarding the use of the peak height as a measure of the initially filled trap concentration it is noted that the heating rate β is then implicitly assumed to be a constant. However, as the variation of the sample temperature is connected with a time constant characteristic of the temperature controller and the sample mounting, the sample temperature initially trails the nominal temperature before it, accompanied by some minor oscillations, settles into the desired linear increase. Thus, if T_d is close to T_{max}, fake peaks can sometimes be observed which however merely reflect the modulation of the genuine TSC signal. It is therefore recommended to utilize the integral of the TSC current instead of the peak height. The integration, which must be started right after the end of the delay period, does not depend on the temperature profile and, according eq. 3.78, is proportional to the concentration of initially filled traps.

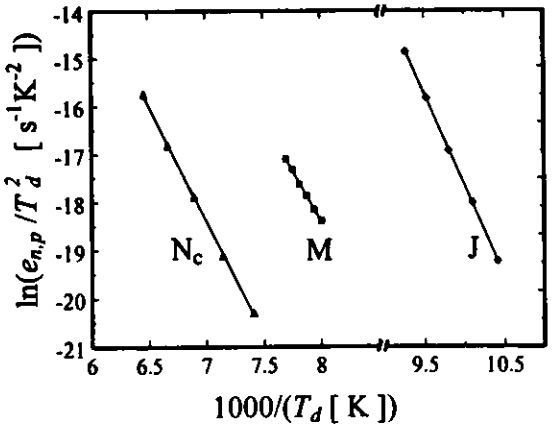

Fig. 3.61 Arrhenius-plots constructed from delayed heating experiments.

Besides peak M, the delayed heating method could in this work successfully be applied for the study of two other transitions, namely the peaks J and N_c, and a compilation of all results is given in Table 3.19. While in the case of M and J the trap filling was achieved by forward current injection, the trap corresponding to N_c has been filled by cooling down under zero bias (Fig.3.54 a)). Further, in the former case the peak heights have been evaluated, whereas in the latter case the integrated current was employed.

It has also been tried to analyze numerous other defect levels, however, only in the above mentioned three cases a reasonable Arrhenius-plot did result. Those studies were chiefly carried out on heavily damaged samples, and it must be concluded that the peak heights or integrals do not reasonably well reflect the concentration of initially filled traps if the deep level concentrations are large. In particular it is noted that the peak studied by the delayed heating method usually is the first TSC signal in the spectrum, which was previously suspected to be seriously affected by the variation of the depletion width encountered during the emission of the trapped carriers, see Section 3.3.3.4. Only the evaluation of peak J was not affected by these circumstances, probably because the transition is located at a unique position in the spectrum, next to the dominant hole trap peak M, which then essentially controls the width of the depletion region. Regarding the more shallow levels (peaks A, C, etc.), it was at times observed that the apparent emission rate was more or less independent of the sample temperature. This unexpected behavior can be understood, if the optical emission due to infra-red stray light is considered which is expected to dominate the total emission rate at low temperatures. Also peak N, as presented in Fig. 3.59, has been subjected to delayed heating. Although the defect concentrations were sufficiently small, a reasonable evaluation was not possible. The peak temperature shifts upwards as function of the delay time, reflecting the composite character of the peak. Only by means of the deconvolution technique a decomposition into several peaks can be obtained, see [HEY96].

The error margins quoted for $\Delta H'$ and σ in Table 3.19 were derived from the fit as described in Appendix D. They therefore reflect the agreement between the data presented in Fig. 3.61 and the straight-line model. The estimated standard errors in the individual data points have not been included in Fig. 3.61, since they hardly can be distinguished from the symbols, confirming the high accuracy of the Arrhenius-plots.

Table 3.19 Delayed heating results (devices M20609 / M20708 $\Phi_m = 9.76\times10^{11}$ cm^{-2} / 3.82×10^{13} cm^{-2}).

Peak	Device	Annealing State	Type	$\Delta H'$ [meV]	$\sigma_\infty, \sigma_{poo}, \sigma_\infty$ [cm^2]	Transition
J	M20708	12 months room temperature	h	326±2	(2.5, 3.2, 4.2)×10^{-13}	?
M	M20609	6 months room temperature	h	363±7	(1.2, 2.4, 4.8)×10^{-15}	$C_iO_i^{(+/0)}$
N_c	M20609	isochronous, after 90 min 210°C	e	413±5	(0.78, 1.1, 1.7)×10^{-15}	$VV^{(-/0)}$

A major source of systematic errors is the limited accuracy of the used temperature sensor. Bearing in mind that this has not been considered, the agreement between the data found on the transitions $C_iO_i^{(+/0)}$ and $VV^{(-/0)}$ and the corresponding values reported in the literature (see Appendix B) must be considered excellent*. It will be noted that the results obtained by the C-DLTS technique on the same cryostat system do match the data presented here even better [MOL96]. Concerning the determination of level parameters this emphasizes the role of the sample temperature, which stabilizes during the particularly long delay periods applied in the delayed heating method and therefore is very accurately known.

* In order to complete the results gained by delayed heating on the cryostat system shown in Fig. 3.33, the values obtained by T. Schulz on the A-center are cited here: $\Delta H_n' = 168$ meV and $\sigma_\infty = 7.7\times10^{-15}$ cm^2 [SCH95].

3.3.3.8 Summary of the Defect Studies Using TSC

- It was shown that the deterioration of TSC spectra (e.g. peak shifts and kinks) observed on heavily damaged high resistivity detectors can be explained by the variation of the depletion width as function of the measuring temperature. An overall reasonable agreement between measurements and simulations was found, leading to a simple recipe for the extraction of accurate defect concentrations.

- TSC spectra were studied on samples irradiated by fluences ranging from 10^{11} to 10^{14} cm^{-2} using three different modes of deep level filling. Chief considerations were the determination of the level type (electron versus hole trap) and defect concentrations.
  1. Cooling down under zero bias.
     Fills majority carrier traps until Fermi level pinning occurs.
     Has given the most accurate introduction rates for electron traps.
  2. Switching to zero bias at low temperature after cooling with reverse bias.
     Fills with majority carriers, predominantly levels with large concentrations and cross sections.
     The bistable defect C_iC_s is prepared in a specific state, which allowed for the determination of the ratio $[C_iC_s]/[VO_i] = 0.19$ for the material studied.
  3. Injecting a forward current of around 1.7 mA at 25 K, 50 K, and 80 K.
     Fills electrons as well as hole traps, however, depending on the injection ratio p/n and the ratio between the capture coefficients c_p/c_n.
     On weakly damaged devices ($N_i < N_{dEff}$) and at sufficiently high temperatures the injection current obeys the Shockley-diffusion model. Otherwise a p-i-n diode like double injection takes over, which was discussed in terms of the recombination length/lifetime in the presence of variable defect concentrations and considering the charges trapped into deep levels.
     A characteristic feature of the p-i-n model, namely, a constant voltage drop across the diode independent of the injected current could be confirmed experimentally.
- An electric field dependent enhancement of the emission rate was observed on one peak, which was tentatively assigned to $C_iP_s(III)^{(0/+)}$.

- After around 400 d storage at room temperature the following introduction rates (equivalent 1 MeV neutron data) were found for the dominant damage-induced defects

  $g_{C_iC_s} = 0.16\,\text{cm}^{-1}$, $g_{C_iO_i} = 1.06\,\text{cm}^{-1}$, $g_{VO_i} = 0.84\,\text{cm}^{-1}$,

  $g_{N_b+VV} = 2.02\,\text{cm}^{-1}$, and $g_{VV} > 0.7\,\text{cm}^{-1}$.

  N_b is a defect related to the left-hand side broadening of the peak arising from the transition $VV^{(-/0)}$.

- The variation of the TSC spectrum as function of the filling temperature was found to be due mainly to a temperature dependent hole capture coefficient of the C_iO_i donor, which was determined to be

$$c_{p,C_iO_i}(T) \propto \exp\left(-\frac{35\,\text{meV}}{k_B T}\right).$$

  This was also shown to consistently explain the variation of the TSC spectrum as function of the duration of the free carrier injection pulse encountered under specific experimental conditions.

- TSC spectra were recorded on one weakly ($\Phi_{eq} \approx 10^{12}$ cm^{-2}) and one heavily ($\Phi_{eq} \approx 4\times10^{13}$ cm^{-2}) damaged device in the course of an isochronous annealing study. All modes of defect filling were used.
  A continuous reduction of the divacancy related peak N ($N_b + VV^{(-/0)}$), a liberation of vacancies, and a disappearance of the peculiarities of the spectrum characteristic of heavy particle damage was observed.
  On the heavily damaged device the height of a single peak was found to be increased after injection of free carriers at room temperature. This was found to be connected with the corresponding increase in the negative space charge related to the excited state of a bistable defect.

- Deep level parameters have been extracted from TSC spectra using the variation of the heating rate and the delayed heating method.
  The accuracy of the variation of the heating rate method was found to be unsatisfactory due to the experimental difficulty of determining the exact sample temperature.
  The following very reliable results were obtained with the delayed heating method,

  $C_iO_i^{(+/0)}$: $\Delta H'_p = 0.363\,\text{eV}, \sigma_p = 2.4\times10^{-15}\,\text{cm}^2$
  $VV^{(-/0)}$: $\Delta H'_n = 0.413\,\text{eV}, \sigma_n = 1.1\times10^{-15}\,\text{cm}^2$

  The unknown hole trap giving rise to peak J has been characterized on a heavily damaged device, which due to the variation of the depletion width might introduce large systematic errors in the evaluated parameters: $\Delta H'_p = 0.326$ eV, $\sigma_p = 3.2\times10^{-13}$ cm^2.

3.3.4 Current DLTS with Optical Filling

Deep Level Transient Spectroscopy (DLTS), as originally introduced by Lang [LAN79], is a very powerful tool for the study of defect levels in semiconductor diodes. Like TSC, DLTS is a so-called space charge spectroscopy method, however, employing a unique technique for the determination of emission rates as function of temperature. ionization enthalpies and cross sections are obtained by constructing an Arrhenius-plot, compare for example the delayed heating method (Section 3.3.3.7). It is the high accuracy and in particular the short time needed to analyze all traps in the sample (in modern systems one temperature scan) which has made DLTS so popular.

This however is strictly valid only for the well-established variant measuring the diode capacitance (C-DLTS), typically at 1 MHz. For the instance of large trap concentrations $N_t > 0.1 \times N_s$, where N_s denotes the shallow doping concentration, or if a considerable series resistance exists due to the neutral bulk, which is a particular problem met with high resistivity samples as used for this work, the standard C-DLTS theory that is based on several simplifications does not hold anymore and the accurate data evaluation is rendered more difficult. Moreover, if the free carrier concentration freezes out due to compensation (e.g. $N_t > N_s$, compare Section 3.3.1.4) it is not possible to apply C-DLTS at all as then neither the high frequency capacitance can be used to probe the width of the field zone nor majority carrier traps can be filled by changing the diode reverse bias.

Now, as already stated in the previous sections, large defect concentrations are frequently encountered in radiation-damaged silicon detectors. Accordingly, there has recently been a growing interest into the I-DLTS technique which utilizes the current signal generated in the field zone by the emission of carriers from the trap in question (no retrapping)*, as generally a current signal can be detected irrespective of the concentration of defects present in the material. Further, optically generated free carriers are used to accomplish the trap filling which has been found more reliable than voltage pulse filling (forward current injection)† [LI395]. Semiconductor laser diodes are commonly used for this purpose because of their good pulsing capabilities and easy instrumentation. However, more experimental efforts are needed as compared to electrical pulsing and in addition the active volume depends on the illuminated spot size which is not very well known. The latter hampers the extraction of accurate trap concentrations, and therefore optical filling has not been used for TSC.

The following paragraphs will develop the theory for the level parameter evaluation, describe the experimental I-DLTS set-up that was used in this work, and present results for the most prominent deep levels. Advantages and short-comings of the method will be discussed.

3.3.4.1 Theory

Basically the DLTS method records the transient signal reflecting the decay of an intentionally prepared non-stationary trap occupation towards the steady state. Because the current signal, which will be explored here, comes from the space charge region and the process takes place at a specific temperature, which is kept constant, the electron occupation of a particular trap $n_t(t)$ at the time t can immediately be deduced from eq. 3.68,

eq. 3.96 $$n_t(t) - n_t^* = \left[n_t(0) - n_t^*\right] \exp\left(-(e_n + e_p)t\right).$$

Here n_t^* and $n_t(0)$ denote the steady state and the initial electron occupation, respectively. Evidently the trap occupation relaxes by both electron and hole emission. In practice, except for close to midgap levels, one of the corresponding emission rates is however found to dominate.

If for example $e_n >> e_p$, which is true for a level in the upper half of the band gap given the capture coefficients are of the same order, it is $n_t^* \approx 0$. That is, in the non steady state situation the trap is occupied with electrons which are emitted into the conduction band during the relaxation. It is due to these circumstances that such levels are called electron traps, compare the discussion in Section 3.3.1.2.

* It is noted that this must not be confused with the PICTS (Photo-Induced Current Transient Spectroscopy) technique which measures the variations of the conductivity in the neutral bulk, see for example [YO183].

† This is especially true for the surface barrier samples used for the DLTS studies in this work, as the Schottky barrier becomes blocking at low temperatures and no current injection is possible at all.

Now eq. 3.96 can be substituted into eq 3.67 which generally holds for the current density j_{tot} related to a single trap in the space charge region. Using the expression derived for the steady state leakage current j_{tot}^* from this trap (eq. 3.75), the resulting equation can be written in the following convenient form

eq. 3.97 $$j_{tot} - j_{tot}^* = -q_0 \frac{e_n\left[n_t(0) - n_t^*\right] + e_p\left[p_t(0) - p_t^*\right]}{2} \exp\left(-(e_n + e_p)t\right) W_g .$$

Although the right-hand side of this equation can be either negative or positive, the total current j_{tot} must always be negative, compare eq. 3.67. However, in some rare situations ($e_n \approx e_p$, appropriate initial occupation) the total current can increase as function of time.

Next one has to determine the initial occupation established by the free carrier injection pulse preceding the transient decay. Injection of very high concentrations of either electrons or holes would just fill electron or hole traps completely, i.e., $n_t(0) = N_t$ or $p_t(0) = N_t$, respectively. However, in the I-DLTS measurements presented in this work the free carriers were injected into the field zone, which can lead to relatively small concentrations, see below. Also simultaneous injection of electrons and holes has to be taken into account. For the sake of conciseness we will restrict to a simple electron trap, i.e., assume $e_p \approx 0$ and $n_t^* \approx 0$, a more general treatment is straight-forward though. Equivalent expressions for hole traps can be found by simply exchanging the subscripts n and p in the expressions that follow. Moreover let us assert that electrons n and holes p are present during the filling pulse with homogeneous concentrations throughout the depleted zone. This premise is erroneous in particular, for example if only electrons are injected at the surface the corresponding drift current $j_n \propto n\mu_n E$ is spatially uniform, however, the electric field E is linearly graded. Thus, the free carrier concentration generally varies with distance. The simplified treatment given here therefore deals with an average value. Otherwise the solution of the problem would be much more complicated and not valuable for the further usage.

Introducing the emission time constant $\tau = 1/e_n$, the electron capture time constant $\tau_0 = 1/(n\,c_n)$, and the electron filling factor $f = (1 + (p\,c_p)/(n\,c_n))^{-1}$ (compare eq. 3.83), which is ranging from 0 to 1. Neglecting hole emission, i.e. $e_p = 0$, the steady state solution of eq. 3.46 governing the trap occupation can be written

eq. 3.98 $$\frac{n_t(0)}{N_t} = f \frac{1}{1 + \frac{f\tau_0}{\tau}} .$$

Complete filling of an electron trap is therefore only achievable if the capture rate for electrons $n\,c_n$ is much larger than a) the corresponding hole capture rate $p\,c_p$ and b) the corresponding electron emission rate e_n. The current I_{tot} which is measured in the external circuit during electron emission from a single trap is given by

eq. 3.99 $$I_{tot} = I_{offset} + \frac{1}{2} q_0 S W_g N_t f \frac{1}{\tau + f\tau_0} \exp\left(-t/\tau\right).$$

Here I_{offset} accounts for the steady state leakage currents from all other traps in the sample and any additional source of leakage current. S is the area illuminated by the laser light and W_g is the active depletion layer thickness.

A schematic representation of eq. 3.99 for the idealistic situation where $f\tau_0$ is much smaller than τ is presented in the upper half of Fig. 3.62. Three different values for the emission time constant have been used in order to illustrate the effect of the sample temperature on the measured signal. It is clear that this systematic variation with temperature can be exploited in order to evaluate the deep level parameters. In principle it is possible to fit eq. 3.99 to the measured transient data which would give an optimized value of the emission time constant $\tau = 1/e_n$ at a particular temperature. Repeating this procedure at various temperatures would then allow to construct an Arrhenius-plot. However, it is desirable to do the data evaluation off-line which would then require a huge amount of transient data to be stored.

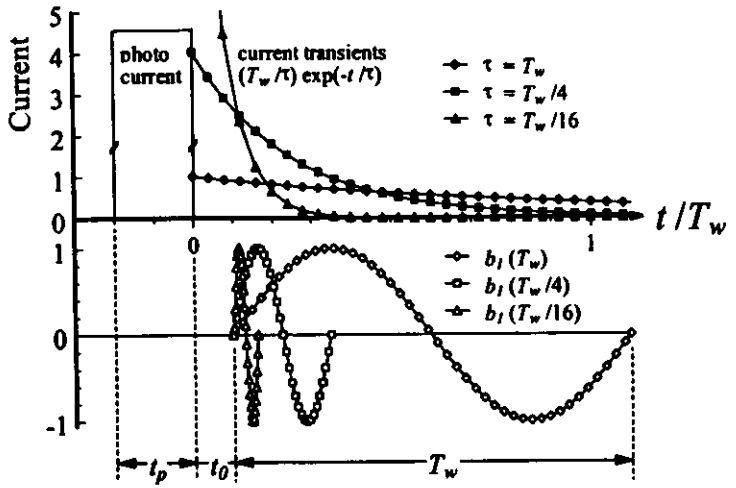

Fig. 3.62 The upper half displays typical current signals observed during the I-DLTS measurement and the lower half shows three of the 14 weighting functions used for the data evaluation. A large photo current is flowing during the pulse period t_p when the optically generated free carriers are injected. After the delay period t_0 the transient data is recorded within the rate-window T_w.

It is mainly for the purpose of data reduction that in DLTS only a reduced numerical representation of the transient data is used. Generally the integral, also often referred to in terms of the correlator signal*, is calculated over the transient using a specific weighting function. The set-up applied in this work uses sine and cosine functions with different period widths T_w^* and applied to different portions of the transient data, see the lower half of Fig. 3.62. At every temperature and for every rate-window T_w a set of 14 coefficients is calculated from the measured current data I_{tot}^{meas} according to the following expressions

eq. 3.100 $$a_l^{meas} = \frac{2}{T_w^*}\int_{t_0^*}^{t_0^*+T_w^*} I_{tot}^{meas}(t)\cos\left(2\pi\frac{t-t_0^*}{T_w^*}\right)dt,$$

eq. 3.101 $$b_l^{meas} = \frac{2}{T_w^*}\int_{t_0^*}^{t_0^*+T_w^*} I_{tot}^{meas}(t)\sin\left(2\pi\frac{t-t_0^*}{T_w^*}\right)dt.$$

Each coefficient carries a label related to the parameters t_0^* and T_w^* as defined in Table 3.20. Since the experimental transient data is recorded into an array, eq. 3.100 and eq. 3.101 are essentially evaluated by a summation procedure which, due to the use of harmonic weighting functions, can be derived from a standard Fast-Fourier-Transformation algorithm, for details see [WEI91]. However, only first order Fourier coefficients are used. Therefore, the method emulates a multiple lock-in DLTS technique rather than it is of the FFT-DLTS type, which has been introduced by [IKE85].

* Historically this stems from the first DLTS set-ups which would not even have the possibility to store data at all but rather had to use box-car integrators or lock-in amplifiers to get an on-line representation of the transients.

Table 3.20 Definition of the b_l and a_l via the parameters t_0^* and T_w^*, compare Fig. 3.62, eq. 3.100, and eq. 3.101.

Coefficient	a_l b_l	a_{lN} b_{lN}	a_{lM} b_{lM}	$a_l(T_w/2)$ $b_l(T_w/2)$	$a_l(T_w/4)$ $b_l(T_w/4)$	$b_l(T_w/8)$	$a_l(T_w/16)$ $b_l(T_w/16)$	$b_l(T_w/32)$
T_w^*	T_w	$T_w/2$	$T_w/2$	$T_w/2$	$T_w/4$	$T_w/8$	$T_w/16$	$T_w/32$
t_0^*	t_0	$t_0+T_w/2$	$t_0+T_w/16$	t_0	t_0	t_0	t_0	t_0

In order to understand the method used for the off-line evaluation of the DLTS temperature scan data it is now instructive to explore which values of the various coefficients are to be expected if the transient signal $I_{tot}^{meas}(t)$ were equal to the one deduced theoretically for a single trap by eq. 3.99. Making use of the abbreviations for the angular frequency

eq. 3.102 $$\omega_0 = \frac{2\pi}{T_w^*}$$

and the signal amplitude

eq. 3.103 $$A = \frac{1}{2}q_0 S W_g N_t f$$

the analytical solution of the integrals eq. 3.100 and eq. 3.101 can be written

eq. 3.104 $$a_l = \frac{2A}{T_w^*}\frac{1}{\tau+f\tau_0}\exp\left(-t_0^*/\tau\right)\left[1-\exp\left(-T_w^*/\tau\right)\right]\frac{\tau^{-1}}{\tau^{-2}+\omega_0^2}.$$

eq. 3.105 $$b_l = \frac{2A}{T_w^*}\frac{1}{\tau+f\tau_0}\exp\left(-t_0^*/\tau\right)\left[1-\exp\left(-T_w^*/\tau\right)\right]\frac{\omega_0}{\tau^{-2}+\omega_0^2}.$$

It is of particular interest to note that any constant leakage current signal cancels out and does not influence the DLTS evaluation. In contrast to TSC, I-DLTS can therefore study levels close to the middle of the band gap. However, the initial assumptions do then not hold true, and a thorough data analysis would require the exact expression according to eq. 3.97 to be used. In this case it should be born in mind that the DLTS signal is also allowed to become negative.

Now, for a given experimental situation, i.e., the rate-window T_w, the delay period t_0, and $f\tau_0$ are fixed to a specific value, eq. 3.104 and eq. 3.105 can be shown to exhibit a unique localized maximum at τ_{max} if plotted as function of the emission time constant τ. As $\tau = 1/e_n \propto 1/(\sigma_n T^2 \exp(-\Delta H'_n/k_B T))$ is a monotonically decreasing function of the temperature, the experimental values obtained for the various coefficients eq. 3.100 and eq. 3.101 plotted versus temperature display a peak for every trap. Thus, for a particular trap the peak temperature T_{max} can be evaluated for all considered coefficients and can be related to the unique emission time constant τ_{max} calculated by numerically maximizing eq. 3.104 and eq. 3.105. Finally, an Arrhenius-plot $\ln(\tau_{max} T_{max}^2)$ versus $1/T_{max}$ is constructed to obtain σ_n and $\Delta H'_n$.

Although there are other ways to obtain the emission time constant as function of the temperature, for example by evaluating the ratio of b_l^{meas} and a_l^{meas}, the so-called maximum-temperature method as described above is the most widely used and has been found very reliable. The major short-coming of the situation analyzed in this work is that it was not possible to neglect the term $f\tau_0$, i.e. the capture time constant, as due to the comparatively small concentration of injected free carriers $f\tau_0$ frequently was found to be of the order of the emission time constant τ. However, $f\tau_0$, which must be known in order to maximize eq. 3.104 and eq. 3.105, is not known a priori. Therefore, initial values τ'_{max} have been determined using the DLTS evaluation computer program, which assumes $\tau_0 = 0$. That is, in the first approximation the amplitude A in eq. 3.104 and eq. 3.105 absorbs the neglected term according to

eq. 3.106 $$A\frac{1}{\tau'+f\tau_0} = A'\frac{1}{\tau'} \Rightarrow A'(\tau') = A\frac{1}{1+f\tau_0/\tau'},$$

resulting in an amplitude A' that depends on the emission time constant τ'. The right-hand side of eq. 3.106 was therefore fitted to the data reported by the DLTS computer program for A'_{max} and τ'_{max} which gives estimates of the true amplitude A and the term $f\tau_e$. A constant relative error has been assumed for the amplitude, i.e., $\ln(A'_{max})$ has been used for the fitting procedure. Corrected values of the time constants τ_{max} were then found by maximizing eq. 3.104 and eq. 3.105, however, now taking the obtained term $f\tau_e$ into account.

3.3.4.2 *Experimental Considerations*

A block diagram of the I-DLTS system representing the electrical circuitry and the used apparatus is shown in Fig. F.3 of Appendix F. Light with an energy above the band gap from three different lasers has been used for optical filling: 670 nm, 830 nm, and 980 nm. Corresponding absorption lengths in silicon and a discussion of the losses in the gold layer of surface barrier detectors is given in Appendix A. While the 670 nm light is absorbed within a short distance below the front contact, the 980 nm light penetrates very deeply into the silicon bulk material. In the presence of an electric field below the front electrode (reverse biased, not inverted detector) electrons will be swept through the space charge region in the former case whereas in the latter case electrons and holes are available for the filling of traps.

The current signals were fed into a current-voltage converter (preamp) which furnishes an amplification of around 10^6 V/A. Any further signal processing was done by the DLTS equipment [COH]. In this system the input voltage signal is first adapted to the following electronics by a variable gain amplifier. An anti-aliasing filter (eighth-order Bessel [WEI91]) is then used to remove high frequency noise from the signal before digitizing it in the ADC. Finally, the signal is digitized and stored in a transient recorder at up to 1024 points. Also averaging of several transients is possible which significantly improves the signal-to-noise ratio. The operation voltage of the laser diodes is supplied by the pulsing unit that also triggers the transient recorder. The preamp electronics was modified to a DC coupled configuration* because otherwise the AC coupling time constant would have interfered with the averaging process in an uncontrolled fashion.

For a given rate-window T_w the coefficients a_i and b_i act on the whole transient and $b_i(T_w/32)$ on the initial $T_w/32$ fraction. One of the most valuable functions of the DLTS system used is that the rate-window can be changed during the temperature scan of the sample, thus, obtaining very accurate transient information within a minimum time period. The useful range of rate-windows is however restricted. A lower limit is given by the minimum time required for one digitization by the ADC in the transient recorder hardware (2 µs). If all coefficients given in Table 3.20 are to be exploited at least 64 points should be recorded per transient, which makes the minimum rate-window equal to 128 µs. A rise-time of 30 µs has however been noticed in the voltage amplifier, and rate-windows smaller than 640 µs were not found suitable. To the other end the limit is imposed by the signal-to-noise ratio. Let us assume the emission time-constant τ were of the order of the rate-window and thus close to the value which maximizes the a_i or b_i coefficients. The total signal amplitude is inversely proportional to τ and correspondingly the absolute current is the smaller the large T_w. Also measurement time becomes an important issue then, in particular since a large number of averages would be desirable in this situation. While several hundred times averaging was possible for the smallest rate-windows, no more than 2 transients were averaged for the largest rate-window of around 5 s. In order to ensure complete filling, pulse periods t_p were mostly chosen of the order of 100 milliseconds, irrespective of the size of the rate-window. The number of digitization points per transient was always chosen as large as possible, chiefly the maximum value 1024 has been used. Rate-window variations were then accomplished by adjusting the conversion time of the ADC. Both the accuracy of the transient digitization and the rise time due to the anti-aliasing filter, which depends on the ADC conversion time, benefit from this way of operation.

As can be seen from eq. 3.99, the amplitude of the current signal is growing for decreasing τ, i.e., increasing temperature (cf. Fig. 3.62). The evaluation of deep level parameters from I-DLTS data therefore puts considerable weight to the initial fraction of the transients. Accordingly, the preamp should recover very swiftly from the overflow condition which due to the large photo-current may occur

* The capacitor coupling the current-to-voltage converter unit and the voltage amplifier unit was short-circuited. The small difference between the DC levels in these two units could be eliminated by a regular offset-compensation applied to one of the op-amps.

during the free carrier injection pulse. Related problems were overcome by applying a convenient delay period t_d. There is however a trade-off between the signal-amplitude and the reduction of the signal distortion. It is noted here that the time elapsing from the end of the filling pulse to the beginning of the transient record must be very accurately known. Especially the analog signal delay due to the Bessel-filter has to be taken into account, see [WEI91]. Moreover, regarding the specifications of the preamp in addition to a large bandwidth which allows for a bigger range of emission rates to be studied also a large dynamic range is desirable.

An overview of the various samples studied, mostly surface barrier detectors with a very thin gold layer establishing the Schottky-contact (40 µg/cm²), is given in Table 3.21. Typically the diodes were operated under a large reverse bias in order to activate a considerable fraction of the detector volume. The mounting of the samples in the closed-cycle helium cryostat was similar to the TSC set-up, see Fig. 3.33 in Section 3.3.2. As outlined there, minor modifications were necessary to allow for optical filling.

Table 3.21 Samples investigated with I-DLTS. Regarding the particle sources, compare Table 3.1.

Device	Φ_{eq} [10^{12} cm^{-2}]	Particle, Source	d [µm]	Bias [V]	Wavelength [nm]
937K03	1.19	n, PTB	390	50	670, 980
937K09	2.35	π^+, 192 MeV	390	10	830
937K13	0	-	390	50	830
937K29	2.86	π^-, 236 MeV	390	50	670, 980
935G23	37.2	π^+, 236 MeV	329	30	830
935G26	45.7	n, PTB	329	20	830
935G30	53.0	p, CERN PS	329	30	830
M21012	0	-	280	50	830

3.3.4.3 *Results*

General Characteristics of the Spectrum

Fig. 3.63 compares two I-DLTS spectra measured on a weakly damaged detector using either 670 nm or 980 nm light for trap filling. The labeling of the peaks is in agreement with the one introduced for the TSC spectra as will be demonstrated below. There are indeed large differences observed in the filling factor of the individual deep levels. Especially the peaks A, C, F, which, as was shown in Section 3.3.3.4, are all arising from electron traps can not be occupied effectively if both electrons and holes are injected. According to the above statements this indicates that in terms of the capture coefficients $c_p > c_n$ at the temperatures where those peaks are observed*. Moreover, other peaks, e.g. M, are found only in the 980 nm data. Correspondingly, those signals stem from hole traps. Further, some peaks are found to be filled by both lasers, for example X, Z, and O. For these cases it must be assumed that c_n is comparable or even larger than c_p. Employing different wavelengths for trap filling is therefore valuable in determining the type of a trap (e-, h-trap) and learning something about the ratio between the capture coefficients.

* It has been asserted here that n is of the order of p which is true if electrons and holes are generated more or less homogeneously throughout the active volume.

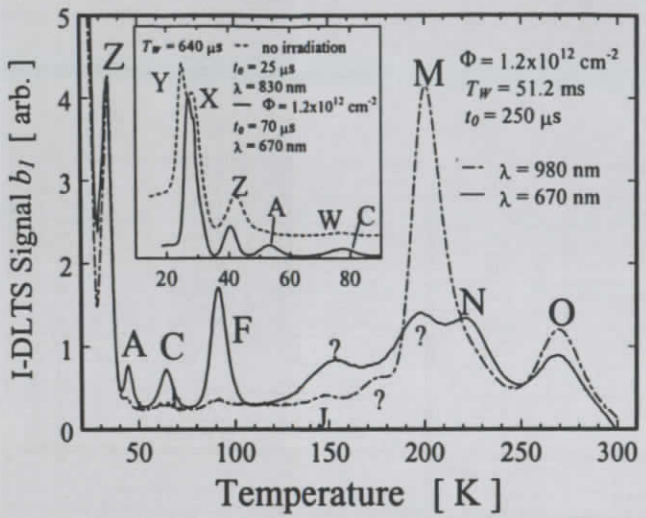

Fig. 3.63 Current Deep Level Transient Spectroscopy spectra measured on a weakly damaged device using optically generated free carriers with two different penetration depths for trap filling (device 937K03). The inset compares the low temperature part of the spectrum to a similar measurement performed on an undamaged device fabricated on the same wafer (937K13).

Compared with the TSC spectra measured on samples in the same fluence range additional signals are seen in Fig. 3.63. Firstly, the I-DLTS method inherently removes the constant leakage current baseline which makes levels close to midgap (e.g. peak O) accessible. Secondly, also shallow levels to the left-hand side of peak A, which was the first peak in the TSC spectra, are observed. The insert in Fig. 3.63 gives a magnified view of the corresponding data measured before and after irradiation for a more suitable, i.e., smaller rate-window. While in I-DLTS the traps are detected at temperatures where their emission time constants τ are of the order of ms, the corresponding TSC peaks require τ to be several orders of magnitudes larger, given typical heating rates. For this reason, the TSC spectra are shifted to lower temperatures as compared to the corresponding I-DLTS spectra, and accordingly, in contrast to TSC, the optical emission of trapped carriers due to the black body radiation and infrared stray light (see Section 3.3.2) does not affect I-DLTS. However, the constant base-line signal observed at the lowest temperatures in Fig. 3.63 is thought to reflect mere optical emission from the shallowest levels.

There are question marks assigned to several peaks in Fig. 3.63 whose level parameters could not be analyzed using Arrhenius-plots, see next section. In part the questionable signals might be related to the Schottky-contact on these diodes whose thermal stability is not well understood. In general, more reliable data are obtained on ion-implanted detectors. However, some of the peaks could originate from device processing-induced defects as already discussed on similar samples in reference [FRE96]. In particular, it was not possible to clearly identify the transition $VV^{(-/-)}$ which probably is hidden within the structure observed around 150 K of the spectrum using 670 nm laser light.

For heavily damaged samples the shape of the peaks, especially in the temperature range in which $C_iO_i^{(+/0)}$ and $VV^{(-/0)}$ are expected, was found to become severely distorted. An explanation as given in Section 3.3.3.3 in conjunction with similar effects observed on TSC peaks applies, i.e., the variation of the depletion width during carrier emission. In addition it should be recalled that for large trap concentrations it is not always easy to tell on which side of the sample the junction is located. Also, the differences between spectra obtained after filling with light of various penetration depths are much less pronounced. In the presence of high defect concentrations the trap filling appears to be established by

diffusion currents and the current signal obtained approaches the one realized in the PICTS method, measuring the conductivity of the neutral bulk. Only on weakly damaged devices an accurate analysis of all traps throughout the band gap was possible. On the more heavily damaged samples reasonable level parameters could however sometimes be obtained in the low temperature range on the left-hand side of peak F.

As already stated for TSC, the evaluation of trap concentrations in the high fluence range (> 10^{13} cm^{-2}) can not be performed in a unique way and is therefore highly questionable. Optical filling renders the extraction of trap densities even more difficult because the illuminated area S defining the active volume must be accurately known. Since S in this work was quite small, lateral diffusion effects and the mechanical stability of the diode laser fixture become important issues. An effort to exploit the peak amplitudes A has not given reliable results and for all the above reasons concentrations derived from I-DLTS measurements will not be given. Finally, it is noted that the investigation of the spectra measured on samples irradiated by different particle types, see Table 3.21, did not exhibit significant qualitative differences, i.e., always the same peaks were found, as expected (compare Section 3.1).

Evaluated Level Parameters

Emission enthalpies $\Delta H'$ and cross sections σ, that is, both parameters of the emission rate written in the form of eq. 3.51 have been determined according to the previously described maximum temperature method. Regarding the assumptions made to reach at eq. 3.51 compare the discussion in Section 3.3.1.4. The type of the trap (electron or hole trap) has previously been inferred from the qualitative observations made using different wavelengths for optical filling and determines the appropriate value of the effective mass. In order to illustrate the first order correction that was applied to the original evaluation furnished by the DLTS computer program, the bottom of Fig. 3.64 shows the signal amplitude A' as function of the corresponding inverse peak temperature for one particular case. The reasonable fit to the data reassures the validity of the above model based on the incomplete filling of the traps due to the high emission rate compared with the capture rate. In addition to the uncorrected Arrhenius-fit, the upper half of the figure displays the corrected data points with the corresponding fit. Both the cross section and the enthalpy derived from the uncorrected data were generally larger than the corrected values.

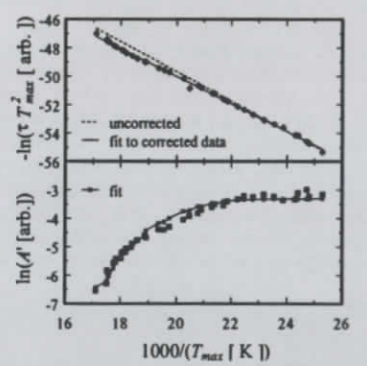

Fig. 3.64 Evaluation of peak A on the sample 937K03, 670 nm filling, compare Fig. 3.63. Top: Arrhenius plot, bottom: signal amplitude.

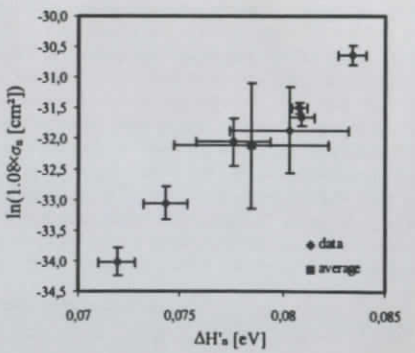

Fig. 3.65 Correlation of the cross sections and the corresponding enthalpies as evaluated for peak A on several samples.

Moreover, all cross sections obtained for peak A from seven evaluations have been plotted versus the enthalpy in Fig. 3.65. The error bars of the individual points were estimated from the χ^2 of the straight-line Arrhenius-fits assuming a constant error in the corresponding $\ln(\tau_{max}\, T^2_{max})$ data. Taking these error bars for granted, the individual evaluations do evidently not deliver the same cross sections and enthalpies but rather does the apparent linear relation between these values indicate a hidden parameter, which was not taken into account. Corresponding observations were made in [SCH95], and it was shown

there that this effect is due to the uncertainty in the measured sample temperature. Therefore, a point representing the unweighted average of the logarithms of the cross sections and the enthalpies has been calculated, and the overall variation of the level parameters has been expressed in terms of the standard deviation errors, see Fig. 3.65. Obviously, these errors are strongly correlated, that is, an experimenter who finds a larger enthalpy for peak A than the average value quoted below necessarily also would have to find a larger cross section in order to be consistent with the data presented here.

Finally, all results are compiled in Table 3.22. The number of evaluations that have been averaged per peak is given in the second column. Lower and upper limits of the cross section, σ_{lo} and σ_{hi}, have been calculated from the standard deviation error that was obtained for $\ln(\sigma)$, compare Appendix D. In order to demonstrate that the assignment of the peak labels is in agreement with the TSC data (compare Table 3.9), the corresponding peak temperature $T_{max,TSC}$ awaited in a TSC measurement with a heating rate of 0183 K/s has been calculated from the average level parameters (second-last column) using eq. 3.79. Most valuable are the results given for peak A and J which have at times been observed in radiation damaged detectors but which have so far not been accurately characterized and whose origin is unclear. Moreover, the shallow peaks W and Z have not been reported before. Since they are present in the unirradiated samples they have tentatively been assigned to thermal donors, compare for example [BEN83]. Although such defects would only be expected in Czochralski type material with large concentrations of oxygen it is argued here that the very small concentrations that have been observed in this experiment could be introduced by the thermal oxidation process. Peak X almost certainly arises from the phosphorus doping impurity which is supported by both the quoted enthalpy and the fact that it is present before irradiation. Peak Y in the insert of Fig. 3.63 could not be analyzed. However, the level is seen only for the 830 nm light filling which penetrates significantly into the silicon and therefore also fills hole traps, and the signal might therefore reflect the boron acceptor level. It must however be stated that the transient current for those shallow traps was not always a simple exponential decay (see next section). Finally, it is noted that it is not clear whether peak O is introduced by the radiation damage or by the processing of the device. The latter seems to be the case as there was no way to reconcile the level parameters and the finding that it is an electron trap with the data obtained with TCT measurements on the deepest levels introduced by radiation damage, which will be presented in a Section 3.3.5. The corresponding I-DLTS signals could however be hidden in peak O.

Table 3.22 Evaluated trap parameters using the I-DLTS method.

Peak	#	Type	$\Delta H'$ [meV]	σ_{lo}, σ_{max}, σ_{hi} [cm^2]	$T_{max,TSC}$ [K] for β = 0.183 K/s	Transition
X	5	e	42.6±4.4	(1.8, 5.7, 30)×10^{-14}	18.8	$P_i^{(0/+)}$
Z	6	e	63.3±2.3	(2.7, 5.6, 12)×10^{-14}	26.9	TD ?
W	1	e	159	(-, 1.2, -)×10^{-11}	53.5	TD ?
A	7	e	78.5±3.8	(0.38, 1.0, 2.9)×10^{-14}	34.6	?
C	7	e	113±6.6	(2.1, 5.9, 17)×10^{-15}	48.9	$C_iC_s(B)^{(-/0)}$
F	6	e	169±3.2	(3.6, 6.1, 9.9)×10^{-15}	70.2	$VO_i^{(-/0)} + C_iC_s(A)^{(-/0)}$
J	3	h	315±18	(0.35, 1.7, 8.0)×10^{-13}	115	?
M	3	h	369±25	(0.65, 2.9, 13)×10^{-13}	149	$C_iO_i^{(+/0)}$
N	2	e	411±11	(0.99, 1.6, 2.6)×10^{-15}	164	? + $VV^{(-/0)}$
O	4	e	533±11	(2.3, 3.9, 6.7)×10^{-15}	202	?

Shallow Impurity Levels in Unirradiated Devices

As outlined in the previous section, the I-DLTS method also provides a convenient tool for the investigation of shallow impurity levels. This is especially noteworthy as the absolute concentration of the shallow dopants phosphorus and boron in the unirradiated material is not well known. Only the net effective doping concentration N_{eff} can be determined, for example using CV measurements. However,

the degree of compensation has hardly ever been determined exactly and accordingly there has always been much room for speculations regarding the radiation-induced removal of phosphorus and boron atoms from substitutional sites and the corresponding annealing behavior.

Table 3.23 Unirradiated samples studied with I-DLTS.

Device	d [µm]	N_{eff} [10^{12} cm^{-3}]
937K13	390	0.268
M21012	280	1.42
BRBI11	375	3.35

In order to demonstrate that the I-DLTS method can be applied to resolve the above questions, basic work was performed here by studying the shallow levels on three differently doped unirradiated devices (Table 3.23). The level spectra, which have all been obtained using a rate-window T_w = 640 µs, a 830 nm optical filling pulse of duration t_p = 1 ms, and a delay period t_0 = 25 µs are displayed in Fig. 3.66. The reverse bias voltage was always equal to 50 V, which due to the varying doping concentrations depletes different fractions of the detector volume. If now free carriers are generated within the undepleted layer by the deeply penetrating 830 nm light, the excess minority carriers will recombine with a lifetime, which at room temperature typically is of the order of ms for unirradiated float zone material. Accordingly, a transient recombination current is resulting, giving rise to an I-DLTS base-line signal. This is found to be slowly growing as function of temperature, reflecting the variation of the recombination lifetime (Fig. 3.66). The effect is more pronounced on the lower resistivity samples as a larger fraction of the detector volume was not depleted by the used bias voltage. Only in the highest resistivity material the applied bias was sufficient to fully deplete the detector, and then the small peak W is resolved from the base-line. However, the most striking feature observed in Fig. 3.66 is that a large effective (n-type) doping concentration does not only correlate with a growth of peak X relative to peak Y, but also results in a larger concentration of peak Z relative to peak X. The former is in agreement with the previous assignments of peak X to phosphorus. If the tentative assignment of peak Y to boron is correct the data presented in Fig. 3.66 suggests that peak Z must be related to a shallow donor level in order to make the material n-type.

The curves shown in Fig. 3.66 must however be taken with care because, as is displayed in Fig. 3.67, the current transients were not always simple exponential decays as expected from eq. 3.99. It was even observed that a current peak emerges in the transient at 33.8 K. Inspection of the corresponding DLTS temperature scan in Fig. 3.63 (T_w = 51.2 ms) reveals that the transient is due to the emission from peak Z. A similar phenomenon has already been studied on the phosphorus and boron levels by Rosencher et al. who could consistently describe their data taking an enhancement of the emission rate by the electric field into account [ROS84]. Thereafter the electric field strength is growing in the vicinity of the junction of the reverse biased diode during emission of the trapped carriers which then increases the emission rate at those places. As argued in Section 3.3.1.4 a field enhanced emission would in the material studied in this work only be expected to arise for a Coulombic potential, i.e., a trap level which is charged after carrier emission. In conclusion, the observation of the peaked transient supports the previous assignment of peak Z to a thermal donor.

Since the evaluation of the DLTS spectra is based on the assumption of exponential decays the determination of concentrations is not straight-forward for the situation described above. I-DLTS can therefore so far only give some qualitative results regarding the shallow levels. Using integrated TSC currents should however give accurate data, whichever is the functional dependence of the emission rates on the temperature or the electric field strength. Given the experimental problems arising from the black body radiation and infrared stray light can be overcome, a combination of the two methods would be very suitable to systematically investigate the shallow level densities as function of irradiation fluence.

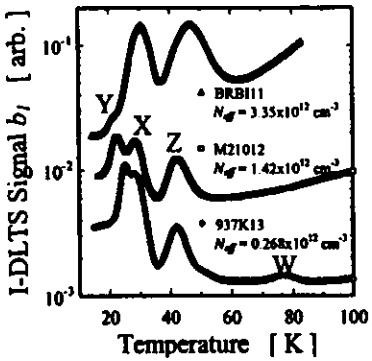

Fig. 3.66 Shallow impurity levels observed on unirradiated samples made from different initial resistivity material. The curves have been arbitrarily scaled for better visibility.

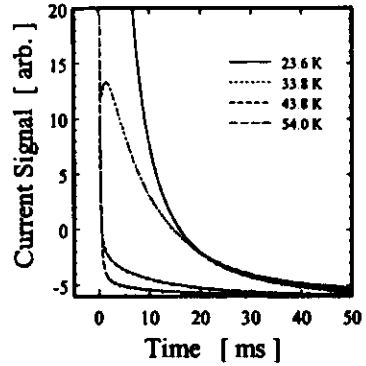

Fig. 3.67 Current transients observed in the low temperature range on the sample 937K03 using 670 nm light for optical filling, compare Fig. 3.63.

3.3.4.4 Summary of the Defect Studies Using I-DLTS with Optical Free Carrier Generation

- The models underlying the current-based deep level transient spectroscopy in conjunction with optical defect filling using a Fourier-DLTS system were outlined.
- It was found that the free carrier capture rate can become small compared with the emission rate, resulting in incomplete defect filling. A procedure has been proposed to correct for the corresponding errors in the Arrhenius-plot used for the extraction of the deep level parameters.
- It was shown that using different wavelengths for optical injection of free carriers the type of the defect levels (electron/hole trap) can be inferred. Further, in contrast to TSC, levels close to the middle of the band gap and very shallow levels can be assessed.
- Deep level parameters (no concentrations) were determined on bulk-damaged detectors and are compiled in Table 3.22.
- Shallow impurity levels in unirradiated samples were investigated on materials with different resistivity. It was found that besides the phosphorus level also other impurities, tentatively assigned to thermal donors, might contribute to the doping.

3.3.5 Investigation of Deep Levels Using TCT

An additional tool for the characterization of defect levels has recently been introduced by V. Eremin et al. in the references [ER294] and [ER295]. It is basically based on the determination of the variation of the total density of charges in the depleted region, N_{effSCR}, as function of the temperature using laser-induced current pulse shapes (TCT Transient Current Technique). TCT measurements have already been described in Section 2.6, and for purpose of orientation the reader may again notice the block diagram of the electrical set-up shown in Fig. F.4 in Appendix F. Also a detailed presentation of the mounting of the samples in the cryostat has been given previously, see Section 3.3.2. The recording of the data typically requires several waveforms to be averaged, and in general there will be a continuous stream of laser light pulses for a certain period of time. The laser light wavelength for all data presented in this section was 830 nm which according to Appendix A penetrates only around 10 µm and 30 µm into the silicon at 300 K and 77 K, respectively. As therefore predominantly one type of carriers is drifting through the field zone, electrons and holes can be studied separately, depending on the electrode which is exposed to the light.

It is now important to realize that under these experimental conditions N_{effSCR} is not given by eq. 3.63 anymore, but rather is affected by the trapping of the injected free carriers. Corresponding observations on a neutron damaged device reflecting the dynamic hole trapping process at 160 K are presented in Fig. 3.68. The transformation of the waveform is a function of the illumination time, and a steady state situation is reached after several minutes. The slope of the current signal in the center of the pulse reflects the gradient of the electric field, see Section 2.6. After 0.34 min illumination the pulse is more or less flat, i.e., the space charge is close to zero. After longer filling times the drifting holes are sensing a larger electric field strength at the end of their passage through the detector, which indicates a positive space charge. This is understood to arise from the accumulation of positive charges by the trapping of the drifting holes. It should be noted here that the free carriers used for probing the electric field and for filling the defect levels are identical. This is the simplest way to set up the experiment, however, utilizing different laser pulses for trap filling and induction of current pulses is conceivable.

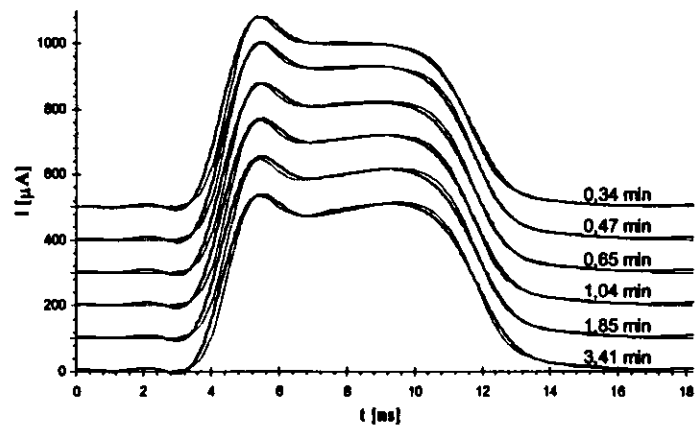

Fig. 3.68 Current pulse shapes measured as function of the illumination time at 160 K (device 504_81). Holes were injected at the rear contact using a laser repetition frequency of f = 100 Hz. A reverse bias of V_{bias} = 100 V has been applied and in order to guarantee reproducible initial conditions the sample has been warmed up to 240 K after each filling process. Thick lines: measurement data, thin lines: simulations. The waveforms have been shifted on the i-axis for better visibility.

Now, as will be argued below, the steady state current pulse shapes reflect a dynamic equilibrium between carrier trapping and emission. The emission process exhibits an exponential dependence on temperature, and accordingly the steady state waveforms vary with sample the temperature, as is shown in Fig. 3.69. Holes and electrons have been used for probing the field and filling the defects in Figure a) and b), respectively. Obviously, more charges can be trapped at low temperature. Also it is obvious that the analysis of electron trapping becomes very difficult due to the high electron mobility at low temperature which results in relatively short pulse lengths compared with the electronic risetime.

a)

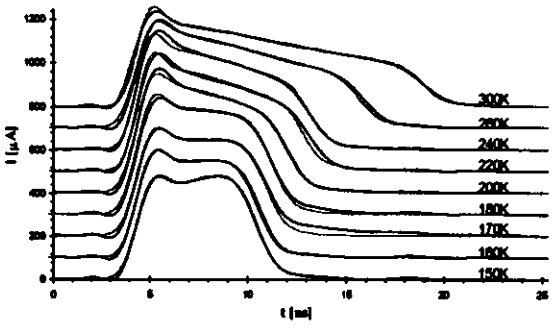

b)

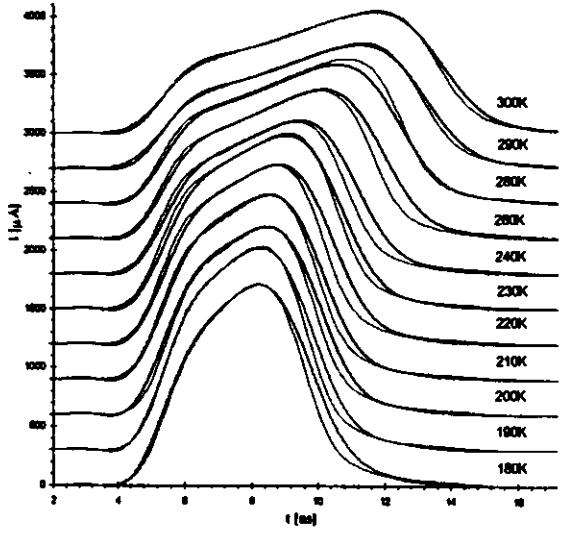

Fig. 3.69 Steady state current pulse shapes measured for temperatures ranging from 150 K to 300 K (device 504_81). The thick lines present the waveforms observed after a 5 min lasting illumination period, the thin lines are the corresponding simulations. The device was warmed up after each measurement.

a) Hole injection at the rear contact (f = 100 Hz, V_{bias} = 150 V).

b) Electron injection at the front contact (f = 100 Hz, V_{bias} = 100 V).

The measured data have always been analyzed by fitting simulated current pulses to the recorded waveforms. This method yields very accurate estimates of $N_{eff,SCR}$ because the dependence of the drift velocity on the electric field and temperature, the variation of the laser light penetration depth with temperature, and the deformation of the pulse by the electronic circuit can be taken into account. The good agreement between the simulated pulses (thin lines) and the measured data (thick lines) in Fig. 3.68 and Fig. 3.69 demonstrates the reliability of this approach.

All samples studied with the TCT method in this work are listed in Table 3.24. They are all p⁺-n-n⁺ ion implanted pad detectors fabricated from initial 3 kΩ cm n-type float zone refined silicon. While the device M21012 was supplied by the semiconductor laboratory of the MPI Munich [MPI], the two other samples were produced by the BNL Instrumentation Division's Silicon Detector Development and Processing Lab [BNL]. In order to allow for the injection of the 830 nm laser light, a hole of around 2 mm diameter was left in the aluminum metallization on the front and rear plane contact of each sample.

Table 3.24 List of the devices on which laser-induced current pulse shapes have been studied as function of temperature. Regarding the particle sources compare Table 3.1. $N_{eff,0}$ and $N_{eff,RT}$ denote the room temperature value of the density of space charges $N_{eff,SCR}$ before irradiation and at the time of the experiments, respectively.

Device	Particle Source	Dose	Annealing History	d [μm]	$N_{eff,0}$ [10^{12} cm^{-3}]	$N_{eff,RT}$ [10^{12} cm^{-3}]
504_81	^{7}Li(p,n)	Φ_{eq} = 3.4×10^{13} cm^{-2}	66.5 h at 80°C	291	1.40	-0.94
504_82	^{7}Li(p,n)	Φ_{eq} = 4.0×10^{13} cm^{-2}	66.5 h at 80°C	291	1.40	-1.14
M21012	^{60}Co-gamma	D = 5.02 MGy	-	280	1.42	-0.35

3.3.5.1 Modeling

Suppose that electrons or holes are injected into the electric field zone of a diode by illuminating the front or rear contact with continuously repeated pulses of short-ranged laser light. Let each pulse introduce N free carriers which drift through all of the diode within a time much smaller than the inverse repetition frequency $1/f$. The corresponding average photo current is then given by

eq. 3.107 $$I_{photo} = q_0 N f = q_0 S\{n,p\} v_{dr,n,p},$$

which on the right-hand side has been identified with the common expression for the drift current, and the illuminated area is denoted by S. Since, on the one hand, the total current must be spatially constant and, on the other hand, in general the electric field and thus also the drift velocity vary with distance, the average free carrier concentrations, either electrons n or holes p, are a function of distance too. The same then also holds true for the concentration of carriers trapped into defects, which renders the analytical approach to the subject very difficult. For the sake of convenience it will therefore be presupposed in the following that the free carrier concentrations can be represented by a constant average value. This in part is justified by the fact that the typically encountered electric fields are quite high such that the drift velocities are close to the saturation value. Moreover, always a good agreement was observed between the simulated current pulses and the corresponding measurements, demonstrating that the electric field strength stays linearly graded, i.e., charges are trapped homogeneously.

As outlined in Section 3.3.1.5, in the space charge region and in the steady state the levels in the upper half of the band gap are devoid of electrons, i.e., by analogy filled with holes, and the ones in the lower half are completely occupied with electrons. While thus only the former can trap electrons, only the latter can trap holes. Injection of either free electrons/holes will therefore change the occupation of each electron/hole trap according to the differential equation

eq. 3.108 $$\frac{\partial \{n_t,p_t\}}{\partial t} = \{n,p\} c_{n,p} \left(N_t - \{n_t,p_t\}\right) - e_{n,p}\{n_t,p_t\},$$

which has been derived from eq. 3.46. It has not been taken into account here that levels very close to the middle of the band gap can have significant emission rates for both electrons and holes. The solution of eq. 3.108 can be given very easily,

eq. 3.109 $$\{n_t(t), p_t(t)\} = \{n_{t,max}, p_{t,max}\}\left(1 - \exp(-t/\tau_{n,p,eff})\right)$$

where the initial value before the illumination must be zero according to the above statements. The effective filling time constant $\tau_{n,p,eff}$ is

eq. 3.110 $$\tau^{-1}_{n,p,eff} = \{n,p\}c_{n,p} + e_{n,p} = X_{n,p}c_{n,p}\left(\frac{\{n,p\}}{X_{n,p}} + N_{C,V}\exp\left(-\frac{\Delta H_{n,p}}{k_B T}\right)\right),$$

and the occupation approaches the steady state value

eq. 3.111 $$\{n_{t,max}, p_{t,max}\} = N_t\{n,p\}c_{n,p}\tau_{n,p,eff} = N_t\left(1 + \frac{X_{n,p}}{\{n,p\}}N_{C,V}\exp\left(-\frac{\Delta H_{n,p}}{k_B T}\right)\right)^{-1}.$$

In eq. 3.110 and eq. 3.111 the emission rates $e_{n,p}$ were substituted from eq. 3.48.

Qualitatively these relations express the following. While at high temperatures there is a very high chance for the trapped carriers to be reemitted immediately, resulting in an occupation close to zero, at low temperatures the carriers stick in the traps and permanently change the occupation to the maximum value. There is a characteristic intermediate temperature for each trap at which both rates for capture and emission are equal and the level is half full.

The resulting total density of space charges, which now is a function of illumination time and temperature, can be written

eq. 3.112 $$N_{eff,SCR}(T,t) = N_{eff,RT} \pm \left\{\sum_{hole\ traps} p_t(T,t),\ \sum_{electron\ traps} n_t(T,t)\right\},$$

where $N_{eff,RT}$ denotes the steady state value without free carrier trapping as it is established at room temperature according to eq. 3.63. As will be shown below, one can employing eq. 3.110 and eq. 3.111 derive the trap concentrations N_t, enthalpies $\Delta H_{n,p}$, and capture coefficients $c_{n,p}$ from systematic studies of the functional dependence of $N_{eff,SCR}$ on the temperature and filling time. It will be noted that the capture cross sections are not assumed to be a constant here. That is, the result of the evaluation is the correct value for the enthalpy, rather than $\Delta H'_{n,p}$, compare eq. 3.51.

3.3.5.2 Data Evaluation

According to the above equations any quantitative evaluation requires the knowledge about the free carrier concentration n or p established by the continuous illumination of the sample with laser light pulses. Rearrangement of eq. 3.107 gives

eq. 3.113 $$\{n,p\} = \frac{I_{photo}}{q_0 S v_{dr,n,p}} = \frac{f N}{S v_{dr,n,p}},$$

which indicates that one can either exploit the correspondingly induced average photo current I_{photo} or the total number of electron-hole pairs N generated by one light pulse. Here the latter is a variable parameter of the current pulse shape simulation and therefore known*. In any case is it necessary to insert appropriate values for the illuminated area S and the drift velocity $v_{dr,n,p}$. Using a graph paper, S was roughly determined to be 0.01 cm^2. As previously stated, the average injected free carrier concentrations are assumed to be spatially constant. Thus, the average electric field strength which is given by V_{bias}/d (compare Fig. 2.19) has been used in eq. A.1 (Appendix A) to calculate the corresponding average drift velocity in eq. 3.113.

* N can also easily be calculated by the integral of the current signal over time divided by the elementary charge, see eq. 2.27.

In this work only the photo current method has been used, and its extraction from the total leakage current I as function of the temperature T is illustrated in Fig. 3.70. The coordinate system was chosen such that in the first approximation the thermally activated bulk generation leakage current falls onto a straight line, see eq. 2.18. According to eq. 3.107, I_{photo} is virtually independent of temperature as it only depends on the light pulse repetition frequency f and the intensity of the laser light controlling the total number of generated electron-hole pairs N. The average of the total current at the lowest temperatures has therefore been identified with the photo current.

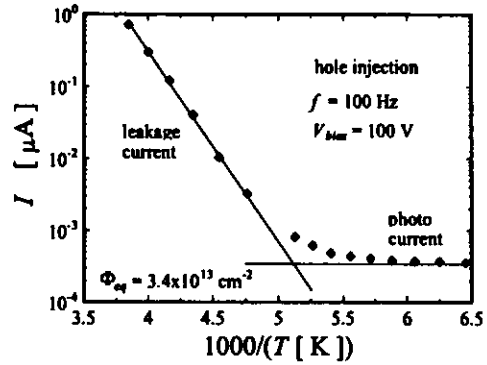

Fig. 3.70 Exploiting the photo current for the determination of the density of free carriers (device 504_82, see Fig. 3.71c)).

Determination of Trap Concentrations and Ionization Enthalpies

The next step of the data evaluation makes use of the steady state current pulse shapes, see for example Fig. 3.69. The sum of all trapped electrons or holes, whichever type of free carrier is injected, is calculated from the $N_{eff,SCR}(T)$ data using eq. 3.112 and is then plotted versus temperature. For five different experimental conditions this has been done in Fig. 3.71. Now, regarding the theoretical modeling in eq. 3.111, each plateau is related to a specific trap level. Taking no more than two traps into account, a reasonable fit to the data was possible by mere variation of their concentration N_t and enthalpy $\Delta H_{n,p}$. Free carrier concentrations were determined as discussed above for each evaluation independently. Evidently, the characteristic temperature of the dynamic filling process can be controlled by the pulse repetition frequency, compare Fig. 3.71 d) and e). As the entropy factor $X_{n,p}$ is not known and there is not enough experimental data to unambiguously determine its value, $X_{n,p}$ has been assumed to be equal to one. All results, i.e. trap enthalpies and concentrations, have been compiled in Table 3.25 and will be discussed below.

It was not possible in any of the experiments in Fig. 3.71 to saturate more than one trap. Here it must be born in mind that the transformation of the space charge also modifies the full depletion voltage (eq. 2.7). Thus, for the quoted reverse bias voltages V_{bias} the diodes were not fully depleted at low temperatures which made the determination of $N_{eff,SCR}$ impossible. The reverse bias could have been adjusted correspondingly, however, the resulting average electric field is very high giving rise to a very short and hard to analyze current pulse shape. It will however be shown below that the saturation of the second trap level at lower temperature would require bias voltages of the order of several thousand volts and it is therefore without prospects to analyze further trap levels at lower temperatures in these heavily damaged samples.

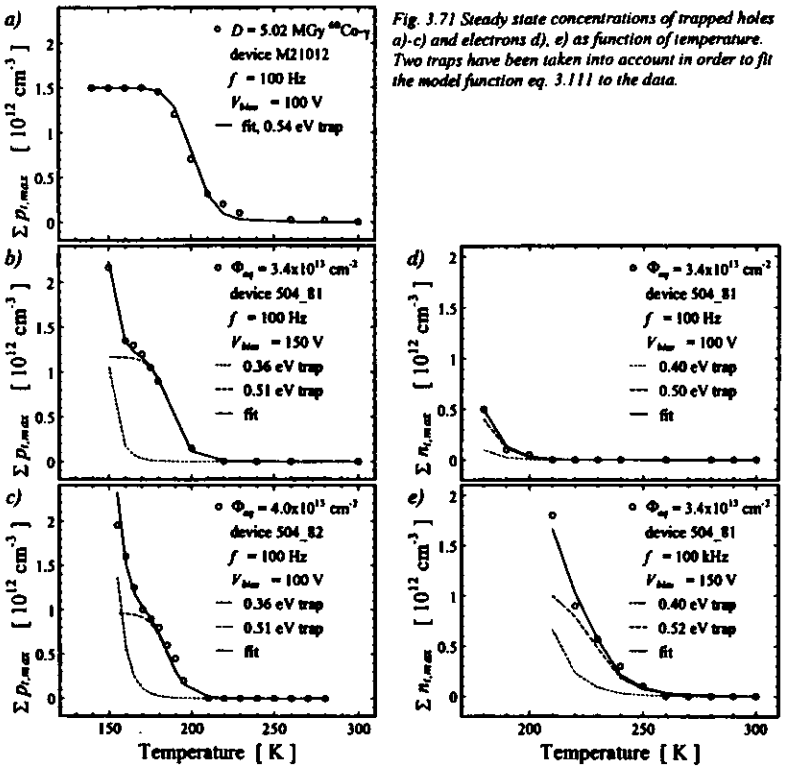

Fig. 3.71 Steady state concentrations of trapped holes a)-c) and electrons d), e) as function of temperature. Two traps have been taken into account in order to fit the model function eq. 3.111 to the data.

Determination of Capture Coefficients

Finally, the $N_{eff,SCR}$ data evaluated as function of the filling time (e.g. Fig. 3.68) can be used to calculate the corresponding variation of the total concentration of trapped carriers, Σp_t or Σn_t by eq. 3.112. Fig. 3.72 shows corresponding experiments which have been conducted on one particular sample for hole injection at four different temperatures. The corresponding steady state measurements shown in Fig. 3.71 b) show that the 170 K and 180 K curves in Fig. 3.72 can reasonably well be ascribed to the 0.51 eV level, whereas the other two result from a superposition of both traps. However, apart from a small constant offset the 150 K data is dominated by the 0.36 eV trap. The functional dependence expected is a sum of terms like eq. 3.109. Therefore, in order to extract the characteristic overall time constant τ governing the filling process, the experimental data have been arranged into the form $\Sigma p_t = \Sigma p_{t,max} - \alpha_0 \exp(-t/\tau)$ by putting $\Sigma p_{t,max}$ equal to the value of Σp_t established at the longest filling time and employing a straight-line fit to the quantity $\ln((\Sigma p_{t,max} - \Sigma p_t)/\Sigma p_{t,max}) = \ln(\alpha_0) - t/\tau$. Except for the 160 K curve, the agreement between the fitted model (solid lines in Fig. 3.72) and the experimental data is reasonable. It will however be noted that the fitted lines allow Σp_t to be distinct from zero at $t = 0$ which according to eq. 3.109 is not adequate. Still it was found advantageous to evaluate the data this way because it was not easy to accomplish short filling times, in particular there might be an offset in the time-axis.

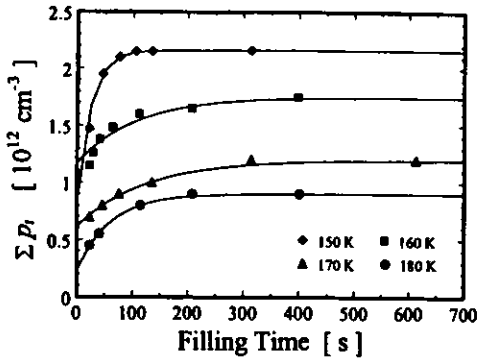

Fig. 3.72 Filled hole trap concentration as function of the filling time, compare the corresponding current pulse shapes at 160 K in Fig. 3.68 and the variation of the steady state values with temperature shown in Fig. 3.71 b). The solid lines were fitted to the data, see text.

The obtained time constants may now be used in conjunction with eq. 3.110 to evaluate the capture coefficients $c_{n,p}$. It is necessary to know the trap enthalpy, which has been determined before, and the free carrier concentration, here p. $X_{n,p}$ was again assumed to be unity. For purpose of easy comparison the relation between the capture coefficient $c_{n,p}$ and a supposedly temperature independent capture cross section σ has been employed (eq. 3.49): $X_{n,p} c_{n,p} = \sigma_{n,p} v_{th,n,p}$. Only the 150 K and the 180 K data appear to reflect the isolated 0.36 eV and 0.51 eV traps, respectively. Thus, only these curves have been used for the evaluation of the cross sections given in Table 3.25.

3.3.5.3 Results and Discussion

Table 3.25 compiles all results from the above data evaluation. Trap concentrations have been normalized to the appropriate irradiation fluence or dose, compare Table 3.24. Moreover, the activation enthalpies have suggested the indicated arrangement scheme and in two cases allow for the tentative assignment of the chemical nature. Regarding the latter it has also been exploited that $VV^{(-/0)}$ and $C_iO_i^{(+/0)}$ are expected to exist in these samples. The annealing history depicted in Table 3.24 does not remove all of the unknown portion (peak N_4) in the left-hand side of the divacancy signal, compare for instance the isochronous annealing study in Section 3.3.3.6.

Table 3.25 Compilation of the results which were derived from TCT measurements, compare Fig. 3.71.

Device	f [kHz]	Type	$\Delta H_{n,p}$ [eV]	$\sigma_{n,p}$ [cm^2], at T	Normalized N_t	Average	Assignment
504_81	0.1	*e*	0.40	-	1.4 cm^{-1}	1.45 cm^{-1}	? + $VV^{(-/0)}$
504_81	100	*e*	0.40	-	1.5 cm^{-1}		
504_81	0.1	*e*	0.50	-	0.030 cm^{-1}	0.031 cm^{-1}	?
504_81	100	*e*	0.52	-	0.032 cm^{-1}		
504_81	0.1	*h*	0.36	1.2×10^{-15}, 150 K	1.1 cm^{-1}	2.3 cm^{-1}	$C_iO_i^{(+/0)}$
504_82	0.1	*h*	0.36	-	3.5 cm^{-1}		
504_81	0.1	*h*	0.51	1.0×10^{-14}, 180 K	0.035 cm^{-1}	0.0295 cm^{-1}	?
504_82	0.1	*h*	0.51	-	0.024 cm^{-1}		
M21012	0.1	*h*	0.54	-	3.0×10^5 cm^{-3}Gy^{-1}	3.0×10^5 cm^{-3}Gy^{-1}	?

With respect to the reliability of the results it is noted that an unambiguous deduction of the trap concentrations and enthalpies is only possible when the steady state occupation can be altered over the full range from zero to its maximum value, see Fig. 3.71. For the given samples this was however only possible for the deepest levels with enthalpies greater than 0.5 eV. Further, the electron trap around 0.51 eV is not well resolved from the divacancy signal. Thus, the characterizations of the deep hole traps around 0.51 eV and 0.54 eV in the neutron and ^{60}Co-gamma irradiated samples, respectively, are more accurate than all other quoted results. Still the introduction rates presented here on the neutron irradiated samples for ? + VV and C_iO_i are close to the data obtained with the TSC method (2 and 1 cm^{-1}, respectively). The corresponding concentrations are of the order of 5×10^{13} cm^{-3}, which would require a reverse bias of around 3000 V to fully deplete the detectors, given those levels were entirely occupied, compare eq. 2.7. It is thus obvious that in the investigated range of fluences the TCT method can only be applied to traps with comparatively small introduction rates and which in addition must be located close to the middle of the band gap.

Concerning the ^{60}Co-gamma irradiated sample, the corresponding introduction rates found in reference [MOL96] predict the concentration of the VV and C_iO_i to be around 8×10^{12} cm^{-3} and 2×10^{14} cm^{-3}, respectively. The latter indicates that a significant portion of the total initial oxygen concentration is removed already. Therefore, higher order defect complexes, e.g. V_2O, are anticipated and might be discussed in conjunction with the observed unknown deep hole trap. Also in this sample is a reasonable investigation of VV and C_iO_i not possible with the TCT method.

As mostly two evaluations of the same level are given in Table 3.25, the statistical error in the data can crudely be estimated by the deviations from the corresponding average. However, the systematic errors would be expected to be much larger, and here a chief source is the value assumed for the concentration of the injected free carriers, see eq. 3.113. Neither is the illuminated area S well known, nor is the assumption of a constant drift velocity $v_{dr,n,p}$ strictly valid. Regarding the latter, also the procedure employed to find the spatial average could be improved if the electric field profile furnished by the simulation of the current pulse were used to average $v_{dr,n,p}(E)$ over distance rather than to employ the drift velocity for the average electric field strength $E_{av} = V_{bias}/d$. Moreover, it is not always possible to uniquely extract the photo current from the total leakage current of the diode, see Fig. 3.70. Instead it were advantageous to make use of the number of electron-hole pairs N in eq. 3.113, as for example was proposed in reference [LI396]. Finally, it will be noted that the developed theoretical modeling is only correct as long as the photo current is larger than the thermally activated bulk leakage current since otherwise significant concentrations of electrons and holes would be present and the corresponding trapping processes for both carriers would have to be taken into account simultaneously. This difficulty would in particular be met with the deepest levels, where furthermore both electron and hole emission would have to be considered. However, this problem did not exist in the evaluations presented here.

The above systematic influences mainly affect the determination of the capture coefficients, which therefore have to be taken with some care. Nevertheless, the result for the transition $C_iO_i^{(+/0)}$ is in good agreement with the TSC and DLTS data presented in the previous sections. Therefore, there is also some confidence into the particularly large cross section quoted for the 0.51 eV hole trap in the neutron damaged samples. While the evaluation of the emission enthalpy is also weakly affected by the error in n or p, the concentrations are not and therefore are supposed to be very accurate. This is however only true for the instances, where the trap under consideration could be saturated, i.e. the > 0.5 eV levels.

The most valuable finding of the TCT studies is the observation of the hole trap levels deeper than 0.5 eV, which so far have not been detected so clearly by other methods. In this context it is noted that virtually no trap levels could be observed on the device M21012 before irradiation and on a control sample fabricated from the same material as the devices 504_81 and 504_82. Therefore, these deep levels unquestionably originate from the high-energy particle irradiation. It is reassuring that using a similar TCT set-up Z. Li et al. have found a similar level in neutron damaged samples [LI396]. This trap is of particular interest as it might contribute significantly to the generation of the bulk leakage current. In this work it has been demonstrated that also in ^{60}Co-gamma irradiated sample a close to midgap hole trap exists, which appears to be slightly shifted with respect to the neutron damaged samples. Except for the concentrations there is however no reason why qualitatively different results should be obtained on the differently damaged devices. In this respect annealing studies would be helpful and might give more insight into the chemical constitution of the corresponding defects.

Moreover, the following suggestions can be made for the future development of the TCT method. Given the determination of the free carrier concentration can be improved considerably, also the unknown entropy factor $X_{n,p}$ could be derived with reasonable accuracy when it is considered to be a further variable parameter for the fitting of the concentration of carriers trapped in the steady state as function of temperature, compare Section 3.3.5.2. Furthermore, in conjunction with the corresponding functional dependence predicted by the above modeling, additional information regarding the deep levels can be gained by experimentally controlling the free carrier concentration via the pulse generator repetition frequency. In order to demonstrate the accuracy of the level parameters derived from TCT studies it would be valuable to investigate weakly damaged samples, which then would allow for an inter-calibration with TSC and DLTS measurements. For the presented experimental set-up this would require the analysis of current pulse shapes at very low temperature, which is hindered by the short pulse length arising from the large drift mobilities. It is therefore recommended that a distinction is made between the laser pulses applied for the filling of trap levels and for the induction of the current pulses. Due to their lower mobility preferentially drifting holes should be used for the probing of the electric field. Trap filling should then be accomplished by independent light pulses aiming at comparatively large concentrations of the injected free carriers, which shifts the characteristic temperatures upwards. Moreover, employing appropriate pulsing schemes for the preparation of a specific initial occupation of the considered trap would allow for the measurement of both electron and hole capture coefficients.

3.3.5.4 Summary of the Defect Studies Using TCT

- The transformation of current pulse shapes at low temperature due to the trapping of optically generated free carriers at deep levels was studied. The models describing the space charge concentration as function of temperature and illumination time were developed from first principles, and methods of extracting the deep level parameters (concentration, ionization enthalpy, capture coefficient) were proposed.

- Besides the well-known $C_iO_i^{(+/0)}$ level, a deep hole trap at around E_V + 0.5 eV with comparatively small introduction rate was discovered in both neutron and ^{60}Co-gamma damaged samples. On one neutron damaged device the capture cross section was determined to be 10^{-14} cm^2. Also the divacancy level $VV^{(-/0)}$ and a deep electron trap at around E_C - 0.5 eV were found, however, with less reliability, see Table 3.25.

- It was found that the method becomes difficulty to apply if for decreasing temperatures short pulse shapes result due to the increasing drift mobility. An other shortcoming is the small range of accessible defect concentrations limited by the poor sensitivity (1×10^{11} cm^{-3}) and by the large reverse bias voltages needed to fully deplete the device (3×10^{12} cm^{-3}). Suggestions were made for future developments improving this situation.

3.3.6 Summary of Microscopic Defect Studies and Comparison between the Spectroscopic Methods

In the following it will be summarized which aspects were considered in order to gain a deeper insight into the macroscopic deterioration of high resistivity silicon detectors by damage-induced deep levels. The used spectroscopic methods will be compared with respect to their ability to furnish valuable information in this field. For more detailed summaries of the results obtained with the TSC, I-DLTS, and TCT methods see the Sections 3.3.3.8, 3.3.4.4, and 3.3.5.4, respectively.

Hints from the theoretical background:

- It was shown that in the simplest approach the negative space charge introduced by bulk damage is related to small concentrations of defects exhibiting an acceptor level in the lower half of the band gap and that levels close to the middle of the band gap are required for generation of leakage current.
- The correct notion of the level energy was found to be inevitable for the accurate extrapolation of the defect properties to room temperature from the values determined by spectroscopic studies at low temperature.
- Defects charged in the space charge region exhibit a large capture cross section and possibly an electric-field enhancement of the emission rate (Poole-Frenkel effect).
- The neutral bulk was found to become strongly compensated by the damage-induced deep levels and Fermi level pinning occurs close to the middle of the band gap upon cooling.

Experimental considerations related to the examined high resistivity material:

- It was shown that large defect concentrations compared with the shallow doping require current rather than capacitance-based spectroscopic methods.
- Optical rather than electrical filling was argued to provide better control of the initial defect occupation in some situations, however, it is more difficult to handle experimentally.
- The severe distortion of TSC and I-DLTS spectra on heavily damaged samples was found to be due to the variation of the depletion width as function of the measuring temperature.
- Defects causing the device deterioration were shown to have comparatively small concentrations and might thus be hidden under the dominant peaks in the spectra.
- Studies on the levels constituting the initial doping, e.g. phosphorus / boron, require low temperatures and good infrared stray-light shielding.

Benefits and shortcomings of the employed spectroscopic methods:

- A highly resolved and unique representation of the defect levels present in the sample is provided by TSC at the smallest experimental effort.
- Due to the leakage current, close to midgap levels can not be studied with TSC but with I-DLTS and with TCT. The latter is particularly well-suited for characterizing the deepest levels.
- Very shallow levels are the domain of I-DLTS. However, given a very good stray-light shielding also TSC is applicable and furnishes more reliable defect concentrations.
- The most accurate defect concentrations are obtained from the integral over the TSC peaks, however, only if complete filling is achieved (e.g. 0 V cooling) and if the width of the space charge region is known (small defect concentrations). Also the values determined with TCT are very reliable, however, the method is less sensitive than TSC. I-DLTS is the least accurate, in particular if optical injection of free carriers is used and a large systematic error arises from the poorly defined active volume.
- With respect to the characterization of defect levels by the enthalpy $\Delta H'$ and emission cross section σ DLTS is the most suitable method as it assesses all levels throughout the band gap in a single temperature scan. Results of similar accuracy can be obtained with TSC delayed heating and with TCT, however, requiring much more experimental effort. In general, reliable results can only be determined for the instance of small defect concentrations compared with the shallow doping.
- In order to accurately calculate the contribution of a particular trap level to the leakage current or space charge it is necessary to determine the corresponding capture coefficients for electrons and holes as function of temperature. This requires special defect filling schemes and has so far only been done with C-DLTS. However, optically generated free carriers for defect filling might also enable such measurements with I-DLTS and TCT.
- The specific modes of defect filling used with TSC make it an interesting tool for the investigation of metastable defects.

3.4 Relation between the Macroscopic Detector Properties and the Microscopic Features of the Radiation Damage

A major objective of the microscopic defect studies is the explanation of the deterioration of the detector performance in terms of the microscopic features of the radiation damage. In particular it is desirable to relate both the absolute magnitude and the annealing behavior of the doping changes and the leakage current increases to the features of the recognized damage-induced levels. A discussion of these subjects will be given in the following, based on the defect concentrations found in this work. A compilation of all dominant defects and their introduction rates determined with the TSC method in Section 3.3.3.4 is given in Table 3.26. The values for C_iC_s and VO_i were calculated from the sum of their introduction rates obtained from the studies using 0 V cooling for defect filling and the ratio between them determined in the studies using switching to 0 V at low temperature.

Table 3.26 Introduction rates of dominant defects measured after around 400 d room temperature storage on neutron-damaged devices fabricated from 3 kΩ cm Wacker float zone material.

Defect	Introduction Rate
C_iC_s	0.16 cm^{-1}
C_iO_i	1.06 cm^{-1}
VO_i	0.84 cm^{-1}
$N_s + VV$	2.02 cm^{-1}
VV	> 0.7 cm^{-1}

The first step towards a deeper understanding is to review the properties of the well characterized dominant defect levels at the reference temperature 20°C, see Table 3.27. Reliable data regarding the level parameters have recently been reported by Hallén et al. on proton irradiated samples after a 30 min lasting annealing at 150°C [HAL96], see also Appendix B. The values obtained for the enthalpy of the transition $VV^{(-/0)}$ in that reference and in this work by the delayed heating method in Section 3.3.3.7 are similar. It is therefore concluded that their annealing was sufficient to remove the apparent broadening of the corresponding peak towards lower temperatures and other peculiarities of the divacancy levels which are only observed after heavy particle damage. The second ionization state of the divacancy was neglected in Table 3.27 because it can hardly be occupied with an electron in the space charge region.

Table 3.27 Parameters of the dominant radiation damage-induced deep level transitions at 293.16 K according to reference [HAL96].

Transition	$VO_i^{(-/0)}$	$C_iO_i^{(+/0)}$	$VV^{(-/0)}$	$VV^{(+/0)}$
c_n [cm^3s^{-1}]	2.37×10^{-7}	3.46×10^{-10}	5.25×10^{-8}	$>> c_p$
c_p [cm^3s^{-1}]	4.23×10^{-4}	3.83×10^{-9}	3.62×10^{-7}	6.49×10^{-9}
ΔH [eV]	-0.164	+0.339	-0.421	+0.194
X	0.29	0.89	0.33	0.56
E_i -E_i [eV]	0.367	-0.222	0.113	-0.355
e_n [s^{-1}]	2.87×10^{9}	3.17×10^{-4}	2.76×10^{4}	
e_p [s^{-1}]	1.26×10^{-2}	1.51×10^{5}	2.48×10^{1}	5.00×10^{7}
$1/(1+(e_p/e_n)^{21})$	4.38×10^{-12}	2.09×10^{-9}	8.97×10^{-4}	
$q_0 e_n e_p/(e_n+e_p)$ [A]	2.02×10^{-21}	5.08×10^{-23}	3.97×10^{-18}	

The Gibbs free energy positions E_i were calculated by eq. 3.38 and are referred to the intrinsic Fermi level E_i, compare Fig. 3.27. In order to be consistent with the evaluation presented in reference [HAL96], the effective masses and the band gap energy were taken from the review given in [GRE90]. Assuming an entropy factor X equal to unity for the $VV^{(-/0)}$ transition, as typically is done if X is not known, places the level at E_i + 0.141 eV. Then the quantity quoted in the last row of Table 3.27 would assume a value of 1.3×10^{-18} A, emphasizing the importance of the correct notion of the trap energy.

3.4.1 Effective Doping Concentration in the Space Charge Region

Regarding the changes in the full depletion voltage V_{dep} of a detector it is inevitable to recall that V_{dep} is determined by the concentration of space charges $N_{eff,SCR}$ in the depleted zone (eq. 2.7) associated with a corresponding ionization state of the defect levels, which has been explored in Section 3.3.1.5. It was shown there that

eq. 3.114 $$N_{eff,SCR} = \sum_{donors} \frac{N_t}{1+e_p/e_n} - \sum_{acceptors} \frac{N_t}{1+e_n/e_p},$$

and, due to the strong dependence of the emission rates on the trap energy, in the first approximation only donors in the upper and acceptors in the lower half of the band gap contribute to $N_{eff,SCR}$, see eq. 3.63. Very rarely a fractional occupation of close to midgap levels is encountered when the emission rates for electrons and holes e_n and e_p are of the same order of magnitude. In the presence of deep defect levels $N_{eff,SCR}$ is usually different from the value of the effective doping concentration N_{eff} established in the undepleted bulk material.

Another crucial point is the question, whether $N_{eff,SCR}$ can be evaluated properly from CV curves by means of the full depletion voltage (Section 2.5.3.1). This has been verified in this work by the examination of current pulse shapes (TCT), showing that irrespective of the annealing time only a small discrepancy of around 0.01 $cm^{-1} \times \Phi_{eq}$ exists. However, in general the TCT data confirm the observations made with CV measurements, and in particular TCT shows that the damage-induced change in the space charge is distributed homogeneously throughout the detector bulk.

3.4.1.1 Origin of the Negative Space Charge

An increase in the negative space charge is generally observed as a consequence of the exposure to bulk damaging radiation, for heavy particles as well as for ^{60}Co-gammas. Therefore, at least a fraction of the negative space charge is related to randomly distributed point defects, rather than to the closer spacing of point defects encountered at the end of the displacement damage cascades initiated by heavy particles. It is now interesting to note that all of the predominating defects (VO_i, C_iO_i, VV, C_iC_s) do not contribute to $N_{eff,SCR}$ according to eq. 3.114. This results from the position and the character (donor/acceptor) of their levels in the band gap, compare the corresponding ionization factors in the second-last row of Table

3.27. Now, the macroscopically noticed change in the concentration of space charges normalized to the ^{60}Co-gamma dose given in Table 3.7 is around a factor 200 smaller than the introduction rates found in the low dose range for VO_i and C_iO_i in reference [MOL96]. It is therefore very difficult to experimentally detect the traces of acceptor levels in the lower half of the band gap which possibly could account for the negative charge. The same holds true for heavy particle damage, it will however be noted that there the corresponding factor between the introduction rates is only of the order of ten (space charge: 0.1 cm^{-1}, defects: 1 cm^{-1}).

In general the small introduction rate of the negative charge points to an acceptor level related to a higher order defect complex. However, it is also conceivable that one of the components of the defect in question is related to a rare impurity, which then should lead to a saturation of the negative charge buildup at high fluences. In this context it is noted that within the experimental errors no influence of the initial resistivity on the introduction rate g_c of the stable acceptors could be observed, implying that the initial doping impurities can not be incorporated in the responsible defects. Also the stable damage concentration N_c does not level off at high fluences, and even at fluences as large as 1.7×10^{15} cm^{-2} was no saturation of the negative space charge noticed [LI296]. Therefore, the defects in question are likely to be higher order complexes of intrinsic displacement damage defects (agglomerates of vacancies/interstitials) and possibly include impurity atoms like oxygen and/or carbon which are present in the material in large concentrations (a few times 10^{15} cm^{-3}). Finally, it will be noted that the similarity of the results obtained on various heavy particle sources (Section 3.2.4) excludes that there is negative space charge resulting from daughter nuclei of nuclear reactions, which potentially can introduce shallow acceptor levels.

One possible candidate has been discovered by the TCT measurements in Section 3.3.5, namely the hole trap at around E_V + 0.5 eV observed in both neutron and gamma irradiated samples. The trap exhibits a large hole capture cross section of around 10^{-14} cm^2, which is considered to be a fingerprint of an acceptor level as the Coulombic attraction enhances the capture. Also the quoted introduction rates (0.03 cm^{-1} (n), 3×10^3 $cm^{-3}rad^{-1}$ (gamma)) would be in agreement with this assignment. However, the obtained level parameters do not unambiguously point to an identical chemical composition for the two considered irradiation sources. Further, so far no systematic study on the variation of the trap concentration as function of fluence or on the annealing behavior has been carried out. This could help to confirm a direct relation between the negative space charge and the defect, which up to now is only tentative.

However, not only damage-induced shallow acceptors can result in negative space charge, but rather are there also two ways, by which a thermally activated space charge can be established. That is, electrons are trapped in the steady state condition of a reverse biased diode on an acceptor level in the upper half of the band gap, which would not be charged in the T = 0 K limit. It can be inferred from eq. 3.62 that in fact the precise division of the band gap is given by the energy E_i - ½ $k_BT\ln(c_n/c_p)$, and therefore for each trap slightly depends on the ratio between the capture coefficients for electrons and holes.

Firstly, any kind of leakage current, not necessarily related to the bulk generation current, can give rise to a sufficient number of free electrons and holes drifting through the field zone, such that the steady state occupation of a specific trap might be affected by the capture of the free carriers. Inspection of the differential equation governing the trap occupation (eq. 3.46) in conjunction with the definition of the emission rates (eq. 3.47) reveals that for close to midgap levels, which due to the relatively small emission rates would be most sensitive to this effect, the free carrier concentration must be of the order of the intrinsic carrier concentration to make this an efficient process. Otherwise the occupation is only controlled by the carrier emission rates. Now, if the damage-induced leakage current is identified with a drift current it can be computed that at full depletion and typical damage constants the average free carrier concentration is much smaller than the intrinsic carrier concentration and thus excludes the proposed mechanism.

Secondly, as was stated above, traps can according to eq. 3.114 exhibit a fractional occupation if e_n and e_p are of the same order, which usually is accomplished for trap energies a few k_BT (25 meV at room temperature) away from the band gap division at E_i - ½ $k_BT\ln(c_n/c_p)$. As the corresponding occupation function (eq. 3.62) is similar to a Fermi distribution, the trap ionization as well as $N_{eff,SCR}$ then usually depends strongly on the temperature. Such ionization ratios are displayed in Table 3.27, demonstrating that even for the divacancy, one of the levels discussed in this field, the ionization at room

temperature is less than 1/1000. Full numerical simulations of these subjects confirming the above statements have been presented by G. Lutz in reference [LUT96], who for purpose of illustration has placed an acceptor level at E_i + 50 meV.

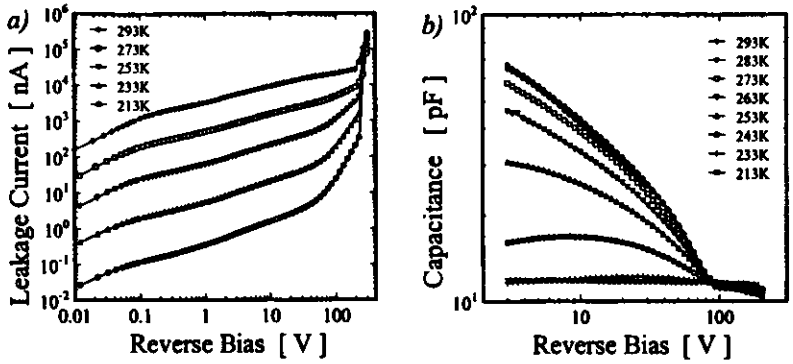

Fig. 3.73 IV a) and CV b) characteristics as function of temperature for a heavily damaged device after storage at room temperature for around one year (device M20708, Φ_{eq} = 3.82×10¹³ cm⁻², f = 1 kHz).

Regarding the well annealed state reached after around one year storage at room temperature it can be confirmed experimentally that the negative space charge is not activated thermally*. While the leakage current in Fig. 3.73 a) is reduced over orders of magnitude by the cooling, the corresponding full depletion voltages in Fig. 3.73 b) do not vary with temperature. The change in the CV characteristics is essentially only due to the increasing series resistance of the undepleted bulk, see eq 2.20. Also the TCT measurements on both the gamma irradiated sample and the 80°C annealed neutron irradiated samples fit into this picture as no variation of the space charge as function of the temperature is seen in Fig. 3.71 unless the occupation of the deepest of the trap levels is altered by the capture of the injected free carriers. In this context it is noted that the particular TSC trap filling mode of switching to zero bias at low temperature discussed in Section 3.3.3.4 confirms the presence of negative space charge in inverted detectors at temperatures as low as 20 K.

Levels close to midgap are according to eq. 3.76 also good candidates for the generation of bulk leakage current, which has been exploited for the correlation of the short term annealing behavior in the doping concentration and the leakage current in reference [SCH95]. Such a correlation would then indicate that acceptor levels close to the middle of the gap are introduced by heavy particle damage, and that they disappear during the short-term annealing period.

3.4.1.2 Donor Removal

There is still an ongoing discussion concerning the question, whether the phosphorus atoms are removed by the displacement damage events in high resistivity silicon, or not. The dependence of the donor concentration on the fluence is generally assumed to be given by

$$\text{eq. 3.115} \qquad N_D(\Phi_{eq}) = N_{D0}\exp\left(-c\Phi_{eq}\right) \approx N_{D0}\left[1 - c\Phi_{eq}\right]$$

where N_{D0} is the initial donor concentration and the right-hand side gives the approximate result valid for $c\Phi_{eq} << 1$. As was outlined by B. MacEvoy in reference [MEV96], the removal constant c can be estimated from the VP_i (E-center) introduction rate g_{VP} if the formation of E-centers is considered to account for the donor removal. Based on the works of Z. Su et al. [SU90] it was shown in Section 3.3.1.1 that for the investigated material ($N_P \approx 10^{12}$ cm^{-3}) g_{VP} is expected to be 350 times smaller than the introduction rate of the A-centers (VO_i, see Table 3.26). If now cN_{D0} in eq. 3.115 is identified with g_{VP}, one gets $c = g_{VP}/N_{D0} \approx (1/350\,\text{cm}^{-1}) / 10^{12}\,\text{cm}^{-3} = 3\times10^{-15}$ cm², which is two orders of magnitude smaller

* Note that the device is heavily damaged, ensuring considerable concentrations of defects compared with the initial doping.

than the typically observed experimental value. Even if it is taken into account that the formation of C_iP_s consumes approximately the same number of phosphorus atoms as VP_i (see [ASO87]) can the macroscopic result hardly be explained by these processes. Only in heavily damaged samples would significant amounts of these rare defects be produced. This accounts for example for the larger change in $N_{eff,SCR}$ noticed on the lower resistivity sample at high doses of ^{60}Co-gamma radiation (Fig. 3.19). Also this enables the tentative assignment of the C_iP_s pair to a certain TSC peak in Section 3.3.3.4.

As was demonstrated in Section 3.2.5, only a fraction of around 30% of the initial doping concentration appears to be removed permanently after a short exposure to a high fluence of fast neutrons. It could therefore be speculated that other donor-like impurities might exist, which exhibit a much larger capture cross section for vacancies or (carbon) interstitials. However, so far no clear picture of the responsible microscopic processes has been gained and as stated in Section 3.2.5 qualitatively different results might be observed after low and high flux irradiations. The I-DLTS measurements performed on unirradiated samples are considered to be basic work in this respect, see Section 3.3.4.3. In principle the method allows for the determination of the concentrations of shallow doping impurities, and thus might serve to monitor them as function of the irradiation fluence directly. Also the trap levels W and Z, which are not well understood and were tentatively assigned to thermal donors, could turn out to be important in this field.

3.4.1.3 The Bistable Behavior Observed on Heavily Damaged and Annealed Samples

The finding that only peak J is growing in the TSC spectra presented in Fig. 3.56 c) upon excitation of state B of the bistable defect (see Section 3.2.3), which leads to an increase in the full depletion voltage (i.e., the effective doping concentration in the space charge region becomes more negative) reflects a correlation between a macroscopic quantity and a microscopic defect of outstanding clarity. This is again illustrated in Fig. 3.74, showing the increase in the peak current resulting from the excitation as function of the corresponding concentration of bistable defects N_B normalized to the fluence Φ_{eq} = 3.82×10¹³ cm⁻². One data point was obtained after each of the four annealing steps at 110°C, 130°C, 150°C, and 170°C. Bearing in mind the experimental errors, a one-to-one relation is fulfilled reasonably well, irrespective of the particular experimental conditions realized in the TSC measurements.

In conclusion the results suggest that peak J is related to a shallow acceptor. Now, it is known that the C_i donor level would give rise to a TSC peak at virtually the same temperature and examples for C_i complexes breaking up under current injection have been reported in the literature (e.g. C_iP_s [GÜR92]). However, besides the donor level, liberated C_i also exhibits an acceptor level in the upper half of the band gap (see Appendix B) displaying a TSC peak at 47.7 K, which is not observed in Fig. 3.56 c). Moreover, the level parameters found for peak J by various methods (Table 3.28) are others than expected for the transition $C_i^{(+/0)}$, see Appendix B. Especially the large capture cross section would appear to be in agreement with the assignment to an acceptor level. The level parameters could however only be evaluated under difficult experimental conditions, and accordingly the data are subject to a considerably systematic uncertainty. The agreement between the results compiled in Table 3.28 is however striking. It will be noted that it is very unlikely that isolated C_i atoms could have been present in the studied samples, because the measurements were performed on devices, which had been stored at room temperature for an extended period of time, but which were not annealed at elevated temperatures. Accordingly, C_i should have disappeared a long time ago with a time constant of the order of a few ten hours at room temperature. Unfortunately so far no results regarding

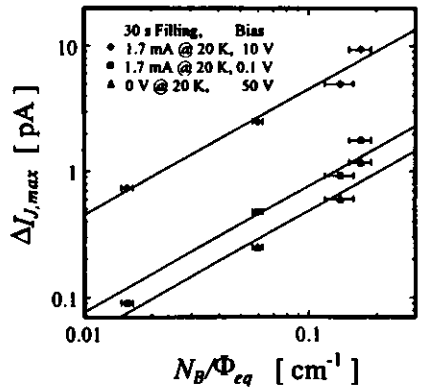

Fig. 3.74 Increase $\Delta I_{J,max}$ of the peak J in the TSC spectrum resulting from a 20 min lasting forward current injection at 290 K, compare Fig. 3.56 c), plotted versus the concentration of the bistable defects B, see Fig. 3.10 a).

the level in question are available on samples that were annealed at elevated temperatures. In particular no efforts have been undertaken to evaluate the level parameters on peak J in the excited state, a laborious but crucial task to unambiguously clarify the subject matter.

Also in agreement with the assignment of an acceptor to peak J is the observation that the peak is growing during the isochronous annealing of the weakly damaged sample while the space charge is becoming more negative (compare Fig. 3.55 b) and Fig. 3.10 a)). It is noted that the concentration of peak J cannot account for all of the change seen in $N_{eff,SCR}$. However, it is possible that the level was not filled completely in the TSC measurements. Moreover, the hole traps Q and N_4, which are found to anneal in (Fig. 3.54 c)), could also turn out to be acceptors, but additional studies are necessary to characterize these new traps.

Table 3.28 Compilation of the spectroscopic results obtained on peak J with various methods.

Method	$\Delta H'_p$ [meV]	σ_p [cm^2]
TSC β - Variation	321	1.5×10^{-13}
TSC Delayed Heating	326	3.2×10^{-13}
I-DLTS	315	1.7×10^{-13}
Average	321±6	$(2.1\pm0.9)\times10^{-13}$

Concerning the bistability of the defect in question it is known that the dissociation of the excited state B into the two components A_1 and A_2 does virtually not take place in the depleted region of the diode, see Section 3.2.3.4. Moreover, no equivalent transient effects were observed on weakly damaged devices for which $N_{eff,SCR} > 0$ during the isochronous annealing, i.e., where in thermal equilibrium free electrons, n, are more abundant than holes, p. Only in the neutral bulk of inverted detectors where $p > n$, as recently was confirmed by Hall-measurements [BIG95], does the dissociation occur, which consequently seems to be mediated by the capture of free holes. This would also explain why the amount of the change in $N_{eff,SCR}$ observed on the weakly damaged sample in Fig. 3.10 a) during the later stages of the isochronous annealing study is larger than on the more heavily damaged sample. In both cases is the bistable defect generated during the isochronous annealing, however, in the n-type sample state B, which accounts for the negative space charge, is the stable configuration.

3.4.1.4 Reverse Annealing (1st Stage)

The first stage of the reverse annealing in the effective doping concentration (see Fig. 3.10 a)) corresponds to the long term annealing behavior observed on samples stored at room temperature. As this annealing effect is missing after high doses of ^{60}Co gamma rays (Fig. 3.18 b)), reverse annealing must be related to the peculiarities of heavy particle damage, i.e., higher order agglomerates of intrinsic displacement defects or a couple of point defects in the vicinity of each others lattice strain. Moreover, it has been demonstrated in this work that the parameters in the reverse annealing model function do not depend on the starting material. Further, no saturation could be noticed up to concentrations of $N_{eff} \approx 5\times10^{12}$ cm^{-3}. Hence, reverse annealing is neither related to the initial doping impurities nor to other defects present in the starting material with small concentrations in the 10^{12} cm^{-3} range. However, as generally holds for the damage-induced defects giving rise to negative space charge, incorporation of carbon and/or oxygen can not be excluded.

With respect to the investigation presented in Section 3.2.6, the microscopic understanding of the reverse annealing processes should be based on first order kinetics. Concerning the quite large value obtained on the corresponding frequency k_{01}, a simple dissociation process appears to be most likely. It is then either possible that the dissociating defect has a shallow donor level, or one of the fragments introduces a shallow acceptor level in the band gap.

Peak J might also play a role in the 1st stage reverse annealing. However, as on weakly damaged samples (Φ_{eq} lower than approximately 10^{12} cm^{-2}) this annealing stage is missing (see Fig. 3.10 a)), a direct correlation between the concentration of peak J and the reverse annealing concentration N_Y can only be achieved using a detector exposed to higher fluences. Unfortunately, due to the large defect concentrations TSC could not be used to determine accurate concentrations of peak J on the heavily damaged sample ($\Phi_{eq} \approx 4\times10^{13}$ cm^{-2}) studied in this work.

3.4.2 Leakage Current

According to the simple Shockley-Read-Hall theory the increase in the volume leakage current at full depletion normalized to the sensitive volume is related to the emission rates $e_{n,p}$ and the concentrations N_t of the radiation damage-induced defects by

$$\text{eq. 3.116} \quad \Delta I/(Ad) = \sum_{\text{all traps}} N_t q_0 \frac{e_n e_p}{e_n + e_p} \approx \sum_{\text{all traps}} N_t q_0 e_<\,,$$

which essentially is eq. 2.17 when the inverse generation lifetime $1/\tau_g$ is replaced with a corresponding sum employing eq. 3.76 for each trap and $W_g \approx d$. The term on the right-hand side is a good approximation if one of the emission rates, namely $e_<$, is much smaller than the other. While eq. 3.116 holds for any temperature, it will be considered here only at 20°C for purpose of comparison with the experimentally observed leakage current increases. These are generally presumed to arise only from the radiation damage-induced bulk generation centers. However, the IV curves are not always unambiguously in agreement with this view, in particular beyond the inversion fluence (Section 3.2.1.3). Moreover, the current related damage constants quoted in this work were obtained on devices either manufactured without guard ring, or otherwise leaving it floating. Its connection usually reduces the overall current. However, typically only by a small fraction of the total current on devices damaged by heavy particles, as compared to high dose ^{60}Co-gamma irradiated samples, where a reduction by a factor of two was possible (Section 3.2.4.3).

3.4.2.1 Magnitude of the Current

The amount of leakage current that is to be expected from the dominant defect levels introduced by displacement damage is basically given by the numbers in the last row of Table 3.27, which according to eq. 3.116 merely have to be multiplied with the appropriate defect concentration. Otherwise, if the current related damage constant is to be deduced, the numbers need to be multiplied with the corresponding defect introduction rate. It turns out that besides the divacancy transition $VV^{(-/0)}$ hardly any other level can contribute significantly. With respect to the $C_i O_i$ donor this is due to the particularly small electron capture coefficient. Indeed, the much more shallow A-center $VO_i^{(-/0)}$ appears to be the second-most efficient generation center. It must however be born in mind that the emission rates were experimentally determined at much lower temperatures (compare Appendix B), and that the results given in Table 3.27 are basing on a noteworthy extrapolation introducing a serious uncertainty.

Table 3.29 gives the current related damage constants α_∞ to be expected after long annealing times at room temperature for exposure to either ^{60}Co-gammas or fast neutrons if only $VV^{(-/0)}$ is taken into account. While the introduction rate quoted for the ^{60}Co-gammas was determined with C-DLTS in reference [MOL96], the value for the PTB Be(d,n) source was taken from Table 3.26, reflecting the state reached after around 400 d room temperature annealing and providing the ultimate upper limit by referring to the overall concentration of the broadened peak N.

Table 3.29 Contribution to the leakage current related damage constant expected from the divacancy transition $VV^{(-/0)}$.

Particle	Introduction Rate	α_∞ from $VV^{(-/0)}$
BNL ^{60}Co-gammas	1.6×10^4 cm^{-3}Gy^{-1} [MOL96]	6.4×10^{-12} Acm^{-3}Gy^{-1}
PTB Be(d,n) neutrons	< 2.0 cm^{-1}	< 7.9×10^{-10} Acm^{-1}

Compared to the experimental value 3.9×10^{-11} Acm^{-3}Gy^{-1} found in Section 3.2.4.3, it can be concluded that for ^{60}Co-gamma irradiation the divacancy can account for around 15% of the overall measured current. However, a major fraction was argued to be due to surface leakage, and it is noted that on the ion-implanted device operated with a grounded guard ring an experimental value for α_∞ of only 1.4×10^{-11} Acm^{-3}Gy^{-1}. This shows that the divacancy can probably contribute half of the total volume current in ^{60}Co damaged samples.

On neutron damaged devices α_∞ is around 30×10^{-19} Acm^{-1} for the room temperature annealing state in question, as can for example be seen in the beginning of the isochronous annealing study on the weakly

damaged device in Fig. 3.10 b) (compare Table E.7 in Appendix E). In contrast to the ^{60}Co damaged samples this value is not affected by surface leakage and therefore the theoretical value quoted in Table 3.29 shows that the divacancy can not account for more than around 25% of the volume current. Taking into account the splitting of the level into N_b and N_c, where only the latter arises from $VV^{(-/0)}$, would further reduce the portion to around the half of the above number, compare [MOL96].

Although the divacancy can therefore always account for a considerable fraction of the total volume leakage current, there seem to be additional sources. Defects closer to the middle of the band gap would therefore be expected to exist. A deep electron trap, labeled O, has been observed with I-DLTS (Fig. 3.63). It is however not clear, whether this defect level was introduced by the irradiation or by the processing of the device. The previously mentioned hole trap around E_V + 0.5 eV observed in the TCT measurements would appear to be a good candidate for both neutron and gamma damaged samples. It was however so far not possible to determine all of the required capture coefficients, which is crucial for the accurate derivation of the current. However, with respect to the divacancy it must be born in mind that the numbers displayed in Table 3.27 have been derived from level parameters measured by C-DLTS in a temperature range of 182 K ... 266 K, see Appendix B. That is, the extrapolation to room temperature might be afflicted with a serious error, and detailed studies on the level parameters at room temperature are inevitable to determine the contribution of the divacancy to the leakage current generation.

3.4.2.2 Isochronous Annealing of the Leakage Current

As shown in Fig. 3.10 b), the bulk generation leakage current anneals out continuously for temperatures ranging from 70°C to 190°C and then stays more or less constant. Only one defect level in the TSC spectrum, namely N_b, the left-hand side of peak N, is found to anneal out at approximately the same rate. This behavior is in good agreement with the findings of S. Watts et al. in reference [WAT96]. Moreover, neither was leakage current annealing observed in this work (Fig. 3.18 a)), nor does peak N_b exist in ^{60}Co-gamma irradiated devices [MOL96]. In conclusion the data found here support the view that N_b correlates directly with the particularly large bulk leakage currents observed after heavy particle damage, which can not be attributed to the divacancy alone [WAT96]. Moreover, as outlined in that reference, simple Shockley-Read-Hall statistics is then unlikely to explain the generation processes.

So far the origin of the peak N_b is not clear. However, it is of particular interest to note that also the maximum temperatures of the peaks N and i, which are both related to the divacancy, exhibit a jump at around 175°C (Fig. 3.55 c)) accompanied by the disappearance of N_b. Thus, N_b might not originate from a defect qualitatively distinct from the divacancy VV, but rather could just arises from a lattice strain-induced broadening of the $VV^{(-/0)}$ transition, see [SVE93]. However, a further smart interpretation has been given in reference [MOL96] pointing towards a silicon interstitial related composition of the crystal defect corresponding to peak N_b. If it is recalled that the displacement damage events always create vacancies and interstitials in pairs, and if it is further claimed that all interstitials and vacancies escaping the recombination are forming more complex defects within the volume under consideration, there should be a subtle balance between all interstitial and vacancy related defects. Besides the small contribution of C_iC_s pairs, a dominant sink for the interstitials is C_iO_i. Further, there are VO_i defects and divacancies, where the latter have to be counted twice and whose introduction rate is surely greater than 0.699 cm^{-1}, see Table 3.26. Therefore it is on the one side ([VO_i] + 2 [VV])/Φ_{eq} > 2.23 cm^{-1} and on the other side ([C_iC_s] + [C_iO_i])/Φ_{eq} = 1.22 cm^{-1}, i.e., the missing N_b in this compilation is likely to be interstitial related. This defect might be stable only in the vicinity of a strained-lattice as it is encountered in the terminal regions of the displacment damage cascades initiated by heavy particle damage. Indeed, the close connection with the divacancy peaks could then indicate a small distance between a divacancy and this unknown interstitial-related defect.

In this context it is interesting to note that the total vacancy concentration appears to be decreasing during the elevated temperature annealing of neutron-damaged high resistivity silicon, as was observed by means of Positron Annihilation Spectroscopy (PAS) in reference [LI296]. The current understanding is that vacancies are liberated from the dense defect zones present after heavy particle damage. This would be in agreement with the observation made in Fig. 3.55 a) that the VO_i concentration is slightly increasing in the course of the isochronous annealing. However, also dissociation of the interstitial-related defects in the neighborhood of divacancies could annihilate divacancies.

With respect to the final stages of the isochronous annealing, where the divacancy is a clearly isolated defect with [VV]/Φ_{eq} ≈ 0.5 cm^{-1} (see Fig. 3.55 a)), a normalized current of around 2×10^{-10} Acm^{-1} would be resulting from the transition $VV^{(-/0)}$. This is a fraction of 40% of the experimentally observed value in Fig. 3.10 b). Now the missing 60% might be attributed to the 0.51 eV trap found in the neutron damaged sample after 66.5 h annealing at 80°C. Its hole emission rate at 20°C is e_p = 2.6×10^3 s^{-1} and the introduction rate is approximately 0.03 cm^{-1}, see Table 3.25. According to eq. 3.116 an electron emission rate of e_n = 820 s^{-1} would then be sufficient, which appears to be conceivable if for example the corresponding values quoted for the divacancy in Table 3.27 are considered. However, the annealing behavior of the E_V + 0.51 eV hole trap has so far not been investigated, and further studies are inevitable to assess its role in the current generation. Also it will be noted that according to the above estimates e_n/e_p would be equal to around 0.3, resulting in a temperature dependent $N_{eff,SCR}$ which might give important clues concerning the electron emission rate.

3.4.3 Charge Collection Deficiency

The concentration of electron-hole pairs created by the passage of an ionizing particle through the sensitive field zone of a detector is typically very small, such that in the first approximation their trapping at defect levels can be regarded as a negligible disturbance of the steady state level occupation maintained in the depleted zone. It is thus justified to employ eq. 3.62 in the continuity equation (eq. 3.57) so that the overall trapping time constant for electrons and holes can be defined by

eq. 3.117 $$\tau_{tr,n,p}^{-1} = \sum_{all\ traps} c_{n,p} \frac{N_t}{1+\left(e_n/e_p\right)^{\mp 1}}.$$

This relation accounts for the circumstance that only levels devoid of electrons can act as electron traps, and vice versa for holes. In the first approximation this holds true only for the levels in the upper and lower half of the band gap, respectively. The experimentally observed charge collection deficiency caused by carrier trapping* is however not affected by those electron/hole traps exhibiting a sufficiently high detrapping rate $e_{n,p}$, such that the captured carriers are released within the shaping time of the electronic readout. Regarding reasonable shaping times of the order of a few 10 ns this is for example realized for the A-center VO_i (compare Table 3.27), and certainly also for the shallow impurity levels arising from the phosphorus or boron doping. It is then clear that only the divacancy $VV^{(-/0)}$ level can efficiently trap electrons, while both the divacancy $VV^{(+/0)}$ and the $C_iO_i^{(+/0)}$ donor levels may be taken into consideration as hole traps. Application of the upper limit of the divacancy introduction rate (see Table 3.26) gives the following upper limits of the inverse electron and hole trapping time constants normalized to the fluence (compare eq. 3.22),

$\gamma_e < 1.1\times10^{-7}$ cm^{2}s^{-1} and $\gamma_h < 1.7\times10^{-8}$ cm^{2}s^{-1}.

While the result for the electrons is only a factor of around 2 smaller than the value 2.4×10^{-7} cm^{2}s^{-1} found in reference [WUN92] (see also Appendix E), a discrepancy of at least one order of magnitude is noticed for the hole trapping. In this context it is noted that the previously discussed deep hole trap at E_V + 0.51 eV is expected to contribute approximately 0.5×10^{-8} cm^{2}s^{-1} using the cross section σ = 10^{-14} cm^2 quoted Table 3.25 and a thermal velocity $v_{th,p} \approx 1.6\times10^7$ cm/s in $c_p \approx \sigma\, v_{th,p}$.

* An equation for the numerical calculation of the charge collection deficiency valid for mips is presented in Section 5.2.3.

3.4.4 Resistivity of the Undepleted Bulk Material

According to eq. 2.2 the calculation of the resistivity ρ of the undepleted bulk material requires the knowledge of the zero field mobility $\mu_{n,p}$, given as function of temperature in Appendix A, and the free carrier concentrations n and p established in the state of thermal equilibrium in a neutral region of the semiconductor. These subjects have already been addressed in Section 3.3.1.3. Here a similar investigation is presented, however, as function of the irradiation fluence exploiting the defect introduction rates given in Table 3.26. In fact again the upper limit has been employed for $VV^{(-/0)}$ in order to account for the full concentration of peak N, while the lower limit has been assigned to the second ionization state of the divacancy. However, its donor level was omitted as it would not affect the results. Further, the deep hole trap at E_V + 0.51 eV denoted by Z was assumed to be an acceptor in order to account for the radiation damage-induced increase in the negative space charge. It was introduced at the average rate 2.95×10^{-2} cm^{-1} quoted in Table 3.25. Moreover, an initial effective donor concentration of 1.42×10^{12} cm^{-3} has been chosen, of which the portion N_{eff} = 0.60×10^{12} cm^{-3} is removed permanently with the donor removal constant c = 2.4×10^{-13} cm^2, see eq. 3.11. As holds true for the introduction rates, these are basically the data obtained on the ion-implanted devices supplied by the MPI, see Section 3.2.5.

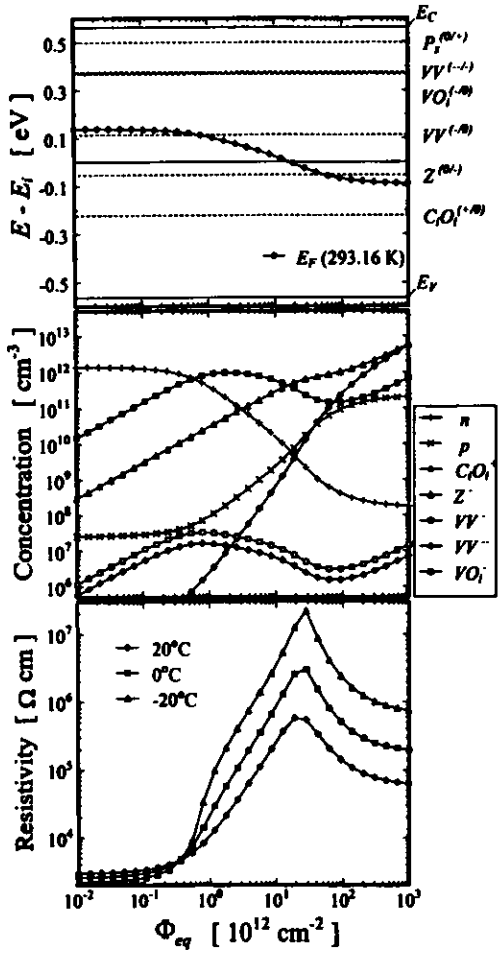

Fig. 3.75 Fermi level a), trap ionization b) and resistivity c) in the thermal equilibrium as function of the irradiation fluence, see text.

Fig. 3.75 shows the variation of the Fermi level E_F as function of the irradiation fluence at room temperature (20°C). E_F is initially positioned slightly above the first acceptor level of the divacancy, enters the lower half of the band gap at around 10^{13} cm^{-2}, crosses the E_V + 0.51 eV level, and eventually settles at an intermediate position between $Z^{(0/-)}$ and $C_iO_i^{(+/0)}$. The corresponding concentrations of free carriers and of ionized defect levels are presented in Fig. 3.75 b). Finally, Fig. 3.75 c) shows the resistivity ρ, which additionally has been determined at 0°C and -20°C. In agreement with the behavior of n and p seen in Fig. 3.75 b), the resistivity is sweeping through a maximum at around the inversion fluence and settles for large fluences at a value in the 100 kΩ cm range. While in the low fluence range the resistivity is decreasing with decreasing temperatures due to the increasing mobility, a significant increase in ρ is noticed for larger Φ_{eq}. The latter reflects the strong dependence of the free carrier concentration on temperature (related to the one of the intrinsic carriers), in contrast to the case of a weakly damaged sample, in which the free electron concentration essentially is equal to the constant effective donor concentration.

The qualitative results presented here are in very good agreement with corresponding experimental data from Hall measurements reported in reference [BIG95]. In the presented model the resistivity at large fluences is only determined by the damage-induced deep levels, rather than the initial shallow doping concentration. Also this circumstance has been observed experimentally in reference [WU196].

3.4.5 Summary of the Relation Between the Macroscopic and Microscopic Features of the Bulk Damage

- The origin of the damage-induced negative space charge was discussed in general. At a well-annealed state after around 1 year storage at room temperature the negative charge was found to be related to a randomly distributed point defect which does not include atoms from the initial doping but rather is comprised of higher order intrinsic defects and possibly carbon and/or oxygen. The deep hole trap at around E_V + 0.5 eV observed with the TCT method was discussed as a possible candidate.

- The relation between the bistable defect governing the decay of the depletion voltage after quenching from the annealing temperature and a single peak in the TSC spectrum was examined. It was shown to be unlikely that the peak is related to the transition $C_i^{(+/0)}$. The role of the defect in the isochronous annealing of weakly and heavily damaged samples was discussed in conjunction with its bistable properties.

- As was found for all annealing effects, reverse annealing is related to the peculiarities of heavy particle damage, namely, a closer spacing of intrinsic defects and/or higher order intrinsic point defects.

- Based on the correct notion of deep level energy it was found that the divacancy transition $VV^{(-/0)}$ can contribute significantly to the overall leakage current. The deep hole trap at around E_V + 0.5 eV was discussed as a possible source for the missing portion. However, heavy particle-damaged samples that were not annealed at elevated temperatures exhibit a particularly large bulk generation leakage current which can not be explained by those defects. In this situation also a characteristic left-hand side broadening of the peak arising from the transition $VV^{(-/0)}$ exists, which appears to be related to the excess leakage current.

- While for electrons the experimental data of the trapping time constant was shown to be of the order of the value expected from the divacancy, the corresponding calculation for the hole trapping time constant underestimates the actually observed trapping effect by one order of magnitude.

- The resistivity of the neutral bulk material was calculated as function of fluence and it was found to be progressively growing up to around the inversion fluence, after which the resistivity slowly decreases and approaches a large (sever 10 kΩ cm at room temperature) saturation value.

3.5 Summary of the Studies on Bulk Damage

- The NIEL hypothesis basing the normalization to equivalent 1 MeV neutron fluences was discussed, and hardness factors were compiled for all sources encountered in this work.

- The models describing the changes in the macroscopic device properties (depletion voltage, leakage current, and charge collection deficiency) were reviewed. Critical tests were performed on the current understanding of the reverse annealing of the doping concentration. The damage constants in the models were compared between various particle types (fast neutrons, 24 GeV protons, 236 MeV pions, ^{60}Co-gammas) and materials of different initial resistivity (0.6×10^{12} cm^{-3} p-type to 2.5×10^{12} cm^{-3} n-type). A summary of the most important results is given in Section 3.2.7.

- Properties of defect levels in silicon were discussed in detail. TSC, I-DLTS, and TCT were used to characterize the microscopic features of heavy particle damage. The influence of large defect concentrations and various modes of defect filling were studied on the TSC method. A more detailed summary and a comparison of the methods is given in Section 3.3.6. Further, summaries of the results obtained with TSC, I-DLTS, and TCT can be found in the Sections 3.3.3.8, 3.3.4.4, and 3.3.5.4, respectively.

- The doping concentration in the space charge region, the leakage current, the trapping time constant, and the resistivity of the neutral bulk were related to the parameters of defect levels. Using the defect concentrations found in this work, the macroscopic damage effects to be expected were calculated and compared with the experimental data. The results of those calculations are summarized in Section 3.4.5.

4 Ionization Damage in the Oxide

Amorphous SiO_2, a very good insulator, can be regarded as a semiconductor with a large band gap of 8.8 eV [BRÄ89]. Therefore free electrons/holes can be trapped into very deep levels associated with defects in the oxide from which the emission back into the conduction/valence band is very unlikely at room temperature. This is basically the reason why, in contrast to crystalline silicon, the oxide is sensitive to ionizing radiation. In the following it will be explored, which changes in the device properties related to the MOS region of the studied surface barrier detectors are observed after exposure to chiefly ionizing radiation, i.e., where bulk damage effects can be neglected.

4.3 Experimental Procedure and Observations

Various surface barrier detectors fabricated on (111)-oriented Wacker float zone n-type material according to the process outlined in Section 2.2.3 with different electrode designs have been investigated. The dry thermal oxides were all deposited by the Ketek company [KET], and they are classified here only by the oxidation date and the oxide thickness, see Table 4.1.

Table 4.1 Basic properties of the studied wafers.

Wafer	d [µm]	$N_{eff,0}$ [10^{12} cm^{-3}]	Oxidation Date	d_{ox} [nm]
911	391.4	0.7	5.89	224
912	392.3	0.65	5.89	224
932	385.1	0.6	12.90	220

Electron-hole pairs were created in the oxide by exposure to 20 keV electrons from a scanning electron microscope (Leitz-AMR 1000) provided by the Gruppe Umweltanalytik of the I. Institut für Experimentalphysik, Universität Hamburg, for details see [SC195]. In addition, a cross check was possible by an irradiation with ^{60}Co-gammas at the BNL source, also encountered in Section 3.2.4. A small change in the silicon bulk properties must therefore be taken into account, whereas the 20 keV electrons cannot displace any silicon atoms. The gamma irradiations were done in normal air atmosphere and the electron exposures were carried out in vacuum (10^{-2} Pa).

The dose D is the ionization energy per mass measured in units of Gray (1 Gy = 1 J/kg = 100 rad). While the ^{60}Co-dose was determined with a calibrated ionization chamber, the electron dose was inferred from the electron fluence Φ and the stopping power S by

$$\text{eq. 4.1} \qquad D = S\Phi = S\frac{I_{beam}t_{exp}}{q_0 A_s},$$

where Φ has been calculated from the electron beam current I_{beam}, the exposure time t_{exp}, and the scanned area A_s. I_{beam}, which was of the order of a few 0.1 nA,

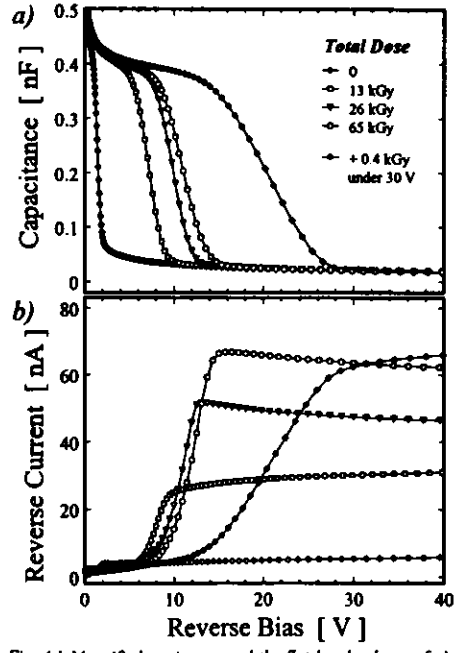

Fig. 4.1 Magnified section around the flat-band voltage of a) CV and b) IV curves as function of the ionization dose. While initially no reverse bias was applied, 30 V have been used during the last irradiation (device 932G01).

could accurately be measured with a Keithley 610 C electrometer by focusing the electron beam onto a Faraday-cup.

The stopping power S is related to the differential energy loss by $\rho S = -dE/dx$, where ρ denotes the density of the material in question (2.32 and 2.33 g/cm³ for SiO_2 and Si, respectively). Employing the compilation of the energy dependent stopping power of electrons in reference [BER82], and accounting for the average energy lost by the 20 keV electrons in the 20 nm gold electrode (about 200 eV), the average stopping power in a 220 nm oxide layer was found to be [SCI95]

$S = 10.8\ \mathrm{MeVcm^2g^{-1}} = 1.73\times10^{-9}\ \mathrm{Gycm^2}$.

As the range of 20 keV electrons in SiO_2 and Si is 4.7 and 4.9 µm, respectively, the impinging electrons leave a homogeneously ionized trace in the oxide layer before they are stopped in the silicon bulk. For an area A, of around 1 cm² the typically realized dose rate follows from eq. 4.1 to be a few 100 Gy/min. Exposure times of several minutes were thus necessary to achieve doses in the kGy range.

Fig. 4.1 a) shows the evolution of CV curves as function of the ionization dose. The data have been plotted in linear scales in order to improve the resolution of the features related to the MOS region. Regarding the analysis of the device characteristics see Section 2.5.3. The initial irradiation under zero bias causes a continuous increase in the flat-band voltage V_{fb}, however, approaching a saturation value. Strikingly the subsequent exposure to a comparatively small dose of electrons under a reverse bias of 30 V leads to a significant further increase in V_{fb}. Moreover, a significant stretch-out of the curve is noticed. Fig. 4.1 b) displays the corresponding IV curves, also reflecting the variation of V_{fb}. In addition, the interface generation current I_{ox} is found to be increasing as function of the irradiation dose, evidently also saturating at high D. However, contrary to V_{fb}, the subsequent irradiation under reverse bias hardly affects I_{ox}.

4.1.1 Mechanism of the Oxide Charge Buildup

The variation of the flat-band voltage is understood to be arising from the trapping of ionization charges and therefore can be expressed by the change ΔN_{ox} in the concentration of oxide-trapped charges Q_{ox}/A_{ox}. According to eq. 2.9 and eq. 2.10 it is

eq. 4.2 $$\Delta V_{fb} = \frac{q_0}{\varepsilon_{ox}\varepsilon_0} x_0 \Delta N_{ox},$$

where x_0 is the center of gravity of all oxide charges which will be assumed to be a constant and to be equal to the oxide thickness d_{ox}. Thus it is implicitly presupposed that all oxide charges are located in the direct vicinity of the Si-SiO_2 interface and that also all additional charge trapping takes place at that position. This is in part justified by the fact that the trapping centers, for example the oxygen-vacancy discussed in Section 2.2.2, are indeed related to substoichiometry and imperfectly grown oxides mainly realized close to the interface (around 5 nm). Regarding further defects capable of trapping positive as well as negative charges the reader is referred to the review given by R. Devine [DEV94].

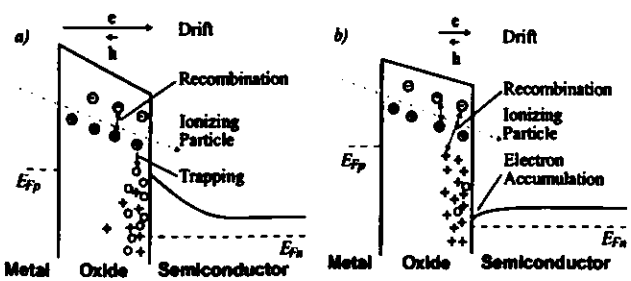

Fig. 4.2 Schematic illustration of the hole trapping and recombination processes

a) $V > V_{fb}$

b) $V < V_{fb}$

As V_{fb} is found to be increasing, hole trapping must predominate over electron trapping. This is qualitatively explained by Fig. 4.2, which also addresses the saturation of V_{fb} at high irradiation doses and the dependence on the reverse bias voltage applied during exposure. The free electrons and holes created in the oxide are driven by the electric field towards the oxide-silicon interface and metal electrode, respectively. Now, the drift mobility is quite large for the electrons (20 $cm^2V_i^{-1}s^{-1}$ at room temperature) while the holes move very slowly by a hopping process (2×10^{-5} $cm^2V^{-1}s^{-1}$) [BRÄ89]. Therefore, the electrons have only a small chance to stick at a defect or to recombine with a hole. More likely will they reach the interface, where they are emitted into the silicon bulk. Contrary, holes created close to the interface will easily get trapped there. If thus the concentration of trapped holes is progressively growing, there will also be an increasing chance for the electrons to recombine with them (Fig. 4.2 b)). Moreover, the positive charge buildup will cause a change in V_{fb} until the applied bias voltage is not sufficient to deplete the silicon below the oxide and an electron accumulation emerges. Similar to the unbiased detector, the electric field strength in the oxide becomes quite small, as do the carrier drift velocities. This results in enhanced recombination of electrons with holes and thus inhibits a further increase in the positive oxide charge (dynamic equilibrium). Therefore, depending on the actual bias voltage a certain saturation value of ΔV_{fb} will be obtained. However, at sufficiently large bias voltages it is also conceivable that all hole traps become exhausted, definitely imposing an upper limit on ΔV_{fb}.

Further, as in the investigated surface barrier detectors the electric field strength at the oxide-silicon interface is a function of the lateral position, a corresponding inhomogeneity of the radiation damage-induced change in the concentration of trapped oxide charges is expected. Based on this idea R. Wunstorf et al. could explain in reference [WUN96] the peculiarities of the proton micro-beam measurements on an electron-damaged surface barrier detector shown in Fig. 4.3. The measurements have been performed as outlined in Section 2.4.1, and the corresponding results found on an undamaged device in Fig. 2.9 may be inspected for reference. Additional dead layers are observed next to the surface barrier contact and in the middle of the MOS region in Fig. 4.3 a) and b). This corresponds reasonably well to the positions where a two-dimensional device simulation (ToSCA) indicated the maximum of the electric field strength in the oxide for the two considered bias voltages of 0 and

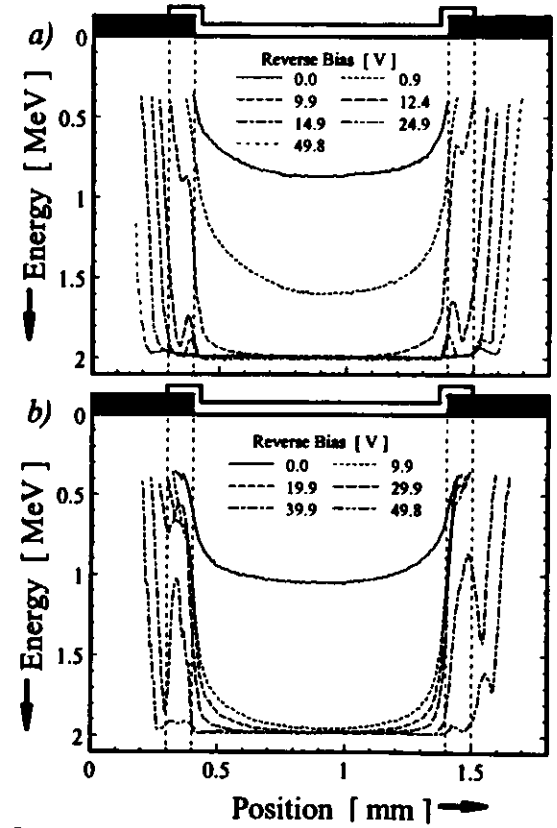

Fig. 4.3 Proton micro-beam study of a surface barrier detector damaged with a dose of 1.99 kGy of 20 keV electrons (100 ns shaping time).

a) Left strip damaged without bias (911L28, V_{dep} = 71 V, V_{fb} = 9.6 V).

b) Right strip damaged under 80 V bias (911R28, V_{dep} = 92 V, V_{fb} = 38 V).

80 V, see [WUN96]. Thus a pronounced accumulation of positive oxide charges has occurred at these positions during the exposure to the ionizing radiation, corresponding to a spatially varying flat-band voltage. Accordingly, upon reverse biasing such a device the depletion of the oxide region will not progress homogeneously, but rather do the device simulations predict a local potential minimum for electrons at the position of the maximum oxide charge density. For sufficiently large reverse bias voltages this results in the formation of an isolated accumulation layer on the otherwise fully depleted Si-SiO_2 interface accounting for the localized energy losses observed in Fig. 4.3.

4.1.2 Changes in the Si-SiO_2 Interface Properties

In Section 2.5.1 the interface generation current has been related to the surface recombination velocity S_0 and accordingly a change in I_{ox} will be regarded as being due to a variation of S_0,

eq. 4.3 $\quad \Delta I_{ox} = q_0 A_{ox} n_i \Delta S_0$.

For n_i the value 6.005×10^9 cm^{-3} has been used at 20°C, as follows from the review presented in [GRE90]. The different MOS areas A_{ox} realized for the different sample designs are given in Table 2.1.

Usually low temperature (450°C) hydrogen annealing is employed to neutralize the dangling bonds on the as-grown oxides [SZE85]: $Si_3 \equiv Si - H$. This results in a possible source for the radiation sensitivity of S_0, because the ionizing radiation can destroy the hydrogen passivation. However, in general the actual processes governing the increase in the density of the interface states are not well understood, but there seems to be a direct relation to the oxide charges trapped next to the interface [BRÄ89].

In addition to the resulting increase in the interface generation current interface states are also expected to cause a stretching of the CV curve around the flat-band voltage, see Section 2.3.2. In regard to the irradiation under reverse bias, the CV data shown in Fig. 4.1 a) would thus suggest an increased number of interface states, in disagreement with the virtually unchanged interface generation current (Fig. 4.1 b)). Therefore, on the devices studied, the stretching is not considered to be a reliable indication of the density of the interface states, but rather may arise from the peculiar expansion of the depleted zone underneath the interface, as discussed on the proton micro-beam investigation.

4.2 Quantitative Evaluation of the Experimental Data

4.2.1 Flat-Band Voltage V_{fb}

Shifts in the flat-band voltage have been determined on various devices either irradiated under a reverse bias voltage of a few 10 V or without bias (Fig. 4.4). A scale representing the oxide charge concentration has been calculated with eq. 4.2 and employing a value of $d_{ox} = 220$ nm. The results obtained on the reverse biased diodes exhibit a similar dependence on the irradiation dose, irrespective of the particular voltage chosen. It must therefore be concluded that the electric fields established in the oxide were always sufficient to reach the saturation in ΔV_{fb} via the exhaustion of all hole traps, in contrast to the devices irradiated without bias. In both cases could the experimental data reasonably well be fitted to the relation

eq. 4.4 $\quad \Delta N_{ot}(D) = b_N\left[1 - \exp(-a_N D)\right]$.

Assuming a constant relative error in ΔN_{ot}, a least-squares procedure gave (solid lines in Fig. 4.4)

b_N (0 V) = 0.947×10^{12} cm^{-2}, a_N (0 V) = 1.68×10^{-4} Gy^{-1},

b_N (≥ 40 V) = 3.42×10^{12} cm^{-2}, a_N (≥ 40 V) = 1.50×10^{-3} Gy^{-1}.

The saturation level is reproduced slightly better when a constant error is assumed in ΔN_{ot}, giving b_N (0 V) = 1.01×10^{12} cm^{-2} and b_N (≥ 40 V) = 3.45×10^{12} cm^{-2}, which might serve as an estimate of the systematic error introduced by the simplified model function eq. 4.4. Regarding the dose calibration, it is reassuring to note that the ^{60}Co-gamma values are in good agreement with the 20 keV electron data.

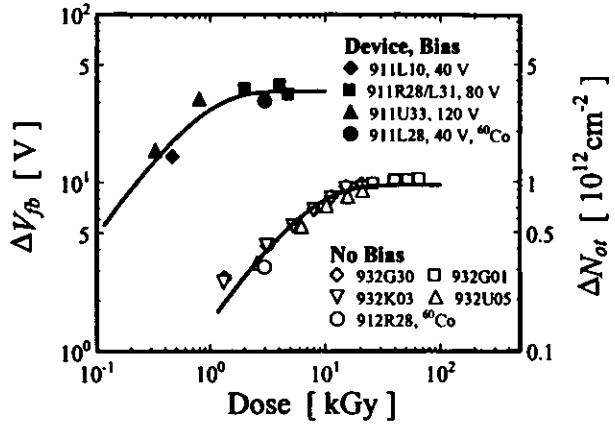

Fig. 4.4 Increase in the flat-band voltage as function of the ionization dose.

While the damage-induced change in V_{fb} on the devices irradiated without bias was found to be decreasing only slightly within a storage period of several days at room temperature, a significant annealing effect was observed on the devices exposed under reverse bias, see Fig. 4.5. The data obtained after the 2 kGy exposure could be fitted to the relation

$\Delta V_{fb}(t) = 41$ V - 0.8 V × ln(t [h]).

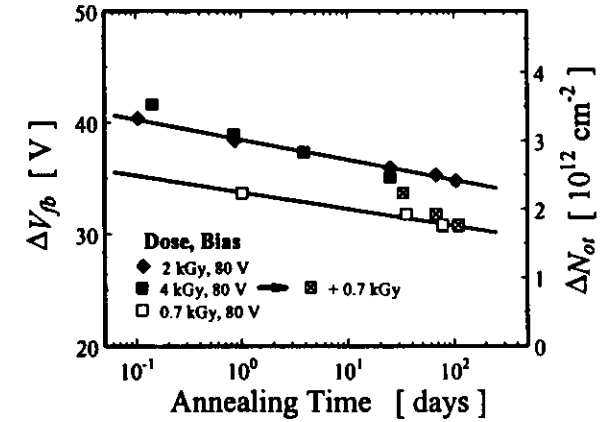

Fig. 4.5 Room temperature annealing under 0 V bias of the flat-band voltage shift measured on two devices that were irradiated under a reverse bias of 80 V (devices 911R28 and 911L31).

This characteristic dependence on the logarithm of the annealing time is in agreement with the observations made by many experimenters and may be explained by the first order tunnel detrapping model, the thermal emission model, or a combination of both, as discussed by P.J. McWhorther et al. [MWH90]. In this context it is important to note that the devices were stored in thermal equilibrium, allowing for the formation of the electron accumulation layer. A more rapid reduction in ΔV_{fb} is observed on the more heavily damaged sample, indicating a dose dependence of the annealing rate. After

around 30 days one sample has once more been exposed to a small dose, and the subsequently measured data cannot reasonably be assigned to the previous annealing curve. However, plotting the measurements with respect to the annealing time elapsed since the second irradiation gives again a straight-line on the logarithmic time scale which is in agreement with the mentioned models. However, the second irradiation has reduced the total amount of trapped positive oxide charges, highly likely by recombination with the free electrons created by the ionizing radiation.

4.2.2 Interface Generation Current I_{ox}

The evaluated interface generation current data are shown in Fig. 4.6, and as for the flat-band voltage shift it is sufficient to distinguish between the devices irradiated under a certain reverse bias voltage or in thermal equilibrium. It is noted that after normalization to the MOS area A_{ox} all data points exhibit the same functional dependence, although the device designs are largely different (see the device names and Table 2.1). This reassures that the interpretation of the interface generation current is correct and that the applied method of extracting the I_{ox} values from the IV curves outlined in Section 2.5.3 is reliable. As for the oxide charges the change in S_0 as function of the dose has been written

eq. 4.5 $\quad \Delta S_0(D) = b_S\left[1-\exp(-a_S D)\right],$

and the corresponding least-squares fits depicted in Fig. 4.6 yield the parameters

b_S (0 V) = 2.91×10^3 cm s^{-1}, a_S (0 V) = 2.20×10^{-5} Gy^{-1},

b_S (≥ 40 V) = 2.41×10^3 cm s^{-1}, a_S (≥ 40 V) = 2.62×10^{-4} Gy^{-1}.

Again constant errors in ΔN_{ox} give more reliable estimates of the saturation levels: b_S (0 V) = 1.91×10^3 cm s^{-1} and b_S (≥ 40 V) = 2.08×10^3 cm s^{-1}. Here the assumption made about the errors has a larger effect because the saturation is not reached in Fig. 4.6 and evidently requires higher doses than encountered with ΔN_{ox}. Moreover, as opposed to the flat-band voltage, the saturation level of ΔI_{ox} does not depend on the biasing conditions realized during the exposure, indicating an upper concentration limit of the surface states contributing to the interface generation current.

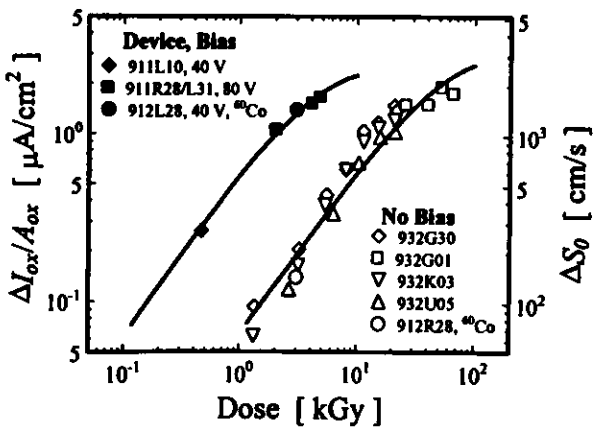

Fig. 4.6 Change in the interface generation current as function of the ionization dose measured on devices that were manufactured with various designs and that were exposed under different reverse bias voltages.

4.3 Summary of the Studies on Ionization Damage

- The radiation sensitivity of the thermally grown oxide passivation (d_{ox} ≈ 220 nm) on high resistivity ($N_{eff,0}$ = 0.65×10^{12} cm^{-3}) (111) n-type silicon has been examined using 20 keV electrons and ^{60}Co-gammas for the generation of the ionization damage.

- The peculiarities of the IV/CV characteristics of the investigated surface barrier devices have been discussed in conjunction with proton micro-beam measurements for different doses and biasing conditions during exposure.

- Flat-band voltages were found to be increasing as function of dose and to reach a saturation level corresponding to concentrations of positive trapped oxide charges of 0.947×10^{12} cm^{-2} (no bias) and 3.42×10^{12} cm^{-2} (reverse bias ≥ 40 V). Annealing proportional ln(t) was observed.

- Also interface generation currents were found to be increasing and to saturate at a level corresponding to a surface recombination velocity of around 2×10^3 cm s^{-1}, regardless of the biasing conditions.

5 Damage Projections for HEP Experiments

After it was realized that the high radiation levels in the inner detector regions of the experiments planned for the LHC can substantially damage the silicon modules comprising the barrel trackers, reliable predictions of their lifetime as function of the position and the operational parameters have become a key design consideration. In the light of the upcoming Technical Proposals it was thus decided to review the bulk damage models, compile the parameters in the model descriptions from all available experimental data, and to develop an appropriate numerical simulation program. While the first task has been accomplished in Section 3.2.1, the other points will be addressed in the following with special emphasize on those subjects, which due to the limited space could not be presented in detail in an earlier publication [CHI95].

5.1 Compilation of Damage Constants

The parameters in the models describing the radiation damage effects were either compiled from literature references or were extracted from experimental raw data available in our own lab or supplied by various groups active in the field ([CAMB,CERN1,DORT,IMPCO,LANL]). The damage constants were determined for different particle types (neutrons, protons, pions) independently, as even after normalization to equivalent 1 MeV neutron values the data might have indicated differences arising from imperfections of the NIEL hypothesis or from insufficiently known damage functions, compare Section 3.1. Further, care was taken of those long term properties being sensitive to the temperature, for instance the leakage current or the annealing rates, as an operation at reduced temperatures is foreseen at LHC. Finally, the gathered data allows for a critical discussion of the errors in the damage constants.

5.1.1 Doping Concentration

Considerable efforts have been made to examine the long term behavior of the radiation damage-induced changes in the effective doping concentration $N_{eff,SCR}$ because the related variations in the full depletion voltage essentially decide on the operability of the detectors. A large number of long term room and elevated temperature isothermal annealing curves measured by various groups around the world have been subjected to the evaluation procedure outlined in Section 3.2.1 in order to obtain the corresponding parameters N_c, N_{c0}, and k_Y.

Employing the hardness factors quoted in Table 3.1 all N_{c0} data were normalized to the equivalent 1 MeV neutron fluence giving the individual introduction rates g_Y (see eq. 3.14), which further were averaged for the different groups*. These averages as well as the corresponding world average of g_Y for each particle type can be found in Table E.1 of Appendix E. The quoted errors are the uncertainty in the averages, compare Appendix D.

As the parameter N_{c0} depends on the type of material predominantly used by a specific group, a straight line was fitted to the N_c versus Φ_{eq} data for each group to obtain their N_{c0}, compare. eq. 3.12. Of course only those data were taken into account, where the donor removal term could be neglected ($\Phi_{eq} > 1/c$). The removal constant c had been compiled previously for each particle type from values reported in the literature at various annealing stages and temperatures, see Table E.2. N_{c0} was subsequently utilized to calculate individual g_c values by $(N_c - N_{c0})/\Phi_{eq}$. These data were averaged as it was done with the g_Y, see Table E.1. The g_c data could also have been taken from the straight-line fit directly. However, then it would have implicitly been assumed that the error in the N_c does not depend on the fluence Φ_{eq}, whereas the method presented here makes the more reasonable assumption that the error scales with Φ_{eq}, see Appendix D. The quoted world average values of N_{c0} are simply the unweighted averages over the different groups, and the range of N_{c0} values encountered is given rather than its statistical error.

* The hardness factor assumed for the PTB Be(d,n) and the CERN PSAIF source were however 1.53 and 1.18, rather than the now revised values of 1.45 and 0.78. While the former basically affects the Hamburg results, which comprise the bulk of the neutron data, the latter concerns the CERN1 neutron values, see Appendix E.

Finally, the reverse annealing rate constant, which characterizes a microscopic process and therefore was not assumed to depend on the particle type, has been averaged at every encountered annealing temperature (see Table E.3). From these data an Arrhenius-plot according to relation eq. C.2 was constructed (Fig. 5.1), and the least-squares straight-line fit gives the activation energy E_a, the frequency factor k_0, and the corresponding errors (Table E.7). Note that the error in the individual $\ln(k_Y\,[\mathrm{cm}^3/\mathrm{s}])$ data was not known and thus was estimated from the χ^2 of the fit to be 0.272, see the error bars depicted in Fig. 5.1. In addition, the cross-hatched area reflects the extrapolation error (see Appendix D) associated with the full covariance matrix of the fitted parameters. As the fitted parameter is $\ln(k_0)$, standard error propagation was not found suitable to estimate the uncertainty in k_0, and accordingly only a lower and upper bound is quoted in Table E.7.

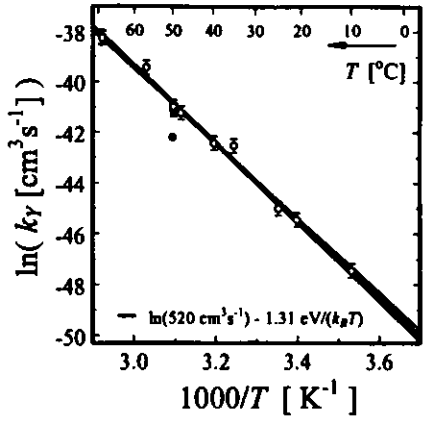

Fig. 5.1 Global Arrhenius-plot of the reverse annealing rate constant. The data point marked with a solid circle was omitted in the straight-line fit. Regarding an explanation of the error bars and the cross-hatched area, see text.

5.1.2 Leakage Current

Due to its strong intrinsic dependence on the temperature excessive leakage currents can very efficiently be reduced by cooling. The crucial parameter is the effective band gap E_g in eq. 2.18, and an average value has been determined from the few values reported in the literature on radiation damaged silicon detectors in the range of temperatures in question (-10°C ... 20°C), see Table E.6.

Further, experimental values of the volume leakage current referring to a long time of annealing (a few months at room temperature) were extracted from various annealing curves according to the procedure outlined in Section 3.2.1. These leakage current data have been assumed to be proportional to the fluence Φ_{eq}. According to eq. 3.19 average damage constants α_∞ were determined for each group providing raw data, see Table E.5.

Finally, the activation energy of the leakage current annealing was determined on a few annealing curves measured by [CERN1] and [DORT] at low temperature. For this purpose the intrinsic dependence on temperature was removed by multiplying the currents with the scaling factor $R(T)$, employing the value for E_g mentioned above. Moreover, the data have been normalized to the active volume $A\,d$ and the fluence Φ_{eq} and were scaled by $g(\infty)/\alpha_\infty$, employing the α_∞ value found above. The resulting quantity $y = \Delta I\,R(T)/(Ad\Phi_{eq})\,g(\infty)/\alpha_\infty$ is according to eq. 3.20 an experimental determination of the normalized annealing curve at a low temperature where the scaling factor θ is larger than unity. Given $g(t_k)$ is the room temperature annealing curve and t_j are the times at which the low temperature annealing data has been taken. A least-squares method of the determination of the scaling factor θ can then be derived from the minimization of

$$\text{eq. 5.1} \qquad Q^2 = \sum_j \left[y_j - g(\theta\, t_j) \right]^2 .$$

That is, we are looking for the roots of the so-called normal equations $f(\theta) = \partial Q^2/\partial\theta$

$$\text{eq. 5.2} \qquad f(\theta) = \sum_j \left[g'(\theta\, t_j)\, \{ y_j - g(\theta\, t_j) \} \right] = 0 ,$$

which can easily be found with Newton's method as also the derivative of f with respect to θ can be written analytically

eq. 5.3 $$\frac{\partial}{\partial\theta} f(\theta) = \sum_j t_j^2 \left[\left\{ y_j - g(\theta\, t_j) \right\} g''(\theta\, t_j) - \left\{ g'(\theta\, t_j) \right\}^2 \right].$$

Here, the derivatives of $g(t_R)$ are of course given by (see eq. 3.18)

eq. 5.4 $$g'(t_R) = \sum_i \left[-\frac{a_i}{\tau_i} \exp\left(-\frac{t_R}{\tau_i}\right) \right], \quad g''(t_R) = \sum_i \left[\frac{a_i}{\tau_i^2} \exp\left(-\frac{t_R}{\tau_i}\right) \right].$$

Fig. 5.2 shows a plot of the y_j as function of the t_j divided by the fitted θ for three different annealing curves that were measured on heavily damaged and thus inverted samples by F. Lemeilleur et al. [CERN1]. The x-axis can be visualized as the 'equivalent room temperature time', and the reasonable agreement with the room temperature annealing curve (solid line) justifies the modeling of the slow-down of the annealing rate at low temperatures by a stretching of the time axis. Further, one annealing curve measured on a weakly damaged sample ([DORT]) has been analyzed using the parameters of the leakage current annealing curve valid for not inverted devices, see Table 3.2. Finally, Table E.4 lists all current annealing activation energies E_i that have been determined from the obtained θ using eq. 3.21.

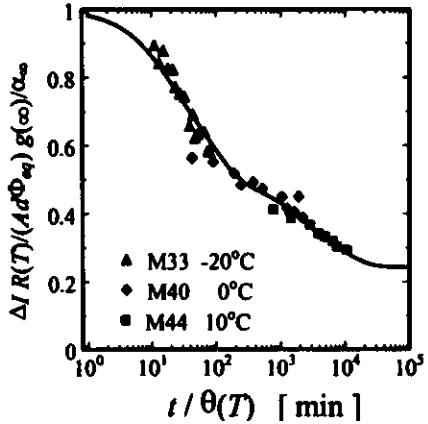

Fig. 5.2 Normalized leakage current as function of the rescaled time $t/\theta(T)$, see text. Annealing data kindly provided by F. Lemeilleur et al. [CERN1].

5.1.3 World Averages and Representation of the Spread in the Raw Data

Table E.7 summarizes all evaluated world average damage constants, and in addition the parameters in eq. 3.22 determining the dependence of the trapping time constants τ_t on the fluence have been cited from reference [WUN92]. Regarding the quantities g_c, g_Y, and α_∞ it will be noted that within the quoted errors the average values found for the different groups are not always compatible, and accordingly the error estimated for the overall weighted world averages is too small. This problem arises from the omission of all sources of systematic errors. They are mainly located in the difficulties met with the determination of equivalent 1 MeV neutron fluences and the differences in the methods employed by the various groups for the extraction of the full depletion voltages and leakage currents from the CV and IV characteristics. With respect to the leakage current related damage constant α_∞ also the quality of the used test devices plays a role, in particular beyond the inversion fluence.

In this context it is noted that the bulk of the pion and neutron data were provided by our own group and were thus mainly determined on surface barrier detectors. After inversion of the space charge sign these devices do even in the long term exhibit an enhanced leakage current increase as function of the irradiation fluence [WUN92], as opposed to the observations made on ion-implanted devices with properly connected guard rings [BAT96]. Moreover, it should be born in mind that the analysis employed on the leakage current annealing curves provides only an upper limit of α_∞, compare Section 3.2.1.

The data evaluation on the pion irradiated devices shown here is only in a preliminary state, and an error of the order of 20% in the damage constants g_c, g_Y, and α_∞ can be estimated from the updated results presented in Section 3.2.4. In conclusion, the differences between the different particle types are not found to be significant, rather are the results in conjunction with the quoted errors misleading and the reader should refer to Section 3.2.4 for a more rigorous investigation of the subject. Although the data are therefore not valuable for a systematic examination of the fluence calibration problem, they still

represent the knowledge about the bulk damage in silicon detectors available around the world at the time of the ATLAS Technical Proposal [ATL94].

As only the failure of a small percentage of the silicon modules is acceptable in order to guarantee an accurate performance of the tracker, it is necessary to ask for the variation in the prediction of the silicon detector properties that arises from the spread in the damage constants. For this purpose, if possible, the standard deviation errors have been quoted in Table E.8, covering around 70% of all inspected data points. An additional difficulty was met with the parameter k since its value needed to be extrapolated towards a low temperature from the experimental data chiefly obtained at room or elevated temperature, see Fig. 5.1. An overall error in the extrapolated $\ln(k_Y\,[\mathrm{cm^3/s}])$ was defined by adding the extrapolation error (cross-hatched area) and the error in the individual $\ln(k_Y\,[\mathrm{cm^3/s}])$ values (error bars) in quadrature. As the resulting uncertainty is comparatively large, the error propagation law was not found suitable, and therefore the average value of k_Y and the appropriate range is given in Table E.8 at the three temperatures considered in the simulations.

5.2 Numerical Implementation of the Damage Models

The model descriptions of the damage-induced changes in the full depletion voltage and the leakage current reviewed in Section 3.2.1 are valid only for a single short term irradiation. However, the prediction of the long term behavior in a low flux environment demands for a simultaneous consideration of the buildup of the damage effects and their annealing. Moreover, variations in the operational temperature have to be taken into account. The numerical simulation assumes the particle flux and the temperature to be constant during certain time periods, i.e., they are both given by step functions. It is then possible to write down analytical solutions valid during these periods, which can be proceeded continuously in the succeeding periods by evaluating the equations at the particular point in time at which the operational parameters are changed, and using these numbers as updated initial values. For the sake of convenience the time t will be assumed to be zero at such a point*.

5.2.1 Doping Concentration

Regarding the stable damage portion N_c, the numerical treatment is straight-forward because N_c depends only on the total absorbed fluence Φ_{eq} that simply needs to be accumulated for the calculation. Short term annealing has been neglected due to the reasons outlined in Section 3.2.1. In accord with the original understanding, reverse annealing has been visualized as a second order reaction of two neutral defects X forming an acceptor Y. Note that then according to the example given in Appendix C the introduction rate and annealing rate of X have to be written $g_X = 2g_Y$ and $k = k_Y/2$. Moreover, while eq. C.7 is valid during the beam-off periods, the term $g_X\phi_{eq}$ needs to be added to the right-hand side of the differential equation eq. C.1 if the 1 MeV neutron equivalent flux ϕ_{eq} is distinct from zero. The solution is then given by

eq. 5.5 $$N_X(t) = N_X^* \tanh\left(N_X^* k t + \operatorname{artanh}\left(N_{X0}/N_X^*\right)\right)$$

where the stationary value reached after long times is

eq. 5.6 $$N_X^* = \sqrt{g_X \phi_{eq}/k}\,.$$

Here N_{X0} always denotes the accumulated concentration of defects X at the time $t = 0$. Concerning the calculation of the concentration N_Y it has been exploited that the defects Y account for the difference between the actually present number of defects X and the concentration $N_{X\infty}$ of X, which would have been obtained if no annealing were to occur. It is $N_{X\infty} = g_X\Phi_{eq}$, where Φ_{eq} is the total absorbed fluence, and $N_Y(t) = (N_{X\infty} - N_X(t))/2$.

* It will be noted that the proper assignment of the continuous simulation time requires the introduction of a time offset.

5.2.2 Leakage Current

Since the annealing curves are different before and after inversion of the sign of the space charge the volume current has been considered to be composed of two fractions. The first anneals with the parameters quoted before inversion and is only introduced as long as $N_{eff,SCR} > 0$, whereas the other portion takes over otherwise. As for the reverse annealing, quantitative results with respect to the simultaneous introduction and annealing of the leakage current requires an assumption about the relation between the current and the corresponding microscopic origins. For the sake of convenience it has been asserted here that every term of the sum of exponentials comprising the annealing function eq. 3.18 corresponds to a specific defect introduced in proportion with the flux and, besides the stable term, exhibits a first order decay. For purpose of illustration the solution of eq. C.1 is given here for $\gamma = 1$ after adding the term $g_X \phi_{eq}$ to the right-hand side,

eq. 5.7 $$N_X(t) = \frac{g_X \phi_{eq}}{k}\left[1 - \exp(-kt)\right] + N_{X0}\exp(-kt).$$

This result is generally valid, also for the instance of $\phi_{eq} = 0$. The rate constant k may now be identified with the individual inverse time constants $1/\tau_i$, and the introduction rate of each term is proportional to the relative amplitude a_i, see Table 3.2. The variation of the annealing rate with temperature has in this context been taken into account by multiplying all time constants τ_i with the scaling factor θ (eq. 3.21).

5.2.3 Charge Collection Deficiency

A deficiency in the collected charge arises from trapping and small electric field strengths, causing collection times larger than the recognition period of the electronic readout. The current pulse signal

eq. 5.8 $$I_{n,p}(t) = \frac{Q_0}{8\tau_{n,p}}\left[(\alpha+1)^2 \exp\left(-t/\tau_{n,p}\right) - (\alpha-1)^2 \exp\left(t/\tau_{n,p}\right)\right]$$

originating from a mip as determined in reference [BAT93] has been used here in order to estimate the influence of these effects. In eq. 5.8 Q_0 is the total charge Nq_e related to the N created electron-hole pairs, α is the ratio between the operational voltage and the full depletion voltage ($\alpha = V_{op}/V_{dep}$), and $\tau_{n,p}$ is the transit time constant for electrons/holes given by eq. 2.33. The simplifications made in [BAT93] for the derivation of eq. 5.8 are the presupposition of a constant drift mobility and the omission of the built-in voltage. In this model, the time $t_{c,n,p}$ needed to collect all electrons/holes is given by

eq. 5.9 $$t_{c,n,p} = \tau_{n,p}\ln\left[(\alpha+1)/(\alpha-1)\right].$$

In order to calculate the charge Q that in the presence of trapping centers is collected within a certain time period T_c, eq. 5.8 needs to be multiplied with $\exp(-t/\tau_{tr,n,p})$, see eq. 2.22, and has to be integrated over the time, compare eq. 2.27,

eq. 5.10 $$Q = \int_0^{T_{c,n}} dt' \exp\left(-t/\tau_{tr,n}\right) I_n(t') + \int_0^{T_{c,p}} dt' \exp\left(-t/\tau_{tr,p}\right) I_p(t').$$

The upper bounds of the integrals are given by $T_{c,n,p} = \min[t_{c,n,p}, T_c]$. Using the abbreviations

eq. 5.11 $$\xi_{n,p} = 1 + \tau_{n,p}/\tau_{tr,n,p} \quad \text{and} \quad \zeta_{n,p} = 1 - \tau_{n,p}/\tau_{tr,n,p}$$

the solution of eq. 5.10 for $\alpha > 1$ is given by

eq. 5.12 $$\frac{Q}{Q_0} = \frac{(\alpha+1)^2}{8}\left[\frac{1 - e^{-\frac{T_{c,n}\xi_n}{\tau_n}}}{\xi_n} + \frac{1 - e^{-\frac{T_{c,p}\xi_p}{\tau_p}}}{\xi_p}\right] + \frac{(\alpha-1)^2}{8}\left[\frac{1 - e^{\frac{T_{c,p}\zeta_n}{\tau_n}}}{\zeta_n} + \frac{1 - e^{\frac{T_{c,p}\zeta_p}{\tau_p}}}{\zeta_p}\right],$$

and for operation below full depletion ($\alpha \le 1$) the full collection times $t_{c,n,p}$ diverge ($T_{c,n,p} = T_c$), and it is

eq. 5.13 $$\frac{Q}{Q_0} = \frac{\sqrt{\alpha}}{2}\left[\frac{1 - e^{-\frac{T_c\xi_n}{\tau_n}}}{\xi_n} + \frac{1 - e^{-\frac{T_c\xi_p}{\tau_p}}}{\xi_p}\right].$$

Note that here Q_0 denotes the charge created by the traversing mip in the activated volume, which is less charge as compared to full depletion. For the calculation of the transit time constants by eq. 2.33, the low field mobility and its functional dependence on temperature has been taken from [SZE81]

eq. 5.14 $$\mu_{c,n}(T) = 1450\frac{\text{cm}^2}{\text{Vs}}\left(\frac{T}{300\text{K}}\right)^{-2.42}, \quad \mu_{c,p}(T) = 450\frac{\text{cm}^2}{\text{Vs}}\left(\frac{T}{300\text{K}}\right)^{-2.20}.$$

Trapping time constants were calculated according to relation eq. 3.22 and depend only on the total absorbed fluence.

A comparison between experimental data on the charge collection efficiency as function of the irradiation fluence and the results of the above calculation is shown in Fig. 5.3, demonstrating a reasonable agreement. However, the simulation tends to give a pessimistic view at large Φ_{eq}.

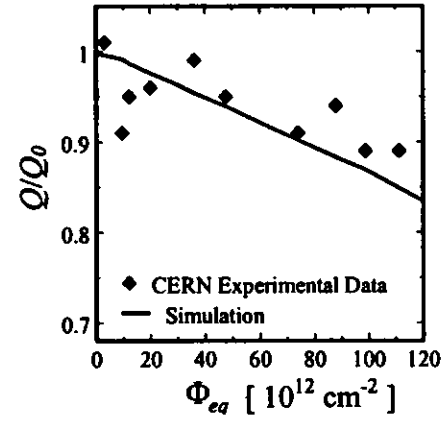

Fig. 5.3 Accuracy test of the model developed for the simulation of the charge collection efficiency as function of fluence (data kindly provided by F. Lemeilleur et al. [CERN1], for details see [LER93], device M4, d = 317 μm).

5.3 Simulations for the ATLAS SCT at LHC

5.3.1 Particle Fluxes

Calculations* of the particle fluxes in the ATLAS SemiConductor Tracker (SCT) were provided by G. Gorfine [GOR95] for a single Transition Radiation Tracker (TRT) design study of the inner detector, which includes a forward calorimeter and is close to the layout presented in the ATLAS Technical Proposal [ATL94], see Fig. 1.1. For those calculations a p-p cross section of 71 mb, a solenoidal magnetic field of 2 T, a full luminosity of $10^{34}\,\text{cm}^{-2}\text{s}^{-1}$, and an operation time of 10^7 s per year were assumed. Further, the fluences were considered for all involved particle types individually in order to allow for the accurate normalization to equivalent 1 MeV neutron fluences. For this purpose, the Van Ginneken proton damage function has been employed for kaons and anti-protons [VGI89], and otherwise the damage functions as shown in Fig. 3.0. The numerical data shown in Table 5.1 are barrel averages

* A Monte Carlo simulation with the FLUKA code in conjunction with DTUJET90.

over the quoted z-range, and a plot of the radial distribution is presented in Fig. 5.4. While for small radii the damage is mainly caused by pions, the albedo neutron background predominates in the outer regions.

Table 5.1 Annual equivalent damage fluences in 10^{12} cm^{-2} for numerous particle types in the ATLAS SCT (single TRT design configuration B, p-p cross section 71 mb, integrated luminosity 10^{41} cm^{-2}, from [GOR95]).

Radius	z	Proton	Pion	Kaon	Anti p	Neutron	Charged	Total
11.5 cm	± 35 cm	5.2	35	7.0	3.1	12	50	62
14.5 cm	± 40 cm	3.3	24	4.3	2.0	9.3	34	43
20 cm	± 55 cm	1.9	14	2.2	1.0	8.2	19	28
30 cm	± 95 cm	1.2	7.6	0.99	0.47	6.2	10	17
40 cm	± 95 cm	0.75	4.9	0.54	0.27	6.0	6.5	12
50 cm	± 95 cm	0.52	3.4	0.35	0.17	5.9	4.4	10
60 cm	± 95 cm	0.35	2.4	0.26	0.11	5.0	3.1	8.1
69 cm	± 95 cm	0.33	1.7	0.18	0.080	4.6	2.3	6.9

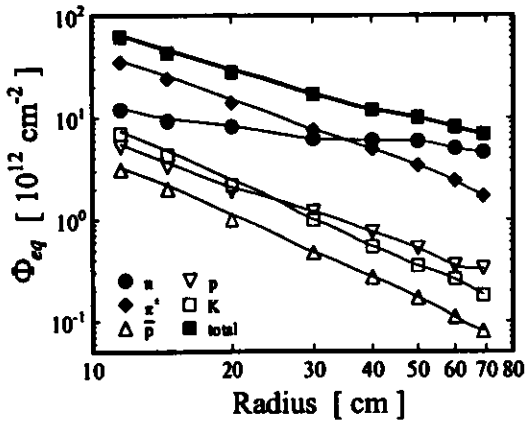

Fig. 5.4 Barrel averages of the annual equivalent 1 MeV neutron fluences at full luminosity as function of the radius for various particles, compare Table 5.1.

5.3.2 Operational Scenarios, Detector Parameters, and Benchmarks

In order to obtain a realistic picture of the operation of the silicon detectors at LHC the variation of the luminosity, the operational temperature, and the applied bias voltages have been considered. In the first three years the luminosity was assumed to be 10^{33} cm^{-2}s^{-1}, followed by seven years at the full luminosity 10^{34} cm^{-2}s^{-1}, that is, the annual fluences during the initial period are one tenth of the values given in Table 5.1. Moreover, the experiment was assumed to be running only during the first seven months of each year, and the corresponding constant particle fluxes have been determined by dividing the quoted fluences by 7 months. Further, a modestly low temperature, typically 0°C, was assumed to be established during all of the ten year operation except for a maintenance period at 20°C (warm-up) in the beginning of the 9th month of each year. Three lengths have been considered for the warm-up: 1 month, 3 days, and 0. Operational voltages V_{op} were assumed to be variable within certain limits, and, if possible, over-biasing of the devices was realized to ensure fast charge collection,

eq. 5.15
$$V_{op} = \begin{cases} 100\ \text{V} & V_{dep} + 50\ \text{V} < 100\ \text{V} \\ V_{op,max} & V_{dep} + 50\ \text{V} > V_{op,max} \\ V_{dep} + 50\ \text{V} & else \end{cases}.$$

Maximum operational voltages $V_{op,max}$ of 200 V and 300 V have been used. Regarding the leakage current I per channel, the total active area in the three pixel layers (radii 11.5 cm ... 20 cm) was assumed to be 50 µm × 300 µm, while 12 cm × 112.5 µm has been used for the strip modules (radii 30 cm ... 69 cm), see reference [ATL94]. Moreover, to make the plots more distinct the device thickness was fixed to 300 µm. While this is reasonable for the strip detectors, smaller values of d have been proposed for the pixels. Concerning the full depletion voltage this is a scaling with the factor $(d/300\ \mu\text{m})^2$, see eq. 2.7. Further, even if the actual operational voltage was not sufficient to fully activate the detector has the full volume Ad been used for the calculation of the leakage current I, also to make the plots more distinct. The initial doping concentration was assumed to be $N_{eff,0} = 5\times10^{11}$ cm^{-3}.

Besides the mentioned maximum operational voltages, benchmark figures have also been suggested for the other detector properties [ATL94]. Regarding the leakage current per channel a limit of 2 µA was deduced from power dissipation considerations and the related difficulties met with thermal runaways. However, for the pixel system also the leakage current related noise needs to be taken into account. Further, 70% of the charge deposited in the detectors should be collected at the electrodes. However, if the operational voltage is not sufficient to fully deplete the detector (partial depletion) the sensitive volume and thus the total charge Q_e is decreasing, which is the prominent effect regarding the deterioration of the signal to noise ratio.

5.3.3 Results and Discussion

For the simulation of the radiation damage effects a distinction was made between charged-hadrons and neutrons. The total damage-induced change in a certain property was assumed to be the sum of two portions calculated from the charged-hadron and neutron fluences using the pion and the neutron damage constants (Table E.7). This ensures that the simulation result reflects the experimental observations underlying the extraction of the damage constants as close as possible.

Fig. 5.5 shows the simulation of the damage-induced changes in the relevant electrical properties for a 10 year operation sequence at LHC using the fluences quoted for the strip layer at a radius of 30 cm. An operation temperature of 0°C, a one month warm-up, and a maximum operational voltage of 300 V has been assumed. Only a minor variation is observed within the initial three years of low luminosity running. Type inversion and a progressively increasing full depletion voltage V_{dep} is anticipated after the first year at full luminosity. During the maintenance periods reverse annealing takes place, adding up to the change in V_{dep} related to the stable damage portion. Contrary, the leakage current per channel I exhibits beneficial annealing in the warm-up cycle, accompanied by much larger numbers due to the strong intrinsic temperature dependence. A plateau is noticed for the charge collection deficiency $1\text{-}Q/Q_0$ in the years 5 through 8. This is due to the increasing amount of trapping centers compensated for by the simultaneously increasing operational voltage, see eq. 5.15, which shortens the collection time and reduces the influence of trapping. Although not relevant for the detector operation, it is interesting to note the increased collection deficiency during warm-up arising from the smaller mobility, which results in slower charge collection. If the maximum operational voltage is not sufficient to fully activate the device, charge collection loss becomes significant.

Fig. 5.6 a) shows the influence of the operating temperature and the length of the warm-up period on the values obtained on the same strip layer after ten years of operation. Low temperature operation in combination with a short maintenance period can significantly reduce the reverse annealing of the depletion voltage. Regarding the benchmark quoted for the leakage current, cooling of the detectors is found to be inevitable. Therefore, also a natural regulation of the reverse annealing is given and the difficulty met with excessive depletion voltages is then found to be chiefly related to the stable portion of the radiation damage-induced change in the space charge concentration. In this context it is noted that even at the lowest temperature operation without warm-up examined the annealing of the leakage current is not found to be significantly frozen. As there seems to be a correlation between the short term annealing of the leakage current and the doping concentration (e.g. [SCH95]), the same would also be

expected to hold for the depletion voltage. In any case could the beneficial short term annealing be propelled by warming up intentionally. Therefore, for an optimized operation schedule the projected change in the depletion voltage and the leakage current can be calculated straight-forward from the accumulated fluence by simply using the relations eq. 3.11 and eq. 3.20.

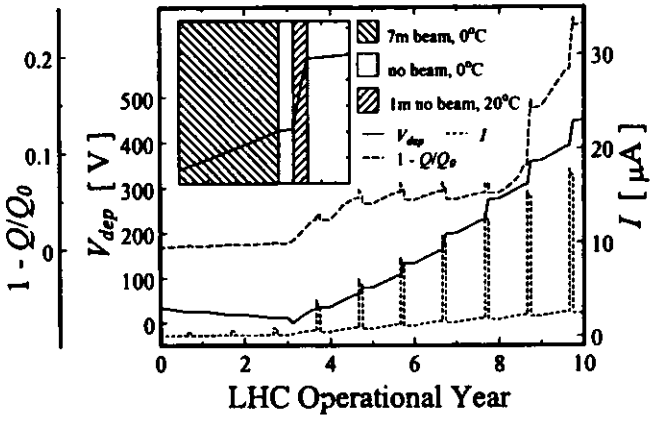

Fig. 5.5 Evolution of the damage-induced changes in the electrical properties for the strip layer at a radius of 30 cm during the operation at LHC, using a warm-up period as illustrated in the inset, showing the V_{dep} data for the last year ($V_{op,max}$ = 300 V).

Fig. 5.6 b) presents the evolution of the radial distribution of the silicon detector properties during the 10 years LHC operation for a constant operating temperature of 0°C. Concerning a maximum operation voltage of 300 V, the strip layers (radius ≥ 30 cm) would survive all of the ten years in this scenario. The pixel layers are becoming partially depleted after a certain time. However, choosing a device thickness of 150 μm rather than 300 μm would reduce the depletion voltages by a factor of 4, which significantly improves the situation. On the other hand, leakage currents are still becoming quite large, recommending a further reduction of the operating temperature.

So far only the barrel averages of the particle fluences have been used. According to Fig. 1.2 there is however a significant variation over the z-direction which results in a corresponding distribution of the damage projections. For the operation at a constant temperature of 0°C the final depletion voltages are plotted in Fig. 5.7 as function of the radius and the z coordinate in a quarter-section of the inner detector. In regard to the z-extent of the layers quoted in Table 5.1 it can be seen that all of the 30 cm and 40 cm strip layer can be fully depleted with 300 V and 200 V, respectively. However, at the position of the MSGC's (see Fig. 1.1), which have been replaced by silicon counters, more damage than would be awaited from the results obtained on the barrels at the same radius is expected.

Finally it will be studied, which uncertainty is introduced in the damage projections by the spread in the raw data (Table E.8) and the errors in the flux calculations. Regarding the latter a conservative estimate of the lower and upper limit of the charged-hadron and neutron fluxes has been quoted in reference [GOR94] to be the average value either divided or multiplied with a factor of 1.6 and 2, respectively. The crosshatched regions in Fig. 5.8 depict the corresponding variations in the device properties reached after a 10 year LHC operation at constant 0°C. Concerning the damage constants, only one parameter has been changed for each simulation and the resulting deviations from the average in the considered quantity were added in quadrature. This is the correct procedure given the correlation between the parameters in the model descriptions is negligible. Evidently, the major uncertainty is arising from the flux calculations and a survival radius can be estimated only very crudely.

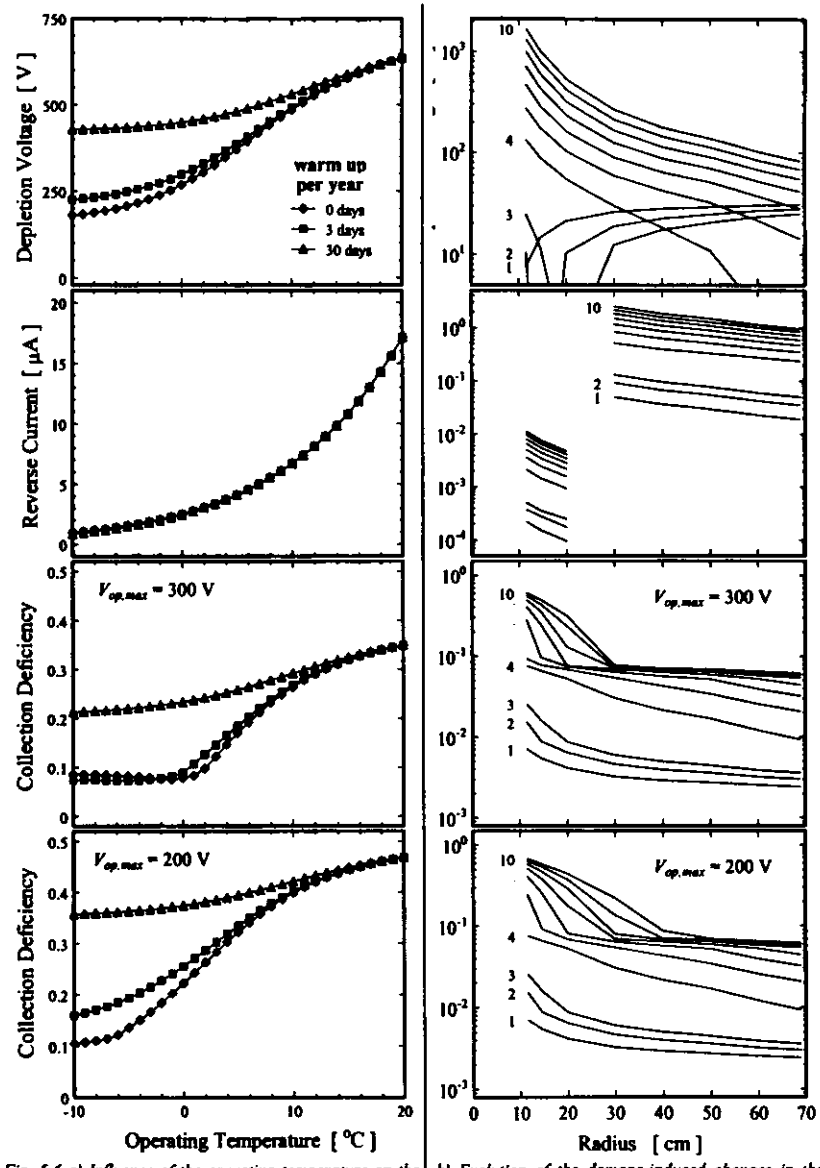

Fig. 5.6 a) Influence of the operating temperature on the performance of the strip layer at a radius of 30 cm (d =300 μm) after 10 years of operation.

b) Evolution of the damage-induced changes in the detector properties as function of the radius for a constant operating temperature of 0°C (no warm-up).

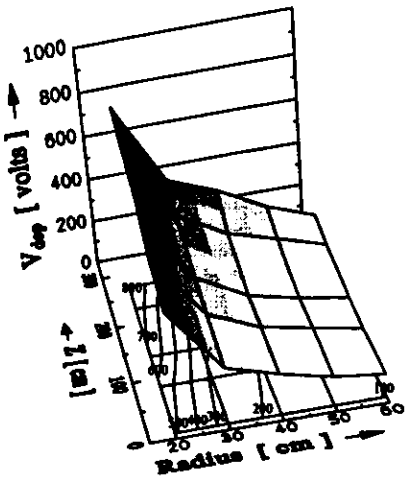

Fig. 5.7 Depletion voltage after ten years of operation at constant 0°C in the r-z-plane of a quarter section of the inner detector (d = 300 μm).

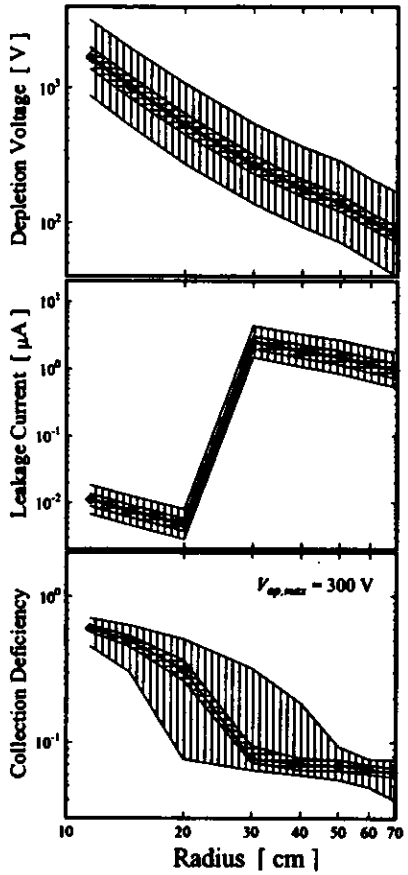

Fig. 5.8 Influence of the spread in the raw data on the final state of the radial distribution (constant 0°C operation). The inner, horizontally crosshatched region is due to the spread in the raw data. The outer, vertically crosshatched domain represents the fluence error.

There are further aspects of the radiation damage which have not been taken into account, although they might be significant. For example, also the ionization doses in the considered environment will be very large, and therefore an increase of the concentration of oxide charges and interface states up to their saturation level is expected. While in usual device designs the interface is not depleted and therefore no contribution to the leakage current would be awaited, the fine segmentation of pixel and strip detectors could result in an enlargement of the voltage required to fully activate the detectors by as much as the flat-band voltage (compare [RIC96]) which, depending on the oxide quality, can become of the order of several ten volts. Moreover, considerable improvements regarding the problem with the depletion voltages could be achieved if lower resistivity material were employed for the manufacture of the detectors, inasmuch as the experimental data presented in Section 3.2.5 suggest that not all of the initial n-type doping is removed, but rather that there is a reservoir of not removable positive space charges. Further, the examination on the rate constant k_Y presented in Section 3.2.6 suggests that the reverse annealing time constant does indeed not depend on the irradiation fluence. This would reduce the danger related to the warm-up period, in particular for the pixel detectors.

5.4 Summary of the Damage Projections

- The parameters in the models describing the damage-induced changes in the doping concentration and the leakage current were compiled from literature references and from the analysis of raw data supplied by various groups.
- An extension of the models accounting for simultaneous buildup of the damage effects and their annealing has been presented in conjunction with the corresponding numerical implementation.
- Various simulations of the damage-induced changes in the depletion voltage, leakage current, and charge collection deficiency to be expected in the ATLAS SemiConductor Tracker during 10 years of operation were shown, exploring the influence of the operational parameters and the position within the experimental environment.
- It was found that:
  - Cooling is inevitable to reduce leakage currents.
  - The most likely failure mode of a silicon detector is the loss of sensitive volume due to progressively growing depletion voltages beyond reasonable values of the maximum operational voltage.
  - If a maintenance warm-up period is scheduled, it should be short to prevent reverse annealing.
  - For the inner detector design and operational parameters considered, only layers at radii greater than about 30 cm remain fully depleted all of the 10 years.

6 Summary

This thesis describes original work in the area of the radiation hardness of particle detectors fabricated from high resistivity ($\rho > 3$ kΩcm) float zone silicon. In the perspective of their application in present-day and future high-energy physics experiments, bulk and surface damage effects have been studied for equivalent 1 MeV neutron fluences ranging from 10^{11} cm^{-2} to 10^{14} cm^{-2} and ionization doses up to approximately 100 kGy. While the radiation sensitivity of the oxide passivation has been addressed only briefly, detailed studies were carried out on the microscopic and macroscopic features of the bulk damage. Special interest was always paid to the parameters determining the long term annealing behavior, as in practice it is necessary to guarantee the reliable operation of the silicon detectors over an extended period of several years. This refers to the leakage current and the change in the doping concentration, which are both known to grow as function of the irradiation fluence. The latter has become a major issue as it determines the minimum operational voltage and, as opposed to the leakage current, exhibits a long term increase (reverse annealing). Microscopic methods well-suited for the characterization of damage-induced defect levels in high resistivity silicon have been explored in detail. A chief objective was the correlation of the microscopic features of the damage with the macroscopically observed deterioration of the detectors.

Changes in the Macroscopic Properties and Damage Projections for ATLAS at LHC

The models describing the bulk damage-induced changes in the effective doping concentration, the volume leakage current, and the charge collection deficiency as function of the irradiation fluence and annealing time have been reviewed and were illustrated by experimental examples. The long term damage parameters related to the doping concentration and the leakage current were compared for 5.3 MeV neutrons, 24 GeV protons, and 236 MeV positive pions. All investigated samples were taken from one wafer, and identical methods were applied for the annealing of the samples and the subsequent data analysis, ensuring a maximum accuracy. The NIEL hypothesis underlying the normalization of the irradiation fluences to equivalent 1 MeV neutron values by means of the hardness factors was found to be appropriate for the irradiation sources and damage constants studied. However, while a good agreement was found between the normalized damage constants for neutrons and pions, objections were raised against the hardness factor currently used for the CERN PS proton source. Thus, an experimental hardness factor was determined by referring the damage constants observed at the proton source to the corresponding values found at the very reliable Be(d,n) neutron generator of the Physikalisch-Technische Bundesanstalt at Braunschweig with a hardness factor of 1.45,

$$\kappa_{exp,CERN\ PS} = 0.582 \pm 0.028 .$$

Moreover, the variation of the pion damage as function of the pion energy has been examined, finding no significant excess of the damage effects around the Δ resonance, and also no difference between positively and negatively charged pions. This detailed assessment of the pion damage is of particular importance as virtually no studies had been performed on this subject before although e.g. at LHC the deterioration of the silicon detectors close to the interaction point will chiefly be due to pions.

A systematic study was carried out on the influence of the initial doping concentration (0.6×10^{12} cm^{-3} p-type to 2.5×10^{12} cm^{-3} n-type) on the long term annealing effects. In order to avoid fluence calibration errors all devices were exposed at the PTB Be(d,n) neutron source. These data are listed in Table 6.1 in conjunction with the corresponding values obtained in a global survey. Regarding the latter, data from various neutron sources were used resulting in a large spread due to insufficient normalization to equivalent 1 MeV neutron fluences. In this work only the total amount of permanently removed donors N_a was found to depend on the initial doping concentration $N_{eff,0}$, and the relation quoted in Table 6.1 is of particular interest as it indicates a 'reservoir of non-removable donors'. With respect to the difficulties met with excessively growing depletion voltages at large irradiation fluences beyond inversion this shows that the radiation hardness of n-type material can be improved if the initial resistivity is lowered. Further, the rate of the long term reverse annealing in the effective doping concentration was found to be

a function of the irradiation fluence, and the relation given in Table 6.1 for the frequency factor k_a holds for an activation energy of E_a = 1.31 eV. It was concluded that the microscopic processes underlying the reverse annealing are in fact first order reactions, in contrast to the second order model suggested by the currently accepted parametrization of the reverse annealing function.

Table 6.1 Damage constants obtained from a global survey and refinement of the damage models achieved in this work.

Parameter	Global Survey	This work (PTB Be(d,n), κ = 1.45)
g_Γ [10^{-2} cm^{-1}]	4.6±1.6	5.66±0.11
g_c [10^{-2} cm^{-1}]	1.77±0.35	2.68±0.14
c [10^{-13} cm^2]	2.29±0.63	2.4±1.4
N_a [10^{12} cm^{-3}]	0.197	(0.3±0.1) × $N_{eff,0}$ [10^{12} cm^{-3}] + (0.1±0.07)
k_a [cm^{3}s^{-1}]	520{128...2110}	(1.9±1.2) × 10^{-16} cm/s × (Φ_{eq} [cm^{-2}])$^{-1}$

Finally, the details of the numerical simulation of the damage projections for the ATLAS SemiConductor Tracker at LHC carried out for the Technical Proposal were presented. For this purpose the parameters in the macroscopic damage models have been compiled from literature references and from the dedicated analysis of raw data supplied by various groups. It was moreover necessary to extend the models to account for the simultaneous buildup of the damage effects and their annealing. Various simulations of the damage-induced changes in the depletion voltage, leakage current, and charge collection deficiency to be expected during 10 years of operation were shown, illustrating the influence of the operational parameters and the position in the experiment. It was found that cooling is inevitable to reduce the leakage currents to an acceptable limit. Further, it was concluded that if a maintenance warm-up period is scheduled, it should be short in order to prevent reverse annealing. In conclusion, for the inner detector design and operational parameters considered, only layers at radii greater than about 30 cm were found to remain fully depleted all of the 10 years.

Microscopic Defect Studies

A close inspection of the properties of defect levels in silicon has been presented, focusing on their action in the space charge region of a detector. Further, the formal theory behind defect characterization tools like TSC (Thermally Stimulated Current), I-DLTS (Current-Deep Level Transient Spectroscopy), and TCT (Transient Current Technique) was developed. In comparison to the otherwise frequently used Capacitance-DLTS these methods have the advantage of remaining applicable even in the presence of large defect concentrations compared with the shallow doping. This situation is typically encountered on radiation-damaged silicon detectors made from high resistivity float zone silicon (e.g. for $\Phi_{eq} > 10^{12}$ cm^{-2}).

However, it is not straight-forward to unambiguously analyze the spectra under such conditions, and substantial efforts have been undertaken to resolve the corresponding peculiarities in TSC measurements. One of the major problems is that the width of the space charge region becomes a function of the measuring temperature, resulting in distorted peak shapes. A simple model was proposed that accounts for these effects and which is capable of predicting the TSC spectra, e.g. the shift of the peak temperatures. The model is valuable in particular as the developed procedure for the accurate extraction of defect concentrations is based on it.

Further, concerning TSC three different modes of defect filling have been examined on a couple of samples irradiated by fluences ranging from approximately 10^{11} to 10^{14} cm^{-2}. These were: cooling under zero bias, switching to zero bias, and injecting a forward current at low temperature. It was shown that by a thorough study of the filling processes it is possible to infer the type of the transition (electron or hole trap) causing a certain peak signal. Only by forward current injection can a significant occupation of all traps be achieved. Thus, forward IV characteristics were systematically studied as function of irradiation fluence and temperature. The data were discussed in terms of the standard Shockley treatment of the diffusion diode and a p-i-n diode model.

The gained insight into the TSC spectra chiefly aids the accurate determination of defect concentrations. Table 6.2 lists the introduction rates (concentrations normalized to equivalent 1 MeV neutron fluences) at a well-annealed state after about one year storage at room temperature if not otherwise indicated. The Table also contains the deep level enthalpies $\Delta H'$ and emission cross sections σ evaluated with TSC, I-DLTS, or TCT. N_b represents a defect related to the left-hand side broadening of the peak corresponding to the transition $VV^{(-/0)}$. The broadening is observed only on heavy particle damaged samples but e.g. not after ^{60}Co-gamma exposures. The level parameters of the peaks with smaller concentrations (peaks A, J, and the E_V + 0.5 eV levels observed with TCT) that so far have not been reported in the literature are of special interest as the dominant defects (VO_i, C_iO_i, C_iC_s, VV) cannot account for the deterioration of the macroscopic properties of the detectors due to the energetic position and character of their levels. The large cross section observed on peak J points towards a Coulombic acceptor level capable of accounting for damage-induced negative space charge. However, it was found that reliable level parameters can be determined with TSC and I-DLTS only if the defect concentrations are comparatively small, which was not always realized. Therefore, the data on peak J might be afflicted with a considerable systematic error and it cannot be excluded unmistakably that the peak indeed arises from $C_i^{(+/0)}$.

As noted in Table 6.2, systematic studies of the TSC spectrum as function of the temperature at which deep levels are filled have shown that the hole capture (c_p) of the C_iO_i deep donor level requires an activation energy of approximately 35 meV to be overcome. Further, on the most heavily damaged device an electric field enhancement of the emission rate was observed on one peak, tentatively assigned to the shallow donor level $C_iP_s(III)^{(0/+)}$. In this context it is noted that with I-DLTS very shallow levels can be investigated. Besides phosphorus, some of the levels found in unirradiated material were tentatively assigned to thermal donors, and such studies might once reveal the puzzling interaction between the shallow dopants with the damage-induced defects.

Table 6.2 Results of the microscopic defect studies using TSC, I-DLTS, and TCT. If not indicated otherwise all data refer to a well-annealed stated reached after about 1 year storage at room temperature.

Transition	Method	$\Delta H'$ [eV]	σ [cm^2]	g_r [cm^{-1}]	Comment
$C_iO_i^{(+/0)}$	TSC	+0.363	2.4×10^{-15}	1.06	$c_p \propto \exp(-35\ \text{meV}/k_BT)$
$VV^{(-/0)}$	TSC	-0.413[a]	1.1×10^{-15}[a]	0.481[a]	
peak N_b + $VV^{(-/0)}$				2.02	
$VV^{(--/-)}$				0.70	
$C_iP_s(III)^{(0/+)}$					Poole-Frenkel, $\Phi_{eq} \approx 10^{14}$ cm^{-2}
$C_iC_s(B)^{(-/0)}$	I-DLTS	-0.113	5.9×10^{-15}	0.16	
$VO_i^{(-/0)}$ + $C_iC_s(A)^{(-/0)}$	I-DLTS	-0.169	6.1×10^{-15}	0.993	
$VO_i^{(-/0)}$				0.84	
peak A	I-DLTS	-0.0785	1.0×10^{-14}	0.085	
peak J	TSC/I-DLTS	+0.321	2.1×10^{-13}	0.095[b]	
	TCT	+0.51[c]	1.0×10^{-14}[c]	0.0295[c]	
	TCT	+0.54			3.0×10^5 cm^{-3}Gy^{-1}, ^{60}Co-gamma

[a] After 130 min at 290°C.
[b] After 130 min at 290°C, $\Phi_{eq} \approx 10^{12}$ cm^{-2}.
[c] After 66.5 h at 80°C.

Correlation between Microscopic and Macroscopic Features of the Bulk Damage

Insights into the correlation between the microscopic and macroscopic features were gained by two crucial experiments. Firstly, samples were exposed to ^{60}Co-gammas because contrary to heavy particle damage the average energy imparted to the PKA (Primary Knock on Atom) is only of the order of the

threshold energy required to displace a single silicon host atom. Accordingly, the generated crystal defects are randomly distributed, and higher order defects (VV etc.) are hardly encountered. Secondly, a weakly and a heavily neutron-damaged device were subjected to isochronous annealing and the evolution of the defect spectra and the macroscopic properties were monitored simultaneously using TSC and IV/CV characteristics, respectively.

Regarding high doses of ^{60}Co-gammas (a few MGy) an increase in the bulk leakage current and introduction of negative space charge (also type inversion) was observed. Most strikingly no annealing was found to take place neither in the effective doping concentration nor in the leakage current, allowing for the conclusion that all annealing effects observed after heavy particle damage are originating from the closer spacing of the intrinsic point defects (e.g. VV) in the terminal regions of the displacement damage cascades and/or from higher order defects.

As negative space charge is introduced in both heavy particle and gamma-damaged samples, however, always at a rate much smaller than the dominant defects, it was concluded that the negative space charge in general is related to a higher order intrinsic point defect, i.e., a complex defect composed of few silicon vacancies and/or interstitials. However, an incorporation of oxygen or carbon cannot be excluded as these impurities are always present in large amounts, both of the order of several times 10^{15} cm^{-3} in the float zone material studied. Further, since the linear term of the stable damage-induced change in the doping concentration was found to be independent of the initial resistivity and also no saturation of the increase in the negative space charge has so far been noticed even for the highest fluences, an incorporation of the initial doping atoms (phosphorus, boron) or any other impurities with similarly small concentrations was ruled out. The hole trap at around E_V+ 0.5 eV observed with TCT was discussed as a possible candidate for the negative space charge because the large cross section would be in agreement with the assignment to an acceptor level and the quoted introduction rates fit the macroscopically observed values. Moreover, the possibility of thermally activated space charge has been discussed, which in the Shockley-Read-Hall treatment requires a trap very close to the middle of the band gap. No thermally activated negative space charge was observed on well-annealed (one year at room temperature) samples heavily damaged by neutrons.

On inverted samples a bistable defect is known to be introduced by elevated temperature annealing. This is manifested in the macroscopic properties by a decay of the depletion voltage (i.e. the negative space charge) after quenching from the annealing temperature. The time constant is several 100 min at room temperature. This process can be reversed, for example by injecting a forward current. This has been exploited in this work to unambiguously relate the negative space charge in the excited state to one particular trap signal in the TSC spectrum, namely, peak J. The corresponding defect could also be connected with the reverse annealing in the effective doping concentration, inasmuch as its concentration was found to be growing in the later stages of isochronous annealing experiments. On the basis of its bistability and its interaction with free carriers, an explanation was given for the large differences observed in the annealing behavior of weakly and heavily damaged samples.

The reverse annealing introduction rate was found to be independent of the initial doping concentration. Thus, the initial dopants are also unlikely to be a constituent of the defects playing a role in this solid-state transformation. Moreover, the revised modeling of the reverse annealing rate constant points towards a dissociation process.

Regarding the volume leakage current, a large fraction can be attributed to the $VV^{(-/0)}$ level in heavy particle damaged samples after elevated temperature annealing (e.g. 90 min 290°C) and in ^{60}Co damaged samples. Again a possible candidate for the remaining fraction is the above mentioned E_V + 0.5 eV level. Contrary, in heavy particle damaged samples which have been annealed only at room temperature for an extended time the divacancy can definitely not account or the observed large volume generation currents. However, isochronous annealing reduces this excess leakage current accompanied by the disappearance of the left-hand side broadening of the peak arising from the transition $VV^{(-/0)}$. The data presented in this work support the view held in the recent literature that the corresponding defect (N_b) is related to the leakage current, which then requires an extension of the simple Shockley-Read-Hall theory. Further, it was confirmed that this defect is likely to be silicon interstitial related and is stable only in the presence of lattice strain as anticipated around terminal clusters.

From the knowledge gained about the defects in the studied samples also the damage-induced change in the trapping time constants and the resistivity of the material in thermal equilibrium (neutral bulk) could be calculated. While half of the macroscopically observed electron trapping could reasonably well

be ascribed to the divacancy transition $VV^{(-/0)}$, a discrepancy of one order of magnitude was observed for the hole trapping. The resistivity was predicted to be maximized around the inversion fluence and to saturate at a large value for increasing fluences.

Outlook

This work is understood to be just a first effort towards the understanding of the relation between the microscopic features of the bulk damage and the deterioration of the detector performance, which once might lead to more radiation tolerant silicon material. Numerous studies on damage-induced defect levels in silicon have already been reported in the literature. However, it was shown here that it is not straight-forward to adapt those results, but rather is there a compelling need for further microscopic defect studies in this field. In particular peak J and the E_V + 0.5 eV hole trap, both candidates for the introduction of negative space charge, are worth to be considered in more detail, e.g., with respect to the annealing behavior and the level parameters (capture coefficients and ionization energies). Concerning the leakage current it is also important to assess the behavior of the divacancy transition $VV^{(-/0)}$ at room temperature more clearly, i.e., without relying on the extrapolation from spectroscopic data obtained at low temperature. This could for example be done with the TCT method, provided suitable procedures for injecting large concentrations of free carriers are developed. In this work important conclusions were drawn from the differences observed between ^{60}Co-gamma and heavy particle damage, and more interesting results in this direction would be expected from irradiations with electrons with variable energies. This would enable a study of the transition between randomly distributed point defects and damage characteristic of heavy particles. Further, insights into the chemical nature of the defects accounting for the detector deterioration could be gained by the study of silicon with modified impurity content, especially oxygen and carbon. As the microscopic composition of the defects in question is not known, a correlation with other spectroscopic methods like EPR, IR, PL (see Appendix B) providing structural information would be very helpful. Finally it is noted that also the damage-induced changes in the macroscopic detector properties need further study, for example with respect to the behavior of the reverse annealing introduction rate at low fluences or with respect to the amount of permanently removed donors which might depend on the irradiation flux.

Appendix A: Material Properties and Constants

Table A.1 Constants.

q_e	1.602×10^{-19} C
m_e	9.109×10^{-31} kg
ε_0	8.854×10^{-14} C/(Vcm)
k_B	1.381×10^{-23} J/K
h	6.626×10^{-34} Js
c	2.998×10^{8} m/s

Table A.2 Densities.

ρ_{Si}	2.33 g/cm³
ρ_{SiO2}	2.32 g/cm³
ρ_{Al}	2.70 g/cm³
ρ_{Au}	18.88 g/cm³

Table A.3 Electrical properties from [SZE81], unless otherwise indicated.

a_{Si}	5.43 Å
ε_{Si}	11.9
ε_{SiO2}	3.9
E_g(300 K)	1.12 eV
E_g(20°C)[a]	1.126 eV
n_i(20°C)[a]	6.005×10^{9} cm⁻³
$\mu_{e,i}$(20°C)[b]	1.48×10^{3} cm²V⁻¹s⁻¹
$\mu_{e,p}$(20°C)[c]	4.86×10^{2} cm²V⁻¹s⁻¹

[a] from [GRE90] and references therein.
[b] from eq. A.3.
[c] from eq. A.4.

Table A.4 Optical absorption data for three wavelengths λ.

λ [nm]	hc/λ [eV]	α^{-1} (77 K) [µm]	α^{-1} (300 K) [µm]	a [cm⁻¹K⁻¹]	b [cm⁻¹]
670	1.85	7.7	3.3	7.6	720
830	1.49	32	13	2.15	145
980	1.27	290	63	0.56	-8.1

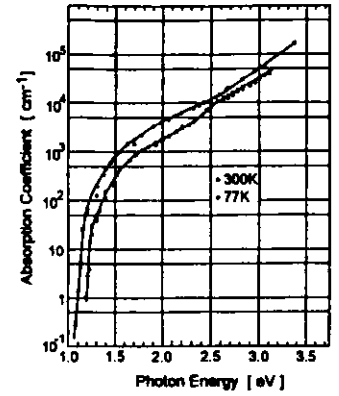

Fig. A.1 Optical absorption constant in intrinsic silicon at 77 K and 300 K as function of the photon energy, from [DAS55].

Optical Absorption

The spatial distribution of electron-hole pairs created by an optical injection pulse (e.g. DLTS or current pulse shape measurements) is determined by the absorption constant α . The light intensity is reduced as function of the depth z in the absorbing medium as $\exp(-\alpha z)$. Fig. A.1 shows the absorption coefficient as function of the photon energy after Dash and Newman [DAS55]. In the range of photon energies encountered in this work (compare Table A.4) the light absorption in silicon takes place by indirect inter-band transitions, i.e., a lattice phonon is incorporated in order to conserve the crystal momentum. Accordingly, the absorption constant reflects the dependence of both the band gap energy and the phonon spectrum on the temperature. This dependence has been parametrized by

eq. A.1 $\quad \alpha(T) \approx a \times T + b$,

and Table A.4 gives the derived values of a and b as well as the penetration depth $1/\alpha$ extracted from Fig. A.1. As the studied devices are about 300 µm thick it is thus clear that the 670 nm light generates carriers mainly close to the illuminated surfaces. However, the penetration depth is just a reduction in the intensity to 1/e of the initial value, i.e., significant amounts of free carriers are generated at larger distances. In this sense the 980 nm laser acts throughout all of the sample thickness, however, except for very low temperatures the injected free carrier concentrations cannot be regarded as homogeneous.

A portion of the incident laser light generally will be reflected at the illuminated surface and, given metallizations are present (e.g. Schottky/ohmic contacts), absorption in thin layers of gold and aluminum needs to be taken into account. The latter is an important subject when surface barrier detectors fabricated according to the standard Hamburg group process are used (see Section 2.2.3) and has been studied for the instance of 820 nm laser light in reference [UHL95]. There it was found that about 20% of the initial intensity can pass through the standard gold metallization of 40 µg/cm² (≈ 20 nm). However, the used 100 µg/cm² (≈ 400 nm) aluminum metallization on the back plane contact does entirely block the light. The transmission improves to about 5% if a 4 µg/cm² (≈ 15 nm) layer is used.

The Drift Velocity in Silicon

In silicon electrons and holes drift with different velocities $v_{dr,n,p}$ in a given electric field. Moreover, $v_{dr,n,p}$ depends on the temperature, the actual electric field strength, and the crystal orientation. The major mechanisms hindering the drift are phonon scattering, predominating at high temperatures, and ionized impurity scattering. Regarding the high purity material studied in this work only the former needs to be taken account. While at low absolute values of the electric field strength $|E|$ the drift velocity v_{dr} grows in proportion with the electric field ($v_{dr} = \mu_0|E|$), v_{dr} approaches a constant value v_s related to the thermal velocity at high fields. The latter is due to the high kinetic energy of the free carriers, which are graded hot in this condition and thermalize with the silicon host lattice.

C. Canalli et al. have employed a time of flight technique on high resistivity float zone silicon samples to accurately determine the drift velocity in the temperature range 77 K - 300 K and for electric fields up to 50 kV/cm [CAN71]. For purpose of easy numerical evaluation their data have been approximated here by the following functional relation

eq. A.2 $$v_{dr,n,p}(|E|,T) = \frac{\mu_{0n,p}(T)|E|}{\left(1+\left(\mu_{0n,p}(T)|E|/v_{sm,p}(T)\right)^{b_{n,p}(T)}\right)^{1/b_{n,p}(T)}},$$

which is related to the theoretically expected dependence [SZE81]. Fitting the above relation to the experimental data on the drift velocities as function of the electric field has furnished an optimum set of the parameters $\mu_{0n,p}$, $v_{sm,p}$, and $b_{n,p}$ at seven temperatures. Their variation with temperature was subsequently approximated by a combination of polynomial and exponential functions. Taking the temperature T in units of degrees Kelvin, the corresponding results for the low field mobility μ_0 are

eq. A.3 $$\mu_{0n}(T) = 2.712\times10^{8}\,\frac{\mathrm{cm}^2}{\mathrm{Vs}}\,T^{-2.133} \text{ and}$$

eq. A.4 $$\mu_{0p}(T) = 8.54\times10^{5}\,\frac{\mathrm{cm}^2}{\mathrm{Vs}}\,T^{-1.075}\exp(1-T/124).$$

At 300 K this gives $\mu_{0n} = 1.41\times10^{3}$ cm^{2}V^{-1}s^{-1} and $\mu_{0p} = 4.48\times10^{3}$ cm^{2}V^{-1}s^{-1}, which is close to the most data found in the literature, e.g. [SZE81]. The saturation velocities are given by

eq. A.5 $$v_{sn}(T) = 1.586\times10^{7}\,\frac{\mathrm{cm}}{\mathrm{s}}\exp(-T/723.6) \text{ and}$$

eq. A.6 $$v_{sp}(T) = 1.445\times10^{7}\,\frac{\mathrm{cm}}{\mathrm{s}}\exp(-T/435.9),$$

which gives $v_{sn} = 1.05\times10^{7}$ cm/s and $v_{sp} = 7.26\times10^{6}$ cm/s at 300 K. Finally, the variable parameter b is written

eq. A.7 $$b_n(T) = -8.262\times10^{-8}T^3 + 6.817\times10^{-5}T^2 - 1.847\times10^{-2}T + 2.429 \text{ and}$$

eq. A.8 $$b_p(T) = 2.49\exp(-T/270.3).$$

The overall difference between the above approximation and the experimental data is around 3%, typically less below 160 K. Only in one case is the agreement worse, namely 6% for the electron data at 245 K.

Appendix B: Compilation of Defect Parameters

Numerous studies on impurities and defects in silicon have been reported in the literature employing various spectroscopic methods. Among the most widely used regarding the disclosure of the microscopic defect structure are the Electron Paramagnetic Resonance (EPR), Infrared Absorption (IR), and Photo Luminescence (PL). Nowadays these tools are often combined with electrical characterization techniques like the very popular Capacitance-Deep Level Transient Spectroscopy (C-DLTS). Taking into consideration the effect of intentionally varied concentrations of oxygen, carbon, or shallow dopants (phosphorus, boron, arsenic, aluminum, etc.) and the observations made in elevated temperature annealing experiments, an unambiguous assignment of the chemical nature of the unknown defect in question is often possible. However, a large fraction of all publications in this field focus on only one particular characterization tool, and one is thus forced to combine the information dispersed over many references. It is then inevitable to be familiar with the various notations used for one specific defect. A corresponding compilation for all impurities anticipated in silicon before and after exposure to bulk damaging radiation is therefore presented on the next pages.

EPR, IR (vibrational modes refer to the most abundant isotope), PL data were taken from [LB89] for the shallow impurity levels, from [SO190,SO290] for C_i and C_iC_s, from [JON92] for C_iO_i, from [SVE92] for VV, and from [EWE95] for V_sO_y. However, the focus is on the electrical level parameters as they are of chief importance for this work. If available the enthalpy ΔH (positive/negative for hole/electron traps), the corresponding entropy factor X, and both capture coefficients for electrons c_n and holes c_p have been quoted along with the appropriate literature reference and the temperature range in which the transition was studied (ΔE_a and θ denote the Gibbs free energy relative to E_C and the normalized absolute temperature $T/300$ K, respectively). For purpose of easier comparison the data have been refitted to an Arrhenius-plot according to the simplified expression for the emission rate given in eq. 3.51 yielding the uncorrected emission enthalpy $\Delta H'_{n,p}$ and the corresponding emission cross section $\sigma_{n,p}$. This is helpful as most references, e.g. this work, quote only $\Delta H'$ and σ, and frequently even the cross section is omitted. Further, for the instances where $\Delta H'$ and σ were available the associated maximum temperature T_{max} of a TSC peak was calculated by eq. 3.79 assuming a heating rate β = 0.183 K/s which has typically been used in this work. Except for C_iC_s, the most reliable information with respect to radiation damage-induced defect levels has recently been provided by A. Hallén et al. [HAL96]. It is noted here that they have taken the quantities n_i, N_C, N_V, and E_g from the review given by M.A. Green [GRE90]. For the multistable defect complex C_iP_s, which was fully characterized by E. Gürer et al. [GÜR92], only the two mostly encountered configurations have been taken into account. C_iP_s IA is the stable configuration and C_iP_s III emerges after injection of free carriers at low temperatures. There are three further configurations that can be observed after a combination of appropriate injection and successive low temperature annealing. Injection of free carriers at temperatures higher than 260 K would dissociate the pair and liberate interstitial carbon C_i.

Regarding the annealing behavior, frequency factors k_0, activation energies E_a, and annealing temperatures T_a are listed in the last column, compare Appendix C. The arrows indicate whether the defect anneals in (↑) or out (↓) or whether it starts migrating (↔). Note that in general the annealing characteristics depend on the defect charge state. The value cited for the neutral C_i refers to the reverse bias annealing of the $C_i^{(-/0)}$ transition [SO190]. Corresponding data in p-type material (transition $C_i^{(+/0)}$) are slightly different $k_0 = 10^8$ 1/s, $E_a = 0.75$ eV, and $T_a \approx$ 30-70. Moreover, considering VP_s, when minority carriers are injected the activation energy can be decreased (recombination enhanced annealing: $E_a = 0.48$ eV, $k_0 = 8.2\times10^3$ s^{-1}, [BAR86]). Finally it is noted that the annealing processes can be complex and the rate might depend upon the total impurity concentration. For example, while the data quoted for the A-center pertains to a 'slow' component, there is also a faster stage which may account for more than 50% in low oxygen materials [SVE86].

Defect	EPR	IR local-mode absorption [cm^{-1}]	PL 0 phonon line [eV]	Energy level parameters (ΔH [meV], X, c_n [cm^3/s], c_p [cm^3/s])	T_{max} [K]	Ref.	Emission Parameters ($\Delta H'$ [meV],σ[cm^2],T_{max}[K])	Annealing behavior k_0 [1/s], E_a [eV], T_a [°C]
C_s		607						↔ -, 3.1, - [1]
O_i		1136						↔ -, 2.53, - [2]
P_s^0 P_s^+		441	1.1502	(-50, -, 6×10^{-6}, -)	9.4	[3]	(-50, 5×10^{-14}, 21.8)	
As_s^0 As_s^+					10	[3]	(-45, 1×10^{-11}, 16.9)	
B_i^- B_i^0		623	1.1510	(+45, -, -, 1×10^{-5})	20	[3]	(+45, 2×10^{-12}, 18.1)	
Al_i^- Al_i^0			1.1500	(+72, -, -, 2.1×10^{-6})	30...40	[3]	(+72, 4×10^{-12}, 29.1)	
Al_i^+ Al_i^{++}						[4]	(+250, 7×10^{-18}, 129)	↓ -, -, 200 [4]
Mg_s^- Mg_s^0				(+380,102,-,$2.1\times10^{-6}\theta^{-1.5}e^{14meV/kT}$)	131-170	[5]	(+340, 7.4×10^{-14}, 126)	
Mg_i^0 Mg_i^+ Mg_i^{++}				ΔE_a = -107.5 ΔE_a = -256.5	4.2 4.2	[6] [6]		
C_i^- C_i^0 C_i^+	Si-L6 Si-G12	930, 921	0.856			[7] [7]	(-110, 6×10^{-15}, 47.7) (+280, 2×10^{-15}, 117)	↓ 5×10^7, 0.74, 30-70 [8] ↓ 1×10^8, 0.75, 30-70 [8]
VV^- VV^+ VV^0 VV^+	Si-G7 Si-G6	5500, 2890, 2768, 2500		(-225, 4.6, $4.7\times10^{-6}\theta^{1.4}$, 7.0×10^{-7}) (-421, 0.33, $5.3\times10^{-6}\theta^{0.4}$, $3.6\times10^{-7}\theta^{-0.3}$) (+194, 0.56, >> c_p, $6.6\times10^{-6}\theta^{0.2}$)	105-155 182-266 104-146	[9] [9] [9]	(-235, 2.2×10^{-15}, 97.8) (-420, 1.5×10^{-13}, 168) (+196, 7.5×10^{-16}, 87.8)	↓ 1.1×10^9, 1.47, - [10]
VO_i^- VO_i^0	Si-B1 A-Center	836		(-164, 0.29, $2.4\times10^{-7}\theta^{0.5}$, $4.3\times10^{-6}\theta^{0.7}$)	80-108	[9]	(-164, 6.1×10^{-15}, 68.3)	↓ 1.6×10^{13}, 2.27, - [11]

184

$V_2O_i^-$ $V_2O_i^0$ $V_2O_i^+$		≈ 830				[12] [13]	(-300, -, -) (+240, 1×10^{-14}, 97.1)	↑ -, -, 100; ↓ -, -, 300 [12] ↑ -, -, 300 [13]
VO_2		889		no level expected				↑ 6×10^{11}, 1.86, 350 [11] ↓ -, -, 450
V_2O^- V_2O^0						[12]	(-270, -, -)	↑ -, -, 300 ↓ -, -, 450 [12]
VO_3		1005, 976, 910						↑ -, -, 450 [14]
VP_s^- VP_s^0	E-Center Si-G8			(-456, 1.7, $4.2\times10^{-6}\theta^{0.5}$, -)	170-230	[15]		↓ 1.7×10^{13}, 1.34, - [16] ↓ 2.4×10^{10}, 1.03, - [16]
$C_iP_s^-$ IA $C_iP_s^0$ IA $C_iP_s^+$ IA	Si-L8					[17] [17]	(-380, -, -) (+480, -, -)	
$C_iP_s^0$ III $C_iP_s^+$ III						[17]	(-230, -, -)	
$C_iC_s^-$ A $C_iC_s^0$ A $C_iC_s^+$ A	Si-G17 Si-G11					[18] [18]	(-170, similar to VO_i) (+86, -, -,>10^{-16} cm^2)	↓ 2.5×10^{13}, 1.7, 300 [1]
$C_iC_s^-$ B $C_iC_s^0$ B $C_iC_s^+$ B	Si-L7	731, 543 [3]	G 0.97 G 0.97 G 0.97			[7] [18]	(-110, 3×10^{-15}, 48.8) (+50, -, -)	see C_iC_s A
$C_iO_i^0$ $C_iO_i^+$	Si-G15	1115, 865, 742, 586, 550, 528	C 0.79	(+339, 0.89, $3.9\times10^{-10}\theta^{3.2}$, $3.9\times10^{-9}\theta^{0.61}$)	160-238	[9]	(+348, 9.4×10^{-16}, 146)	↑ -, -, 30; ↓ -, -, 400 [19]

183

Table References

[1] [DAV89]
[2] [LON90]
[3] [LB89]
[4] [KIM76]
[5] [BAB88]
[6] [HO72]
[7] [MOL96]
[8] [SO190]
[9] [HAL96]
[10] [EVW76]
[11] [SVE86]
[12] [KIM77]
[13] [TR295]
[14] [EWE95]
[15] [BRO82]
[16] [BAR86]
[17] [GÜR92]
[18] [SO290]
[19] [MOO77]

Appendix C: Analysis of Annealing Data

Annealing is the alteration of a specific material property as function of time taking place at a rate that typically is strongly increasing with temperature. In a solid-state material these processes are visualized to be arising from quasi-chemical reactions between the various ingredients, for instance dislocations, impurity atoms, or crystal defects. In the following it will tacitly be assumed that we are dealing with defects, however, the basic concepts are more general. Given the concentration of a defect is denoted by N_X, then the disappearance of X is usually governed by the differential equation

eq. C.1 $$\frac{dN_X}{dt} = -k(T)N_X^{\gamma},$$

where $k(T)$ is the temperature dependent rate constant. The order of the reaction γ assumes the values 1 or 2 for monomolecular or bimolecular reactions, respectively. While the latter requires two components X_1 and X_2 with similar concentrations $N_{X1} \approx N_{X2}$, or X_1 and X_2 to be identical, the former is observed when the concentrations are largely different. In addition to these diffusion limited reactions, which have been worked out by T.R. Waite [WAI57], also a simple dissociation of X may take place, resulting in a reaction order of $\gamma = 1$. In any case is the dependence of the rate constant on temperature given by an Arrhenius-relation

eq. C.2 $$k(T) = k_0 \exp\left(-\frac{E_a}{k_B T}\right).$$

Here E_a denotes the characteristic activation energy, which is the energy required to either dissociate X or, for diffusion limited processes, to enable a migration of X over a distance of one lattice site. The generalized frequency factor k_0 is related to the attempt-to-escape frequency that reasonably well can be estimated by the most abundant phonon frequency $k_B T/h$ [COR66]. It is of the order of $10^{13}\,s^{-1}$ for elevated annealing temperatures (200°C). In conclusion it is justified to write

eq. C.3 $$k_0 = c\frac{k_B T}{h},$$

where for the case of $\gamma = 1$ a value of c close to unity is characteristic of a dissociation, requiring only a single jump, while $c \ll 1$ indicates a long range migration. In the latter case $1/c$ is considered to be the number of jumps necessary before the reaction that removes X can succeed, and moreover c is proportional to the concentration of the dominant sink, in silicon usually interstitial oxygen or substitutional carbon. Regarding a second order ($\gamma = 2$) diffusion limited process, it can be shown that c is related to the effective capture radius R and the lattice constant a by

eq. C.4 $$c = 4\pi a^2 R.$$

While for neutral defects $R \approx a$, significantly enlarged values can result from attractive Coulombic forces on charged defects. Then R can be estimated by

eq. C.5 $$R \approx \frac{Z_1 Z_2 q_0^2}{\varepsilon\varepsilon_0 k_B T}.$$

The solution of eq. C.1 with the initial value $N_X(t=0) = N_{X0}$ is straight-forward. For $\gamma = 1$ it is

eq. C.6 $$N_X(t) = N_{X0}\exp(-k(T)t),$$

and for $\gamma = 2$

eq. C.7 $$N_X(t) = N_{X0}\frac{1}{1 + k(T)N_{X0}t}.$$

The annealing rate depends on the concentration N_{X0} in the latter case, e.g., the half-life of X is $\tau_{1/2} = (k(T)N_{X0})^{-1}$.

While the temporal variation of the reaction products for $\gamma = 1$ can be deduced very easily from eq. C.6, it will be noted that for a second order reaction X + X → Y, where $2N_Y(t) + N_X(t) = N_{X0}$, the evolution of the concentration of Y is given by

eq. C.8 $$N_Y(t) = N_{Y,\infty}\left(1 - \frac{1}{1 + k_Y(T)N_{Y,\infty}t}\right),$$

with $N_{Y,\infty} = N_{X0}/2$ and $k_Y = 2k$.

Annealing experiments are aiming at the evaluation of the activation energy E_a and the constant c (or the frequency factor k_0), i.e., the unknown parameters in the Arrhenius relation eq. C.2. It is therefore necessary to measure k at various temperatures in order to extract the parameters from fitting a straight-line to a plot of $\ln(k/(k_B T/h))$ versus $1/T$. In practice the weak dependence of the most abundant phonon frequency on the temperature can often be neglected. That is, k_0 can reasonably well be assumed to be a constant, and it is sufficient to analyze $\ln(k)$ versus $1/T$. Now, the evolution of a certain defect concentration can be monitored during the storage of the sample at a specific elevated temperature (isothermal annealing). It is then possible to determine k at the considered temperature by fitting the functional dependence eq. C.6 or eq. C.7 to the measured data. Repeating the isothermal annealing at various temperatures T thus gives the desired $k(T)$ values.

More frequently used is the isochronous annealing procedure, which considers the defect concentration as function of a progressively augmented annealing temperature and employs a fixed storage period Δt (a typical value is 15 min). Reaching the so-called defect annealing temperature T_a, a strong decrease of the concentration is observed. For a reaction order $\gamma = 1$ this can be identified with the particular temperature at which the concentration drops by a factor exp(-1), i.e., where $k(T_a)\Delta t = 1$. According to eq. C.2 the activation energy is thus related to T_a and Δt by

eq. C.9 $$E_a = k_B T_a \exp(k_0 \Delta t).$$

Therefore, if a reasonable assumption can be made about k_0 (e.g. $c = 1$ for a dissociation, see eq. C.3) eq. C.9 can be used to obtain E_a. It must however be born in mind that the defect annealing temperature depends on the storage period Δt, which however frequently is not given in publications. As was outlined by S. Dannefaer et al. [DAN76], an Arrhenius-plot can also be constructed from isochronous annealing data, giving much more accurate estimates of E_a and also furnishing the constant c (or k_0). Consider a sequence of annealing steps $(T_i, \Delta t_i, N_{Xi})$ where N_{Xi} denotes the concentration measured after the i^{th} annealing. Then the quantity $Y_{1,i}$ computed according to

eq. C.10 $$Y_{1,i} = \ln\left(\ln\left(\frac{N_{Xi-1}}{N_{Xi}}\right)\right) - \ln\left(\frac{k_B T_i}{h}\Delta t_i\right) = \ln(c) - \frac{E_a}{k_B}\frac{1}{T_i}$$

for $\gamma = 1$ or according to

eq. C.11 $$Y_{2,i} = \ln\left(\frac{N_{X0}}{N_{Xi}} - \frac{N_{X0}}{N_{Xi-1}}\right) - \ln\left(\frac{k_B T_i}{h}\Delta t_i\right) = \ln(cN_{X0}) - \frac{E_a}{k_B}\frac{1}{T_i}$$

for $\gamma = 2$ should settle on a straight line if plotted versus the corresponding $1/T_i$ values. That is, standard least-squares straight-line fitting may be employed to obtain E_a and c. Note the usage of the initial concentration of defects N_{X0} in eq. C.11 arbitrarily introduced for purpose of removing the dimension from the arguments of the logarithms. If care is taken of the units of the considered quantities N_{X0} can be put equal to unity in eq. C.11.

Appendix D: Statistics

Frequently one searches for the unknown parameters $\vec{\alpha}$ of a model $f(x;\vec{\alpha})$ that is supposed to describe the functional dependence of a certain physical quantity y on an other quantity x, see Fig. D.1. Note that $\vec{\alpha}$ is meant to be a vector of dimension r. Given N data points y_i have been measured at specific x_i and there is also some knowledge about the uncertainty σ_i of each datum, then optimal values of the parameters can for example be found by minimizing the following expression with respect to $\vec{\alpha}$

eq. D.1 $$\chi^2 = \sum_{i=1}^{N}\left(\frac{y_i - f(x_i;\vec{\alpha})}{\sigma_i}\right)^2 .$$

This is the celebrated method of least-squares which has, as holds true for all items addressed in the remainder of this section, extensively been studied in the literature, see for example [EAD71].

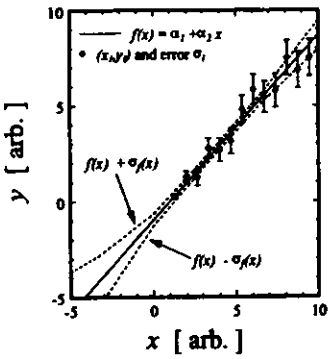

Fig. D.1 Schematic illustration of the statistical terms encountered on a straight-line fit.

If correct values of σ_i have been furnished, it is evident that the average of the terms of the sum in eq. D.1 is close to one such that χ^2 is expected to be of the order of N. A more refined statistical treatment reveals that the minimum of χ^2 obeys the so-called χ^2 distribution function, which has the mean value $n = N - r$, also referred to as the number of degrees of freedom. The reliability of the given errors can therefore be tested by calculating the minimized χ^2 and comparing with n.

The optimum values of $\vec{\alpha}$ obtained by the minimization of eq. D.1 are a function of the y_i. Their error σ_i will thus result in a corresponding uncertainty in $\vec{\alpha}$, which can be calculated by means of error propagation, see below. Regarding the two most widely used model functions, namely, a constant and a straight-line, analytical expressions for the parameters $\vec{\alpha}$ and their errors will be given in the following.

Data with a Common Mean

If all data points are supposed to have a common mean the model f does not depend on x and it can be written $f(x;\vec{\alpha}) = \alpha_1$. The unique value of α_1 minimizing eq. D.1 is*

eq. D.2 $$\alpha_1 = \frac{\sum_{i=1}^{N} y_i/\sigma_i^2}{\sum_{i=1}^{N} 1/\sigma_i^2},$$

also called the weighted average or mean value of the y_i. Due to its close relation to the analyzed data this quantity is often denoted by $\bar{y}$. Standard error propagation yields the statistical error of the weighted average

eq. D.3 $$\sigma_{\alpha_1} = \frac{1}{\sqrt{\sum_{i=1}^{N} 1/\sigma_i^2}}.$$

If the individual errors σ_i are not known, it is necessary to assume a common error $\sigma_i = \sigma_y$ for each datum. Then eq. D.2 simplifies to the well known equation of the (not-weighted) average

eq. D.4 $$\alpha_1 = \frac{1}{N}\sum_{i=1}^{N} y_i .$$

* Note that no extra symbols have been introduced for the particular values of the parameters minimizing χ^2.

Since now also σ_y is an unknown parameter, its optimum value must be inferred by minimization of eq. D.1, yielding the so-called standard deviation error*

eq. D.5 $$\sigma_y = \sqrt{\frac{1}{N-1}\sum_{i=1}^{N}(y_i - \alpha_1)^2} .$$

Evidently the error in the average α_1 can now be equated by (compare eq. D.3)

eq. D.6 $$\sigma_{\alpha_1} = \sigma_y/\sqrt{N} .$$

Straight-Line Fit

A straight-line fit supposes the model $f(x;\vec{\alpha}) = \alpha_1 + \alpha_2 x$, see Fig. D.1. The optimum values of the two parameters can be calculated by

eq. D.7 $$\alpha_1 = (S_y S_{xx} - S_x S_{xy})/D, \quad \alpha_2 = (S_1 S_{xy} - S_x S_y)/D,$$

where the following abbreviations have been used

eq. D.8 $$S_{\{1,x,y,xx,xy\}} = \sum_{i=1}^{N}\left\{1, x_i, y_i, x_i^2, x_i y_i\right\}/\sigma_i^2, \quad D = S_1 S_{xx} - S_x^2 .$$

Error propagation (see below) is used to determine the covariance matrix V of the fitted parameters

eq. D.9 $$V = \begin{pmatrix} V_{\alpha_1\alpha_1} & V_{\alpha_2\alpha_1} \\ V_{\alpha_1\alpha_2} & V_{\alpha_2\alpha_2} \end{pmatrix} = \frac{1}{D}\begin{pmatrix} S_{xx} & -S_x \\ -S_x & S_1 \end{pmatrix}$$

where the diagonal elements denote the squared error, i.e., the variance of the fitted parameters,

eq. D.10 $$\sigma_{\alpha_1} = \sqrt{V_{\alpha_1\alpha_1}}, \quad \sigma_{\alpha_2} = \sqrt{V_{\alpha_2\alpha_2}},$$

and the off-diagonal elements, which must be equal, the corresponding correlation coefficients.

If now, as often is the case, the errors σ_i are not known and a common error σ_y needs to be assumed, the evaluation of eq. D.7 and eq. D.8 is still possible because σ_y cancels out. In analogy to eq. D.5 by the common error can be determined

eq. D.11 $$\sigma_y = \sqrt{\frac{1}{N-2}\sum_{i=1}^{N}(y_i - [\alpha_1 + \alpha_2 x_i])^2} .$$

It will be noted that the term in the root is just the χ^2 according to eq. D.1 for the instance of $\sigma_i = 1$. It will therefore sometimes be stated that the error has been estimated from the χ^2. Regarding the numerical computation, it is also advantageous to put $\sigma_i = 1$ for the tentative calculation of the covariance matrix according to eq. D.9. After eq. D.11 has been evaluated, the correct V is then readily obtained by multiplication with σ_y^2.

Error Propagation

Consider a function $f(\vec{\alpha})$ of a set of variables $\vec{\alpha}$ whose covariance matrix is V. The law of error propagation says that the error in f is given by the quadratic form

eq. D.12 $$\sigma_f = \sqrt{(\vec{\nabla}_{\vec{\alpha}} f)\, V\, (\vec{\nabla}_{\vec{\alpha}} f)},$$

which in one dimension simplifies to

* Note that this relation also can be obtained by assuming eq. D.1 to be equal to its mean value $n = N - r$.

eq. D.13 $$\sigma_f = \left|\frac{\partial f}{\partial \alpha_i}\right| \sigma_{\alpha_i}.$$

However, the law is basically derived from the first order term of the expansion of f into a Taylor-series, and therefore only holds true for sufficiently small σ_{α_i}.

The difficulty which one meets when the error of a cross-section determined by an Arrhenius-plot is quoted may serve as an example. Suppose a function $f(\alpha_i) = \exp(\alpha_i)$. Then it is $\sigma_f = f(\alpha_i)\sigma_{\alpha_i}$. If the error σ_{α_i} is larger than 1, the range $f \pm \sigma_f$ allows for negative values which is not compatible with the definition of f. It is then better to quote the upper and lower bounds according to $f_{hi,lo} = \exp(\alpha_i \pm \sigma_{\alpha_i})$.

An other important application of the error propagation is the determination of the interpolation and extrapolation errors in a fitted model. That is, we are asking for the error in $f(x;\vec{\alpha})$ at an arbitrary point x. Concerning the straight-line fit from above we get

eq. D.14 $$\vec{\nabla}_{\vec{\alpha}} f(x;\vec{\alpha}) = \begin{pmatrix} 1 \\ x \end{pmatrix}.$$

Further, using eq. D.12 and eq. D.9 it is

eq. D.15 $$\sigma_f(x) = \sqrt{V_{\alpha_1\alpha_1} + 2V_{\alpha_1\alpha_2}x + V_{\alpha_2\alpha_2}x^2} = \sqrt{\frac{S_1}{D}\left(x - \frac{S_x}{S_1}\right)^2 + \frac{1}{S_1}},$$

which has been used in Fig. D.1 to calculate the curves $f(x) \pm \sigma_f(x)$. It must therefore be born in mind that a number predicted by a model at a point x outside the range covered by experiments can be afflicted with a large error. Moreover, this error can only be calculated accurately, if the full covariance matrix of the fitted parameters is known.

Appendix E: Damage Parameter Extraction

Table E.1 Parameters determining the variation of $N_{eff,SCR}$ as function of the equivalent 1 MeV neutron fluence.

Particle	Source	g_T [10^{-2} cm^{-1}]	#	g_c [10^{-2} cm^{-1}]	#	N_{eff} [10^{11} cm^{-3}]	#
Neutrons	Hamburg	5.1±0.2	21	1.75±0.07	19	3.31±0.22	19
	[IMPCO]	3.1±0.6	6	1.83±0.22	6	0.62±2.37	6
	[CERN1]	2.4	1				
	Mean Value	4.6±0.3	28	1.77±0.07	25	1.97{0.62...3.31}	2
Protons	[LANL]	5.9±0.3	20	1.24±0.11	34	6.49±1.51	34
	[CAMB]			0.98±0.09	4	4.08±3.99	4
	[CERN1]	4.3	1	0.79±0.05	4	6.85±0.96	4
	Mean Value	5.8±0.3	21	1.15±0.09	42	6.29{4.08...6.85}	3
Pions	Hamburg	7.5±0.5	6	2.09±0.06	7	3.87±0.53	7
	[CERN1]	9.8±0.4	2	1.89±0.03	4	3.92±0.20	4
	Mean Value	8.1±0.5		2.01±0.05	11	3.90{3.87...3.92}	2

Table E.2 "Donor Removal" constant.

Particle	Source	T [°C]	c [10^{-15} cm^2]
Neutrons	[ANG93]	20	1.47
	[LEM92]	25	1.87
	[WUN92]	21	3.54
	Mean Value		2.29±0.63
Protons	[ZIO94]	26	1.52
		1.4	0.98
	[BAR93]	26	1.16
		26	0.82
		1.5	1.79
	[PIT92]	24	0.51
		24	0.42
	[BAT94]	25	0.50
	Mean Value		0.96±0.19
Pions[a)]	P.A. Aarnio et al., Helsinki University		2.31
			3.10
			3.09
	K.T. Knöpfle et al., MPI Kernphysik, Heidelberg	9	0.86
		25	1.15
		9	0.83
		25	0.66
	CERN ECP	20	2.26
	CERN PPE	20	0.74
	Mean Value		1.64±0.29

[a)] Preliminary results presented on the post irradiation SIRAD meeting, see Section 3.2.4.

Table E.3 Reverse annealing rate constant.

Source	T [°C]	k_T [cm^{3}s^{-1}]	#
[LANL]	10	2.46×10^{-21}	8
[IMPCO]			6
[CERN1]	25	2.89×10^{-20}	2
[LANL]			4
[LANL]	35	3.45×10^{-19}	12
	50	4.70×10^{-19}	4
Hamburg	21	1.87×10^{-20}	9
	39.8	3.82×10^{-19}	1
	47.9	1.26×10^{-18}	1
	49.8	1.51×10^{-18}	2
	56.9	7.50×10^{-18}	1
	68.9	2.47×10^{-17}	2

Table E.4 Current annealing activation energy.

Source	T [°C]	E_I [eV]
[CERN1] M33	-20	1.22
[CERN1] M40	0	1.40
[CERN1] M44	10	0.74
[DORT] UA2	0	1.01
Mean Value		1.09±0.14

Table E.5 Reverse current normalized to the fluence.

Particle	Source	α_∞ [10^{-17} A/cm]	#
Neutrons	Hamburg	3.63±0.33	16
	[IMPCO]	1.64±0.13	9
	[CERN1]	2.35	1
	Mean Value	2.86±0.18	28
Protons	[CAMB]	1.92±0.06	9
	[CERN1]	2.85	1
	Mean Value	2.22±0.10	15
Pions	Hamburg	3.64±0.20	7
	[CERN1]	4.32±0.38	4
	Mean Value	3.89±0.20	11

Table E.6 Effective band gaps.

Source	E_g [eV]
[GIL92]	1.34
[BAR93]	1.23
Hamburg	1.14
Mean Value	1.24±0.06

Table E.7 World averages of the damage constants and the error in the averages.

Parameter	Neutrons	Protons	Pions
g_r [10^{-2} cm^{-1}]	4.6±0.3	5.8±0.3	8.1±0.5
g_c [10^{-2} cm^{-1}]	1.77±0.07	1.15±0.09	2.01±0.05
N_{eff} [10^{11} cm^{-3}]	1.97{0.62...3.31}	6.29{4.08...6.85}	3.90{3.87...3.92}
c [10^{-13} cm^2]	2.29±0.63	0.96±0.19	1.64±0.29
E_a [eV]		1.31±0.04[a]	
k_0 [cm^{3}s^{-1}]		520{128...2110}[a]	
α_∞ [10^{-17} A/cm]	2.86±0.18	2.22±0.10	3.89±0.20
E_g [eV]		1.24±0.06	
E_t [eV]		1.09±0.14	
$\gamma_e, \gamma_e^*, \gamma_h$ [10^{-4} cm^2/s]		0.24, 1.01, 0.24	

[a] Covariance matrix of the fitted parameters $\ln(k_0$ [cm^3/s]) and E_a/k_B [K]:

$$\begin{pmatrix} 1.973 & -6.195\times10^{2} \\ -6.195\times10^{2} & 1.952\times10^{5} \end{pmatrix}.$$

Table E.8 Standard deviation and extrapolation errors.

Parameter	Neutrons	Protons	Pions
g_r [10^{-2} cm^{-1}]	±1.6	±1.4	±1.5
g_c [10^{-2} cm^{-1}]	±0.35	±0.61	±0.16
k_T(273.16 K) [10^{-22} cm^{3}s^{-1}]		3.48 {2.43...4.99}	
k_T(283.16 K) [10^{-21} cm^{3}s^{-1}]		2.46 {1.76...3.42}	
k_T(293.16 K) [10^{-20} cm^{3}s^{-1}]		1.55 {1.15...2.10}	
α_∞ [10^{-17} A/cm]	±0.95	±0.39	±0.67
E_g [eV]		±0.10	
E_t [eV]		±0.28	

Appendix F: Block Diagrams of the Experimental Set-Ups

PROTON MICRO-BEAM

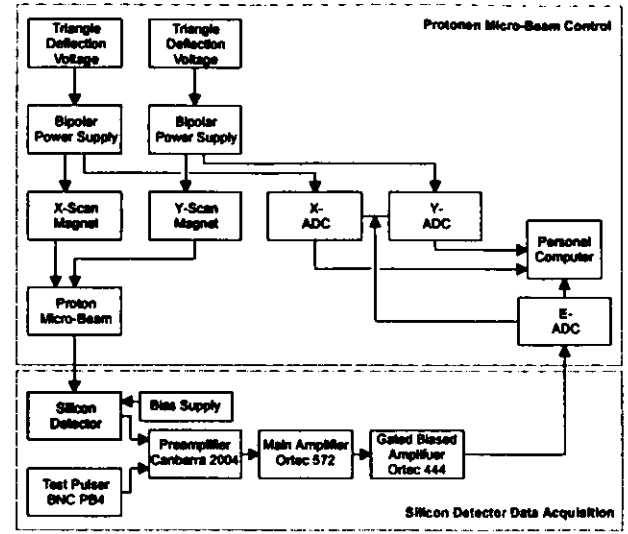

Fig. F.1 Proton micro-beam steering control and standard electronic readout of a silicon detector.

CV AND IV

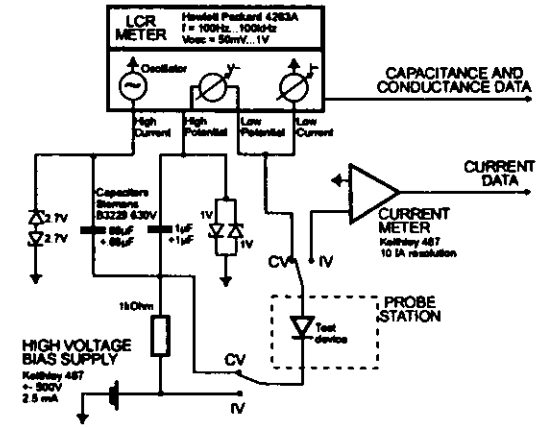

Fig. F.2 Electrical set-up employed for the recording of capacitance and current-voltage characteristics.

DLTS AND TSC

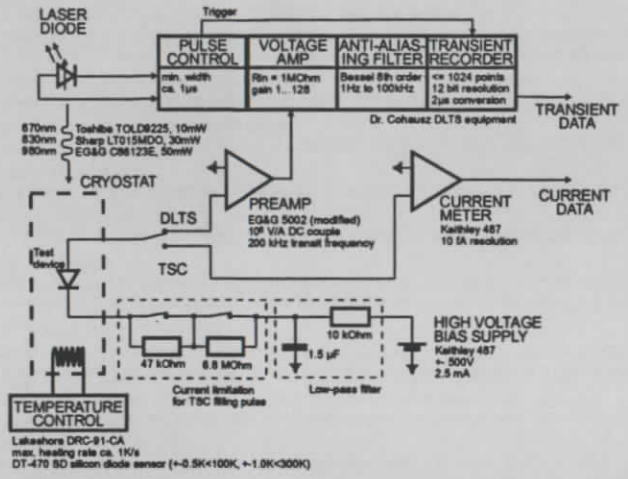

Fig. 0.1 Electrical circuitry for TSC and DLTS measurements. In order to improve the signal to noise ratio of the DLTS apparatus the transient recorder can be programmed to perform a specific number of averagings, 2 up to 1024 have been used. The total system noise of the TSC measurements is approximately 20 fA, which is close to the resolution of the current meter. The power specified for the diode lasers refers to the continuous wave (cw) mode.

CURRENT PULSE SHAPES (TCT)

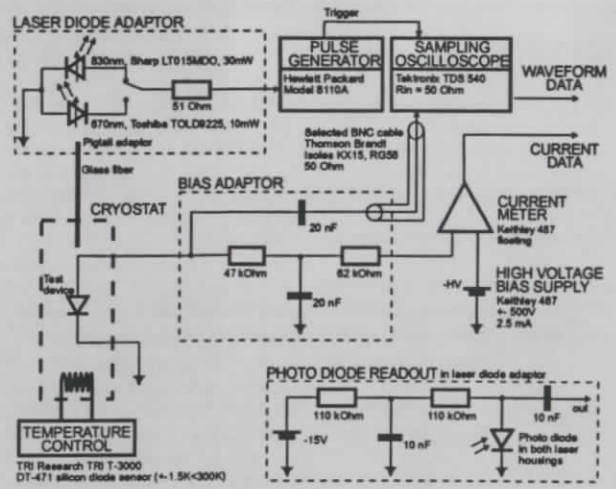

Fig. 0.2 Electrical set-up of the current pulse shape measurements (TCT) as constructed by V. Eremin [ER295]. The used glass fibers have a 62.5 µm Ø core and a 125 µm Ø cladding.

References

[ALS93] P. Alscher „Untersuchungen zu den elektronischen Eigenschaften von Siliziumdetektoren" Diplomarbeit Universität Hamburg (1993).

[ANG93] F. Anghinolfi et al. „Neutron irradiation of silicon diodes at temperatures of +20°C and -20°C" Nucl. Instr. and Meth. A 326 (1993) 365.

[ANG95] F. Anghinolfi et al. „Some recent results of the silicon detector radiation damage study by the RD2 collaboration" Nucl. Instr. and Meth. A 360 (1995) 455.

[ANG96] T. Angelescu and A. Vasilescu „Comparative radiation hardness results obtained from various neutron sources and the NIEL problem" Nucl. Instr. Meth. A374 (1996) 85.

[ASO87] M.T. Asom et al. „Interstitial defect reactions in silicon" Appl. Phys. Lett. 51 (1987) 256.

[ATL94] ATLAS Collaboration, Technical Proposal, CERN/LHCC/94-43, LHCC/P2 (1994).

[BAB88] N. Baber et al. „Evidence for a substitutional Mg acceptor level in silicon" Phys. Rev. B 38 (1988) 10483.

[BAL93] A. Baldini and M. Bruzzi „Thermally stimulated current spectroscopy: Experimental techniques for the investigation of silicon detectors" Rev. Sci. Instrum. 64 (1993) 932.

[BAR86] C.E. Barnes and G.A. Samara „Forward bias induced annealing of the E center in silicon" Appl. Phys. Lett. 48 (1986) 934.

[BAR93] E. Barberis et al. „Temperature effects on radiation damage to silicon detectors" Nucl. Instr. and Meth. A 326 (1993) 373.

[BAT93] S. Bates et al. „Study of neutron irradiated silicon counters with a fast amplifier" Nucl. Instr. and Meth. A 337 (1993) 57.

[BAT94] S. Bates et al. „Recent results of radiation damage studies in silicon" Nucl. Instr. and Meth. A 344 (1994) 228.

[BAT96] S.J. Bates et al. „Pion-induced damage in silicon detectors" Nucl. Instr. and Meth. A 379 (1996) 116.

[BEN83] J.L. Benton et al. „The oxygen donor effect in silicon" Physica 116B (1983) 271.

[BER82] M.J. Berger and S.M. Seltzer „Stopping Powers and Ranges of Electrons and Positrons" National Bureau of Standards, Department of Commerce, Technical Report NBSIR 82-2550-A (1992).

[BIG94] U. Biggeri et al. „Studies of Deep Levels in High Resistivity Silicon Detectors Irradiated by High Fluence Fast Neutrons Using a Thermally Stimulated Current Spectrometer" IEEE Trans. Nucl. Sci. 41 (1994) 964.

[BIG95] U. Biggeri et al. „Hall effect analysis on neutron irradiated high resistivity silicon" Nucl. Instr. And Meth. A 360 (1995) 131.

[BLA74] J.S. Blakemore „Solid State Physics" 2nd edition, W.B. Saunders Company, Philadelphia (1974).

[BNL] BNL Instrumentation Division's Silicon Detector Development and Processing Lab, Bldg. 535B, Upton, Long Island, NY 11973-5000, USA.

[BO191] E. Borchi et al. „Leakage current, annealing, and deep defect production studies in neutron irradiated n-type Si-detectors" Nucl. Instr. and Meth. A 301 (1991) 215.

[BOR91] E. Borchi et al. „Thermally Stimulated Current Analysis of Neutron Irradiated Silicon" Nucl. Instr. and Meth. A 310 (1991) 273.

[BÖT97] R. Böttger et al. „Radiation damage studies of high resistivity silicon detectors at various neutron energies", to be published in Nucl. Instr. and Meth. Section A.

[BRA79] P. Bräunlich et al. in „Topics in Advanced Physics, Volume 37, Thermally Stimulated Relaxation in Solids" Springer-Verlag Berlin Heidelberg New York 1979.

[BRÄ89] D. Bräunig „Wirkung hochenergetischer Strahlung auf Halbleiterbauelemente" Springer-Verlag (1989).

[BRE89] H.J. Brede et al. „Neutron yields from thick Be targets bombarded with deuterons or protons" Nucl. Instr. and Meth. A 274 (1989) 332.

[BRO82] S.D. Brotherton and P. Bradley „Defect production and lifetime control in electron and γ-irradiated silicon" J. Appl. Phys. 53 (1982) 5720.

[BRU95] M. Bruzzi „TSC data-analysis on heavily irradiated silicon detectors" Nucl. Instr. and Meth. A352 (1995) 618.

[BUE72] M.G. Buehler „Impurity centers in pn junctions determined from shifts in the thermally stimulated current and capacitance response with heating rate" Solid-State Electron. 15 (1972) 69.

[BUE76] M.G. Buehler and W.E Phillips „A study of the gold acceptor in a silicon p'n junction and n-type MOS capacitor by thermally stimulated current and capacitance measurements" Solid-State Electron. 19 (1976) 777.

[CAH59] J.H. Cahn „Irradiation Damage in Germanium and Silicon due to Electrons and Gamma Rays" J. Appl-Phys. 30 (1959) 1310.

[CAMB] S. Bates, Cambridge University, private communication.

[CAN71] C. Canalli et al. „Drift velocity of electrons and holes and associated anisotropic effects in silicon" J. Phys. Chem. Solids 32 (1971) 1707.

[CAV71] G. Cavalleri et al. „Extension of Ramo's theorem as applied to induced charges in semiconductor detectors" Nucl. Instr. and Meth. 92 (1971) 137.

[CERN1] F. Lemeilleur and S. Bates, CERN/ECP, private communication.

[CHI95] A. Chilingarov et al. „Radiation studies and operational projections for silicon in the ATLAS inner detector" Nucl. Instr. and Meth. A 360 (1995) 432.

[COH] Dr. L. Cohausz, Halbleitermeßtechnik GmbH, 85368 Moosburg, Germany.

[COR66] J.W. Corbett „Electron Radiation Damage in Semiconductors and Metals" Academic Press (1966).

[COR70] J.W. Corbett „Radiation damage in silicon and germanium" Radiation Effects 6 (1970) 3.

[DAN76] S. Dannefaer et al. „Influence of defects and temperature on the annihilation of positrons in neutron-irradiated silicon" Phys. Rev. B 14 (1976) 2709.

[DAS55] W.C. Dash and R. Newman „Intrinsic Optical Absorption in Single-Crystal Germanium and Silicon at 77°K and 300°K" Phys. Rev. 99 (1955) 1151.

[DAV89] G. Davies and K.T. Kun „Annealing the di-carbon radiation damage centre in silicon" Semicond. Sci. Technol. 4 (1989) 327.

[DEA80] B.E. Deal „Standardized Terminology for Oxide Charges Associated with Thermally Oxidized Silicon" IEEE ED 27 (1980) 606.

[DES67] R.Y. Desphande „Detection mechanisms in semiconductor counters" Nucl. Instr. and Meth. A 57 (1967) 125.

[DEV94] R. Devine „The Structure of SiO_2, its Defects and Radiation Hardness" IEEE NS 41 (1994) 452.

[DORT] A. Rolf, Universität Dortmund, private communication.

[DRE90] P. Dreier „High resistivity silicon for detector applications" Nucl. Instr. and Meth. A288 (1990) 272.

[EAD71] W.T. Eadie et al. „Statistical Methods in Experimental Physics" North Holland (1971).

[EDW90] M. Edwards and D.R. Perry „The Radiation Hardness Test Facility" RAL Report RAL-90-065 (1990).

[EDW91] M. Edwards et al. „Neutron radiation damage studies of silicon detectors" Nucl. Instr. and Meth. A 310 (1991) 283.

[ENG83] O. Engström and A. Alm „Energy concepts of insulator-semiconductor interface traps" J. Appl. Phys. 54 (1983) 5240.

[ER294] V. Eremin and Z. Li „Determination of the Fermi Level Position for Neutron Irradiated High Resistivity Silicon Detectors and Materials Using the Transient Charge Technique (TCHT)" IEEE Trans. NS 41 (1994) 1907.

[ERE95] V. Eremin et al. „Elevated temperature annealing of neutron induced reverse current and corresponding defect levels in low and high resistivity silicon detectors" IEEE Trans. NS 42 (1995) 387.

[ER295] V. Eremin et al. „Trapping induced N_{eff} and electrical field transformation at different temperatures in neutron irradiated high resistivity silicon detectors" Nucl. Instr. and Meth. A 360 (1995) 458.

[ER196] V. Eremin, private communication.

[ERE96] V. Eremin and Z. Li „Effect of deep level trapping of free carriers on the stabilization of current-voltage characteristics of high resistivity silicon detectors irradiated by high fluence of neutrons" Nucl. Instr. and Meth. A 383 (1996) 528.

[EVW76] A.O. Evwaraye and E. Sun „Electron-irradiation-induced divacancy in lightly doped silicon" J. Appl. Phys. 47 (1976) 3776.

[EWE95] C.P. Ewels et al. „First principles investigation of vacancy oxygen defects in Si" Mat. Sci. Forum Vols. 196-201 (1995) 1297.

[FEI93] H. Feick „Temperaturabhängigkeit der Langzeitausheilung neutronengeschädigter Silizium-Detektoren" diploma thesis, Universität Hamburg (1993).

[FE196] H. Feick et al. „Long term damage studies using silicon detectors fabricated from different starting materials and irradiated with neutrons, protons, and pions" Nucl. Instr. and Meth. A 377 (1996) 217.

[FE296] H. Feick et al. „Analysis of TSC spectra measured on silicon pad detectors after exposure to fast neutrons" Proceedings of the International Conference on Radiation Effects on Semiconductor Materials, Detectors and Devices, Florence, Italy, 1996, to be published in NIM.

[FE396] H. Feick et al. „Correlation of Radiation Damage Effects in High Resistivity Silicon Detectors with Results from Deep Level Spectroscopy" presented at the IEEE 1996 Nuclear Science Symposium & Medical Imaging Conference, Anaheim, California, accepted for publication.

[FLO93] E.L. Florian an M. Tavlet, CERN/TIS-CFM/IR/93-07 (1993).

[FOR71] L. Forbes and C.T. Sah „On the determination of deep level center energy and concentration by thermally stimulated conductivity measurements using reverse-biased *p-n* junctions" Solid-State Electron. 14 (1971) 182.

[FRE70] E. Fretwurst et al. „Current pulse shapes of semiconductor detectors, measured with an averaging technique" Proceedings, Symposium on Semiconductor Detectors for Nuclear Radiation, München (1970), 44.

[FRE87] E. Fretwurst et al., „Development of large area silicon detectors", Nucl. Instr. and Meth. A 253 (1987) 467.

[FRE90] E. Fretwurst et al., „Silicon detector developments for calorimetry: Technology and radiation damage", Nucl. Instr. and Meth. A 288 (1990) 1.

[FRE94] E. Fretwurst et al. „Reverse annealing of the effective impurity concentration and long term operational scenario for silicon detectors in future collider experiments" Nucl. Instr. and Meth. A 342 (1994) 119.

[FRE96] E. Fretwurst et al. „Neutron induced defects in silicon detectors characterized by DLTS and TSC methods" Nucl. Instr. and Meth. A 377 (1996) 258.

[FUR95] C. Furetta et al. „Fluence and dosimetric measurements for a π^+ irradiation facility" CERN-ECP/95-2.

[GER96] J. Gerhardt „Charakterisierung strahleninduzierter Defekte in Silizium-Detektoren mit Hilfe des TCT-Verfahrens (Transient Current Technique)" diploma thesis, Universität Hamburg (1996).

[GIL92] K. Gill et al. „Radiation damage by neutrons and photons to silicon detectors" Nucl. Instr. and Meth. A 322 (1992) 177.

[GOG90] D. Goguenheim and M. Lannoo, J. Appl. Phys, 68 (1990) 1059.

[GOR93] B.J. Gordon „C-V Plotting: Myths and Methods" Solid State Technology, January 1993, 57.

[GOR94] G. Gorfine „Studies of Radiation Levels in the Large Hadron Collider and of Radiation Damage to Silicon Detectors" PhD thesis, University of Melbourne (1994).

[GOR95] G. Gorfine, private communication.

[GOS59] B.R. Gossick „Disordered Regions in Semiconductors Bombarded by Fast Neutrons" J. Appl. Phys. 30 (1959) 1214.

[GRE90] M.A. Green „Intrinsic concentration, effective densities of states, and effective mass in silicon" J. Appl. Phys. 67 (1990) 2944.

[GÜR92] E. Gürer et al. „Configurational Metastability of Carbon-Phosphorus Pair Defects in Silicon" Mat. Sci. Forum Vol. 83-87 (1992) 339.

[HAL52] R.N. Hall „Electron-Hole Recombination in Germanium" Phys. Rev. B 87 (1952) 387.

[HAL96] A. Hallén et al. „Lifetime in proton irradiated silicon" J. Appl. Phys. 79 (1996) 3906.

[HEI76] H.M. Heijne et al. „TSC defect level in silicon produced by irradiation with muons of GeV-energy" Radiat. Eff. 29 (1976) 25.

[HEN77] C.H. Henry and D.V Lang „Nonradiative capture and recombination by multiphonon emission in GaAs and GaP" Phys. Rev. B 15 (1977) 989.

[HEY96] P. Heydarpoor „Spektroskopische Untersuchung von Kristallschäden in Silizium-Detektoren nach Neutronenbestrahlung mit Hilfe des TSC-Verfahrens" diploma thesis, Universität Hamburg (1996).

[HO72] L.T. Ho and A.K. Ramdas „Excitation Spectra and Piezospectroscopic Effects of Magnesium Donors in Silicon" Phys. Rev. B 5 (1972) 462.

[HOL62] N. Holonyak et al. „Double injection with negative resistance in semi-insulators" Phys. Rev. Lett. 11 (1962) 426.

[HUH93] M. Huhtinen and P.A. Aarnio „Pion induced displacement damage in silicon devices" Nucl. Instr. and Meth. A 335 (1993) 580.

[IKE85] K. Ikeda et al. „Photo-Deep-Level Fourier Spectroscopy in Semi-Insulating Bulk Materials" Jap. J. Appl. Phys. 11 (1985) 1454.

[IMPCO] G. Hall, London Imperial College, private communication.

[JEL82] G.E. Jellison, Jr. „Transient capacitance studies of an electron trap at $E_C - E_T = 0.105$ eV in phosphorus-doped silicon" J. Appl. Phys. 53 (1982) 5715.

[JON92] R. Jones and S. Öberg „Oxygen Frustration and the Interstitial Carbon-Oxygen Complex in Si" Phys. Rev. Lett. 68 (1992) 86.

[KEG96] G.H.R. Kegel et al. „Fluences and spectra of accelerator generated fast neutrons" to be published.

[KEM80] J. Kemmer „Fabrication of low noise silicon radiation detectors by the planar process" Nucl. Instr. and Meth. 169 (1980) 499.

[KEM88] J. Kemmer and G. Lutz „New structures for position sensitive semiconductor detectors" Nucl. Instr. and Meth. A 273 (1988) 588.

[KET] Ketek GmbH, 81241 München-Pasing, Germany.

[KIM76] L.C. Kimerling „New Developments in Defect Studies in Silicon" IEEE NS-23 (1976) 1497.

[KIM77] L.C. Kimerling „Defect states in electron-bombarded silicon: capacitance transient analysis" Inst. Phys. Conf. Ser. 31 (1977) 221.

[LAM62] M.A. Lampert „Double Injection in Insulators" Phys. Rev. 125 (1962) 126.

[LAN79] D.V. Lang „Space-Charge Spectroscopy in Semiconductors" in Thermally Stimulated Relaxation in Solids, Topics in Applied Physics, Volume 37 edited by P. Bräunlich, Springer-Verlag Berlin (1979).

[LANL] H.-J. Ziock, Los Alamos National Laboratory, private communication.

[LAZ87] M.S. Lazo et al. „Silicon and silicon dioxide neutron damage functions", Technical Report SAND87-0098 Vol. I, (1987).

[LB89] O. Madelung and M. Schulz in „Landolt-Börnstein, Band 22b) Halbleiter" Springer-Verlag Berlin (1989).

[LED78] C.M. Lederer and V.S. Shirley „Table of Isotopes" 7th edition, John Wiley & Sons, New York (1978).

[LEM92] F. Lemeilleur et al. „Neutron-induced radiation damage in silicon detectors" IEEE Trans. NS 39 (4) (1992) 551.

[LER93] C. Leroy et al. CERN/ECP 93-12.

[LI91] Z. Li and H.W. Kraner „Studies of Frequency Dependent C-V Characteristics of Neutron Irradiated p'-n Silicon Detectors" IEEE Trans. NS 38 (1991) 244.

[LI295] Z. Li „Experimental Comparisons Among Various Models for the Reverse Annealing of the Effective Doping Concentration of Ionized Space Charges (N_{eff}) of Neutron Irradiated Silicon Detectors" IEEE Trans. NS 42 (1995) 224.

[LI395] C.J. Li and Z. Li „Development of current-based microscopic defect analysis methods and associated optical filling techniques for the investigation on highly irradiated high resistivity silicon detectors" Nucl. Instr. and Meth. A 364 (1995) 108.

[LI196] Z. Li et al. „Investigation on the N_{eff} reverse annealing effect using TSC/I-DLTS: relationship between neutron induced microscopic defects and silicon detector electrical degradations" Nucl. Instr. and Meth. A 377 (1996) 265.

[LI296] Z. Li et al. „Microscopic analysis of defects in a high resistivity silicon detector irradiated to $1.7x10^{15}$ n/cm²" IEEE Trans. NS 43 (1996) 1590.

[LI396] Z. Li et al. „Direct observation and measurements of neutron induced deep levels responsible for N_{eff} changes in high resistivity silicon detectors using TCT" Proceedings of the International Conference on Radiation Effects on Semiconductor Materials, Detectors and Devices, Florence, Italy, 1996, to be published in NIM.

[LIT95] A.M. Litke and A.S. Schwarz „The Silicon Microstrip Detector" Scientific American, May 1995, 76.

[LON90] C.A. Londos „Carbon-related radiation damage centres and processes in p-type Si" Semicond. Sci. Technol. 5 (1990) 645.

[LOW80] J.E. Lowther „Carrier Capture at Amphoteric Deep Level Defects in Silicon" J. Phys. C: Solid St. Phys. 13 (1980) 3681.

[LUT95] G. Lutz „A simplistic model for reverse annealing in irradiated silicon" Nucl. Instr. and Meth. B 95 (1995) 41.

[LUT96] G. Lutz et al. „Effects of deep level defects in semiconductor detectors" Nucl. Instr. and Meth. A 377 (1996) 234.

[MAR81] P.A. Martin et al. „Electric field enhanced emission from non-Coulombic traps in semiconductors" J. Appl. Phys. 52 (1981) 7409.

[MCL88] V. McLane et al. „Neutron Cross Sections, Volume 2, neutron cross section curves" Acad. Press (1988).

[MEE79] J.M. Meese et al. „A review of transmutation doping in silicon" IEEE NS 26 (1979) 4858.

[MEI92] E. Meijer and H.G. Grimmeis „Transient current measurements for the characterization of deep defects in semiconductors" Semicond. Sci. Technol. 7 (1992) 188.

[MES92] G.C. Messenger „A Summary Review of Displacement Damage from High Energy Radiation in Silicon Semiconductors and Semiconductor Devices" IEEE Trans. NS 39 (1992) 468.

[MEV96] B.C. MacEvoy „Defect evolution in irradiated silicon detector material" Nucl. Instr. and Meth. A 374 (1996) 12.

[MIC] Micron Semiconductor Ltd., Lancing, Sussex, BN15 8UN, England.

[MIC95] R. Michel et al. „Nuclide production by proton-induced reactions on elements ($6 \le Z \le 29$) in the energy range from 800 to 2600 MeV" Nucl. Instr. and Meth. B 103 (1995) 183.

[MOI95] M. Moll „Temperungsexperimente an strahlengeschädigten Silizium-Detektoren" diploma thesis, Universität Hamburg (1995).

[MOL95] M. Moll et al. „Observation of a bistable defect generated and activated by heat treatments in irradiated high resistivity silicon detectors" Nucl. Phys. B (Proc. Suppl.) 44 (1995) 468.

[MOL96] M. Moll et al. „Comparison of defects produced by fast neutrons and ^{60}Co-gammas in high resistivity silicon detectors using Deep Level Transient-Spectroscopy", proceedings of the International Conference on Radiation Effects on Semiconductor Materials, Detectors and Devices, Firenze, Italy 1996, to be published in NIM Section A.

[MOO77] P.M. Mooney et al. „Defect energy levels in boron-doped silicon irradiated with 1-MeV electrons" Phys. Rev. B 15 (1977) 3836.

[MPI] Max Planck Institut für Physik und extraterrestrische Physik, Halbleiterlabor, 81245 München, Germany.

[MUL74] J.C. Muller et al. „Thermally Stimulated Current Measurements on Silicon Junctions Produced by Implantation of Low Energy Boron Ions" Solid-State Electron. 17 (1974) 1293.

[MWH90] P.J. McWhorther et al. „Modeling the anneal of radiation-induced trapped holes in a varying thermal environment" IEEE Trans. NS 37 (1990) 1682.

[NIC82] E.H. Nicollian and J.R. Brews „MOS (Metal Oxide Semiconductor) Physics and Technology" John Wiley & Sons (1982).

[OSI95] C. Osina „Untersuchungen von Silizium-Detektoren verschiedener Herstellungstechnologie mit einer 2-MeV Scanning-Protonen-Mikrostrahlsonde" Diplomarbeit, Universität Hamburg (1995).

[PIT92] D. Pitzl et al. „Type inversion in silicon detectors" Nucl. Instr. and Meth. A 311 (1992) 98.

[RAW87] K.J. Rawlings „The generation lifetime in high resistivity silicon" NIM A260 (1987) 201.

[RHO88] E.H. Rhoderick and R.H. Williams „Metal-Semiconductor Contacts" Clarendon Press, Oxford (1988).

[RIC96] R.H. Richter et al. „Strip detector design for ATLAS and HERA-B using two-dimensional device simulation" Nucl. Instr. and Meth A 377 (1996) 412.

[ROS84] E. Rosencher et al. „Transient-current study of field-assisted emission from shallow levels in silicon" Phys. Rev. B 29 (1984) 1135.

[SAH70] C.T. Sah et al. „Thermal and optical emission and capture rates and cross sections of electrons and holes at imperfection centers in semiconductors from photo and dark junction current and capacitance experiments" Solid-State Electron. 13 (1970) 759.

[SC195] P. Schlichthärle „Untersuchung von Oberflächeneffekten in Silizium-Detektoren nach Schädigung mit 20 keV Elektronen" diploma thesis Universität Hamburg (1995).

[SCH94] T. Schulz et al. „Long Term Reverse Annealing in Silicon Detectors" IEEE Trans NS 41 (4) (1994) 791.

[SCH95] T. Schulz „Investigation on the Long Term Behaviour of Damage Effects and Corresponding Defects in Detector Grade Silicon after Neutron Irradiation" PhD thesis, Universität Hamburg (1995), see also DESY report 96-027.

[SHI90] Y. Shi et al. „A numerical study of cluster center formation in neutron-irradiated silicon" J. Appl. Phys. 67 (1990) 1116.

[SHO52] W. Shockley and W.T. Read, Jr. „Statistics of the recombinations of holes and electrons" Phys. Rev. B 87 (1952) 835.

[SI171] J.G. Simmons and G.W. Taylor „Nonequilibrium Steady-State Statistics and Associated Effects for Insulators and Semiconductors Containing an Arbitrary Distribution of Traps" Phys. Rev. B 4 (1971) 502.

[SI271] J.G. Simmons and G.W. Taylor „High-Field Isothermal Currents and Thermally Stimulated Currents in Insulators Having Discrete Trapping Levels" Phys. Rev. B 5 (1971) 1619.

[SO190] L.W. Song and G.D. Watkins „EPR identification of the single-acceptor state of interstitial carbon in silicon" Phys. Rev. B 42 (1990) 5759.

[SO290] L.W. Song et al. „Bistable interstitial-carbon-substitutional carbon pair in silicon", Phys. Rev. B 42 (1990) 5765.

[SON88] L.W. Song et al. „Bistable Defect in Silicon: The Interstitial-Carbon-Substitutional-Carbon Pair" Phys. Rev. Lett. 60 (1988) 460.

[SU90] Z. Su et al. „Determination of oxygen in silicon by ratio of *A* center to *E* center" J. Appl. Phys. 67 (1990) 1903.

[SUM93] G.P. Summers et al. „Damage correlations in semiconductors exposed to gamma, electron and proton radiations" IEEE Trans. NS 40 (6) (1993) 1372.

[SVE86] B.G. Svensson and J.L. Lindström „Kinetic study of the 830- and 889-cm^{-1} infrared bands during annealing of irradiated silicon" Phys. Rev. B 34 (1986) 8709.

[SVE91] B.G. Svensson et al. „Divacancy acceptor levels in ion-irradiated silicon" Phys. Rev. B43 (1991) 2292.

[SVE92] B.G. Svensson and J.L. Lindström „Generation of divacancies in silicon by MeV electrons: Dose rate dependence and influence of Sn and P" J. Appl. Phys. 72 (1992) 5616.

[SVE93] B.G. Svensson et al. „Generation rate of point defects in silicon irradiated by MeV ions" Nucl. Instr. Meth. B80/81 (1993) 583.

[SZE81] S.M. Sze „Physics of semiconductor devices" 2nd edition, John Wiley & Sons (1981).

[SZE85] S.M. Sze „Semiconductor Devices: Physics and Technology" John Wiley & Sons (1985).

[TR195] M.-A. Trauwaert et al. „Low-temperature anneal of the divacancy in p-type silicon: A transformation from V_2 to V_2O_2 complexes?" Appl. Phys. Lett. 66 (1995) 3057.

[TR295] M.-A. Trauwaert et al. „On the behaviour of the divacancy in silicon during anneals between 200 and 350°C" Mat. Sci. Forum Vols. 196-201 (1995) 1147.

[UHL95] T.-M. Uhlmann „Untersuchungen mit laserinduzierten Stromimpulsen an neutronengeschädigten Silicium-Detektoren" diploma thesis, Universität Hamburg (1995).

[VAS97] A. Vasilescu et al. „Overview on the radiation environment in ATLAS and CMS SCT and the irradiation facilities used for damage tests" ROSE TN 97/3.

[VEC76] J.A. Van Vechten and C.D. Thurmond „Entropy of ionization and temperature variation of ionization levels of defects in semiconductors" Phys. Rev. B14 (1976) 3539.

[VGI89] A. Van Ginneken „Non Ionizing Energy Deposition in Silicon for Radiation Damage Studies", Technical Report FN-522, Fermi National Accelerator Laboratory (1989).

[VLI87] V.A.J. Van Lint „The physics of radiation damage in particle detectors" Nucl. Instr. and Meth. A 253 (1987) 453.

[WAC] Wacker-Chemitronic, 84489 Burghausen, Germany.

[WAI57] T.R. Waite „General Theory of Bimolecular Reaction Rates in Solids and Liquids" J.Chem. Phys. 28 (1958) 1.

[WAT96] S.J. Watts et al. „A new model for generation-recombination in silicon depletion regions after neutron irradiation" presented at the IEEE Nuclear & Space Radiation Effects Conference, 15-19 July 1996.

[WEI91] S. Weiss „Halbleiteruntersuchungen mit dem DLTFS (Deep-Level Transient Fourier Spectroscopy-) Verfahren" PhD thesis Gesamthochschule Kassel, Universität des Landes Hessen (1991).

[WOL69] H.F. Wolf „Silicon Semiconductor Data" International Series of Monographs on Semiconductors, Pergamon Press (1969).

[WUI96] R. Wunstorf et al. „Investigations of donor and acceptor removal and long term annealing in silicon with different boron/phosphorus ratios" Nucl. Instr. and Meth. A377 (1996) 228.

[WU296] R. Wunstorf et al. „Simulation of Irradiation-Induced Surface Effects in Silicon Detectors", proceedings of the International Conference on Radiation Effects on Semiconductor Materials, Detectors and Devices, Firenze, Italy 1996, to be published in NIM Section A.

[WUN91] R. Wunstorf et al. „Radiation damage of silicon detectors by monoenergetic neutrons between 1 and 14 MeV and 1.8 MeV electrons" Nucl. Phys. B 23A (1991) 324.

[WUN92] R. Wunstorf „Systematische Untersuchungen zur Strahlenresistenz von Silizium-Detektoren für die Verwendung in Hochenergiephysik-Experimenten" PhD thesis, University Hamburg, see also DESY FH1K-92-01 (1992).

[WUN96] R. Wunstorf et al. „Damage-induced surface effects in silicon detectors" Nucl. Instr. and Meth. A 377 (1996) 290.

[YOI83] O. Yoshie and M. Kamihara „Photo-Induced Current Transient Spectroscopy in High-Resistivity Bulk Material" Jap. J. Appl. Phys. 22 (1983) 621.

[ZHA93] X.D. Zhan and G.D. Watkins „Electron paramagnetic resonance of multistable interstitial-carbon-substitutional-group-V-atom pairs in silicon" Phys. Rev. B 47 (1993) 6363.

[ZIE68] A. van der Ziel „Solid State Physical Electronics" 2nd Edition, Prentice-Hall (1968).

[ZIE77] J.F. Ziegler Volume 3 (Hydrogen) and 4 (Helium) of „The Stopping and Ranges of Ions in Matter" Pergamon Press, New York (1977).

[ZIO91] H.-J. Ziock et al. „Tests of the Radiation Hardness of VLSI Integrated Circuits and Silicon Strip Detectors for the SSC Under Neutron, Proton, and Gamma Irradiation" IEEE Trans. NS 38 (2) (1991) 269.

[ZIO94] H.-J. Ziock et al. „Temperature dependence of the radiation induced change of depletion voltage in silicon pin detectors" Nucl. Instr. and Meth. A 342 (1994) 96.

[ZUL89] W. Zulehner „Defects in CZ Silicon" p. 127 in Semiconductor Silicon edited by G.C. Harbeke and M.J. Schulz, Springer-Verlag Berlin Heidelberg 1989, see also [LB89].

Acknowledgements

I would first like to express my deep appreciation to all members of the 'Gruppe Nukleare Meßtechnik' at the University of Hamburg for their continuous support of this work. I am especially grateful to Prof. Dr. Dr. hc. Gunnar Lindström and Dr. Eckhart Fretwurst for supervising this thesis and for their tireless assistance.

I am further indebted to the people manufacturing test structures in our semiconductor lab and providing invaluable technical support: Dipl. Ing. Uwe Pein, Sascha Epifantsev, and Peter Buhmann. Thanks are also due to the MPI Munich for providing test devices. To my colleagues in physics, Torsten Schulz and Michael Moll, I am indebted for generous advice and suggestions. I thank the diploma students Jens Gerhardt, Parwin Heydarpoor, Carsten Osius, Philipp Schlichthärle, and Thomas-Michael Uhlmann for constructive comments and for their assistance on the examination of innumerable samples. Further, for general contributions to social life I thank Uwe Bokelbrink, Michael Henkel, Wolfgang Hildesheim, Martin Kuhnke, Gerald Lopez, Jörn Luckow, Enrico Panaro, Christian Schütze, and Mattias Seidel.

I would like to thank the various persons enabling the access to the irradiation facilities: Dr. R. Böttger, Dr. H. Schölermann, and the steering crew at the PTB, Dr. A. Hess, H. Thurmann, and M. Thom at the UKE, and R. Horisberger, K. Gabathuler, and R. Frosch at the PSI. Special thanks go to Francois Lemeilleur and Andreas Rolf for exposing samples at the CERN PS, and to Jim A. Kierstaed and Zheng Li for supervising the ^{60}Co-gamma irradiations at the BNL. Moreover, I wish to thank M. Niecke and D. Vogt (University Hamburg) for providing the proton micro-beam facility and the scanning electron microscope, respectively.

With respect to the projections of the damage at ATLAS I have benefit significantly from suggestions made by Alexander Chilingarov and Shaun Roe. For supplying raw data for the compilation of damage constants I would like to thank Steve Bates (Cambridge University), Francois Lemeilleur (CERN ECP), Hans Ziock (LANL), Geoffrey Hall (London Imperial College). I would like to single out William Grant Gorfine (Melbourne University) for tirelessly providing the particle fluxes.

I wish to thank Zheng Li and Chengji Li, who encouraged me to undertake microscopic defect studies. Thanks are further due to Vladimir Eremin for setting up the TCT apparatus and working on the analysis of TCT signals. I am grateful to Renate Wunstorf and Ugo Biggeri for many valuable suggestions. Finally, I would like to appreciate the continuous and fruitful discussions within the CERN collaborations RD2, ATLAS, and RD48 (ROSE).